Molecular beam epitaxy of van der Waals heterostructures based on ferromagnetic Cr2Te3 for spintronics

Quentin Guillet

To cite this version:

Quentin Guillet. Molecular beam epitaxy of van der Waals heterostructures based on ferromagnetic Cr2Te3 for spintronics. Condensed Matter [cond-mat]. Université Grenoble Alpes [2020-..], 2023. English. NNT : 2023GRALY068 . tel-04536816

HAL Id: tel-04536816
https://theses.hal.science/tel-04536816

Submitted on 8 Apr 2024

HAL is a multi-disciplinary open access archive for the deposit and dissemination of scientific research documents, whether they are published or not. The documents may come from teaching and research institutions in France or abroad, or from public or private research centers.

L'archive ouverte pluridisciplinaire **HAL**, est destinée au dépôt et à la diffusion de documents scientifiques de niveau recherche, publiés ou non, émanant des établissements d'enseignement et de recherche français ou étrangers, des laboratoires publics ou privés.

THÈSE

Pour obtenir le grade de

DOCTEUR DE L'UNIVERSITÉ GRENOBLE ALPES

École doctorale : PHYS - Physique
Spécialité : Physique de la Matière Condensée et du Rayonnement
Unité de recherche : Spintronique et Technologie des Composants

Réalisation d'hétérostructures van der Waals à base de l'alliage ferromagnétique Cr_2Te_3 par épitaxie par jets moléculaires pour la spintronique

Molecular beam epitaxy of van der Waals heterostructures based on ferromagnetic Cr_2Te_3 for spintronics

Présentée par :

Quentin GUILLET

Direction de thèse :

Alain MARTY CADRE SCIENTIFIQUE DES EPIC, Université Grenoble Alpes	Directeur de thèse
Matthieu JAMET DIRECTEUR DE RECHERCHE, CEA-Grenoble	Co-directeur de thèse

Rapporteurs :

Pierre SENEOR
PROFESSEUR, Université Paris Saclay
Marcelo LOPES
DIRECTEUR DE RECHERCHE, Paul Drude Institut Berlin

Thèse soutenue publiquement le **6 novembre 2023**, devant le jury composé de :

David Ferrand PROFESSEUR, Université Grenoble Alpes	Président du Jury
Pierre SENEOR PROFESSEUR, Université Paris Saclay	Rapporteur
Marcelo LOPES DIRECTEUR DE RECHERCHE, Paul Drude Institut Berlin	Rapporteur
Lisa MICHEZ PROFESSEURE, Université de Aix-Marseille II et III	Examinatrice
Massimiliano MARANGOLO PROFESSEUR, Sorbonne	Examinateur

Invités :

Alain MARTY CADRE SCIENTIFIQUE DES EPIC, Université Grenoble Alpes	Directeur de thèse
Matthieu JAMET DIRECTEUR DE RECHERCHE, CEA-Grenoble	Co-directeur de thèse
Hervé BOUKARI INGENIEUR CHERCHEUR, Institut Néel	Encadrant de thèse

Abstract

The field of spintronics aims at using the spin degree of freedom of electrons to store and transport information. In this sense, achieving large-scale growth of two-dimensional (2D) ferromagnetic materials with high Curie temperature (Tc) and perpendicular magnetic anisotropy (PMA) is highly desirable for the development of ultra-compact magnetic sensors and magnetic memories. The van der Waals (vdW) ferromagnet Cr2Te3 appears as a promising candidate due to the high quality of the interfaces formed with other vdW or 2D materials as well as the possibility to tune its magnetic properties by strain or electric field. In the bulk, the Tc of this ferromagnet is 180 K and the easy axis of magnetization is out-of-plane. First, structural and magnetic characterization of vdW heterostructures of Cr2Te3 on 2D materials were carried out. Samples were grown on the semimetal graphene, the semiconductor WSe2 as well as the topological insulator Bi2Te3. The heterostructures were characterized using a full set of tools ranging from atomic force microscopy (AFM) to study the layer morphology, Raman spectroscopy and x-ray diffraction for the crystal structure, transmission electron microscopy to image the interfaces, Rutherford back scattering (RBS) to determine accurately the stoichiometry and SQUID, MOKE and x-ray magnetic circular dichroism at synchrotron facilities for magnetic properties. The magnetic anisotropy of thin films (5 unit cell thick) is found to be dependent on the crystalline structure that is determined by the energy given to the system during growth. The choice of the 2D template for the epitaxy was found not to affect the crystal structure, due to weak vdW interaction. In a second step, the magnetic ordering temperature of the material was tuned with the help of post-growth annealing up to 700°C. An increase of the Tc up to 250 K was measured, associated to a change of the layers composition. Besides, electrical characterization of vdW heterostructures based on Cr2Te3 was carried out to study the Hall resistivity of the film as a function of the electronic band structure and charge transfer with the 2D material substrate. Spin-orbit torques induced by Bi2Te3 were finally measured for the electrical control and reversal of the magnetization of the 2D ferromagnetic layers.

Résumé

Un des buts de la spintronique est d'utiliser le degré de liberté de spin des électrons afin de stocker et d'utiliser des informations. En ce sens, réussir la croissance sur de larges surfaces de matériaux bidimensionnels (2D) ferromagnétiques ayant une haute température de Curie (Tc) et une anisotropie perpendiculaire magnétique est hautement importante pour le développement de capteurs et de mémoires magnétiques ultra-compactes. Le matériau van der Waals (vdW) Cr2Te3 est un candidat prometteur grâce à la bonne qualité des interfaces formées avec d’autres matériaux vdW ou 2D, ainsi que par la possibilité de contrôler ses propriétés magnétiques par des contraintes ou un champ électrique. Pour échantillon massif, la Tc de ce matériau est de 180 K et son axe d’aimantation facile est hors du plan. Premièrement, des caractérisations structurelles et magnétiques d’heterostructures vdW à base de Cr2Te3 sont présentées. La croissance des échantillons a été réalisée par épitaxie par jets moléculaires sur des couches du semi-métal graphene, du semi-conducteur WSe2 ainsi que de l’isolant topologique Bi2Te3. Ces heterostructures ont été étudiées à l’aide de multiples techniques expérimentales telles que la microscopie à force atomique pour vérifier la surface des couches, la spectroscopie Raman et la diffraction aux rayons X pour la structure cristalline, la microscopie par transmission électronique pour imager les interfaces, la rétrodiffusion Rutherford afin de de déterminer précisément la stœchiométrie et enfin par SQUID, MOKE et dichroïsme circulaire magnétique au synchrotron pour les propriétés magnétiques. La dépendance de l’anisotropie magnétique de fines couches (d’une épaisseur de 5 mailles cristallines) en fonction de la structure cristalline est mise en évidence, qui est elle-même déterminée par l’énergie fournie au système durant la croissance. Le choix de la couche 2D sous le Cr2Te3 n’affecte pas la croissance de ce dernier par conséquence des faibles interactions vdW. Dans un second temps, la température de transition de phase magnétique du matériau a été modifiée à la suite de recuits jusqu’à 700°C. Une augmentation de la Tc jusqu’à 250 K a été mesurée et corrélée avec un changement de la stœchiométrie des couches. De plus, des mesures de transport électrique ont été réalisées sur des heterostructures à base de Cr2Te3 afin d’étudier la dépendance de la résistivité transverse dans des barres de Hall en fonction de la structure de bandes du matériau ferromagnétique et de potentiels transferts de charges avec les matériaux 2D à proximité. Enfin, les couples spin-orbites induits par des couches de Bi2Te3 interfacées avec du Cr2Te3 ont été mesurés afin d’obtenir, par des courants électriques, un contrôle et même le retournement de l’aimantation.

Contents

Acknowledgements

First and foremost, I want to express my deepest gratitude to all the people who contributed to my PhD work and that helped within and outside the lab during these three years of my PhD. I will write this part in french, and the rest of the manuscript in english.

Tout d'abord, je voudrais remercier David Ferrand pour avoir accepté de présider mon jury de thèse et pour ses remarques attentionnées et pleines d'enseignement lors de ma soutenance. Je souhaite aussi remercier Marcelo Lopes et Pierre Seneor pour avoir corrigé mon manuscrit et pour leurs questions pertinentes. Je remercie enfin Lisa Michez et Massimiliano Marangolo pour avoir été présents lors de ma soutenance et pour l'intérêt qu'ils ont porté à mon travail.

Je remercie par ailleurs Lucian Prejbeanu et Olivier Fruchart pour m'avoir accueilli à Spintec dans l'institut qu'ils dirigent avec bienveillance et une recherche continuelle d'optimisation des conditions de travail. Ils resteront des exemples de management pour le reste de ma carrière. Je remercie également l'École Polytechnique pour avoir accepté de financer ma thèse via le biais de l'Université Grenoble Alpes.

Je voudrais rendre un vrai hommage à Matthieu Jamet, pour avoir accepté de me prendre dans son équipe et m'avoir proposé un sujet de thèse. Je n'aurais jamais pu mener ce projet à bien sans ses conseils et ses enseignements. Matthieu se rend sans cesse disponible auprès des étudiants afin de nous montrer sa passion pour la physique et tout son savoir expérimental. J'ai également adoré toutes nos discussions et mon seul regret aura de n'avoir finalement jamais pu aller skier ou jouer une partie de squash ensemble ! De la même façon, j'associe Alain Marty et Hervé Boukari pour leur soutien pendant ces trois années et tout ce qu'ils m'ont appris: Alain est une bible de la cristallographie et de la MBE, son savoir m'aura toujours bluffé et Hervé m'a appris tellement d'astuces qui ont énormément simplifié mon travail au laboratoire. Son sens pratique et sa joie au boulot ont été une source infinie de motivation et un réel plaisir de travailler ensemble.

De manière plus générale, j'adresse mes remerciements à toute l'équipe 2D: Céline Vergnaud pour tous ses enseignements sur les techniques de nanofabrication et pour nos pauses cafés vives en couleurs, Frédéric Bonell pour sa connaissance du magnétisme et nos échanges fructueux sur la MBE 1. Isabelle de Moraes, qui est arrivée au milieu de ma thèse, a été un vrai soleil pour toute l'équipe tant sa bonne humeur et ses solutions à tous nos problèmes imaginables sont sans limite. Enfin, je veux remercier tous les post-docs que j'ai pu côtoyer en commençant par Mario Ribeiro et ses blagues, Victor qui n'est malheureusement pas resté assez longtemps pour que l'on fasse mieux connaissance, Jules Courtin pour qui les expériences n'avaient aucun secret et Vincent Polewczyk pour toutes nos discussions au labo comme à l'extérieur. Par ailleurs, je veux saluer Hasan Abdukayumov, qui a effectué sa thèse en même temps que moi et avec qui j'ai pu passé de super moments. Nous avons été pendant longtemps les exilés du C5, mais grâce à lui et la fin de la pandémie, nous avons pu nous intégrer avec tout le reste de l'institut et passer de belles années à Grenoble. Son amabilité et sa gentillesse auront été un grand soutien. Enfin,

je remercie Mohamed pour son passage en stage chez nous et ses blagues ainsi que Cyriack Jego, qui aura la joie (espérons :)) d'effectuer sa thèse dans la continuité des recherches que nous avons effectuées.

Tout mon travail n'aurait jamais pu aboutir sans les nombreuses collaborations de notre groupe. Je remercie tout d'abord l'équipe des calculs ab initio de Spintec et notamment Mairbek Chshiev pour son analyse et nos discussions et surtout Libor Vojacek pour son intelligence, sa gentillesse et son énergie infinie. Leur apport sur toutes nos mesures de transport nous a permis d'enfin émettre des hypothèses avec une cohérence physique et une crédibilité à la fois qualitative et quantitative. Je remercie Djordje Dosenovic et Hanako Okuno pour leurs participations régulières à nos réunions d'équipe et leur apport significatif sur la compréhension de nos empilements grâce à leurs images de microscopie des coupes de nos échantillons. Je remercie Denis Jalabert pour ses explications et ses analyses des mesures de stœchiométrie par RBS, ainsi que Jean-François Jacquot pour tout son soutien sur les mesures SQUID. Son ingéniosité nous a sorti de nombreux problèmes ! Je remercie toute l'équipe de la ligne DEIMOS au synchrotron Soleil pour leur aide précieuse lors de nos semaines d'expérience et notamment Fadi Choueikani pour sa patience et tout le temps consacré, y compris le soir et le week-end. J'adresse aussi des remerciements à Roberto Sant pour nous avoir accordé du temps de faisceau au synchrotron ESRF afin de mener des études préliminaires sur nos matériaux. Je remercie enfin tout le personnel de la PTA pour leurs formations et leur encadrement de la zone technique dédiée à la nanofabrication ainsi que Vincent Renard et Abelkarim Ouerghi pour nous avoir fourni de nombreux échantillons de graphène qui ont servi de terreau pour le développement de nos matériaux.

Je souhaite de plus remercier tous les professeurs qui m'ont tant appris depuis de longues années. Je souhaite avant tout remercier Wolfgang Kuch, qui m'a pris dans son groupe à Berlin pour ma deuxième année de master et qui m'a initié à la MBE et aux mesures en synchrotron. Mon année dans son équipe aura été rayonnante malgré la pandémie de COVID 19. Je remercie également Ziliang Ye, qui m'a fait découvrir les matériaux bidimensionnels pendant mon M1 lors d'un stage de recherche à l'université de Vancouver. Enfin, je voudrais saluer Mme Gillette, qui m'a donné le goût de la physique lors de ma première année de classe préparatoire à Versailles.

Enfin, je veux exprimer ma joie d'avoir pu rencontrer tant de belles personnes au labo qui sont maintenant devenus des amis. Je ne peux pas toutes les citer, mais je les remercie de m'avoir fait passer de belles années et d'avoir été présents à ma soutenance. Je remercie aussi tous mes amis d'avant qui ont su me remonter le moral quand nécessaire et surtout me faire rire.

Je remercie toute ma famille, pour s'être déplacée jusqu'à Grenoble à de nombreuses reprises, y compris pour assister à la longue séance de questions de ma soutenance. J'espère avoir réussi à leur partager mon intérêt pour notre travail et leur avoir montré notre engagement et les enjeux de nos recherches. Je les embrasse et je sais que je pourrai compter sur eux toute ma vie, comme ils peuvent compter sur moi.

Et last but not least comme disent les anglais, je remercie énormément ma très chère Marine. Je ne pourrais citer toutes les raisons et ce n'est de toute façon pas le lieu, mais son soutien à Grenoble et tous nos moments de complicité n'ont pas de prix ni de mots pour être pleinement exprimés. J'espère pouvoir la soutenir aussi bien pour sa soutenance qu'elle l'a fait pour moi. Ces quelques moments de repos après ces trois dernières années vont être pour nous l'occasion de continuer à s'accompagner en toutes circonstances, et je suis persuadé que cela nous mènera tous les deux vers un avenir radieux.

Preamble

The continuous downsizing of electronic devices since the discovery of the transistor in the 1950s is limited nowadays by quantum limits emerging for few nanometers-size architectures. New approaches are therefore required in order to keep improving the performance of computers and electronic chips. The field of spintronics proposes solutions, where the spin degree of freedom of electrons is used as a way to store information, using the giant magnetoresistance effect, but also to transport it, with spin polarized or pure spin currents, and to manipulate it thanks to electrical torques. Heterostructures are developed to bring in proximity ferromagnetic materials with a net remanent magnetization, in order to store information without the need of an external magnetic field, with source of spin currents, to be able to control the magnetization using only electrical means.

One of the current cHallenge for these technologies is the realisation of atomically sharp interfaces. This is required to avoid scattering effects between the materials that would limit the spin diffusion length as well as the efficiency of the described architectures. The discovery of two-dimensional (2D) and van der Waals (vdW) materials with the exfoliation of graphene in 2004 by A. Geim and K. Novoselov opened new opportunities for the realisation of ultra clean interfaces. These materials only exhibit weak vdW interactions between the different atomic planes. This allows the stacking of any material of this family without matching restrictions of the in-plane lattice parameters. Ever since the discovery in 2017 of ferromagnetism down to the monolayer (ML) limit with CrI_3 and $CrGeTe_3$, intense research has been carried out to develop new vdW heterostructures exhibiting high T_C and the possibility to manipulate efficiently the magnetization thanks to spin-orbit torques (SOTs).

During my PhD work, I developed the growth by molecular beam epitaxy (MBE) of the vdW ferromagnet Cr_2Te_3, that is a promising candidate for the field of spintronics. It exhibits in the bulk strong perpendicular magnetic anisotropy (PMA) and a T_C of 180 K, with highly tunable magnetic properties, as will be detailed in this manuscript. VdW heterostructures were achieved of Cr_2Te_3 on other promising layered materials such as the 3D topological insulator (TI) Bi_2Te_3 the transition metal dichalcogenides (TMD) semiconductor WSe_2 or the semimetal with linear energy dispersion graphene. The aim of this thesis was to characterize these heterostructures and to tune their growth conditions in order to obtain large-scale deposition (of the order of few cm^2) with close to room temperature (RT) operation.

The first chapter of the manuscript is an introduction to 2D and vdW materials and their unique properties. The main discoveries over the past 20 years are detailed with a thorough description of their crystalline and electronic properties. The bases of magnetism are also explained and a literature review of the reported properties in 2D and vdW ferromagnets is conducted. Finally, the important advances of the field of spintronics are discussed in order to present the bases of my PhD work.

In the second chapter, the various experimental techniques that were used for this project are detailed. First, the operation of an MBE chamber is explained as well as the working principle of the in-situ electron diffraction. Further structural characterization tools are introduced such as x-ray diffraction

(XRD), atomic force microscopy (AFM), Raman spectroscopy, scanning transmission electron microscopy (STEM) and Rutherford backscattering spectrometry (RBS). The magnetic properties of the grown layers were investigated using magneto-optical Kerr effect (MOKE), superconducting quantum interference device (SQUID) and x-ray magnetic circular dichroism (XMCD). Finally, electrical measurements techniques are presented such as Hall bars patterning and low temperature DC and AC experiments.

Chapter 3 reports on the epitaxial growth of thin films of Cr_2Te_3 (5 unit cells thick) on 2D materials. The crystal structure is studied carefully with a determination of the lattice structure using XRD, of the film stoichiometry with RBS and with an imaging of the interface thanks to cross-sectional STEM. Despite the large lattice mismatch with the underlying 2D materials, a relaxed structure for Cr_2Te_3 layers is found. Sharp interfaces separated by a vdW gap are revealed between the 2D and vdW materials. Moreover, the energy given to the system during growth, in the form of the sample temperature, is determined to be the driving factor to control the crystal structure of the ferromagnet. Finally, magnetic measurements evidence a T_C close to the bulk value of 180 K for these thin films and a correlation between the magnetic anisotropy energy and the crystal structure. *Ab initio* calculations are also performed to confirm these experimental observations.

In chapter 4, an annealing study of thin Cr_2Te_3 films grown on graphene/SiC is presented. The goal is to achieve a change of the stoichiometry of the layers in order to tune their magnetic properties. Samples are heated for 10 min after growth under Te flux at temperatures ranging from 450°C to 700°C. An increase of the Cr:Te ratio is verified using RBS and is associated to an increase of the T_C up to 250 K. An analysis of the crystal structure is also performed and changes of the magnetocrystalline anisotropy are evidenced with XMCD experiments at the Soleil synchrotron.

Electrical measurements on Cr_2Te_3 based heterostructures are presented in the fifth chapter. Magneto-transport is studied in Hall bars processed in a clean room environment. The longitudinal and transverse resistivities are measured and the metallic nature of Cr_2Te_3 is evidenced. In a first part, the anomalous Hall effect (AHE) is measured as a function of temperature for Cr_2Te_3 grown on different materials. It is shown that the intrinsic contribution to the AHE, related to the Berry phase of the material, can lead to a sign change of this effect with temperature depending on the Fermi level position and the residual strain in the layers. In a second part, second harmonic measurements are presented in order to evaluate possible spin-orbit torques in Cr_2Te_3/Bi_2Te_3 heterostructures. Using the symmetry of the effects, thermal contributions caused by the anomalous Nernst effect (ANE) are subtracted from experimental observations, and a strong field-like torque is measured.

Finally, preliminary results of MBE growth of a new class of material are presented. The type II Weyl semimetals have exotic spin textures that can be used for very efficient spin-charge interconversion. 1T'-WTe_2 is a 2D material with distorted crystal structure exhibiting unique properties, as presented in this chapter. The epitaxial growth on graphene/SiC is also detailed as well as the structural characterization of the obtained layers. Besides, another way to tune the properties of Cr_2Te_3 is presented with the incorporation of Sn in the material (the targeted phase is $CrSnTe_3$, from the same family as $CrGeTe_3$). An increase of the T_C up to 280 K is reported with a conservation of the perpendicular magnetocrystalline anisotropy.

CHAPTER

1

Introduction to magnetism and spintronics in low-dimensionality

1.1 Introduction to two-dimensional materials

1.1.1 Crystallographic structure

In order to properly introduce 2D materials, one has to come back to the definition and the properties of a crystal. Taken from the encyclopedia Britannica [1], the definition states: “A crystal is any solid material in which the component atoms are arranged in a definite pattern and whose surface regularity reflects its internal symmetry.” The keywords here to understand a crystal are pattern and symmetry, which will be discussed in details in this manuscript.

1.1.1.1 Bravais lattices and reciprocal space

First of all, the different patterns of crystals will be introduced. Two elements are needed to characterize a crystal: the basis, which will be reproduced and the lattice, which describes how or where the basis will be replicated.

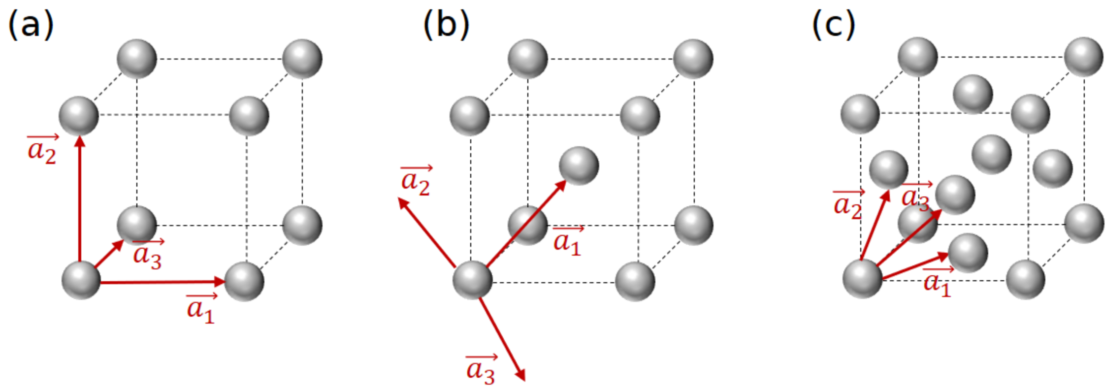

Figure 1.1: Examples of cubic Bravais lattices and primitive lattice vectors. (a) Simple cubic. (b) Body centred cubic. (c) Face centred cubic.

The most simple example will be a basis consisting of one atom reproduced periodically along all the directions, which gives a simple cubic lattice. However, most metals found in the nature like iron or gold are crystallized in a slightly different structure, as illustrated in Fig. 1.1. In the nature, Fe atoms are found structured along a body centered cubic (bcc) lattice (Fig. 1.1.(b)) and Au ones in a face centered cubic (fcc) lattice (Fig. 1.1.(c)).

In order to define a Bravais lattice [2], three vectors are needed: examples are given for each cubic lattice in Fig. 1.1. They are used to define a coordinate system to locate any point in space and they must not be coplanar. The volume formed by these vectors (see the cubes in Fig. 1.1) is called a unit cell. It is a piece of the lattice that can be replicated along the lattice in order to reproduce the crystal. The vectors and unit cells are defined as primitive if they form one of the smallest unit cell that allows to reproduce the crystal when duplicated in every direction. Examples of primitive vectors are indicated in red in Fig. 1.1. Every site in a Bravais lattice is equivalent (which means that it is invariant under a translation of any primitive vector) and has the same number of nearest neighbours (the closest sites for any site in the lattice) also called coordination. The formation of any real crystal results from the minimization of the potential energy from the positioning of the elements summed with the entropy cost related to the temperature. Condensed structures with large coordination are usually more stable explaining why bcc (coordination of 8) and fcc (coordination of 12) are much more common in nature than simple cubic lattices (coordination of 6).

The second element needed to describe a crystal is the basis, which will be reproduced at each point of a Bravais lattice. Unlike in the picture of Fig. 1.1, the basis is not a point, even in the case of a single atom, which has its own volume. Moreover, the basis can consist of several atoms (for instance in the case of salt, with one atom of each species Na and Cl, as shown in Fig. 1.2). Here a large unit cell is displayed, evidencing the cubic character of the crystal. Nevertheless, the primitive unit cell consists of the volume around the basis shown in red delimited by half of the distance to the nearest neighbours. In order to obtain one primitive unit cell, one can draw the medians between the neighbouring atoms: the obtained volume is called the Wigner-Seitz unit cell.

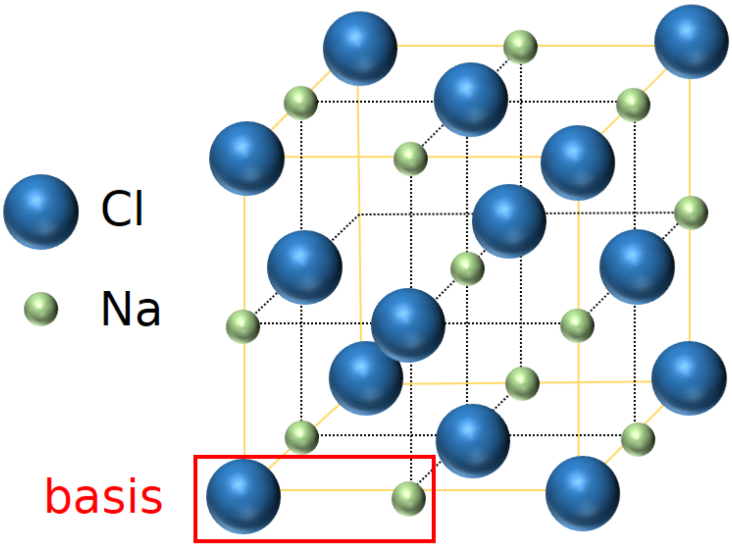

Figure 1.2: Crystal structure of salt with the basis highlighted in red.

Another way to see this structure is two fcc sublattices for each element translated by half of a cube edge. However, the representation of a unit cell with the two elements (where again, the atoms do not equal lattice sites) is the most intuitive way to understand the crystal structure of salt, as it describes in one figure both the lattice and the basis.

Finally, the concept of reciprocal space will be introduced and its utility will be evidenced later notably with the diffraction experiments on various crystals. As explained earlier, a Bravais lattice is defined by three non coplanar vectors that will be called $\vec{a}_1$, $\vec{a}_2$ and $\vec{a}_3$. The reciprocal space is another Bravais lattice defined with the vectors $\vec{a}_1^*$, $\vec{a}_2^*$ and $\vec{a}_3^*$ such that for i, j in $\{1, 2, 3\}$.

$$\vec{a}_i.\vec{a}_j^* = \begin{cases} 0, & \text{if } i \neq j \\ 2\pi, & \text{if } i = j \end{cases}$$

In such periodic lattice, electrons are described by Bloch states and the reciprocal space is equivalent to the electron momentum space. It allows to define the electron velocity in the crystal as the group velocity of an electron wave packet. Electrons are also assigned an effective mass related to the curvature of the energy dispersion curve.

1.1.1.2 Specificity of 2D materials and van der Waals interactions.

The first definitions and descriptions of lattices mentioned above characterize any crystallized material. The specificity of 2D materials will now be introduced and discussed. The bonds between atoms and molecule are electrostatic interactions, and their strength decreases very rapidly with the distance in between them. Therefore, in the case of a gas, atoms or molecules are quasi not bonded to another and mostly act as free particles in space. In condensed matter (liquid or solid), the atoms or molecules are on the other hand interacting. The strongest bonds are the ones inside a molecule: covalent or ionic bonds. The wave functions of neighbouring atoms overlap and the energy needed to break these bonds is very large (of the order of several eV). In a liquid, the bonds between the molecules are rather weak in comparison and can be of several origins: hydrogen bonds or vdW interactions (of the order of tens to hundreds of meV). In a 3D solid, all the atoms are connected through strong bonds, which explains the rigidity of solids. In a 2D material (which is also a solid), atoms organize in planes or layers, where they are connected to their neighbours with covalent or ionic bonds. However, these layers are only weakly bonded by vdW interactions, that originate from dipolar attractions and which are detailed just below in Fig. 1.3.

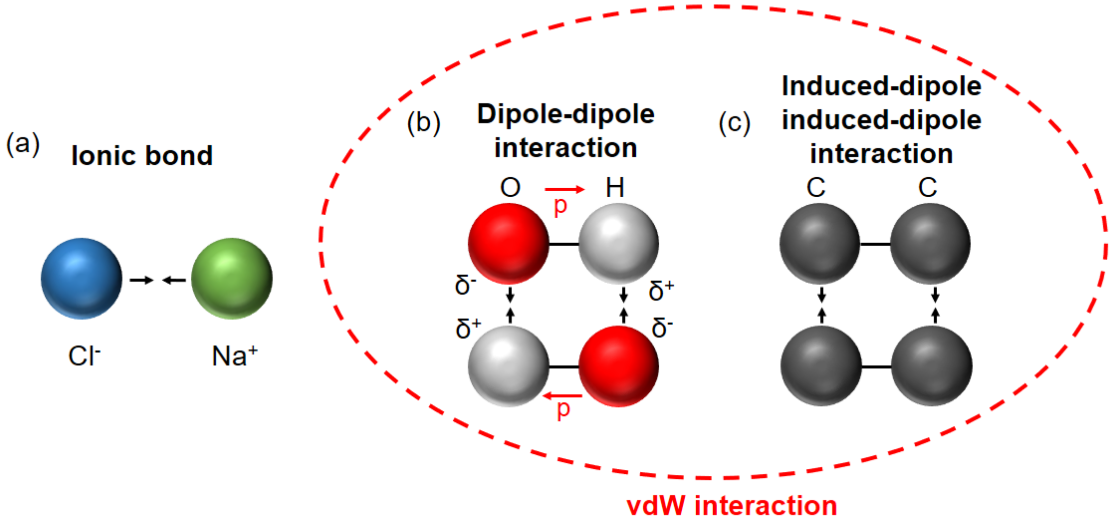

Figure 1.3: Electrostatic bonds between atoms. (a) Bond between two ions. The two opposite charges attract each other and create a strong bond. (b) Bond between two dipoles. Oxygen is more electronegative than hydrogen, resulting in a fraction of an electron charge carried by the oxygen and depleted from the hydrogen. The bond with an opposite dipole is attractive but weaker than the ionic bond due to the lower charge. (c) Bond between two induced dipoles. On average, carbon atoms will not hold any charge due to symmetry but Brownian displacement of electrons will give rise to transient dipoles that can attract each other. This bond is the weakest.

The absence of covalent bond perpendicular to the layer planes has many consequences that affect drastically the properties of 2D materials. As explained above, vdW interactions are quite weak and as a result, the neighbouring planes are much more distant than the nearest atoms inside a plane. Electrons will be therefore mostly confined inside one layer plane. Confinement at the nanoscale implies a lot of quantum consequences, as will be shown with all the exotic properties of 2D materials. Their electronic properties are notably very different compared to classical 3D solids as will be shown in the next section with the examples of graphene and TMD. Another consequence of the vdW interaction between the layers is the ability to create heterostructures of 2D materials without any crystallographic matching consideration [3]. For 3D materials, when trying to grow a crystal on top of another one (the substrate) with different lattice parameters, the grown crystal will first experience strain to match the lattice structure of the substrate. This is induced by the dangling bonds at the interface of the substrate. After a certain thickness, the energy associated with this strain will be released and the crystal on top will relax to its most stable phase. Dislocations form that alter the crystallographic order of the material. Therefore, it is usually required to grow 3D crystals on a substrate with matching crystal symmetries and lattice parameters. In the 2D case, the lack of these dangling bonds releases this constraint, allowing the image of "Lego" blocks that can be freely stacked following the imagination of scientists, as pictured in Fig. 1.4.

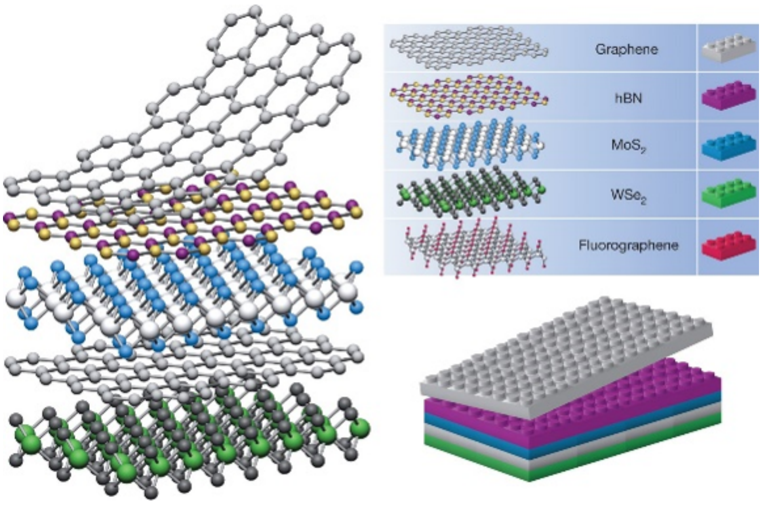

Figure 1.4: Stack of several 2D materials taken from [3]. The ability to bring in proximity very different materials with different intrinsic properties such as superconductivity or ferroelectricity opens the way for the discovery of new physical effects.

1.1.2 Brief historical overview and examples of 2D materials

1.1.2.1 The discovery of graphene by exfoliation

For a long time, the scientific community believed that 2D materials could not exist due to their environmental instability [4]. The suffix "ene", used to designate one layer foil of a material was introduced by Boehm in 1962 and some works dedicated to the atomic structure and the electronic properties of germanene and silicene were already carried out in 1994 [4]. Then, the works on linear structures of carbon like the carbon nanotubes from 1991 eventually led to the discovery in 2004 of graphene by K. S. Novoselov et al. [5], which was the final proof of the stability of 2D materials down to the monolayer (ML) limit.

As stated just above, graphene layers are carbon planes which were mechanically separated from graphite for the first time in 2004. To understand what is graphene, one has to know that carbon atoms can arrange in various structures as illustrated in Fig. 1.5. The two most common solid phases of carbon in nature are diamond and graphite, which are both only carbon atoms. Nevertheless, the first one is the hardest material on earth and is transparent to light, whereas the latter is the lead of our pencils and is completely black. It demonstrates again that crystal order drastically affects the properties of the materials. As can be seen in Fig. 1.5.(b), graphite is a stack of graphene sheets. Using mechanical peeling with scotch tape repeatedly, one can obtain very few layers (even single-layer) graphene and transfer it onto another substrate such as Si or SiO$_2$. This technique is called mechanical exfoliation and allows the transfer of very thin flakes without any deterioration of the crystal quality. The typical lateral size of the obtained crystallites is of the order of a few micrometers, which is enough to carry out transport or optical measurements. However, all industrial wafers for electronics have at least several inches of diameter and other preparation techniques yielding larger areas are required for potential applications.

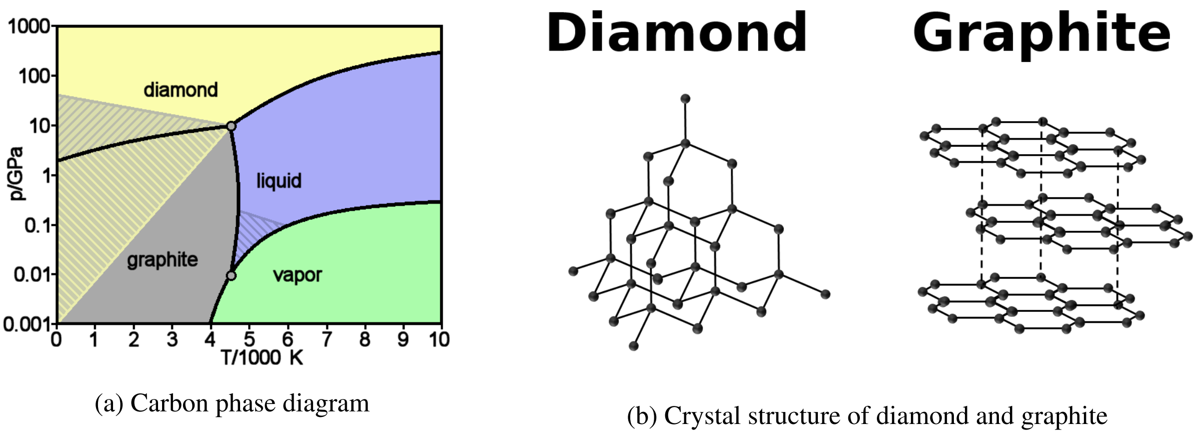

(a) Carbon phase diagram

(b) Crystal structure of diamond and graphite

Figure 1.5: Depending on the pressure and temperature, carbon atoms can arrange in different orders. (a) Phase diagram of carbon taken from [6]. Hatched areas are metastable, where two phases can be found depending on previous conditions, explaining why we can find graphite and diamond in nature. (b) The diamond structure is isotropic in all directions whereas graphite is a stack of 2D graphene layers.

1.1.2.2 Structural and electronic properties of graphene

As shown in Fig. 1.5.(b), carbon atoms organize in an hexagonal lattice for graphene layers, more precisely in a honeycomb lattice sketched in Fig. 1.6.(a). It is a triangular Bravais lattice with a basis of two atoms (the green and the orange ones). In the case of graphene, the two atoms are carbon but they are both needed as the translation from the green to orange atom does not form a vector of the lattice. The shaded area corresponds to one primitive unit cell of the honeycomb lattice. In the reciprocal space, the hexagon shown in Fig. 1.6.(b) is called the first Brillouin Zone (BZ). It is one primitive unit cell of the reciprocal lattice. Different high-symmetry points are evidenced: Γ is the centre of the BZ and K, K' are the 6 corners. This representation is used to describe the electronic states of electrons in the crystal.

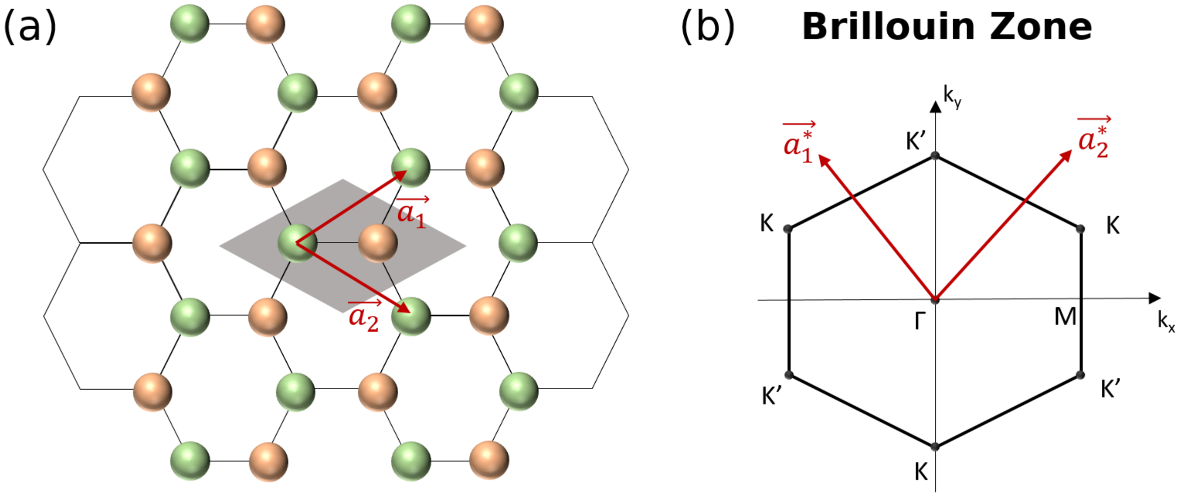

Figure 1.6: (a) The honeycomb lattice can be constructed with a triangular Bravais lattice in the plane with a basis of two atoms (the green and the orange one). A primitive unit cell is shaded in grey. (b) The first BZ and the high-symmetry points of the honeycomb lattice.

By solving Schrödinger's equation for electrons in graphene considering only nearest neighbour interaction, the band structure can be fully calculated using the tight binding model [7] and some unique features are evidenced as shown in Fig. 1.7. First of all, it can be observed that graphene is a semimetal, as the valence and conduction bands meet each other at 6 points in the BZ : the K and K' points. The most remarkable property nevertheless is the energy dispersion of the band around these 6 points. One can show mathematically that the energy is linearly proportional to the momentum, exactly like photons, whose energy are also proportional to momentum. The curvature of an electronic band allows to give an effective mass to the electrons. For graphene, around the K and K' points, the effective mass is zero because of the linear behaviour and the electrons behave as massless particles like photons. This unique band dispersion is called a Dirac cone as shown in Fig. 1.7.(b). One of the consequence of this energy dispersion is the record mobility of large area graphene layers (which is maximum when encapsulated in hexagonal boron nitride (hBN) to protect from defects) up to 70,000 cm^2/Vs at RT and more than 120,000 cm^2/Vs at T=9K [8], which could allow the fabrication of ultrafast electronic devices. hBN is another 2D material, which crystallizes also in a honeycomb lattice where B and N occupy the 2 atomic sites of the basis. It is a very good insulator with a bandgap larger than 6 electronvolt (eV) [9] and it is as well an excellent dielectric layer for the application of an electric field using a bias voltage. These characteristics make hBN a very promising candidate for future 2D heterostructures and a lot of research is dedicated to the growth and the development of this material.

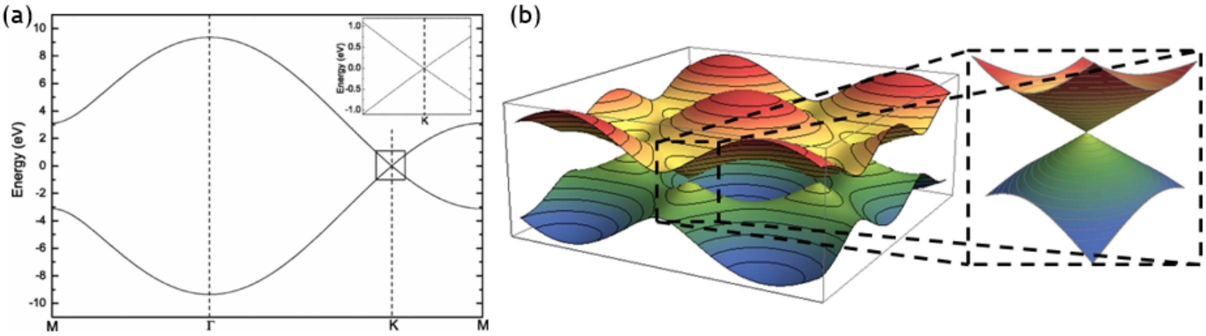

Figure 1.7: (a) Calculated electronic band structure of graphene taken from [7]. Graphene is a semimetal with the valence and conduction bands crossing at K and K'. Energy dispersion around these points is linear, forming the so called Dirac cones. The inset is a zoom of the Dirac cone. (b) 3D visualisation of the bandstructure with a zoom on the Dirac cone.

Nevertheless, to build transistor channels, which are one of the most common elements in microelectronics, semiconducting materials are needed in order to modulate the conductivity of the channel. Moreover, in the field of optoelectronics, a bandgap is necessary for light emission/absorption and the fabrication for instance of lasers or light emitters and sensors. A class of materials very similar to graphene was discovered shortly after that meets these requirements: the TMDs.

1.1.2.3 Transition metal dichalcogenides

TMDs are layered materials of the class MX_2, where M is a transition metal like Mo, W, etc. and X is a chalcogen (S, Se or Te). They have been exfoliated and thinned down to monolayers since 2005, just after graphene. Their crystal structure is sketched in Fig. 1.8 and is very resembling the one of graphene as they share the same lattice. The basis is nevertheless different as each layer of TMD consists of three atomic planes: the one of the transition metal being sandwiched between two chalcogen planes. If the chalcogen are placed exactly on top of each other as in Fig. 1.8, this is called the 1H structure. When the two chalcogen planes are rotated by 60° with respect to each other, the structure is called 1T. Each TMD will have one structure which is more stable than the other and this will impact its physical properties. By choosing appropriate conditions or substrates, metastable structures can also be obtained.

All of the firstly discovered TMDs (MoS_2, $MoSe_2$, WS_2 and WSe_2) are semiconductors with a bandgap between 1 and 2 eV. As shown in Fig. 1.9.(i), they exhibit a transition from an indirect bandgap (the top of the valence band is at a different momentum than the bottom of the conduction band) for bulk and multi-layer films to a direct bandgap semiconductor in the monolayer form due to quantum confinement effects. A direct consequence is a significant increase of the photoluminescence signal because photons

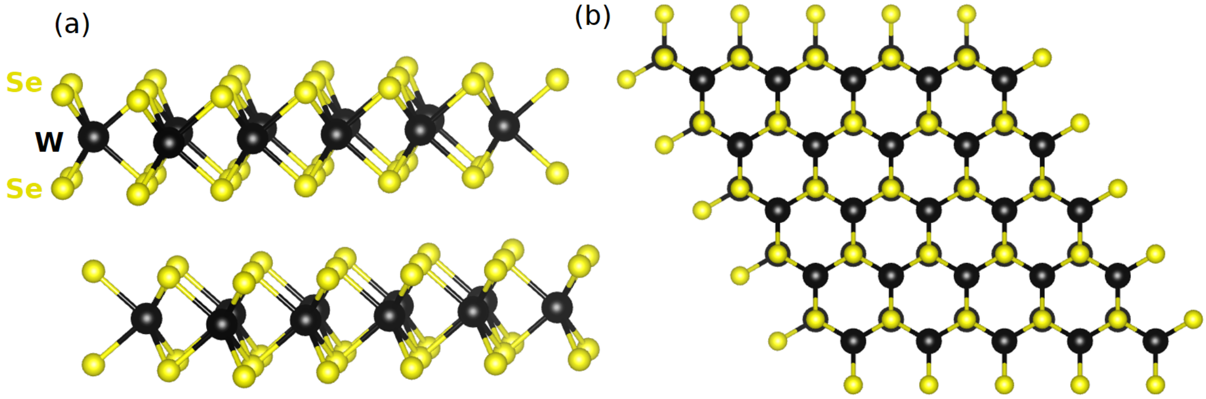

Figure 1.8: Crystal structure of 1H-WSe$_2$, a TMD, visualized with the Vesta software [10]. (a) Side view of 2 layers. The transition metal atom is in between two chacogens planes. (b) Top view. The crystal structure is following the honeycomb lattice with two chalcogens atoms on top and below.

have negligible momentum compared to electrons and because of the conservation law of momentum, the transitions from one electronic band to another by emitting a photon are only vertical transitions in the band structure. In the case of a direct bandgap semiconductor, photon emission is an efficient way for electrons in the conduction band to relax to the valence band. In the case of indirect bandgap, processes including lattice vibrations called phonons will be dominant but less efficient.

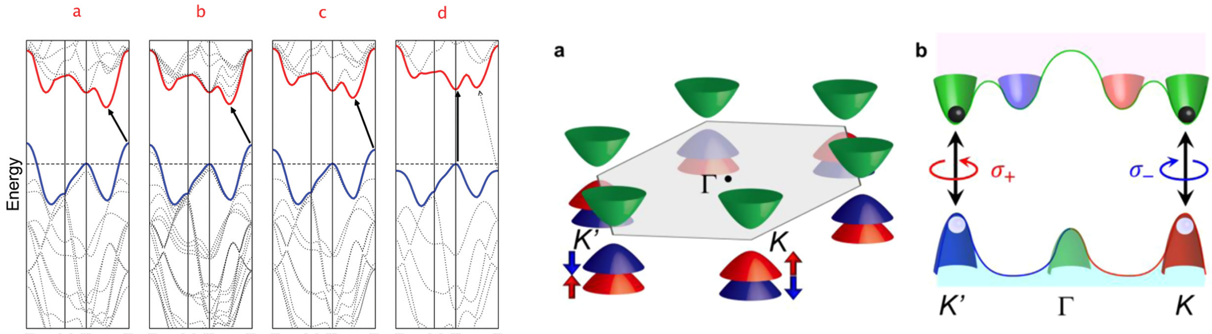

(i) Thickness-dependent band structure

(ii) Valley effect in TMDs

Figure 1.9: (i) Calculated band structure of 1H-MoS$_2$ taken from [11]. a For bulk MoS$_2$, the bandgap is indirect as evidenced by the black arrow. b For 4 layers, the bandgap is still indirect. c Idem for a bilayer. d In the monolayer form, the bandgap is direct at the K point of the BZ. (ii) The valley effect in TMDs taken from [12]. **a** Sketch of the spin splitting of the valence band in energy for each valley. Red and blue bands stand respectively for spin up and down. **b** The top valence band and the selection rule for optical transition according to the light helicity.

Furthermore, due to the presence of elements with larger atomic weight than carbon, spin-orbit coupling (SOC) is much stronger than in graphene [13]. This interaction will be treated thoroughly in section 1.3.1.2. but, as can be seen in Fig. 1.9.(ii), it is causing the spin-valley locking effect in TMDs. SOC lifts the degeneracy of the electronic bands for spin up and down (both in the conduction and the valence band but the effect is one order of magnitude stronger in the valence band). Typical values are of the order of 183 meV for MoSe$_2$ and 456 meV for WSe$_2$ [14]. Because of time-reversal symmetry (K' is the symmetric of K and spin down is the symmetric of spin up), the splitting is opposite in the two valleys (K and K'). Experimentally, one consequence is the ability to access independently one or the other of the valley using Fermi's golden rule. It states that the transition rate from an initial state to a final state after a weak perturbation is proportional to the density of states of the final and initial states as well as the coupling between the two states. For an optical transition (absorption or emission of a photon), this coupling will depend on the scalar product of the electron spin and the light polarization. In the case of circularly polarized light (σ^+ and σ^-), this scalar product will be 1 or 0 depending on the helicity and the spin. Figure 1.9.(ii).**b** shows that if the photon energy is at least equal to the bandgap, optical transitions will be valley dependent according to the light helicity. This intrinsic property of the TMDs could be used to store information (0 and 1 according to the valley) and light could allow to read and write this information, which could be much more energy efficient than today's devices. The absorption of σ^+ (respectively σ^-) circularly polarized light generates electron-hole pairs in the K' (K) valley. Similarly, the emission of photons are associated with the recombination of these pairs. This corresponds the field of valleytronics [15]. Valleys can also be addressed electrically by injecting a spin current or by proximity effects. However, the valley lifetime (the average time before an electron scatters to the other valley) is very short (in the nanosecond range) which represents an experimental challenge for the development of this field.

Today, many more TMDs have been experimentally synthetized with various properties (metallic (1T-TaS_2 [16]), superconducting (1H-$NbSe_2$ [17]), ferromagnetic (1T-$CrTe_2$ [18–20]), etc.). VdW heterostructures of TMDs are also an active field of research notably with the so-called twistronics [21] (two layers with an angle or two layers with a slight lattice mismatch) that form Moiré patterns [22] (substructure forming a lattice with a much larger parameter). Finally, Janus layers have been experimentally obtained and investigated, which are TMDs with two different chalcogens on the top and the bottom layer of the transition metal [23, 24]. They are of particular interest due to the broken mirror symmetry in the system forming ultimately thin polar systems, as shown in Fig. 1.10.

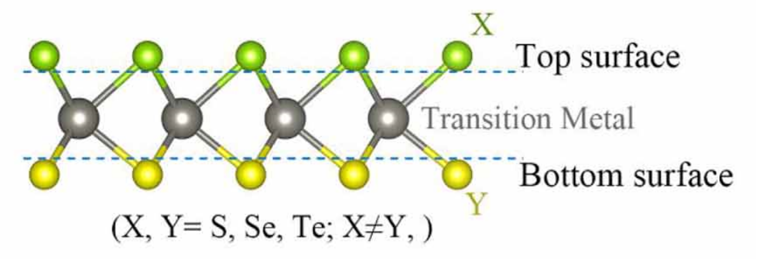

Figure 1.10: Crystal structure of a Janus monolayer, adapted from the reference [25]. The top and bottom atomic planes are composed of two different chalcogens atoms among S, Se and Te.

1.1.2.4 The first 2D ferromagnets and their crystal structure

As mentioned already, one great advantage of 2D materials is the possibility to create an infinity of vdW heterostructures of materials, to bring in contact different materials with various properties. Symmetries in crystals are a key to understand what effects are or not possible. To make new observations, it can be interesting to suppress some symmetry of a system like inversion or time reversal. One possibility, for time reversal symmetry, is to apply a magnetic field but that requires an external factor. Another possibility is to add a layer with a net magnetization, i.e. an unbalance of spin moments. Some materials can retain such a magnetization without any external field: they are called ferromagnets. However, until 2017 and the discovery of $CrGeTe_3$ [26] and CrI_3 [27], no 2D materials exhibited any ferromagnetism. It was even believed that such spin ordering was not possible in the 2D limit, as will be discussed later.

Nevertheless, several materials have been discovered since 2017 and three classes will be presented: the CrX_3, $CrGeTe_3$ and Fe_xGeTe_2. These systems have attracted the most interest in the community due to their early discovery and easy exfoliation for the first two and for its high T_C for the latter one. Several compounds of CrX_3 exist such as CrI_3, $CrBr_3$ and $CrCl_3$. The first two are ferromagnets whereas the latter one is an antiferromagnet but they all share the same lattice structure pictured in Fig. 1.11.(a). Their properties will be further developed after the introduction of magnetism.

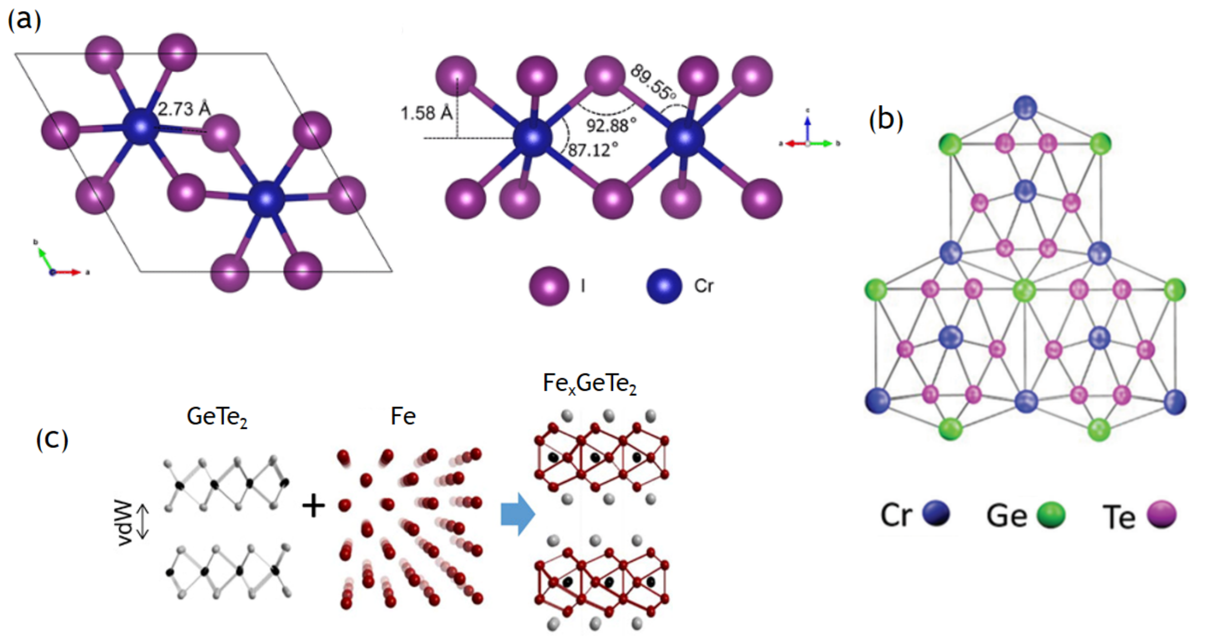

Figure 1.11: (a) Top view and side view of CrI$_3$ crystal, taken from [28]. (b) Top view of the structure of CrGeTe$_3$, extracted from [29]. (c) The crystal structure of Fe$_x$GeTe$_2$ is the sum of the TMD GeTe$_2$ and a bcc Fe lattice (image adapted from [30]).

CrGeTe$_3$ structure is represented in Fig. 1.11.(b). Other materials have a similar structure like CrSiTe$_3$ or CrSnTe$_3$, which will be presented in the perspectives of this manuscript. Finally, Fe$_x$GeTe$_2$ (x = 3, 4 or 5) is a metallic ferromagnet with a structure composed of the sum of the TMD GeTe$_2$ and a bcc Fe lattice as can be seen in Fig. 1.11.(c). The position of the Fe atoms vary with the stoichiometry as well as their coordination, which explains the variation of the reported magnetic properties, discussed in the next section.

1.1.2.5 The Cr$_{1+x}$Te$_2$ family

This family of compounds is going to be at the centre of this thesis's manuscript. Their magnetic and electronic properties will be detailed in the following sections, but their crystal structure will be introduced here. Different structures are obtained depending on the stoichiometry of the compound. Films are indeed experimentally stable for $0 \leq x \leq 1$, x being any number. More precisely, it implies that the number of Cr atoms can vary from one phase to another. Figure 1.12.(a) sketches the crystal structure of Cr$_2$Te$_3$, an example of the Cr$_{1+x}$Te$_2$ family for x=1/3. The crystal is an alternation of Cr and Te planes but half of the Cr planes are only partially filled (the ones with the dark red Cr$_I$ atoms). These planes are called in the literature intercalated planes of Cr atoms even though they belong fully to the crystal structure. They are named so because they separate planes of the TMD 1T-CrTe$_2$, as shown in Fig. 1.12.(a). They are also labelled differently because they have a different chemical surrounding compared to the atoms in the fully occupied planes, as evidenced by the different bonds in Fig. 1.12.(b). Differently to the previously presented 1H-TMDs, the two planes of Te atoms below and above the Cr$_{II}$ atoms are rotated by 60° with respect to each other (1T structure) as can be seen by the lateral shift of the Te atoms on the first two planes in Fig. 1.12.(b). Finally, it has to be noted that when x > 0, Cr$_{1+x}$Te$_2$ compounds are not 2D materials as evidenced by the yellow bonds in Fig. 1.12.(b). Nevertheless, the most stable interface with other 2D materials is a full layer of Te atoms that only bonds through vdW interaction to the neighbouring material forming a vdW gap. Cr$_{1+x}$Te$_2$ layers are therefore called vdW materials. Similarly to graphene and TMDs, Cr$_{1+x}$Te$_2$ films have an hexagonal lattice as can be seen from the top view of the crystal structure in Fig. 1.12.(c).

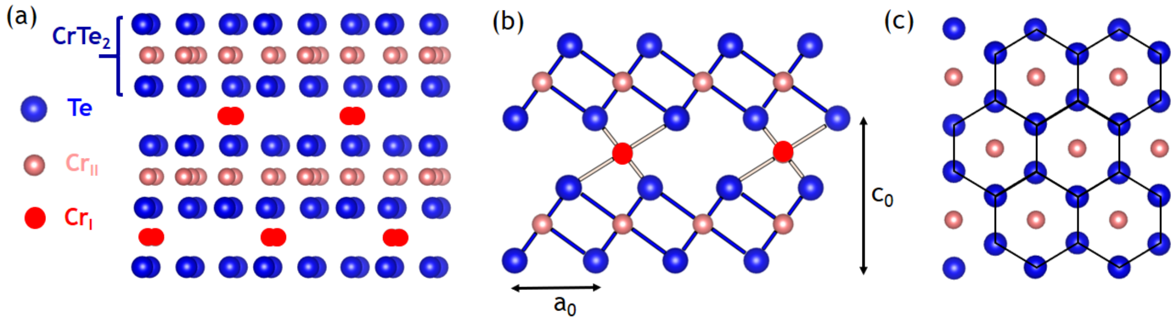

Figure 1.12: Crystal structure of Cr_2Te_3, an example of the $Cr_{1+x}Te_2$ family for x=1/3. (a) Side view of the crystal structure. Blue atoms indicate Te, light red Cr in fully occupied planes and dark red Cr in partially filled planes. (b) Another side view to highlight the rotation of every second Te planes by 60°. In case of x>0, all atoms are linked to another by crystal bonds as shown with the light coloured bonds, meaning the material is not strictly speaking vdW. (c) Top view of the crystal structure showing the hexagonal symmetry in the plane. It has to be noted that the black lines do not indicate covalent bonds, as Te are not nearest neighbours to each others.

All the phases of $Cr_{1+x}Te_2$ have very similar lattice structures both in terms of symmetries and lattice parameters, as can be seen in Table 1.1. In particular, lattice parameters only vary by few percents. The epitaxial growth of $Cr_{1+x}Te_2$ can induce lattice parameter variations in the same range which prevents the exact determination of the film stoichiometry from the only structural characterization.

Stoichiometry	**in-plane parameter a_0 (Å)**	**Out-of-plane parameter c_0 (Å)**	**Reference**
$CrTe_2$ (x=0)	3.789	6.096	[18]
Cr_2Te_3 (x=1/3)	3.933	6.035	[31]
Cr_3Te_4 (x=1/2)	3.934	6.170	[32]
CrTe (x=1)	3.997	6.222	[33]

Table 1.1: Lattice structure of a few phases of the $Cr_{1+x}Te_2$ family. In order to ease the comparison, the distance given for each structure corresponds respectively to the distance between fully occupied Cr planes (the one between nearest Cr atoms in these planes) for out-of-plane (in-plane) lattice parameters, as shown in Fig. 1.12.(b). They match the unit cell of $CrTe_2$ but not the ones of the other phases.

Lasek et al. [34] proposed to use the diffraction peaks induced by the superstructures (a new periodicity is introduced, as can be observed Fig. 1.13) when x is a particular fraction in $Cr_{1+x}Te_2$ to identify with low-energy electron diffraction (LEED) the stoichiometry. However, experimentally, films always exhibit some disorder, so that they introduced a machine learning algorithm to determine from the diffraction images what was the most probable stoichiometry. However, if the defects density is too large, this technique might not be suitable to identify the crystal structure.

These are a few reasons why some confusion in the literature emerged as some films have been reported with various stoichiometries for growths in very similar conditions. External characterization such as Rutherford backscattering spectrometry (RBS) or x-ray photoelectron spectroscopy (XPS) are therefore essential to obtain the stoichiometry of one particular film.

Finally, a few words on the air stability of these compounds will be added, as this is a key element for the development of the crystal growth and its exfoliation/transfer. Gao et al. reported that $Cr_{1+x}Te_2$ samples grown by chemical vapour deposition (CVD) were air stable [35]. They compared the roughness of fresh samples and after 4 months of air exposure as well as the hall resistivity. They found very little change. However, they did not perform any control chemical analysis, which was done in other studies that

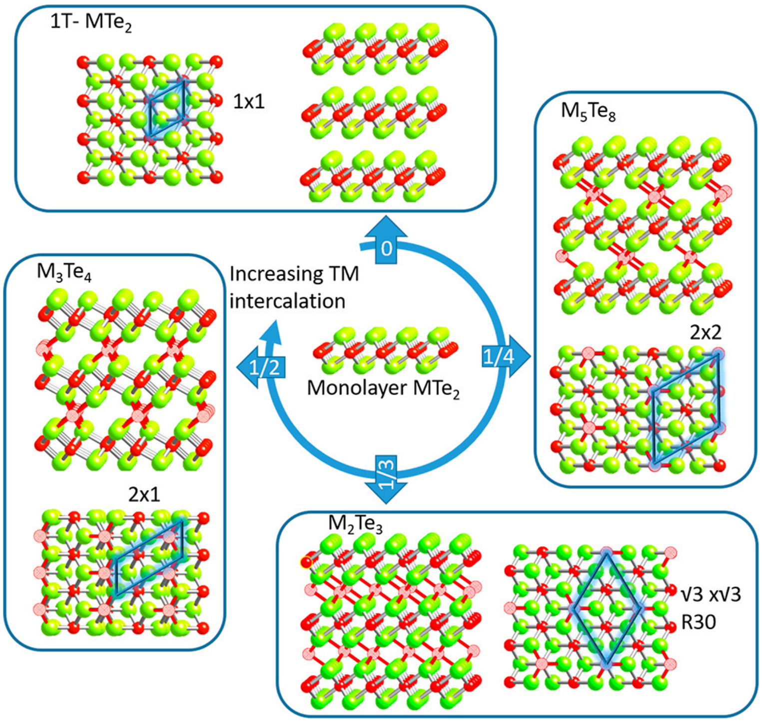

Figure 1.13: Crystal structure of the $Cr_{1+x}Te_2$ family and lattice superstructure (the unit cell varies according to the number of Cr atoms in the intercalated layer) taken from [34].

lead to very different conclusions. Raman analysis [36, 37] and XPS revealed the extreme air sensitivity of these materials as can be seen in Fig. 1.14. Most studies are now performed on samples protected by capping layers to prevent surface oxidation.

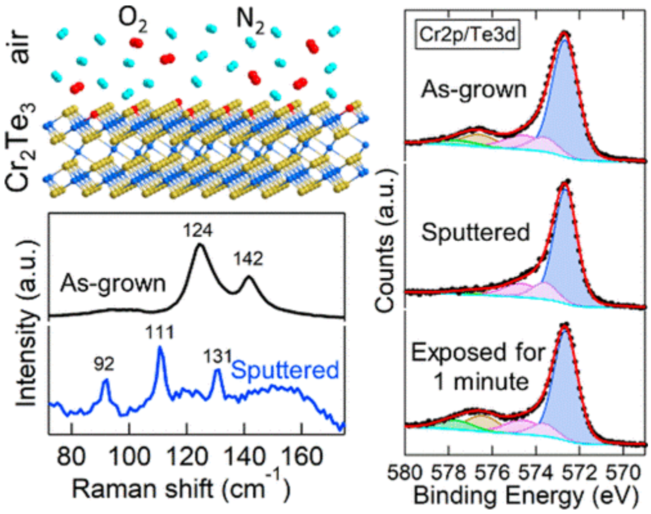

Figure 1.14: Extracted from [37]. Raman spectra reveal alloy changes after air exposure. The shift of the peaks toward higher values usually indicate the oxidation of the material. The elemental bonding with O is also evidenced by XPS. First, the grown sample shows the presence of oxidation evidenced by the yellow fitted peak. After in-situ sputtering of the surface, oxygen is removed but the oxidation of the surface is visible again only after 1 min exposure to air.

1.2 Magnetic order in reduced dimension

1.2.1 Basics of long-range magnetic order and coupling

1.2.1.1 Paramagnetism, diamagnetism, ferromagnetism and antiferromagnetism

Magnetism refers to the ordering of the spins at the macroscopic scale. Several models exist to explain its origin and to quantify the ordering of a set of spins but this is not the goal of this thesis to give such a lecture, which can be found for example in chapter 17 of the book of Girvin and Yang [2]. To sum up the main information, the orientation of spins in a material is determined by a competition of several energies such as the exchange interaction. This exchange interaction determines the relative orientation of two neighboring spins and originates from the Pauli exclusion principle of fermions and is expressed with the following equation, with E the energy, J a coupling factor and $\vec{s_a}$, $\vec{s_b}$ two spin moments:

$$E = -J\vec{s_a}.\vec{s_b} \tag{1.1}$$

This is a short-range interaction, that can be positive (leading to ferromagnetism) or negative (antiferromagnetism) depending on the atoms in a crystal as well as its structure. At a finite T, entropy will tend to disorganize the system, adding an energy cost to a specific ordering (the order of magnitude is k_BT, with k_B being the Boltzmann constant). Finally, in the presence of an external magnetic field, a Zeeman energy adds up with μ_0 the vacuum permeability and $\vec{H}$ an external magnetic field:

$$E = -\mu_0\vec{s}.\vec{H} \tag{1.2}$$

It will tend to align the spins along the field direction. Other parameters will influence this picture but these are the required parameters to understand long-range ordering of spins in any material. These long-range spin orderings are presented in Fig. 1.15.

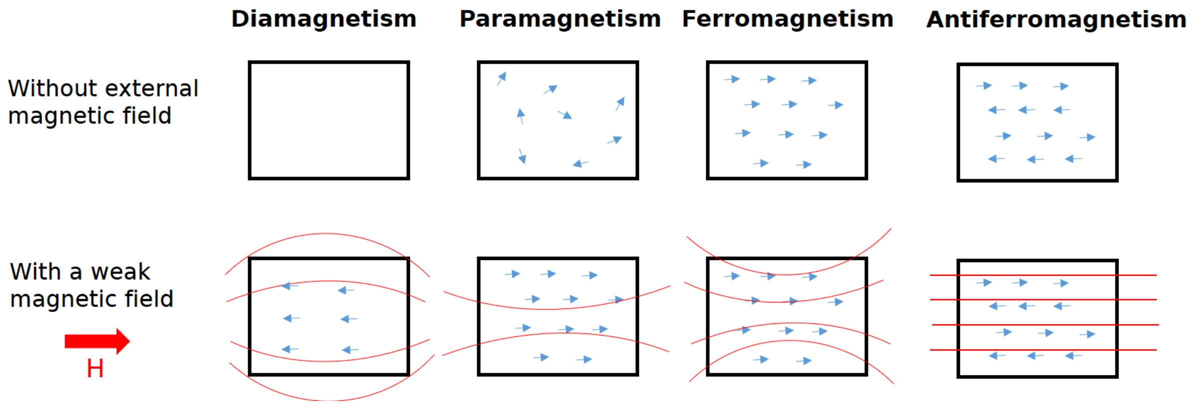

Figure 1.15: Sketches of the macroscopic spin ordering with and without external field. Blue arrows denote electron spins in a material and red lines are magnetic flux density lines. Inside a magnetized material, the magnetic flux density $\vec{B}$ is equal to $\mu_0(\vec{H}+\vec{M})$.

In the case of diamagnetism, all atoms have only paired electrons (spin up and down), so that no net spins are present (blue arrows in the figure). When an external magnetic field H is applied, the material has a negative susceptibility (which means it creates an opposite contribution to the magnetic flux density B inside the material), deflecting field lines away from itself. For paramagnetism, spins orientation is random without external field giving a zero net magnetization. However, when a field is applied, the Zeeman energy will preferentially align the spins with the field giving rise to a net magnetization. The susceptibility is positive, which means that the intensity of B is larger inside the material. For ferromagnetism, due to positive exchange interactions, spins will align even without external field. The susceptibility is also positive, like for paramagnetism, but orders of magnitude larger. All ferromagnetic systems show a transition above a certain temperature to a paramagnetic state: it is called the Curie temperature (T_c). In the case of antiferromagnetism, the exchange coupling is negative favouring an ordered antiparallel alignment of the spins: the net magnetization is zero. The susceptibility is also positive but weaker in the directions of the spins (for a collinear structure). However, if the field is large enough, a spin flop transition will happen and all the spins will partially align with the external field giving rise to a net magnetization. Antiferromagnets will also become paramagnetic at high temperature with a critical temperature called the Néel temperature (T_N).

1.2.1.2 Magnetic anisotropy

The focus will now be on the ferromagnetic case. It has been explained that the spins tend to align together due to exchange interaction giving rise to a macroscopic magnetization. When the energy of the system is varying with the angle of the magnetization, it indicates the presence of magnetic anisotropy. There are two origins to this phenomenon: the shape of the system as well as some magneto-crystalline anisotropy caused by SOC. The anisotropy will create some favoured directions for the magnetization called easy axis. This can be of great importance for industrial applications in order to control the magnetization of a material and to restrict it inside a plane or along a given direction, allowing better manipulation.

Shape anisotropy

The first origin of magnetic anisotropy as stated before is the shape of the system. This is due to the magnetic susceptibility of the material and the demagnetizing field. The example of an infinite thin film with a magnetization $\vec{M}$ will be used. Maxwell's equation of electromagnetism states that $\nabla.\vec{B} = 0$. As can be seen in Fig. 1.16, if $\vec{M}$ is oriented out of the film plane, a finite magnetic flux appears at the interface because the magnetization is 0 in vacuum. To respect the absence of divergence, a demagnetizing field H will be present giving rise to a demagnetization energy $E_{demag} = -1/2\mu_0\vec{M}.\vec{H}$, that is positive. If the magnetization is parallel to the film, because it is infinite, there is no flux at interfaces, leading to $\vec{H}$=0 and $E_{demag} = 0$. Shape anisotropy will therefore tend to align the magnetization of a film in its plane.

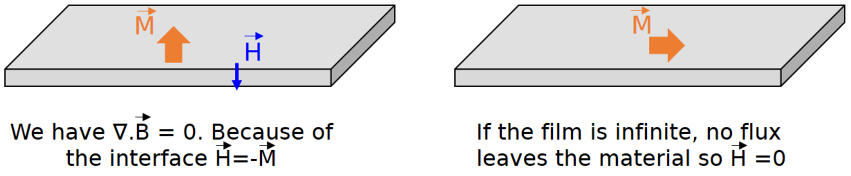

Figure 1.16: Demagnetizing field of an infinite thin film with a net magnetization perpendicular or parallel to the film.

Magneto-crystalline anisotropy

In a crystallized material, the orbital momentum of atoms is quenched due to the translation symmetry. However, due to SOC, it is not strictly zero and the coupling of the orbital momentum with the crystal field gives also rise to magnetic anisotropy. It is usually approximated with the first order of a decomposition in polynomial terms, which is called uniaxial anisotropy. Depending on the materials, the easy axis of magnetization can be along any of the crystal axis, including out of the plane for a 2D material. In this case, it is called PMA. Some terms of the polynomial can be zero due to symmetry in the crystal structure. Nevertheless, at interfaces with other materials, some symmetries (for example out-of plane translation) can be suppressed giving rise to a surface anisotropy. This effect will decrease with the inverse of a film thickness.

1.2.1.3 Band structure and magnetism

For now, magnetization has been described as the sum of individual moments of electrons in a material. In a metal, conductions electrons are not localized on specific atoms but form Bloch states that are delocalized. The image of a sum of individual moments is not appropriate to model these systems. A better picture is to use density of states for opposite spins. In a non-magnetic material and in the absence of external magnetic field, the density of states will be identical for spin up and spin down. In the Stoner band model, exchange interaction in ferromagnetic materials will shift the density of states of the electronic bands close to the Fermi level depending on the spin direction as can be seen in Fig. 1.17.

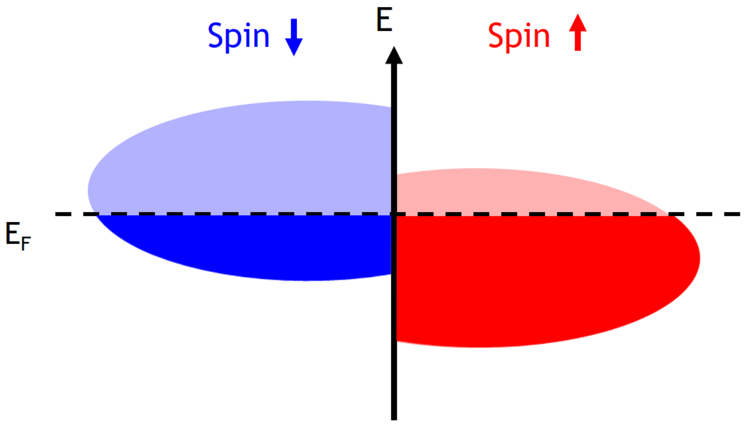

Figure 1.17: Stoner model of ferromagnetism. Density of states close to the Fermi energy for opposite spin directions. Unoccupied states (above E_F) are shaded.

Since electronic bands are occupied up to the Fermi level, the larger number of states below E_F in the case described above of spin up electrons will lead to a net magnetization in the system. The study of electronic bands can therefore give information about the magnetic properties.

1.2.2 Phase transition in magnetism

The phase transition between different states of matter (gas, liquid and solid) with temperature has been an intensive field of research in statistical physics. Long-range order of spins in materials can undergo similar phase transitions (for example from ferromagnetic to paramagnetic) and similar mathematical tools and diagrams can be used. Some examples will be presented and their consequences on the magnetic properties of the materials.

1.2.2.1 Spin dimensionality

First of all, the spin dimensionality will be introduced, which is the number of dimensions along which the spins can move. Depending on this number, several models have been developed to calculate whether magnetic phase transitions are possible and their behaviour with respect to temperature.

Ising model

In the Ising model, the spin dimensionality is 1. The spin is restricted along one direction and can therefore only take two possible values, opposite to each other. The different spins are positioned on a lattice that can be of any dimension. In the absence of an external field, the hamiltonian of the system is H = - $\Sigma_{i,j}\, J_{i,j}\, \vec{s_i}.\vec{s_j}$, with $J_{i,j}$ the exchange parameter and i, j the different sites of the lattice. Usually, only nearest neighbours interaction are considered, which means that $J_{i,j} = 0$ if i and j are not nearest neighbours. For symmetry reasons, for all nearest neighbours, $J_{i,j}$ is usually taken as a constant J. In the simplest case of an unidirectional lattice (see Fig. 1.18), which is the 1D Ising model, it has been shown by Ising in 1925 that there cannot be any phase transition, *i.e.* long range ferromagnetic order is not stable in one dimension according to this model. As explained before, magnetism is a competition between the exchange energy and the entropy gain of randomized spins. In the 1D case, each spin has only two nearest neighbours and the exchange energy is always lower than the entropy gain, leading to the absence of ferromagnetic order.

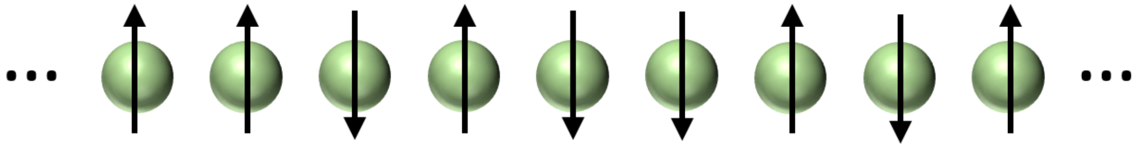

Figure 1.18: Ising chain of spins in one dimension. Spins can only have two "values", up or down.

However, for dimensions greater or equal to 2, Peierls demonstrated in 1936 [38] that ferromagnetic order is present at a finite temperature. In the proof, the number of opposite spin pairs are counted at the statistical equilibrium and it is shown that for low enough temperature, it must be small compared to the total number of pairs. This describes a ferromagnetic order thus proving the statement.

XY model

In the XY model, the spin dimensionality is 2. The spin is restricted inside a plane and can take a continuous number of values $\vec{s} = e^{i\theta}\vec{u}$ with $\vec{u}$ being an arbitrary vector defining the spin plane and θ any angle. The hypothesis of this model are the same than for the Ising model and it cannot be solved analytically for finite temperatures. It has nevertheless been well studied with Monte Carlo simulations to investigate phase transitions. In 2D, there are no strict ferromagnetism at low temperature but a transition to a quasi-ordered state, called the Kosterlitz-Thouless transition.

Heisenberg model

This model is a generalization of the Ising and XY models to a spin dimensionality of 3 (with no restriction on the spin direction). In a 3D lattice, a ferromagnetic transition can be evidenced but not in 2D (this is the Mermin-Wagner theorem). The explanation will be given in the following section, and was the reason why it was predicted that ferromagnetic order could not be preserved in the 2D limit, as real spins can take moments in all directions. However, in the presence of PMA, the spin moment can be mostly pinned at low temperature in one direction realizing the Ising model. This explains how ferromagnetic order was observed in monolayers of CrI_3 [27].

1.2.2.2 Spin waves and the Mermin-Wagner theorem

A spin wave, or a magnon, is a quasi-particle corresponding to a fluctuation of the spins lattice or a collective excitation of the spin structure. It is similar to phonons, which are fluctuations or vibrations of the atomic positions with respect to the lattice. They are bosons of spin 1 and can be viewed as a precession of spins along the magnetization direction as pictured in Fig. 1.19.

Magnons reduce the net magnetization of a ferromagnetic material due to the induced tilt of the spins. When the temperature is increased, the density of magnons increases until the ferromagnetic order is destroyed. In order to understand the Mermin-Wagner theorem, that forbids ferromagnetic order in dimension equal or less that 2 (for isotropic spins, as in the Heisenberg model), we can look at the ground

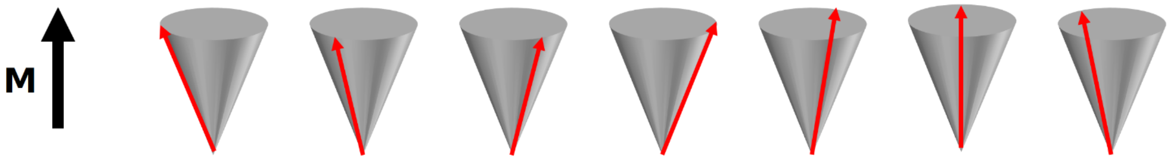

Figure 1.19: Spin wave on a 1D chain of spins. The red arrows are the spin moments and the grey cone the precession motion.

state of a ferromagnet (all spins aligned) perturbed by single spin flips (magnons). For N 1/2 spins, we will have the relation (see the book of Girvin and Yang [2], page 493):

$$M = N/2 - \Sigma_{\vec{q}}\, b^{\dagger}_{\vec{q}} b_{\vec{q}} \tag{1.3}$$

M is the total magnetization, $\vec{q}$ is a momentum in the BZ and $b_{\vec{q}}$ is the creation operator of the magnon, the conjugate being the annihilation operator. This equation is just stating that the magnetization is reduced by 1 for each spin flip (the notations are in reduced units, as the magnetic moment of one electron spin is -μ_B = - $\frac{e\hbar}{2m_e}$). At low temperatures, only long-wavelength magnons are excited, and therefore a quadratic approximation of the magnon dispersion can be made allowing to simplify the equation:

$$M \approx N/2 - \frac{V}{(2\pi)^d} \int_0^{\infty} dq \frac{d\, q^{d-1}}{e^{Aq^2/k_B T} - 1} \tag{1.4}$$

V is the volume of the system, d its dimension, A is the spin stiffness and T the temperature. For $d \leq 2$, the integral diverges in zero, which means that for any finite temperature, magnons will destroy the ferromagnetic order. A more thorough proof by Hohenberg, Mermin and Wagner for d = 1 and 2 at non-zero temperature establishes this result for several spin models. However, for d = 3, we get the simple form (by introducing the temperature scale $T_C \propto$ A/k$_B$):

$$M = N/2 \left[1 - \left(\frac{T}{T_C} \right)^{3/2} \right] \tag{1.5}$$

This polynomial law models accurately the magnetization dependence at low temperature but it is not appropriate to express the singularity at the phase transition. For this purpose, critical exponents have been introduced as will be now discussed.

1.2.2.3 Curie temperature and critical exponents

Before the phase transition at T_C, the different characteristics of the ferromagnetic phase like the magnetization M or the susceptibility χ will vary with T showing a discontinuity at T_C (hence the name of phase transition). Close to the transition, the parameters dependence can be approximated with a power law, defining the so-called critical exponents (see Fig. 1.20). They will depend on the chosen model for the spins and the interactions. When performing experimental measurements, one can compare extracted coefficients with the ones of the different models to get insight on the real magnetic system (for example about spin dimensionality).

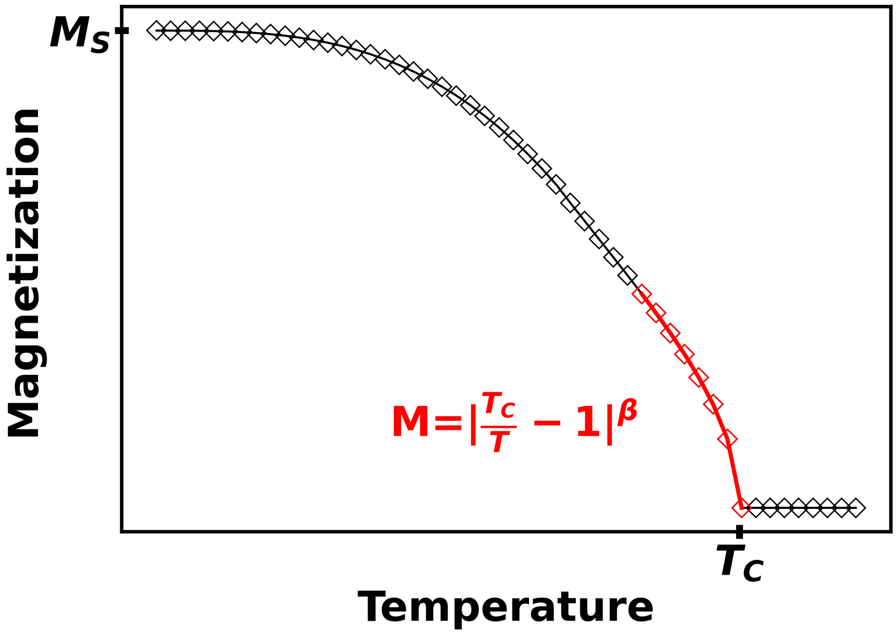

Figure 1.20: Model of a remanent magnetization curve. M is calculated from a polynomial law for $T \leq \frac{2}{3}T_C$ and using a critical exponent $\beta = 0.5$ for $\frac{2}{3}T_C \leq T \leq T_C$.

Example in the mean-field approximation

First, the model of the mean-field theory (developed by Weiss in 1907) will be developed because of its relative simplicity. As explained before, ferromagnetism originates from the exchange interactions between nearest neighbour spins. In the mean-field approximation, we reuse the Heisenberg model but the interaction is taken only between individual spins and the average value of the surrounding spins (which is proportional to the magnetization). We rewrite $\vec{s}_i$ = (<$\vec{s}$> + ($\vec{s}_i$ - <$\vec{s}$>)). Then, the Hamiltonian becomes:

$$H = cst - 2\Sigma_{i,j}J_{i,j}\vec{s}_i. < \vec{s} > +\Sigma_{i,j}J_{i,j}(\vec{s}_i - < \vec{s} >).(\vec{s}_j - < \vec{s} >) \tag{1.6}$$

In the mean-field theory, we neglect the interacting term (the last one) and work with an effective field $\vec{H}_{eff}$ caused by the exchange interaction proportional to (Σ_j $J_{i,j}$) <$\vec{s}$> which is equal to z*J <$\vec{s}$> with z being the coordination number at each lattice position. Using a Boltzmann distribution, we derive that M $\propto$ ||< $\vec{s}$ >|| = tanh($\mu_0 H_{eff}$/k$_B$T). By developing the expression of $\vec{H}_{eff}$, we derive the following equation after defining T_C = zJ/k$_B$:

$$arctanh(M) - \frac{T_C}{T}M = 0 \tag{1.7}$$

Close to T_C, M will tend to zero so that arctanh(M) $\approx$ M + M^3/3. The non zero solutions to the equation are, for T $\leq$ T_C, M $\propto$ $\pm$ (T_C/T -1)$^{0.5}$, which can be generalized for the other models to M $\propto$ $\pm$ (T_C/T -1)$^{\beta}$, β being a critical exponent. In order to take all the interactions into account, the critical exponents can be derived from numerical simulations and are summarized in Table 1.2:

Model	Mean-field	2D Ising	3D Ising	3D XY	3D Heisenberg
Exponent β	0.5	0.125	0.325	0.345	0.364

Table 1.2: Computed critical exponents describing the temperature dependence of the magnetization near T$_C$ for different models of ferromagnetic order.

Other critical exponents can be obtained for instance for the magnetic susceptibility, the spin correlation length above T_C.

1.2.3 Magnetic properties of 2D and vdW ferromagnets

After having introduced the basics of magnetism, the focus will now be on the state of the art on 2D and vdW ferromagnets. One can refer to the comprehensive review by Wang et al. [39], which gives a broad overview of current materials, challenges and opportunities (in 2022). Here, we will not be as thorough but the most important breakthroughs from the last years will be presented.

1.2.3.1 Magnetic doping of 2D materials, semiconducting and metallic 2D ferromagnets

As explained before, the first discovered 2D ferromagnets were CrI_3 and $CrGeTe_3$. They are both semiconducting materials with T_C of respectively 41 and 30 K in the mono or bilayers form [26, 27] with strong PMA. This anisotropy is the reason, as mentioned earlier, why the thermal fluctuations do not kill the ferromagnetic order. The magnetic properties were first studied by magneto-optical Kerr effect (MOKE) and contrary to bulk ferromagnetism in CrI_3, an interlayer antiferromagnetic order was evidenced for few layers as pictured in Fig. 1.21. A transition occurs at large field for a bilayer and the spins align perpendicularly to the layers plane along the applied field. For lower fields, the atoms remain ferromagnetically coupled inside each layer but antiferromagnetically coupled to the adjacent layers. This is confirmed by the signal of a trilayer, where the high field signal intensity is three times the one of the low field.

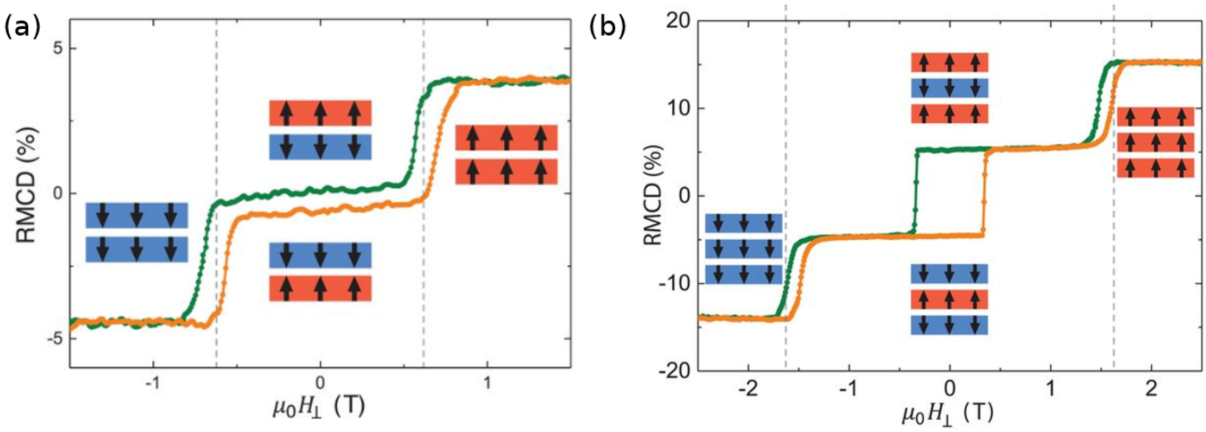

Figure 1.21: MOKE measurements at 2 K of few layers CrI_3 taken from [40]. (a) For a bilayer. Green (orange) curve is the measurement for decreasing (increasing) magnetic field. (b) Same measurement for a trilayer.

The origin of this deviation compared to the bulk order is a strain induced on the crystal structure during the exfoliation, showing again that 2D materials are very sensitive to external constraints. Another way to tune the magnetic properties of 2D ferromagnets is with an external electric field, for example by adding a dielectric material or an ionic gel on top of the film. In a metal, the electric field is screened by the conduction electrons (Faraday effect) but not in an insulator or a semiconductor. The Fermi level can be therefore easily tuned by controling the gate voltage. An example is shown in Fig. 1.22, where the T_C of a $CrGeTe_3$ film is increased from 60 K to 200K [41] by applying an electric field to the layer. The magnetic anisotropy is changed as well from out-of-plane to in-plane (as can be seen by the change of sign of the difference of saturation fields in Fig. 1.22.(b)).

This result opens the way to achieve close to room-temperature 2D ferromagnetic heterostructures. Other materials with higher T_C have also been discovered like the Fe_xGeTe_2 family with x = 3, 4 or 5. This metallic material has only vdW bonds between the Te planes. In the Fe_3GeTe_2 phase, layers have PMA and a T_C of 230 K in the bulk (see Fig. 1.23.(a)) . Ferromagnetism is conserved up to the monolayer form with a T_C of 130 K [42]. In the case of Fe_5GeTe_2 (see Fig. 1.23.(b)), ferromagnetism is conserved above room-temperature [43] but the easy-axis of magnetization is in the plane, which can be an issue when thinning down the material to the monolayer limit due to the Mermin-Wagner theorem. Besides,

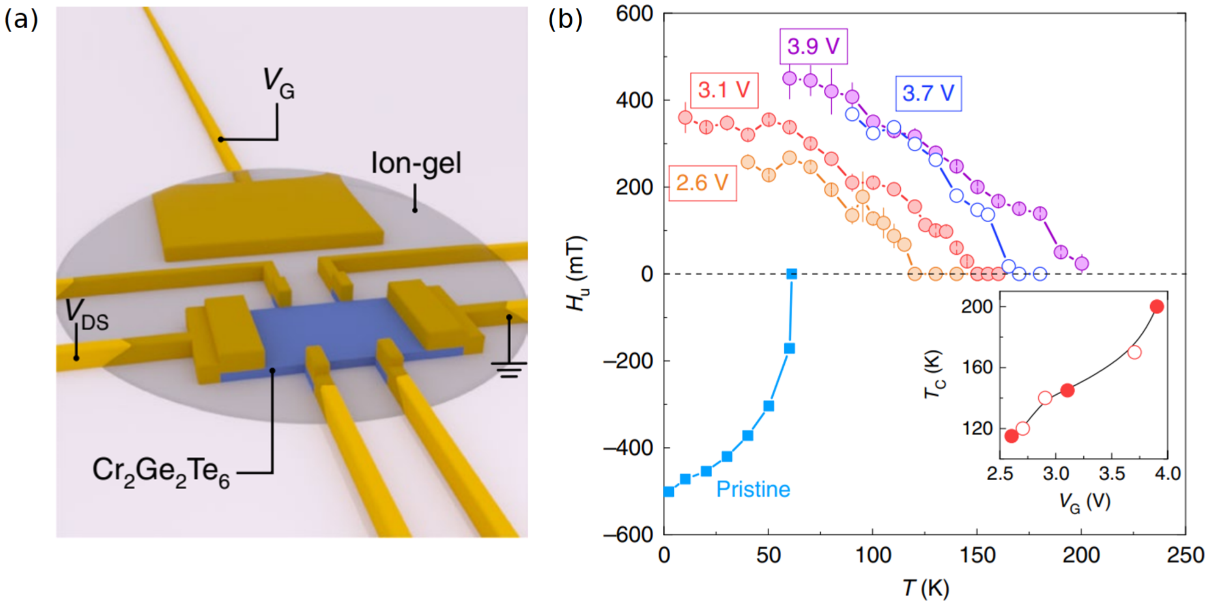

Figure 1.22: Electrical measurements on 22 nm-thick films of $CrGeTe_3$ taken from [41]. (a) Sketch of the electronic device. A current is injected in the film by applying a voltage between source and drain (V_{DS}), while a gate voltage V_G modulates the properties of the film. (b) Deduced magnetic anisotropy ($H_u = H^{\perp}_{sat} - H^{//}_{sat}$) of the films as a function of the applied gate voltage and temperature. The T_C of the film is plotted in the inset as a function of the gate voltage.

as will be presented in the spintronics part, PMA is desirable for future applications [44]. The research for high T_C materials with PMA is therefore still very active and the number of potential candidates ever growing.

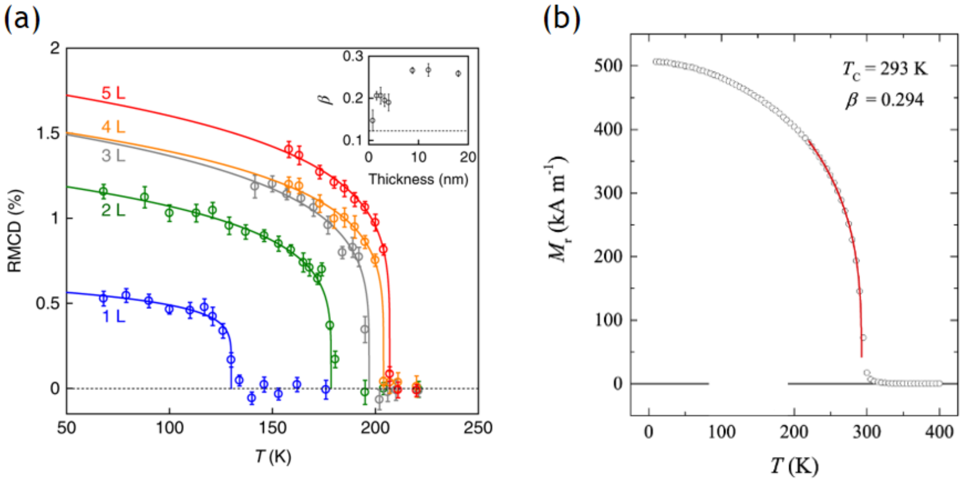

Figure 1.23: Magnetic properties of layered Fe_xGeTe_2 compounds. (a) Remanent curves of Fe_3GeTe_2 for different thicknesses taken from [42]. The inset shows the evolution of the critical exponent β as a function of the thickness showing that for thin samples, the ferromagnetic order changes from a 3D like to a 2D system (see critical exponents in table 1.2). (b) Remanent curve of Fe_5GeTe_2 taken from [43] showing the fit with a critical exponent close to the 3D system value.

Finally, another way to obtain ferromagnetism in 2D materials is doping TMDs with ferromagnetic atoms, using the example of Fe doped MoS_2 that remains ferromagnetic at room-temperature [45]. Such films are obtained by low-pressure chemical vapour deposition (LPCVD), that is a growth technique performed at high temperatures. Fe_3O_4 gas is injected during the growth of a monolayer of the TMD MoS_2.

Some Mo atoms (around 0.5 % in the article) will be substituted by Fe atoms as shown in Fig. 1.24.(a). Using optical techniques, and notably magnetic circular dichroism (a technique that will be detailed in the next chapter with the example of x-ray magnetic circular dichroism (XMCD)), the authors have been able to evidence ferromagnetism up to room-temperature (see Fig. 1.24.(b)) in Fe doped MoS_2 layers.

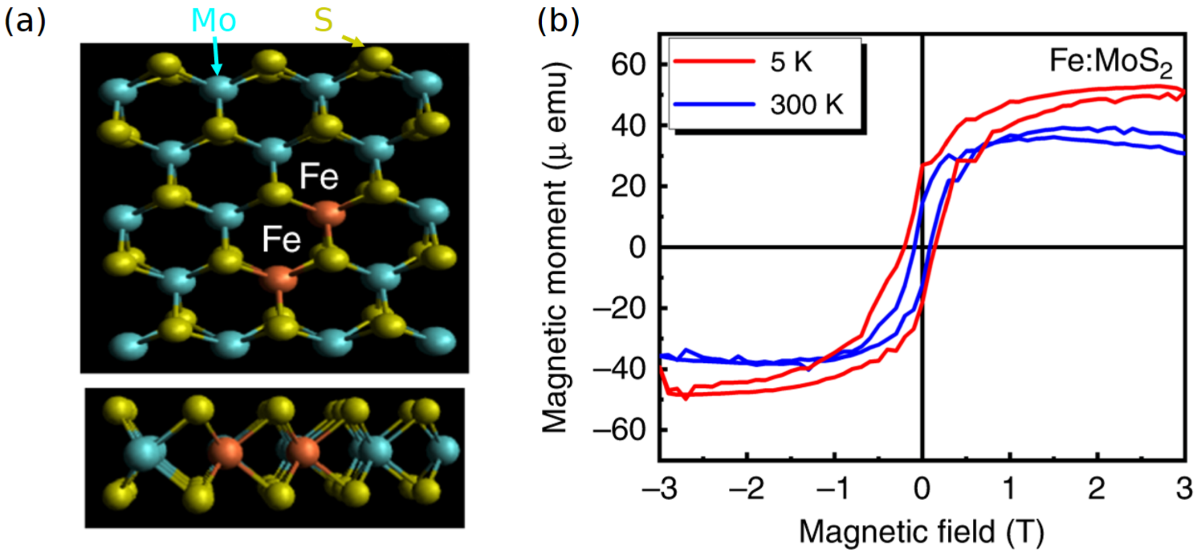

Figure 1.24: Fe doped MoS_2 monolayer, adapted from [45]. (a) Sketch of the crystal structure from the top and from the side. Fe atoms (in orange) substitute some Mo atoms. (b) Magnetization curves at two different temperatures obtained from SQUID magnetometry after subtraction of the diamagnetic contribution of the substrate.

This method of atomic doping allows to add ferromagnetism in materials with various properties such as strong photoluminescence in the case of MoS_2 monolayer. However, it only yields small magnetic moments due to the low amount of magnetic dopants and the atomic substitution can lead to the formation of defects in the crystal structure. Recent results on $Cr_{1+x}Te_2$ compounds will now be presented in order to compare with the state of the art on other vdW and 2D ferromagnets.

1.2.3.2 State of the art of the magnetic properties of $Cr_{1+x}Te_2$ compounds

As this is the heart of this thesis, the reported results on the $Cr_{1+x}Te_2$ family will be developed in details, starting with some bulk results. These compounds were already studied in the 80's and in a study by Dijkstra et al. [46], the authors performed *ab initio* calculations on several stoichiometries (Cr_2Te_3, Cr_3Te_4, CrTe) and compared their results with experimental works for bulk crystals. As can be seen in Fig. 1.25, they obtained positive exchange splitting for the three phases, indicating in all cases ferromagnetic order. The magnetization increases with the Cr content, which is explained in the calculation by a change of sign of the spin moments of the Te 5d electrons. However, they noticed that experimental values of magnetization for Cr_2Te_3 were significantly lower, of the order of 2 μ_B per Cr atom. They also reported varying T_C for the different stoichiometries of respective values 180, 320 and 340 K for Cr_2Te_3, Cr_3Te_4 and CrTe. Finally, they discussed some neutron diffraction experiments revealing a non collinear spin structure of the Cr atoms in the intercalated layers, without being able though to fully resolve the spin texture of the material. Up to now, this remains a central point to explain some of the properties of Cr_2Te_3 samples, which is not yet fully understood.

Some more recent works like the one from Coughlin et al. [47] propose a canted spins structure (see the right panel of Fig. 1.26) compared to the one aligned with the easy axis of magnetization (that is perpendicular to the layer in the case of Cr_2Te_3). Cr atoms can have antiferromagnetic coupling, for

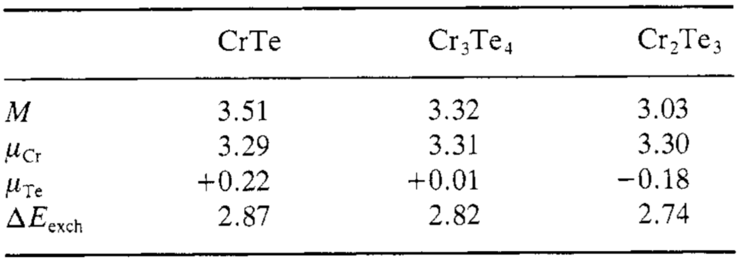

	CrTe	Cr_3Te_4	Cr_2Te_3
M	3.51	3.32	3.03
μ_{Cr}	3.29	3.31	3.30
μ_{Te}	+0.22	+0.01	−0.18
ΔE_{exch}	2.87	2.82	2.74

Figure 1.25: Calculated magnetic parameters of bulk $Cr_{1+x}Te_2$ compounds by Dijkstra et al. [46]. Total magnetic moment and per atom in μ_B and exchange splitting ΔE_{exch} between spin up and down in eV.

example in Cr oxides. In this crystal structure, most exchange parameters are positive as revealed by the calculations of Dijkstra and the fact that Cr_2Te_3 is a ferromagnet but some might be negative leading to a non collinear structure [48]. The canted spins angle can vary with temperature and stoichiometry. The spins are however not decoupled from the fully occupied layer making it very difficult to evidence experimentally.

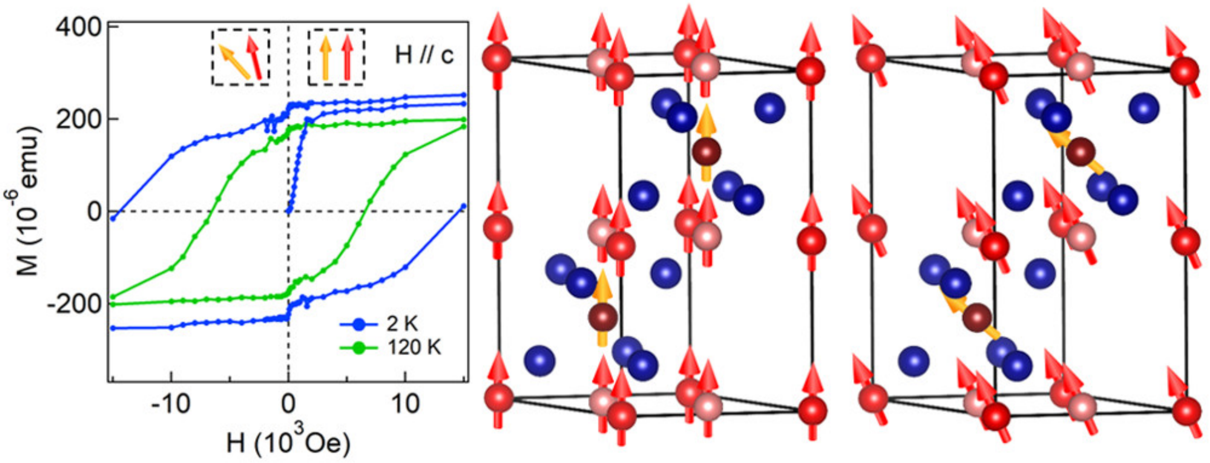

Figure 1.26: Canted spin structure of Cr_2Te_3, taken from [47]. On the left, SQUID measurements of a thin Cr_2Te_3 film (8 nm thick). In the middle, an Ising spin model, and a canted one on the right. Cr atoms in the intercalated layers do not have the same canting angle as the one of Cr atoms in the fully occupied planes.

Another study by Wen et al. [49] focused on the thickness dependence of Cr_2Te_3 magnetic properties. As shown in Fig. 1.27.(a), the T_C sharply increases (almost to the double) for low thicknesses of Cr_2Te_3. When the number of layers is thinned down to a few, the average number of surrounding atoms decreases, changing the exchange parameters in the layers. Moreover, some surface effects will have a larger contribution, whereas they are negligible in the bulk. This explains how the authors have been able to evidence different properties for thin Cr_2Te_3. However, all other studies on this material have shown a different and more usual tendency of a decrease of the T_C with the thickness. The significant increase of the Hall resistivity in Fig. 1.27.(b) has never been reproduced.

Other methods have nevertheless been proposed to tune the magnetic properties of these materials, notably by adjusting the stoichiometry and more precisely the amount of Cr atoms in the intercalated layers [50–52] or inducing some strain on the crystal structure [53–55]. The results of all these references will not be treated in details but the main information are summarized using some graphs reported in Fig. 1.28.

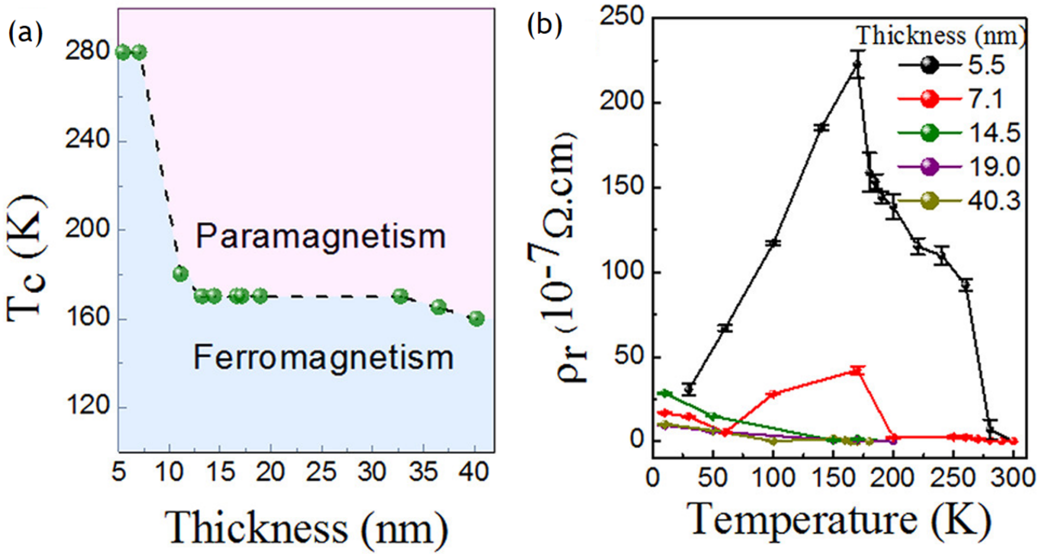

Figure 1.27: Sharp T_C increase in few layers Cr_2Te_3, extracted from [49]. (a) Tc as a function of the film thickness. (b) Hall resistivity at remanence for different thicknesses.

Figures 1.28.(a-c) show two studies on the magnetic properties of relatively thick $Cr_{1+x}Te_2$ films grown by MBE as a function of their stoichiometry. In the first, the sample growth temperature is varied between 275°C and 375°C with an associated phase variation between $Cr_{1.436}Te_2$ and $Cr_{1.854}Te_2$. They observe a shift of the T_C from 175 K to 295 K and a change from PMA to slightly in-plane magnetic anisotropy. In the second study, they perform all the growths at 300°C but carry out a one hour-long post-growth annealing under Te flux for temperatures between 450°C and 700°C, where the layers fully degrade. They observe similar tendency with an increased amount of Cr from $Cr_{1.33}Te_2$ to $Cr_{1.80}Te_2$ associated with an increase of T_C from 180 K to above RT at 340 K as well as a shift to an in-plane magnetic anisotropy.

Figures 1.28.(d-e) are from an *ab initio* study on the strain effects in ML Cr_2Te_3. They reveal a shift from ferromagnetic coupling to antiferromagnetic for a tensile strain around 1.5 % and an increase of the PMA with compressive strain. All these results are promising as they open the way for tuning the magnetic properties for future vdW heterostructures. These samples are however not 2D materials, except the TMD phase $CrTe_2$ of the family. Freitas et al. [18] synthesized this phase for the first time in 2015.

$CrTe_2$ crystals were first obtained by chemical vapour transport (CVT). First of all, a crystal of $KCrTe_2$ is obtained, where the K atoms intercalate between $CrTe_2$ planes. It was grown by heating at 900°C for eight days a molar mixture of K, Cr and Te in a quartz tube under Ar atmosphere. After the synthesis of a few mm large crystal grains, a chemical treatment in a solution of iodine in acetronitrile was used to deintercalate the K atoms. These crystals were found to be metastable with a degradation to a Cr_2Te_3 phase above 330 K. Purbawati et al. [19] reproduced this method in 2020 and then performed mechanical exfoliation on the synthesized crystal to obtain thin films of $CrTe_2$. Figure 1.29 shows magnetic measurements they performed using x-ray magnetic circular dichroism photoelectron emission microscopy (XMCD-PEEM). They evidenced an above RT T_C of 315 K and in-plane magnetic anisotropy, with domains oriented every 120° (in agreement with the crystal symmetry).

In conclusion, a large set of magnetic properties have been reported in the $Cr_{1+x}Te_2$ family, among which above RT ferromagnetism, tunable magnetic anisotropy and non collinear spin structure. This makes it an ideal platform to engineer new vdW heterostructures for the future spintronics applications, as will be further developed in the next section.

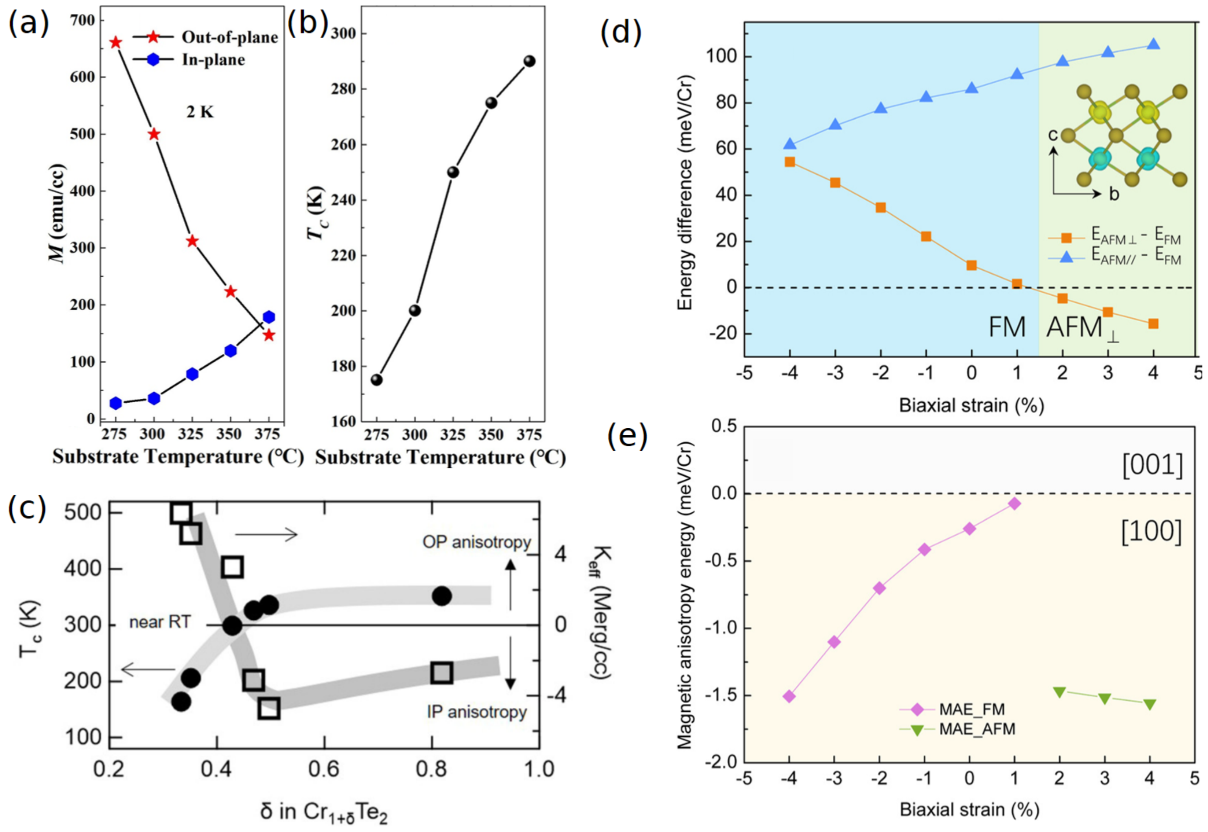

Figure 1.28: Variation of the magnetic properties of $Cr_{1+x}Te_2$ films with stoichiometry and strain. Figures (a-b) are extracted from [52], (c) is taken from [50] and (d-e) from [54]. (a) Magnetic moment at the remanence measured at 2 K after saturation perpendicular or parallel to the film. Several samples on STO with a 50 nm thickness are presented with increasing temperature growth. (b) T_c of the same samples as a function of the temperature growth. (c) Black points indicate the T_c of 80 nm thick $Cr_{1+x}Te_2$ samples on sapphire as a function of Cr amount in the intercalated layer x. Empty squares indicate the magnetic anisotropy of the same samples. Grey lines are visual guides. (d) Calculated exchange energy for one ML Cr_2Te_3. The energy difference between an antiferromagnetic and ferromagnetic arrangement is plotted as a function of the strain in the layer. Blue area indicates where ferromagnetism is energetically favourable whereas green indicates antiferromagnetism with a perpendicular Néel vector. (e) Same calculation showing the magnetic anisotropy. Negative values indicate an out-of-plane easy axis of magnetization.

1.3 2D materials for spintronics

1.3.1 Introduction to spintronics

The beginning of the field of spintronics is usually associated with the discovery of the giant magnetoresistance effect by the groups of Albert Fert [56] and Peter Grünberg [57], for which they were rewarded with the Nobel price in 2007. This effect describes a large difference of resistance for an electric current flowing through two parallel or antiparallel magnetized layers. Its origin is the spin dependent scattering probability, and it is implemented everywhere in today's electronic devices. Before this effects is properly explained, some basic principles of electronics and spin properties need to be detailed.

1.3.1.1 Charge and spin currents

Every electron is carrying an electrical charge e = -1.6 * 10^{-19} C. In metals, some electrons called free electrons are delocalized and can be displaced (statistically) to create an electrical current. If an electric gradient of the potential V is applied, an electron flow will be created described by the charge current I_c, that is the rate of electrical charges through a given surface. If N is the number of charges e and S a surface,

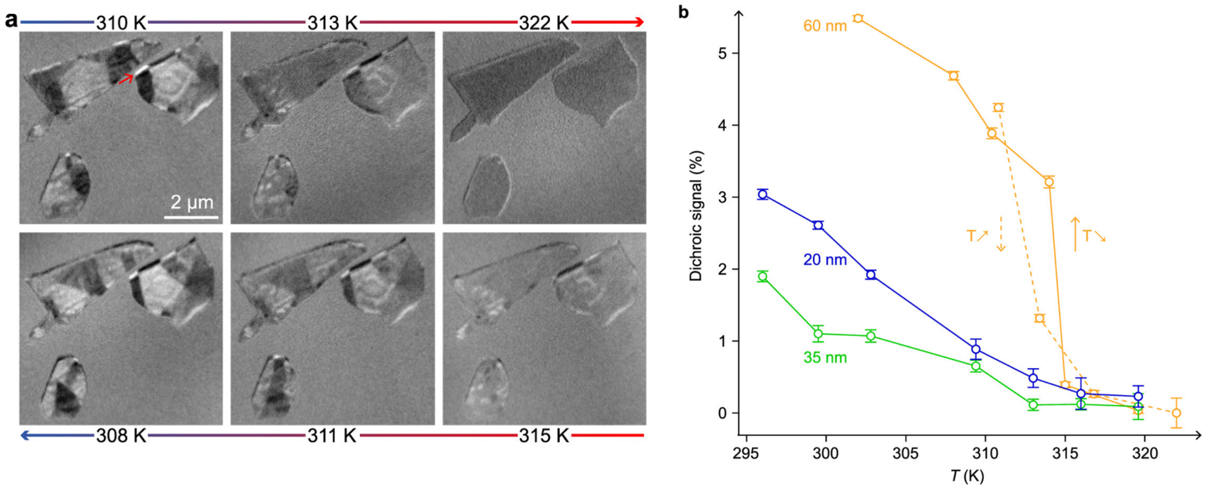

Figure 1.29: Magnetic properties of thin $CrTe_2$ films extracted from [19]. (a) PEEM images of the same 60 nm thick flakes of $CrTe_2$. On top, the temperature is increased from 310 K to 322K, and on the bottom it is reduced from 315 K to 308 K. (b) Temperature dependence of the magnetic contrast for different flakes.

the current I_c flowing through S is defined as: $I_c = e\,\frac{dN}{dt}$. For most materials, there is a proportional relation between the difference of potential V and the current flowing though it given by the Ohm law: $V = R * I_c$, where R is the electric resistance of the material. However, diodes or batteries (among others) have non linear current-voltage characteristics and do not obey this law. A famous relationship for ohmic materials is the energy dissipation due to the heating of the materials when a current is flowing: $P = R * I_c^2$. This is the main origin of energy losses in today's electronics devices and a limitation to the miniaturization of chips.

Electrons are also carrying angular momentum as we have explained in the previous section with the orbital momentum μ_l (mostly quenched in crystals) and the spin momentum μ_s. We can define the spin current by analogy to the charge current as the rate of angular momentum through a given surface. The spin is represented by a vector and usually expressed in solid state physics by the Pauli matrices. Mathematically, the spin current is therefore a tensor. However, to simplify, if we consider a two spins collinear system (up and down), we can write $I_{\uparrow(\downarrow)} = e\,\frac{dN_{\uparrow(\downarrow)}}{dt}$ for the spin up (down) current. We can then express charge and spin current as:

$$I_c = I_\uparrow + I_\downarrow \tag{1.8}$$

$$I_s \propto I_\uparrow - I_\downarrow \tag{1.9}$$

For homogeneity, a factor $\hbar/2e$ needs to be added in equation 1.9 as I_s is a flow of angular momentum and not charges. Nevertheless, these relations allow to distinguish the different types of currents, as pictured in Fig. 1.30. For most materials, the conduction electrons are not spin polarized as in Fig. 1.30.(a), leading to a pure charge current. However, if there is an imbalance in the spin populations at the Fermi level as is the case with a ferromagnet for example, the electrical current will also be spin-polarized as shown in Fig. 1.30.(b). Finally, pure spin currents can exist in the case of opposite flows of spin up and down electrons as sketched in Fig. 1.30.(c). This situation can arise with spin pumping in ferromagnets, in helical edge states in topological insulators (TIs) or by the spin Hall effect for example.

Historically, electronic devices have used charge currents to store and manipulate information. Spintronic devices aim to use spin polarized or pure spin currents to transport and write information in a more energy efficient way to reduce power losses due to Joule heating.

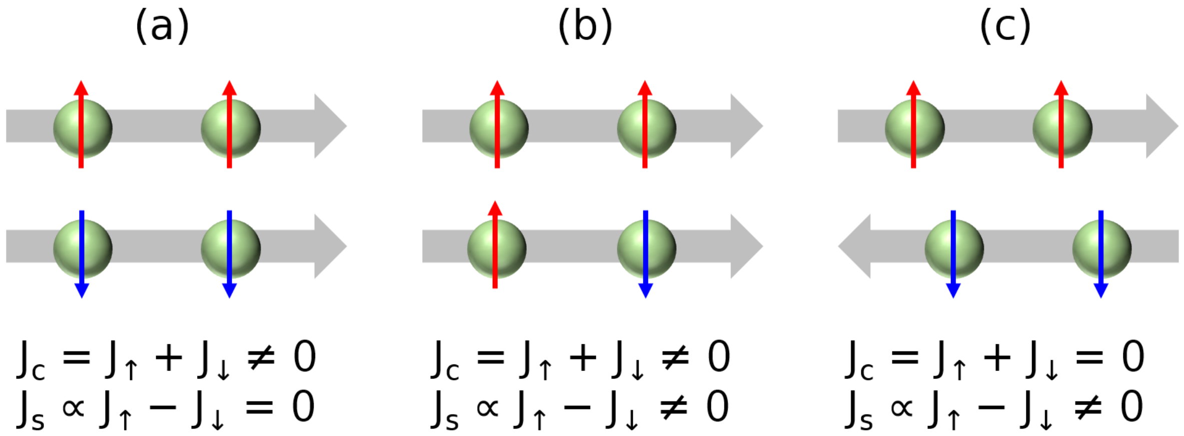

Figure 1.30: Schematic drawings of electrical currents. (a) Pure charge current. (b) Spin-polarized current. (c) Pure spin current.

1.3.1.2 Spin-orbit coupling

As already mentioned in this manuscript, SOC is a key interaction in solid state physics to describe several phenomena such as magneto-crystalline anisotropy or the spin Hall effect (SHE) that will be introduced in the next subsection. It is a relativistic interaction between a particle's spin, its motion and an electric field. For example, it will shift in the electrons atomic energy levels, due to electromagnetic interaction between the electrons angular momentum, their orbital motion and the electrostatic field of the positively charged nucleus.

Because of Lorentz transformation in the theory of relativity, the nucleus will exert an effective magnetic field on electrons. Using a semi-classical approach of the hydrogen model (qualitatively in good agreement with experimental observations), where an electron is rotating at a speed $\vec{v}$ around a proton creating an electrostatic field $\vec{E}$, the effective magnetic field is expressed with the equation:

$$\vec{B}_{eff} = -\frac{\vec{v} \times \vec{E}}{c^2} \tag{1.10}$$

This effective magnetic field creates a Zeeman splitting of energetically degenerate electronic states. The electric field created by a proton is radial and equals to $\vec{E} = \frac{1}{4\pi\varepsilon_0}\frac{e\vec{r}}{r^3}$. With $\vec{L} = \vec{r} \times \vec{p}$ the orbital momentum, we obtain the new equation:

$$\vec{B_{eff}} = \frac{e}{4\pi\varepsilon_0 mc^2 r^3}\vec{L} \tag{1.11}$$

Finally, the interaction of this effective field with the spin of the electron leads to the SOC contribution to the hamiltonian of the system: $\mathrm{H}_{SOC} = \lambda_{SOC}\, \vec{s} \cdot \vec{L}$. λ_{SOC} is proportional to the electric field radiated by the nucleus. In the hydrogen-like model of atoms, this constant scales with Z^4, where Z is the proton number. Because of the electron screening of the radiated nucleus field, a more accurate model shows that SOC scales with Z^2 [58]. In both cases, this explains why SOC has comparably a much bigger impact on the electronic properties of heavy elements such as W (Z = 74) or Bi (Z = 83) and negligible effects on light atoms like C (Z = 6).

1.3.1.3 Spin-charge interconversion

The magnetic field allows to interact with spins because it exerts a torque on any magnetic moment causing the Larmor precession. This torque is expressed as $\vec{\Gamma} = -\gamma\, \vec{B} \times \vec{\mu}_s$, with γ the gyromagnetic ratio, $\vec{B}$ the magnetic field and $\vec{\mu}_s$ the spin moment. Moreover, the magnetic field also interacts with the charge of the electrons as described by the Lorentz force, stating that a charge q with a velocity $\vec{v}$ in an electromagnetic field is subjected to the force $\vec{F} = q\,(\vec{E} + \vec{v} \times \vec{B})$. A direct consequence discovered in 1879 by Edwin Hall is the so-called Hall effect sketched in Fig. 1.31.(a). When a current is flowing in a metal or a semiconductor with a magnetic field applied perpendicularly to the current direction, a transverse voltage can be measured due to the deflection by the magnetic field. Negative charges (electrons) will be deflected to one side, whereas positive ones (holes in semiconductors for example) to the other one, creating a net voltage. A similar effect was measured two years later in 1881 in ferromagnets, is called the anomalous Hall effect (AHE) and is sketched in Fig. 1.31.(b). The measured signal is a function of the material's magnetization. The origin of the effect is however very different as the predominant contribution is not caused by the self induced magnetic field. Depending on the materials, this effect is caused by extrinsic (spin dependent scattering due to SOC on impurities) and/or intrinsic effects (function of the Berry phase that is a topological property of a material related to the band structure at its Fermi level). Finally, a third Hall effect (spin Hall effect (SHE), see Fig. 1.31.(c)) was proposed by Diakonov and Perel in 1971 [59] leading to a spin accumulation at the material edges rather than a charge accumulation as in the two others. It shares the same physical origin with the AHE but does not lead to a transverse voltage because the two spin states have the same population in a non magnetized sample.

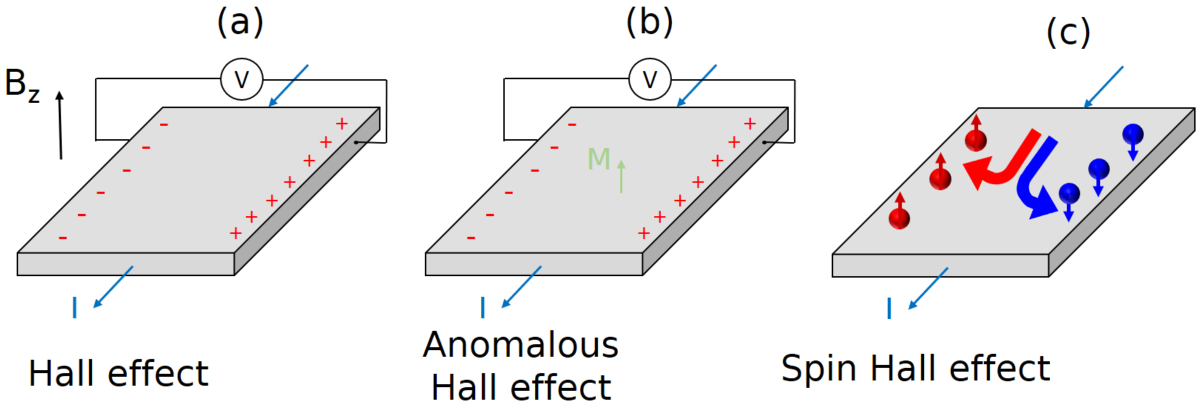

Figure 1.31: Sketch of different Hall effects. (a) Normal Hall effect caused by an external magnetic field. (b) Anomalous Hall effect as a function of the magnetization of a layer leading to a transverse voltage. (c) Spin Hall effect leading to a spin accumulation at the edges.

In the latter case, a longitudinal charge current is injected in the material and a transverse spin current is generated, which is an example of charge-to-spin conversion. The reciprocal effect called the inverse spin Hall effect also exists and transforms spin current into a charge current. The efficiency of the conversion is defined by the spin Hall angle $\theta_H = \frac{|J_s|}{|J_c|}$. The first experimental observations of the SHE was done in semiconductors [60] but the efficiency was quite small, with $\theta_H \approx 10^{-3}$-10^{-4}. Due to its large SOC, SHE was then evidenced in Pt with a spin Hall angle between 0.01 and 0.1 [61]. Finally, it was then shown that it was possible to obtain $\theta_H > 1$ in TIs [62]. This is due to the surface states of these materials with full spin-momentum locking that will be introduced just after as well as the Rashba effect.

Bychkov and Rashba introduced in 1984 a new effect related to SOC to explain electron spin resonance in 2D systems [63] when inversion symmetry is broken in a crystal. In a non magnetic system without external field (*i.e.* with time reversal symmetry) and with inversion symmetry, electronic states must respectively obey the relations E(k,↑) = E(-k,↓) and E(k,↑) = E(-k,↑). Together, we obtain that the electronic states must be spin degenerate. However, when the inversion symmetry is broken in a 2D system, electrons experience a perpendicular electric field. Following the same reasoning that for SOC, electrons will also experience an effective magnetic field that lifts the spin degeneracy, leading to a splitting of the bands in energy, as can be seen in Fig. 1.32:

$$E_{\uparrow(\downarrow)} = \frac{\hbar^2 k^2}{2m^*} + (-)\alpha_R k \tag{1.12}$$

This splitting of the bands induces a full spin-momentum locking as sketched in Fig. 1.32.(b). If a charge current is applied (by a voltage difference, *i.e.* by an electric field), this Fermi contour will be shifted

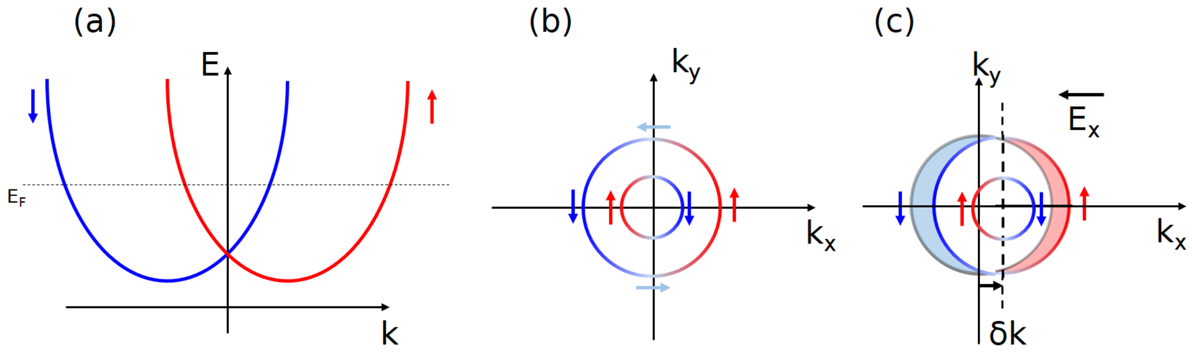

Figure 1.32: Sketch the spin splitting induced by broken inversion symmetry. (a) Fermi contours with spin resolution. The inner (outter) contour shows a clockwise (counter clockwise) helical spin texture. (b) Cross section in momentum of the dispersion at the Fermi energy. (c) When an electrical current is applied, the electric field will shift the Fermi contour by δk. As a consequence, the area shaded in blue is replaced by the one shaded in red. In total, an accumulation of up oriented (red) spins is generated, *i.e.* a transverse spin current with respect to the charge current. The spin accumulation is partially compensated by the inner contour.

(Fig. 1.32.(c)), creating a spin unbalance and therefore a spin accumulation. This is the Rashba-Edelstein effect, that also enables to obtain charge-to-spin conversion (the inverse Rashba-Edlestein effect allows with the same principle spin-to-charge conversion).

1.3.1.4 3D Topological insulators

A new class of materials will now be briefly introduced, among which some (for instance Bi_2Se_3 or Bi_2Te_3) are layered materials. A 3D TI is a material with an insulating bulk but that exhibits conductive states on its surface. The concept of topology is difficult to grasp but can be understood as a property that cannot be changed by continuous transformation. A famous example is the number of holes in an object: a cup can be continuously distorted into a doughnut (see Fig. 1.33) but not into a ball because the formation or destruction of a hole is a discontinuity in space. The number of holes is called a topological invariant and defines a class of elements, which are topologically protected from elements of another class. In our example, a Pretzel has a topological number of 3 and is therefore protected with respect to the doughnut. It means that small perturbations will not be able to transform an element from one class to another from a different class. In quantum physics, one says that topological states are therefore robust because they cannot be destroyed by small thermal noises.

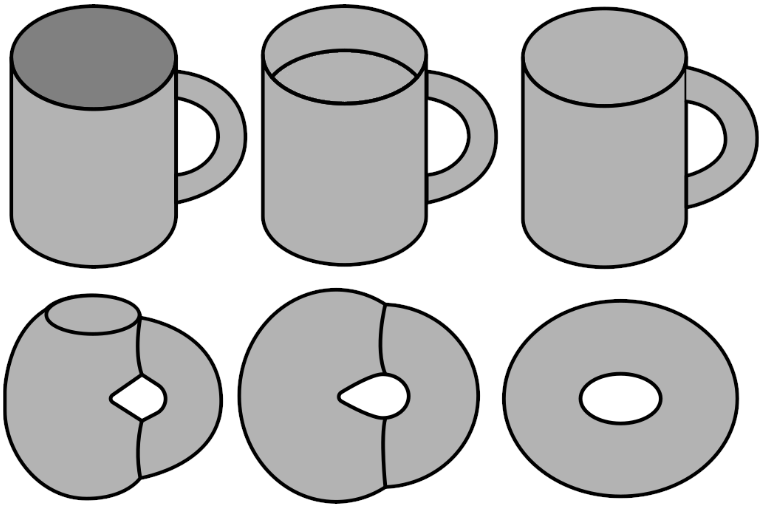

Figure 1.33: Sketch of the continuous transformation of a cup into a doughnut, adapted from [64].

For TIs, the topological invariant is called the Chern number and is related to the band structure and the Fermi level of a material. If the Chern number is zero, a material is said topologically trivial. Similarly to the number of holes, the Chern number is an integer and is related for TIs to the number of conducting surface states. Figure 1.34 shows the band structure of a 3D TI. Some surface states will be conducting at the interface and a simplified band structure is sketched in Fig. 1.34.(a). Depending on the TI, a finite number of surface states will connect the valence to the conduction band. It is worth noting that the energy dispersion of the surface state also forms a Dirac cone with complete spin-momentum locking as illustrated in Fig. 1.34.(b). These materials are therefore ideal candidates to realise experimentally the Rashba-Edelstein effect, and this explains why such high spin Hall angles were reported in the literature.

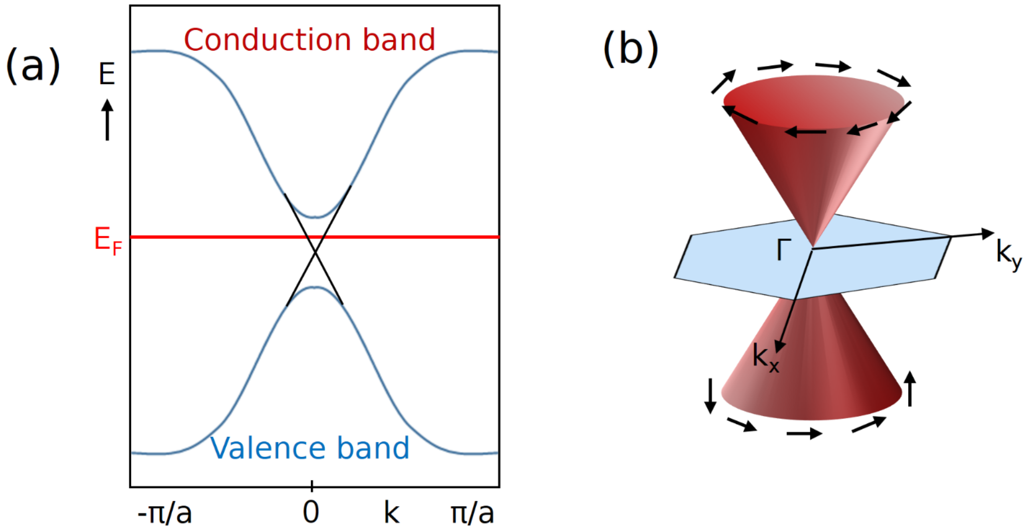

Figure 1.34: Surface states of a 3D TI. (a) The band structure of the TI close to the Fermi energy (E_F). E_F is located in the bandgap of the material but some topological surface states with linear dispersion are connecting the valence and the conduction band. (b) Spin-momentum locking of the surface states in the BZ. Black arrows indicate the spin moment of electrons as a function of their orbital momentum.

1.3.1.5 Spin transfer torque and spin-orbit torque

One of the goal of the generation of spin currents, especially in spintronics, is to interact and even modulate the magnetization of ferromagnetic layers. As mentioned earlier, nowadays electronic devices use magnetic bits to store information. In order to change a 0 to 1 or vice versa, one needs to reverse the magnetization of one bit. By injecting a current in a wire close to the bit, a transient Oersted field is generated to create a Larmor torque to switch the magnetization direction. This process is however not energy efficient as it causes great losses by Joule heating.Two other mechanisms using spin polarized currents will now be presented to modulate the magnetization with higher efficiency.

To describe the magnetization dynamics and its precessional motion that we introduced with the Larmor torque, an equation has been derived by Landau, Lifshitz and Gilbert (the LLG equation):

$$\frac{\partial \vec{M}}{\partial t} = -\gamma \left(\vec{M} \times \vec{H_{eff}} - \frac{\alpha}{M_s} \vec{M} \times \frac{\partial \vec{M}}{\partial t} \right) \tag{1.13}$$

Here, γ is the gyromagnetic ratio, M_s the saturation magnetization and α is a dimensionless constant called damping factor, which is material dependent. $\vec{H}_{eff}$ is the effective magnetic field, comprised of the external field, the demagnetizing field as well as the relativistic corrections such as SOC. The first part of the equation (in red) induces a precession of the magnetization around the effective field whereas the second one (in blue) causes a damping tending to align the magnetization with $\vec{H}_{eff}$. A sketch of the dynamic is shown in Fig. 1.35.(a). Let's now assume a situation with two ferromagnetic layers separated by a non magnetic spacer (exchange interaction would align the magnetization of the two layers without the spacer), as illustrated in Fig. 1.35.(b). We consider that the two layers have different magnetization direction and a charge current is injected from one to the other. The current is spin polarized along the magnetization of the first layer due to the unbalance of spin populations at the Fermi level. This creates two additional terms (in orange) in the LLG equation called the spin transfer torque (STT) (see Fig. 1.35.(c)):

$$\frac{\partial \vec{M}}{\partial t} = -\gamma\left(\vec{M}\times \vec{H_{eff}} - \frac{\alpha}{M_s}\vec{M}\times\frac{\partial \vec{M}}{\partial t}\right) + g(\theta)\sigma\left[T_{DL}\vec{M}\times(\vec{M_{ref}}\times\vec{M}) + T_{FL}\vec{M_{ref}}\times\vec{M}\right] \tag{1.14}$$

g(θ) is an angular dependency of the spin transfer (several model exist like the one of Slonczewski [65]), σ is the spin transfer efficiency (inversely proportional to the second film thickness). The first term is dependent on T_{DL}, the damping-like efficiency, and acts in the same direction as the damping contribution. Depending on the reference magnetization as well as the current direction, the STT can lead to negative damping, which causes the magnetization of the second layer to reverse without the need of any external magnetic field. The second contribution is the field-like torque and also contributes to the precession of the magnetization.

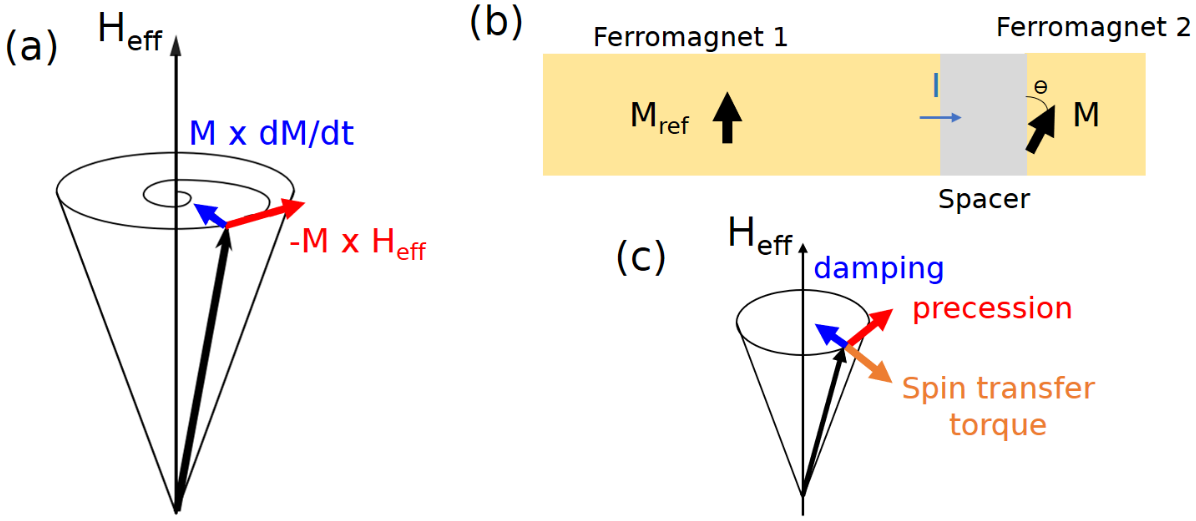

Figure 1.35: (a) Magnetization dynamics with the torques of the LLG equation. The spiral is the trajectory of the magnetization due to the precession and the damping. (b) Configuration for the spin transfer torque. A current is injected from the first ferromagnet to the second. (c) In some situation depending on the material, the angle as well as the current direction, STT can lead to negative damping and therefore magnetization reversal.

A similar effect was evidenced in 2011 by Miron et al. [66] and is called the spin-orbit torque (SOT). The principle is the same as for the STT, *i.e.* injection of a spin current non collinear with the magnetization. A single ferromagnetic layer is needed as sketched in Fig. 1.36.(a) plus a strong SOC material in contact with the ferromagnet. Due to the SHE, when a charge current is applied in the Pt plane, a perpendicular spin current is injected in the ferromagnet. A small in-plane assistance field is needed to obtain deterministic switching by breaking the mirror symmetry in the plane, as shown in Fig. 1.36.(b).

Similarly as for STT, damping-like (DL) and field-like (FL) torque can be generated thanks to SOTs. Here, one has $T_{DL} \propto \vec{M}\times(\vec{\sigma}\times\vec{M})$, with $\vec{\sigma}$ the spin polarization vector of the spin current and $T_{FL} \propto \vec{\sigma}\times\vec{M}$.

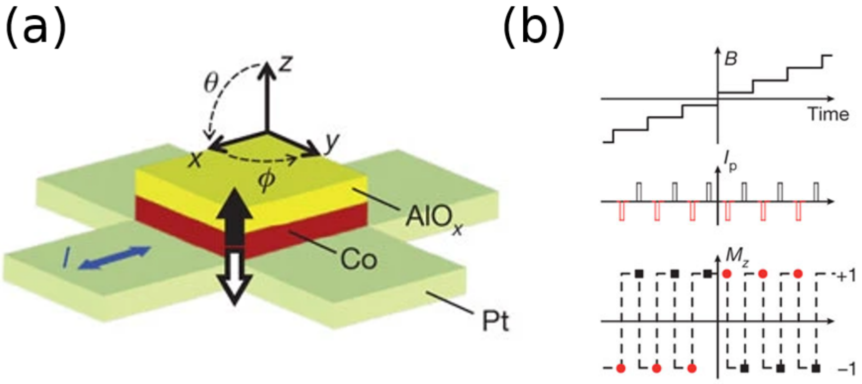

Figure 1.36: Evidence of the spin-orbit torque, adapted from [66]. (a) Sketch of the sample. Co is magnetized out-of-plane, a current is injected in Pt and a small in-plane magnetic field is applied to break the symmetry. (b) On top, the in-plane field as a function of time, in the middle the current pulses and on the bottom, the resulting magnetization switching due to the SOT.

As developed in the reference [67], the efficiency of the DL SOT per unit of current density ξ^j_{DL} can be estimated with:

$$\xi^j_{DL} = T_{int}\theta_{SH}\frac{\tau_M^{-1}}{\tau_M^{-1}+\tau_{SO}^{-1}} \tag{1.15}$$

$\frac{\tau_M^{-1}}{\tau_M^{-1}+\tau_{SO}^{-1}}$ is the percentage of the spin current relaxed via the spin-magnetization exchange interaction (τ_M^{-1} is the spin relaxation rate) and the spin-orbit scattering (τ_{SO}^{-1}). T$_{int}$ is the interfacial spin transparency (lower than 1 due to spin backflow) and θ_{SH} is the spin-Hall angle or the efficiency of the charge-to-spin conversion. No quantitative understanding of the FL SOT is yet admitted by the scientific community. In order to reverse a magnetic layer with a low current density, both a clean interface (for a high interfacial transparency) as well as a material with a large spin Hall angle are required.

In order to switch electrically a magnetic layer with PMA, it is possible to inject a spin current with out-of-plane spin polarization. Symmetry imposes that the torques are zero because spins and magnetization are parallel. However, if a small in-plane magnetic field is applied to break the symmetry, the DL SOT can then efficiently switch the magnetization direction.

1.3.1.6 Applications for data storage technologies

Based on the two effects of the previous part, several applications have been developed in the field of spintronics such as efficient memories.First of all, one has to come back to what has been described as the birth of spintronics: the discovery of the giant magnetoresistance effect by the groups of Albert Fert [56] and Peter Grünberg [57]. A sketch of the experimental setup is shown in Fig. 1.37.(a-b): two ferromagnetic layers are stacked on top of each other separated by a non magnetic spacer. The perpendicular resistance of the stack is then measured when the layers' magnetization are aligned or opposite with one another. Electron scattering events in ferromagnets are usually spin dependent because of the unbalance of density of states at the Fermi level. One spin state will therefore experience more scattering, giving rise to a more resistive path through the ferromagnet. This is symbolized in Fig. 1.37.(c-d) by a higher resistance R. On the other hand, the second spin state will experience less scattering and the path is represented by the low resistance r. As seen earlier, a charge current can be decomposed in the sum of two opposite spin polarized currents. In an electric circuit, this is sketched as two parallel spin channels. In the case where the layer magnetizations are aligned, one spin state will have a very low resistive path (2r) and the other one a high one (2R). In the antiparallel configuration, both channels lead to average resistivity (r+R). We obtain that the total resistivity is lower in the first case than the second, which is called the giant magnetoresistance effect.

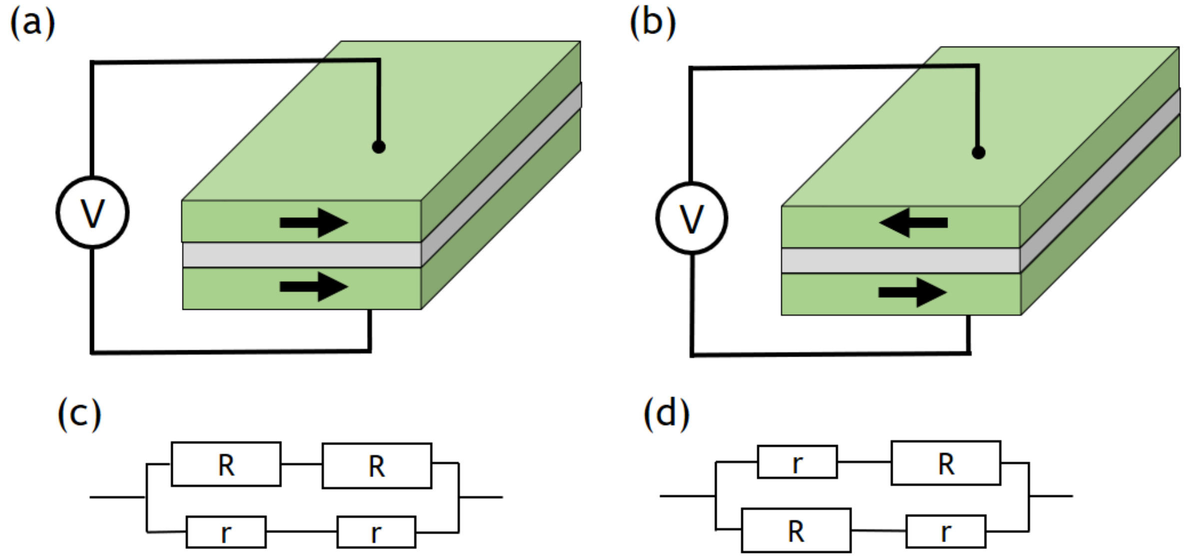

Figure 1.37: Illustration of the giant magnetoresistance effect. (a-b) Experimental setup: the resistance is measured perpendicular to a stack of two ferromagnetic layers separated by a non magnetic spacer. The magnetizations are either aligned or opposite with each other. (c-d) Equivalent electrical circuits of the setups above. The two current channels indicate the conduction of the two spin states. R stands for a larger resistance than r.

In a magnetic random-access memory (MRAM), information is stored in similar stacks where one layer has a fixed magnetization. It is called the reference layer (RL), and the second one is the free layer (FL). The two resistive states are the equivalent of the 0 and 1 bits. Technologies exist now to read and write these bits without external field as sketched in Fig. 1.38. The spacer used is an insulator (a tunnel barrier) to form a magnetic tunnel junction (MTJ), allowing an even bigger difference of resistive states due to what is called the tunnel magnetoresistance.

However, some technological challenges remain like the stabilization of the reference layer with downsizing or efficient switching of the free layer. The competition with the existing technologies such as flash memories based on semiconductors did not allow these technologies to be implemented at large scale in today's products. Nevertheless, with the end of the miniaturization due to quantum limits that conventional silicon-based technologies are experiencing now, new architectures are needed to continue to increase the performance of electronic devices. The research field on 2D materials is one of the proposed solutions to solve these issues, as can be seen in Fig. 1.39 and well explained in the review by Yang et al. [68] or the study on SOTs in reference [67].

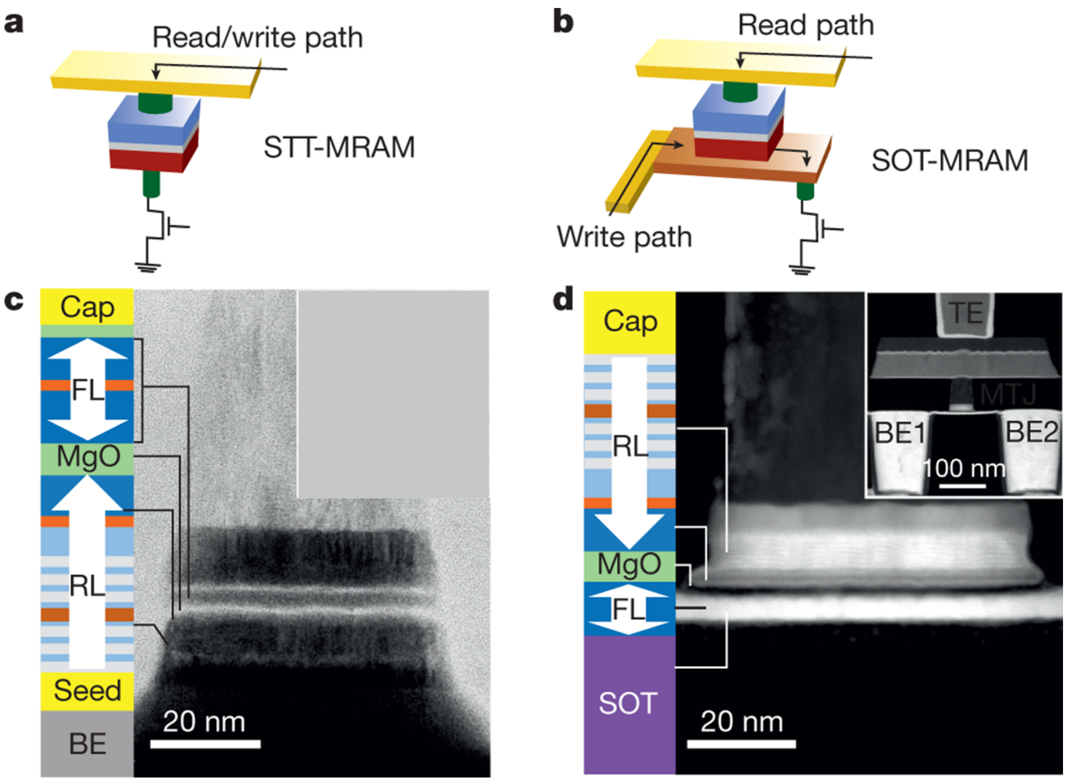

Figure 1.38: Schematics of STT-MRAM (a) and SOT-MRAM (b) cells with PMA adapted from [68]. (c) Bottom-pinned STT-MTJ sketch and transmission electron microscopy (TEM) cross-section of a 45-nm-diameter STT-MTJ consisting of a CoFeB FL, a MgO tunnel barrier and a CoFeB/spacer/Co/Ru/[Co/Pt] RL. (d) Top-pinned SOT-MTJ sketch and TEM cross-section of a 60-nm SOT-MTJ. Inset: a typical SOT-MRAM cell where the write current is injected from bottom electrode BE1 to BE2, and the read current from the top electrode (TE) to BE2.

1.3.2 Advantages of 2D materials for spintronics

Figure 1.39 introduces the challenges that the industry is facing nowadays to develop energy efficient MRAMs. The many unique properties of 2D materials open the way to address these challenges, and a comparison of actual solutions with opportunities based on vdW heterostructures is displayed. As some of them are not related to the work carried out in our lab and this manuscript, not all categories will be discussed. First of all, the importance of the high quality interfaces of vdW heterostructures will be stressed again, as interfacial intermixing is a limiting factor of current applications. In different sections, the importance of low symmetry structures in 2D materials will then be presented for the generation of in-plane as well as out-of-plane spin current polarization as well the opportunities opened by the high susceptibility of vdW heterostructures to external control such as an electric field.

As seen with the presentation of SOTs, the quality of the interface between the source of spin current and the magnetic layer directly impacts the efficiency of the manipulation of the magnetization. During epitaxial growth, substrates are heated in order to allow the formation of well crystallized layers. However, this can also lead to diffusion of some atoms of one material into another: this phenomenon is called intermixing and creates defects in the obtained materials. These defects will also create scattering events, that impact the efficiency of the SOTs (see equation 1.15). For vdW materials, a gap separates each layers, which prevents (drastically reduces the chances at least) this intermixing process and results in atomically smooth interfaces, as presented in Fig. 1.39.(f). This is one of the main reason why development of 2D materials is required for future spintronic applications.

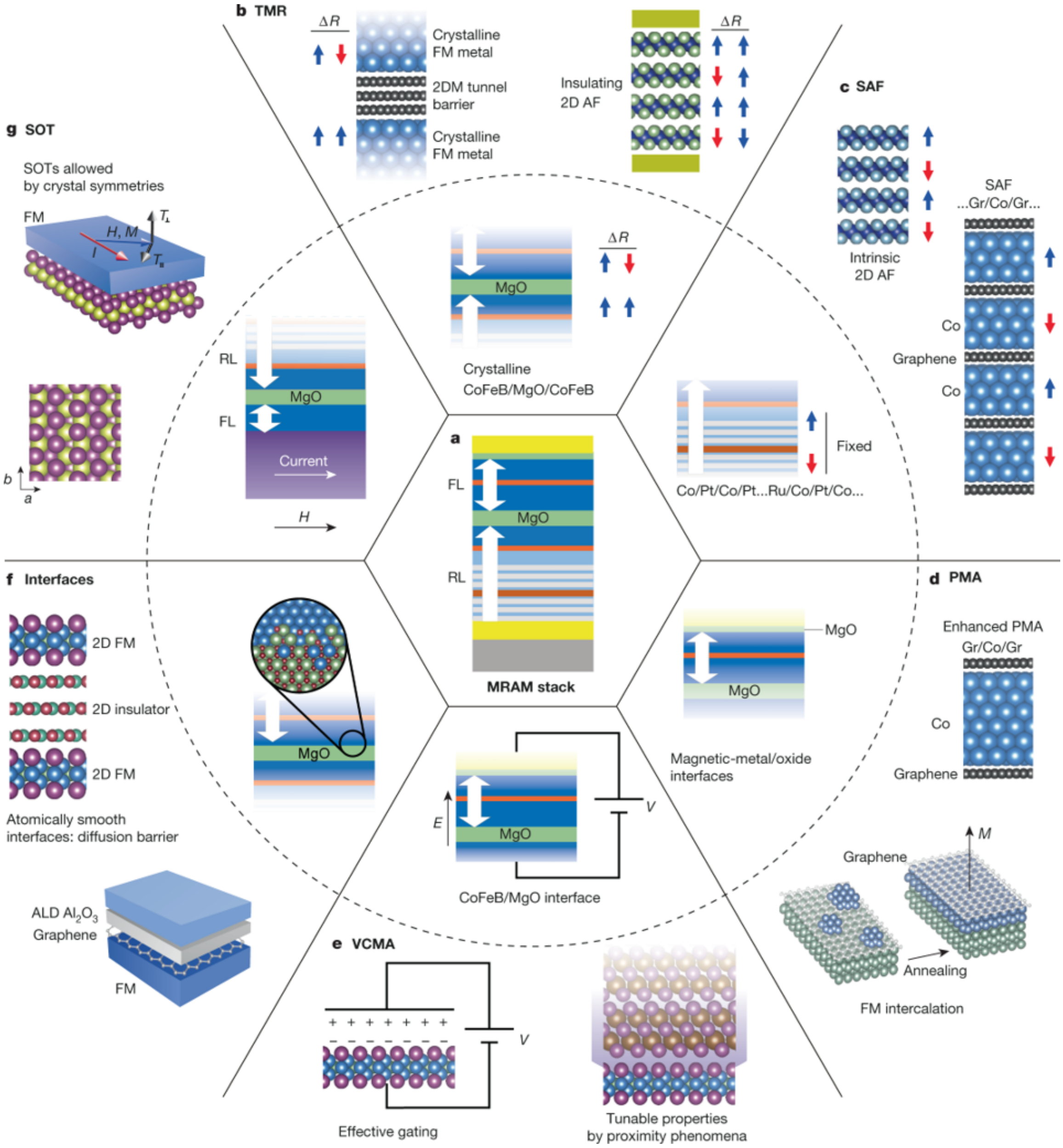

Figure 1.39: Perspectives of improvements of MRAMs technologies thanks to 2D materials, taken from [68]. (a) Current solutions are represented in the dashed circle, whereas potential solutions thanks to 2D heterostructures are shown on the outside. (b) 2D MTJ stacks. (c) Synthetic 2D antiferromagnets (SAFs) to pin the RL. (d) PMA enhancement of Co at the interface with graphene. (e) Voltage controlled magnetic anisotropy (VCMA) with proximity effects in 2D. (f) High quality interfaces thanks to vdW interaction. (g) Large SOTs in 2D materials due to low crystal symmetry.

1.3.2.1 Low symmetry and large spin-orbit coupling

As mentioned in Fig. 1.39.(g), research on new materials is needed for the development of SOT-MRAMs, as current technologies with Pt suffer from a very low spin Hall angle. It has been shown with the Rashba effect that in the case of broken inversion symmetry, spin textures with spin momentum locking like surface states of 3D TIs can lead to efficient charge-to-spin conversion. Several investigations have been carried out to show strong Rashba-Edelstein effect in TMDs. Despite the apparent 6 fold symmetry of the honeycomb lattice, the two valleys are not identical as discussed previously due to broken inversion symmetry. Different lattice structures exist for TMDs such as 1H and 1T, as presented. Another phase has also been reported: the 1T' in the case of WTe_2. This material will be intensively discussed in the last chapter of this manuscript as the realisation of Cr_2Te_3/WTe_2 is one of the perspective of the PhD. It will be nevertheless said here that this crystal structure is distorted with a breaking of the rotational symmetry by 120°. A consequence of this distorted structure is the presence of edge states with full spin momentum locking (same as for 3D TIs). Spin current were reported in this material with large out-of-plane polarization, which is forbidden by symmetry in systems with inversion symmetry. This is a crucial aspect for the electrical switching of magnetic materials with PMA.

Besides, Shao et al. reported strong Rashba-Edelstein effect on heterostructures of CoFeB on ML MoS_2 and WSe_2 [69]. These materials exhibit in-plane spin textures that can be also used to generate SOTs when interfaced with ferromagnetic materials with in-plane easy axis of magnetization. In order to measure their efficiency, the authors carried out second harmonic measurements, that will be introduced in more details in the chapter 5 of this thesis. They fitted the second harmonic hall resistivity angular dependence (see Fig. 1.40.(a)) to extract the torques induced by the 2D material and compared them to those in a Ta/CoFeB stack. They obtained results in the same order of magnitude for field-like torques but negligible values of damping-like one, which is promising for 2D materials but still not efficient enough to overtake existing technologies.

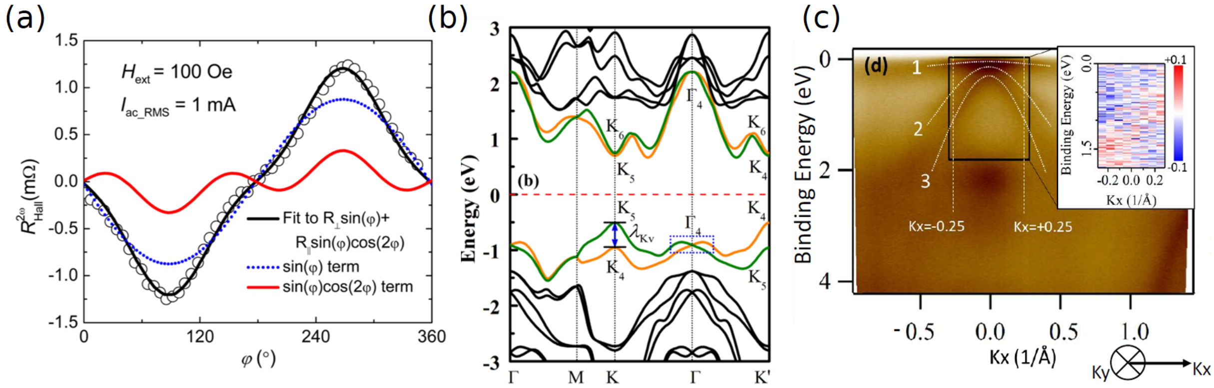

Figure 1.40: Rashba effect in 2D materials. (a) 2nd harmonic angular dependence of the Hall resistivity, extracted from [69]. An in-plane field of 100 Oe is applied and the sample is rotated. SOTs lead the magnetization to oscillate around its equilibrium position giving rise to this 2nd harmonic signal. (b) Electronic band structure calculation of WSeTe ML, adapted from [70]. Green and orange bands match two opposite spin states. (c) Spin-ARPES measurements of one ML $V_xPt_{1-x}Se_2$, with the spin polarization in the inset, taken from [71].

The research for other TMDs continued therefore and a new class of materials was introduced: the Janus monolayers. Instead of the classical MX_2 composition of the TMDs, these materials are in the form MXY with X and Y two different chalcogens (see Fig. 1.10). Yao et al. performed ab initio calculations to obtain the band structures of ML WSeTe as an example[70]. By introducing the SOC in their calculation, they evidence giant Rashba splitting at the gamma point, as illustrated in Fig. 1.40.(b). These systems have broken mirror symmetries, allowing the generation of spin currents with out-of-plane polarization. These materials could yield high values of damping-like torque and could be model systems for applications, but are experimentally very challenging to realise.

Finally, some results on the family of $V_xPt_{1-x}Se_2$ compounds will be reported, with $0 \leq x \leq 1$. These systems exhibit strong SOC due to the Pt atoms and magnetism at low temperature thanks to V atoms. Using spin and angular-resolved photoemission spectroscopy (spin-ARPES), our 2D group at Spintec has been able to evidence Rashba splitting in these materials [71] when grown on monolayer graphene. Figure 1.40.(c) shows the valence bands close to the gamma point. The two shifted Dirac cones can be recognised in the inset for the two opposite spin polarizations. The Rashba spin splitting is due to the graphene proximity that creates an interface dipole and electric field. Added to the SOC of Pt atoms, it leads to the observed experimental spin splitting.

1.3.2.2 High susceptibility to external control

Due to the possibility of reducing the thickness of 2D materials down to the ML, the surface/volume ratio is very important. One consequence is that these materials are highly sensitive to any type of surface effects, which are inversely proportional to thickness. 2D materials properties can therefore be tuned using strain, light or electric field for example. Before, the increase of the T_C in $CrGeTe_3$ with applied gate voltage [41] was already reported. Another famous effect is the observation of the quantum Hall effect in graphene as a function of the carrier density [72]. The Hall conductivity in graphene exhibits plateaus with the gate voltage corresponding to integer number of times e^2/h (see Fig. 1.41, where the resistivity is $1/n$ h/e^2) at low temperature and in the presence of large magnetic field. This effect is caused by the quantum confinement of the electrons that leads to quantized eigenstates, similarly as in a periodic oscillator.

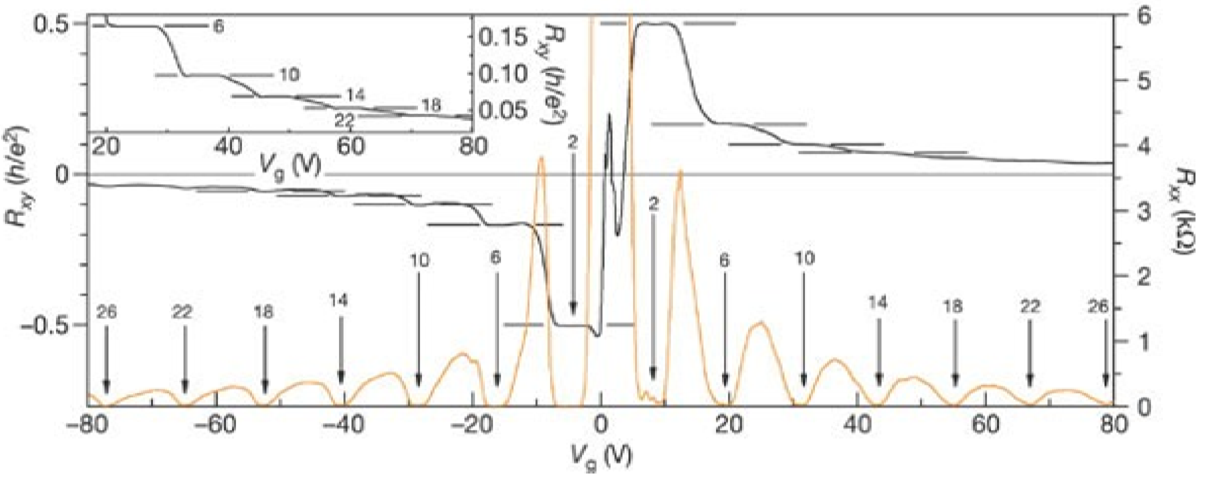

Figure 1.41: Hall resistance (black) and magnetoresistance (orange) as a function of gate voltage at fixed magnetic field B = 9 T, measured at 1.6 K. Measurements are extracted from the reference [72]. The inset shows the plateaux at high gate voltage of the transverse resistance measured at 30 mK.

As mentioned, the properties of Cr_2Te_3 have also been extensively modulated using strain [53–55], with the possibility to change from ferromagnetic to antiferromagnetic coupling. Furthermore, we have seen that TMDs valley degree of freedom could be accessed by using circularly polarized light. Several pseudo particles can be generated such as excitons or trions that are combinations of electrons and holes by vdW interactions. All these systems open the way for new generations of devices based on the intrinsic and tunable properties of all these materials.

Finally, another common method to tune the properties of 2D materials is by using proximity effects from other materials close by, as will be presented using the example of the $Cr_{1+x}Te_2$ family.

1.3.2.3 Magnetotransport in $Cr_{1+x}Te_2$ heterostructures

Magnetotransport properties of $Cr_{1+x}Te_2$ compounds have been studied with great interest since 2019 with the first report of the topological Hall effect (THE) in Cr_2Te_3/Bi_2Te_3 heterostructures [73]. It has been shown with 3D TIs that topological effects are protected from any continuous deformation, for example from small disorder. In this case, the topological objects are spin structure called skyrmions and sketched in Fig. 1.42. They are spins vortices that are comparable to knots or loops. The topological index is the equivalent of the number of knots. If the spins make one or several full rotations as in Fig. 1.42, they are topologically protected. On the other hand, if the spins make half a rotation and another one in the opposite direction, they are topologically trivial.

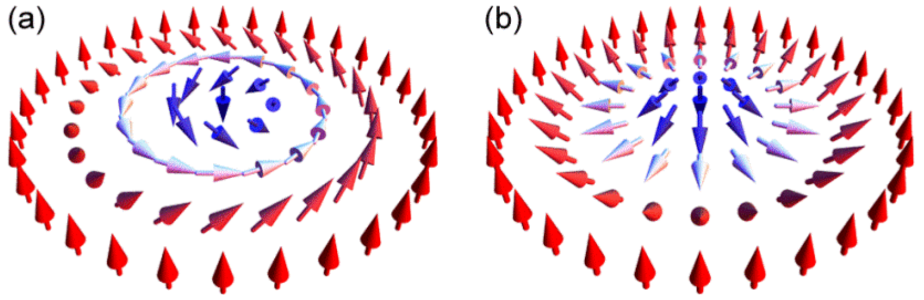

Figure 1.42: Sketch of skyrmions taken from [74]. (a) In a Bloch-type skyrmion, spins rotate perpendicularly to the radial direction. (b) In a Neel-type skyrmion, spins rotate along the radial direction.

These structures form due to the Dzyaloshinskii-Moriya interaction (DMI), that is an antisymmetric contribution to classical magnetic exchange interaction. It is proportional to the cross product of two neighbouring spins, and favours therefore canting of the spin instead of collinear structures. This interaction is forbidden in an inversion symmetric system but even then, it can be present at the interface between two materials. One particularity of these spin structures is that they are stable because of their topological nature and can be moved very fast (more than 100 $m.s^{-1}$ [74]). They are of great technological interest due to the very low energy needed to displace them. When measuring Hall resistivity in a material where skyrmions are present (usually close to the coercive field), these spin structures will contribute as an additional channel to the transverse voltage. Experimentally, it can be measured as a hump in the Hall resistivity attributed to the so-called THE.

Several groups have reported the THE in Cr_2Te_3/Bi_2Te_3 heterostructures [73, 75, 76] and an example of the measured signals is given in Fig. 1.43.(a). Similar effects were also reported in heterostructures of Cr_2Te_3 with the antiferromagnet Cr_2Se_3 [77]. When varying the temperature, the anomalous Hall resistivity coefficent changes sign and some hump features appear close to this changing sign temperature.

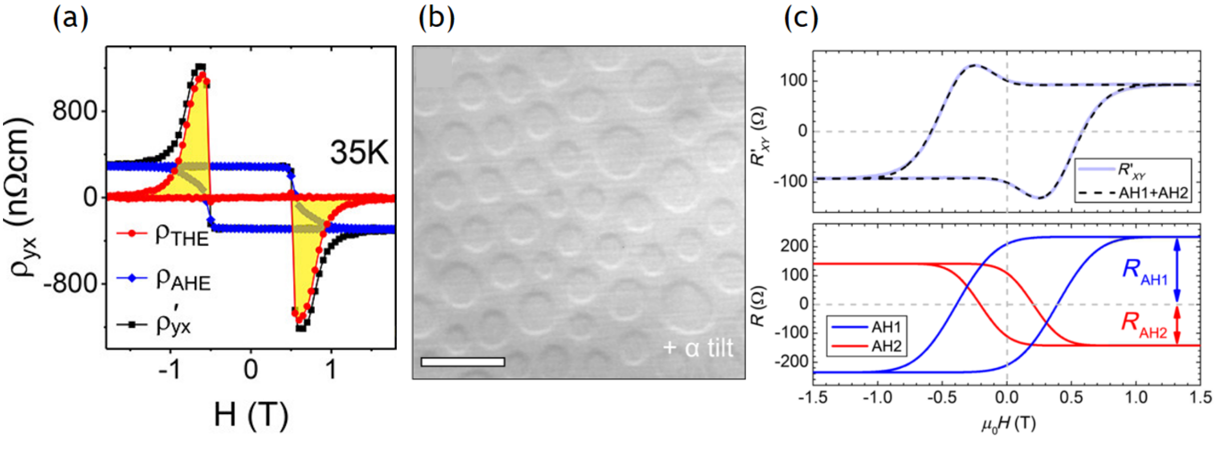

Figure 1.43: Non trivial magnetotransport signal in Cr_2Te_3 heterostructures. (a) Reported THE in Cr_2Te_3/Bi_2Te_3 from [76]. The experimental signal in black is fitted as the sum of AHE in blue and THE in red. (b) Lorentz TEM image of spin textures in Cr_2Te_3/Bi_2Te_3 identified as skyrmions, extracted from [78]. (c) Mimicking of the hump in the Hall resistivity signal as the sum of two opposite AHE, taken from [79].

Using Lorentz transmission electron microscopy (Lorentz TEM), the group of Stuart Parkin imaged spin textures in these heterostructures [78] and identified them as skyrmions, as can be seen in Fig. 1.43.(b). However, there is still some debate in the community about the origin of this effect, as some scientists have demonstrated that observation of THE had to be done with great care, as similar signals could be obtained with two AHE loops with opposite signs [80], as shown in Fig. 1.43.(c). This will be further discussed in chapter 5 with the presentation of our own measurements and results.

CHAPTER

2

Experimental techniques and methods

2.1 Crystal growth and structural characterization

Most of this thesis work was focused on various experimental techniques, that will be intoduced in this chapter. I performed all of them except the structural characterization by x-ray diffraction (XRD), done by Alain Marty, the scanning transmission electron microscopy (STEM) performed by Djordje Dosenovic and Hanako Okuno as well as the RBS data analysis made by Denis Jalabert.

2.1.1 Molecular beam epitaxy

MBE is a technique to achieve the epitaxial growth of crystallized thin films. This means that the materials are grown on crystalline substrates obtained by other methods and/or bought from companies. In conventional epitaxy, the grown material will be forced to adopt the in-plane crystal structure of the substrate. If the two materials have a lattice mismatch, some strain will be induced in the layers, which has an energy cost. Above a threshold thickness, the accumulated strain will be released and the grown material will relax to its minimum energy structure suddenly, which usually induces many dislocations at the interface between the grown material and the substrate. In order to perform epitaxial growth, the choice of substrates is therefore very limited. In the case of vdW epitaxy [81, 82], the choice of substrate is much larger because interlayer interaction is very weak. As will be present in the next chapter, in-plane orientation is usually partially preserved, leading to the choice of a substrate respecting at least crystal symmetries. For TMDs, substrates with 3-fold or 6-fold symmetry are therefore needed. Cubic crystals can however still be used if cut perpendicular to the [111] diagonal, because the resulting surface plane exhibits hexagonal symmetry.

The operation of this technique will now be presented as well as the specificity of our setup, shown in Fig. 2.1. The MBE chamber is wrapped with aluminium foils because of the frequent baking cycles of the chamber after an opening to restore the ultra-high vacuum (UHV). Liquid nitrogen is supplied to the panel to cool down the cold panel around the chamber. Samples are transferred from an UHV tube connecting the two MBE chambers. Atoms are evaporated from two e-gun evaporators (containing 5 different metallic elements each) as well as six effusion cells. The manipulator, where the sample is placed during operation, can be heated up to 1000°C.

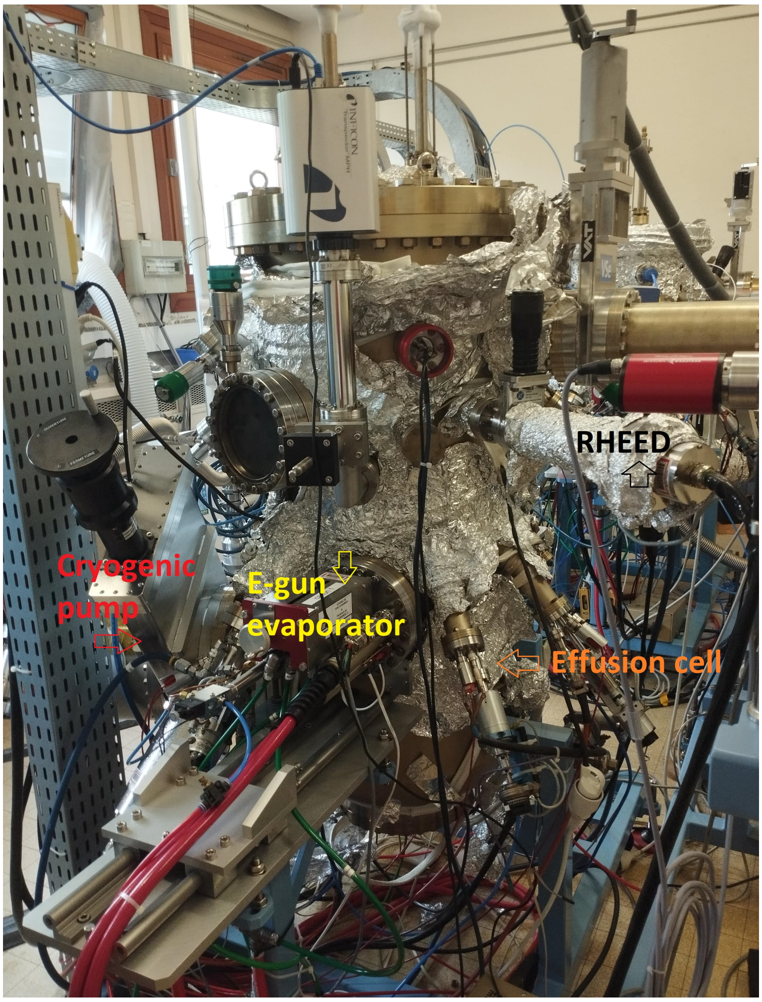

Figure 2.1: MBE setup at Spintec. Some key components are indicated on the picture.

2.1.1.1 Ultra-high vacuum technology

In the MBE setup, the evaporation of materials is performed under UHV (with pressure ower than 10^{-8} mBar). This is required to ensure the high quality and purity of the grown materials. Usual growth rates are relatively slow, of the order of 1 nm/min. The technological impact is however very important as it is very challenging to obtain and maintain UHV.

We use three types of pumps to obtain UHV in the MBE chamber: primary pumps that bring the pressure from 1 Bar to below 1 mBar, turbo pumps that achieve a vacuum of the order of 10^{-6} - 10^{-9} mBar and either ionic or cryogenic pump to reach UHV. These last two types are more fragile and already need a high vacuum before they can be started hence the role of the primary pump. In order to reach these conditions, the water that naturally adsorbs on the walls of the chamber needs to be fully removed. After each opening of the chamber, a baking of the chamber and all the equipment inside is carried out for one week. Resistive wires are surrounding the chamber and a current is running to heat the MBE at around 120°C. Maintenance on this equipment has therefore a big impact on scientific schedule and we always tried to plan ahead the filling of the cells as well as the reparation in order to limit the number of openings of the MBE.

Another way to improve the vacuum during operation is the use of a cold panel around the chamber. It is filled with liquid nitrogen (at 77 K) bringing the inner walls of the chamber to a much lower temperature than the manipulator. The atoms remaining inside the chamber can statically be anywhere but when there is such a big temperature difference, they get trapped when adsorbed on the walls because they do not have the energy to desorb. Overnight, the walls reheat back to RT and all the evaporated elements of the day that were trapped are released and pumped away. Pressures in the range of 10^{-10} mBar are measured with the help of an ionic gauge: an electric field is applied to ionize the vacuum. The measured current is proportional to the number of atoms or molecules in the chamber, allowing to deduce the pressure inside the chamber. We also use a quadrupole mass spectrometer to measure the partial pressure of the different elements to know what gas are present in the chamber (typically H_2, H_2O, CO_2 and N_2).

A benefit of working under UHV is also the stability for the grown materials. Many transition metal ditellurides are indeed air sensitive. As long as they are kept inside the equipment, it is not required to cap them with a protective layer. A tube was installed in 2022 in order to connect the MBE used to grow these materials with another one dedicated to the growth of hBN as well as other characterizing tools such as XPS or STM/AFM (they were only planned at the time of my PhD). This allows to study, for instance, chemical composition or surface topography prior to any degradation in air.

2.1.1.2 Evaporation techniques

As mentioned before, MBE is a growth technique based on the co-evaporation of elements to create crystalline structures on adequate substrates. A sketch of the growth process is shown in Fig. 2.2.

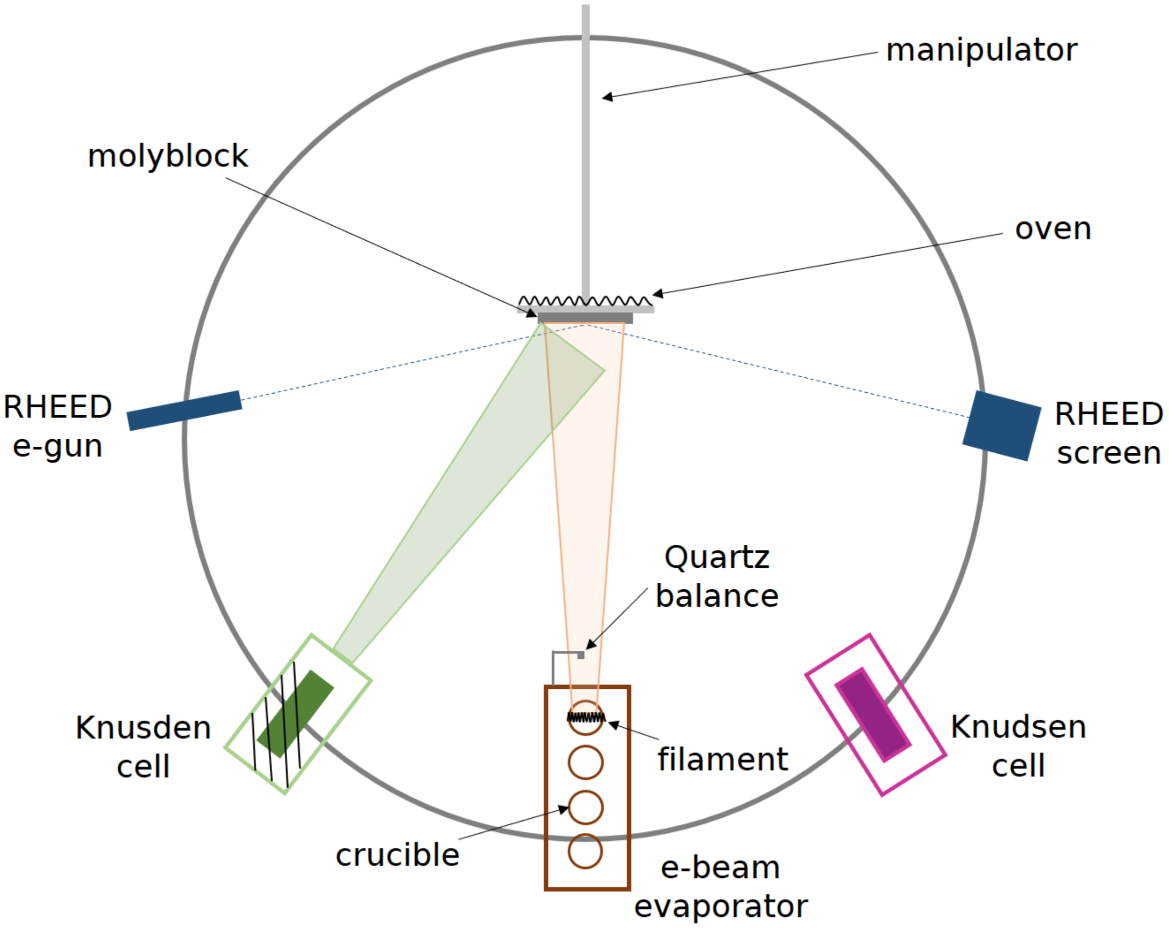

Figure 2.2: Sketch of a crystalline growth in a MBE chamber showing key components.

The substrate is attached to a so-called molyblock which is just a sample holder made of molybdenum and transferred prior growth to the chamber manipulator, that can be heated to the desired temperature. It is worth noting that the temperature is measured by a thermocouple placed at the backside of the molyblock. There can be therefore some discrepancy from one sample holder to another. The power applied to the oven is a good indicator as well when trying to reproduce previous growth conditions. The method to attach the sample to the molyblock will also affect the thermal contact and can also have an impact on the temperature, as will be discussed in more details in the next chapter. Besides, the crystalline order can be controlled in-situ using electron diffraction. Then elements can be evaporated following two techniques.

The first one, that we used for metallic elements is the e-beam evaporator. We have several crucibles for the different elements. A tungsten filament is used to extract extract electrons that are accelerated with a high voltage to hit the materials we want to evaporate. If the power is high enough, the element can be evaporated and the flux is directed toward the sample. The high power of such e-beam evaporator allows to evaporate highly refractory materials like Mo, W, Nb or V. A quartz micro balance is used to monitor the evaporated quantity and thus the deposition rate. Its resonance frequency is indeed shifted when elements are deposited on top and after calibration, this can be used to deduce accurately the thickness evaporated on the sample.This however requires thermal stability as the frequency also shifts when the quartz temperature varies. For elements like W that radiate a lot when heated, long stabilization times are required. The second evaporation technique is with a Knudsen or effusion cell, which is evaporating material just by Joule heating. In our MBE setup, we do not have a quartz balance to measure the evaporation rate but we use a flux gauge. It is another ionic gauge that we can orientate toward the effusion cell. When elements are evaporated, the measured pressure will increase and we can relate this elemental flux, after calibration, to a deposition rate. In the case of tellurium, we have a slightly more complex cell called a cracker cell. We have three heating sources for the reservoir with the Te charge, the tube leading to the chamber and the extremity of the cell called the cracker. We respectively heat them at (this is an example, it depends on the required flux) 350°C, 600°C and 1000°C to have a heat gradient. This prevents the accumulation of Te in the tube that could lead to the formation a cork. The high temperature at the extremity allows to break Te chains formed when evaporating. The Te atoms are then much more reactive when deposited on a surface and can be more easily incorporated in an alloy.

In both cases, we use high purity targets (at least 99.9999 % *i.e.* 4n purity) that ensures (with the UHV) the high purity of our grown materials. The advantages of MBE growth is the high quality and large variety of possible alloys to be grown. The drawbacks are the high complexity of the equipment and the difficulty of maintenance, which takes a long time due to the need of obtaining UHV.

2.1.1.3 Substrate preparation

During my PhD, I have worked with several crystalline substrates both for their own properties as well as for their ability to provide templates for 2D or vdW epitaxy. The first step for any substrate is to prepare adequate sample sizes. Several factors come into consideration: some substrate can be costly or in a limited quantity when provided by collaborators, which prompts us to choose small sample sizes. Moreover, for samples intended for superconducting quantum interference device (SQUID) magnetometry, the diameter of the equipment is 9 mm, which limits to squares of around 6 mm side. However, when performing x-ray diffraction, bigger sample sizes is favoured to enhance the measured signal. It is also required to have bigger samples for devices preparation in the clean room as the edges of the resist after spin coating (usually one to 2 mm) are much thicker. Samples were therefore cleaved, usually in a square shape, with lateral sizes ranging from 5 to 15 mm. This cleaving method is illustrated in Fig. 2.3 and is inspired by the way one separates squares of a chocolate bar.

An aluminium foil is used as a working surface to avoid any scratch on the top surface and a glass slide to immobilize the substrate, with the backside facing up (see Fig. 2.3.(a)). The surface is then repeatedly scratched with a diamond tip to obtain a linear notch on the surface. Pressure is then put on one side when holding the substrate between two other glass slides (see Fig. 2.3.(b)) until the substrate is cleaved along the notch. Most substrates tend to preferably cleave along their high symmetry crystalline direction. When working with hexagonal or triangular lattices, it is not easy to obtain square shaped samples but this technique was the one with the highest success rate we could find.

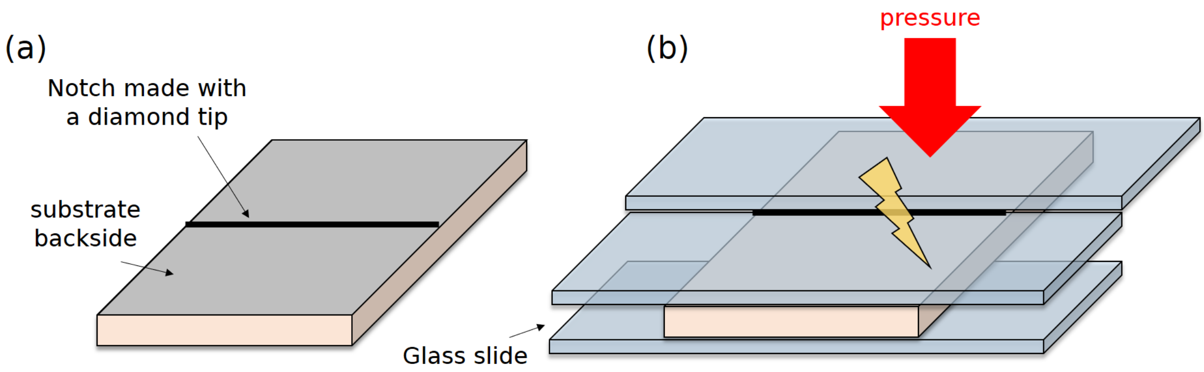

Figure 2.3: Schematic drawing of the steps to cleave a substrate. (a) We scratch the backside of the substrate using a diamond tip along the desired cleaving direction. (b) With the help of three glass slides, we put pressure to cleave along the notch, similarly to the method to separate squares of a chocolate bar.

A common template we use in the lab to perform the growth of 2D materials is one ML graphene on top of SiC. They are obtained by the controlled graphitization of 4H-SiC(0001) [83] in another reactor (from our collaborators). This process consists in the annealing at very high temperature of SiC until the formation at the surface of a free standing graphene layer on top of a so-called buffer layer of carbon bonded to SiC. This substrate does not require any further preparation and is very stable. We only perform in-situ annealing at 650°C to desorb organic molecules as well as water from the surface. However, graphene is a semimetal which is not suitable for magnetotransport measurements. Other substrate such as sapphire and GaAs (111) were therefore also used. Some treatments were sometimes necessary like annealing in air or the use of chemicals, that will be developped more in details in the results chapters.

Once the substrate prepared, we attached them to the molyblock either using Mo or W clamps fixed with screws on the side of the molyblocks or using indium gluing. Clamps are a reliable way to attach the samples but the thermal contact between the substrate and the molyblock is not perfect (depending on the roughness of the molyblock) and not reproducible, as it depends on the strength applied to tighten the screws. Indium is a metal that melts at 157°C and that wets surfaces due to surface tension above this point. To attach a sample with an In ball, one first melts it by heating the molyblock on a hot plate and then spreads In on the surface. By slowly moving the substrate on the melted In, the backside will also be wet by In. The sample is then completely fixed due to surface tension even above the melting temperature of In. The thermal contact is optimal as In is metallic insuring the same temperature of the molyblock and the sample. It is however possible at very high temperature (above 800°C) that shocks detach the sample. This technique requires therefore great care when manipulating hot samples. Its final advantage compared to clamps is for electron diffraction, because screws can shade the sample from the reflective high-energy electron diffraction (RHEED) e-gun.

2.1.1.4 Reflective high-energy electron diffraction

One of the common and very useful tool of MBE setups is the ability to perform diffraction in-situ during the whole growth process. An electron beam is shined on the sample surface, as shown in Fig. 2.4.(a). Due to the wave-particle duality, electrons will diffract similarly as light on the crystalline structure giving rise to diffraction patterns as can be seen in Fig. 2.4.(b). These pattern yield direct information on the crystalline structure of the material.

As sketched in Fig. 2.2, the electron gun of RHEED is placed at a grazing incidence with respect to the sample ($\theta \approx 1-3$). This has the consequence that diffraction only occurs at the first atomic planes of the sample. Electrons have indeed a limited penetration depth in crystals due to scattering events (wave coherence is then lost). RHEED is thus a surface sensitive technique. This allows to follow the crystalline order during all the stages of growth as well as the morphology of the surface.

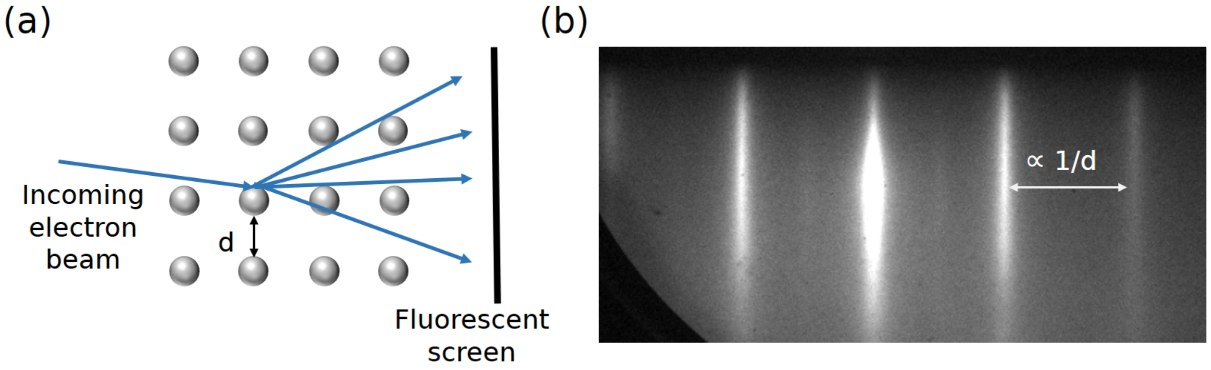

Figure 2.4: (a) Sketch of the RHEED working principle. The diffraction of an electron beam on a crystal creates interference patterns on a fluorescent screen. (b) Example of such pattern. The bright rods indicate constructive interferences. The periodicity is inversely proportional to the in-plane lattice parameter.

If the deposited film is amorphous (no periodic order), all interferences will be destructive and the RHEED pattern will be diffuse without any bright spots (see Fig. 2.5.(a)). When the grown surface is rough as in Fig. 2.5.(b), the grazing incident electron beam will diffract on average on more crystalline planes leading to diffraction spots. If the roughness is lower, the pattern can consist of modulated rods. Some materials tend to form islands during epitaxial growth when the wetting of the substrate is not favoured. In some cases, the grown layer is polycrystalline with crystallites showing random orientation, especially if the substrate is amorphous and this gives rings (diffraction occurs in every direction) in the pattern as can be seen in Fig. 2.5.(c). Finally, for ideal 2D growth, streaks appear on the RHEED screen as pictured in Fig. 2.5.(d). For a perfect film, there should only be spots but the diffraction pattern results from the crossing of the Ewald sphere (whose radius is proportional to the energy of the electrons) with the diffraction rods. Due to the energy dispersion of the beam, the sphere is thickened resulting in diffraction rods (the sphre is very large because we use a 12 kV high-tension voltage hence the elongated rods). Moreover, the distribution of lattice parameters of the layers caused by defects as well as the coherence length of the electrons yield a finite thickness to these diffraction rods. When the crystal grains are smaller than this coherence length (around 30 nm), the rods width increases. This allows to control the quality of the crystallinity by observing the full width at half maximum (FWHM) of the diffracted rods.

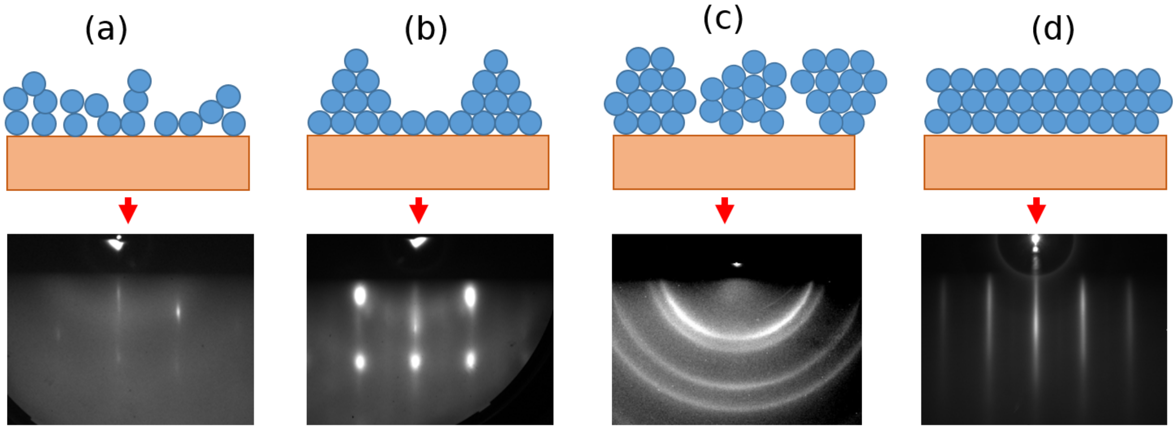

Figure 2.5: Schematic drawings of typical growths and corresponding RHEED patterns. (a) amorphous growth *i.e.* no crystalline order causing diffuse RHEED pattern (the remaining bright rods are from the crystalline substrate). (b) Rough surface induces rod modulation or spots in the RHEED image. (c) Polycrystalline film *i.e.* random orientation of crystal grains leads to rings in the diffraction pattern. (d) Flat and ordered surface with corresponding streaks.

Moreover, we have experimentally access in our MBE setup to a rotation of the sample around the normal to the layers plane called the azimuthal rotation. This allows to change the orientation of the crystal axes with respect to the electron beam. For single crystals *i.e.* samples with only one domain or all aligned grains, like most substrates for instance, diffraction rods will only be visible when the incident beam is aligned with the high symmetry directions of the crystal. In the case of hexagonal symmetry, rods are visible every 30° along the (100) and (110) direction. Each rotation of 60° brings back to a similar diffraction pattern. However, as explained, RHEED is only sensitive to the surface of the material, and it can diffract only between atomic planes perpendicular to the surface, giving information about the crystal structure in the layers plane. Besides, if the crystal structure evolves in later stages below the surface, it is not accessible in-situ during MBE growth using RHEED.

2.1.2 X-ray diffraction

Another diffraction tool that we commonly use in the lab to solve this issue is XRD. This is an ex-situ measurement *i.e.* after taking the sample out of the MBE setup. The work principle is the same as in the case of RHEED except that the diffracted wave is x-ray light in this case. The Bragg's law (see equation 2.1) allows us to accurately measure the lattice structure of any crystal as a function of the wavelength of the beam λ and the angle of diffraction θ. The distance between lattice planes d is obtained with the equation, where n in an integer defining the diffraction order:

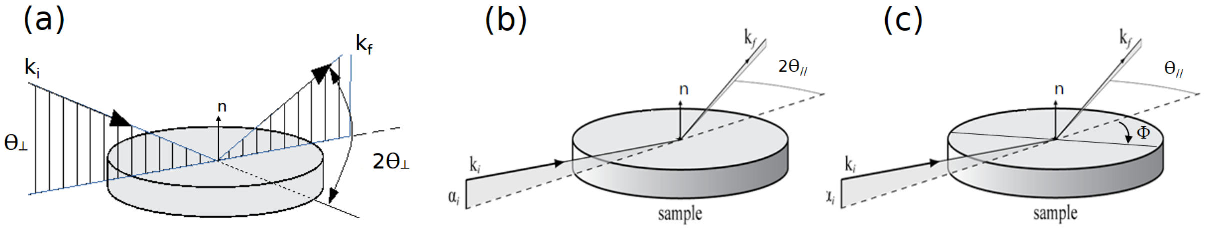

Out-of-plane specular scan In-plane radial scan In-plane azimuthal scan

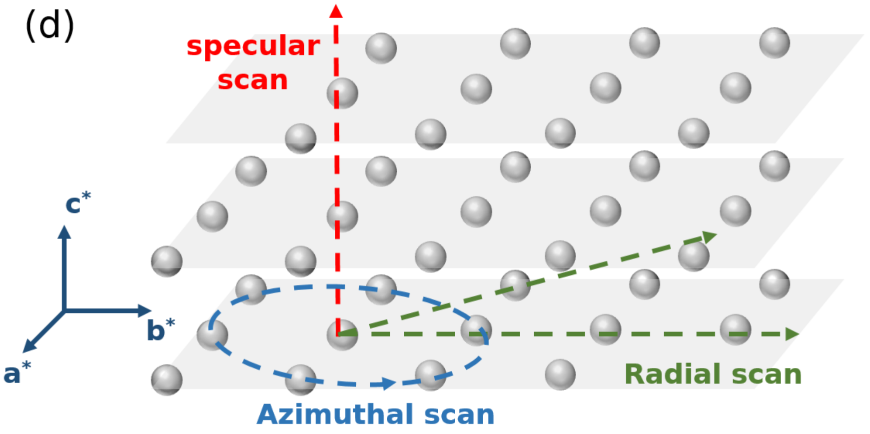

Figure 2.6: Sketches of the geometrical configuration for XRD measurements. k_i and k_f are the initial and final wave vectors and n is the normal to the sample plane. (a) For a specular scan or θ-2θ scan, the incident angle $\theta_\perp$ is varied simultaneously with the detector direction to measure the out-of-plane lattice spacing. For in-plane scans (b-c) , the incident angle is grazing and fixed close to the critical angle (related to refraction at the sample interface). (b) For radial scan, the detector is rotated ($\theta_{//}$ is varied) to perform a θ scan-2θ scan in the sample plane. This allows the mapping of the reciprocal space in the azimuthal direction of the incident x-rays. (c) For an azimuthal scan, the detector is fixed along the direction of a diffraction peak of the material. The sample is then rotated around the normal direction n to perform a Φ scan. (d) Reciprocal space and trajectory of the three different scans. a*, b* are the in-plane directions of the reciprocal space and c* the out-of-plane. Shaded areas are visual guides for the different atomic planes.

$$n\lambda = 2dsin(\theta) \tag{2.1}$$

In order to select the interplanar distance to measure, several geometries can be used for the measurement as illustrated in Fig. 2.6. The reciprocal space of a real crystal is a 3D object. During each scan, we perform a measurement along 1 dimension of the space. We usually perform three types of scans presented in Fig. 2.6.(a-c). Their trajectory in the reciprocal space are sketched in Fig. 2.6.(d). By combining the information of several scans, and usually comparing with a crystallographic database, one can identify which crystalline phase was obtained after growth and potential strain in the system. Moreover, for crystal layers of finite thickness with parallel and smooth interfaces, constructive interferences will result in fringes with decreasing intensity around the Bragg peaks. Their spacing is related to the number of layers and thus allows to obtain the thickness of a thin crystalline film (an example is shown in chapter 3). It has to be noted that for films in the 2D limit (very few layers), the out-of plane periodicity disappears, and only in-plane diffraction scans can be carried out. Finally, in a similar way to RHEED, the width of the diffracted peaks can give information on the average crystalline domains size.

In our lab, the out-of-plane XRD measurements are performed using a Panalytical Empyrean diffractometer operated at 35 kV and 50 mA, with a cobalt source, (Kα = 1.79 Å). A PIXcel-3D detector is allowing a resolution of 0.02° per pixel, in combination with a divergence slit of 0.125° on the source side. Grazing in-plane XRD measurements are performed with a SmartLab Rigaku diffractometer equipped with a copper rotating anode (Kα = 1.54 Å) operating at 45 kV and 200 mA. Collimators with a resolution of 0.5° are used both on the source and the detector sides. Both diffractometers are equipped with multi-layer mirrors on the source side and Kβ filter on the detector side.

2.1.3 Atomic force microscopy

Atomic force microscopy (AFM) is a measurement tool used to map the topography of a surface, with a subnanometer resolution in height. Lateral resolution is in the range of few tens of nm which makes this

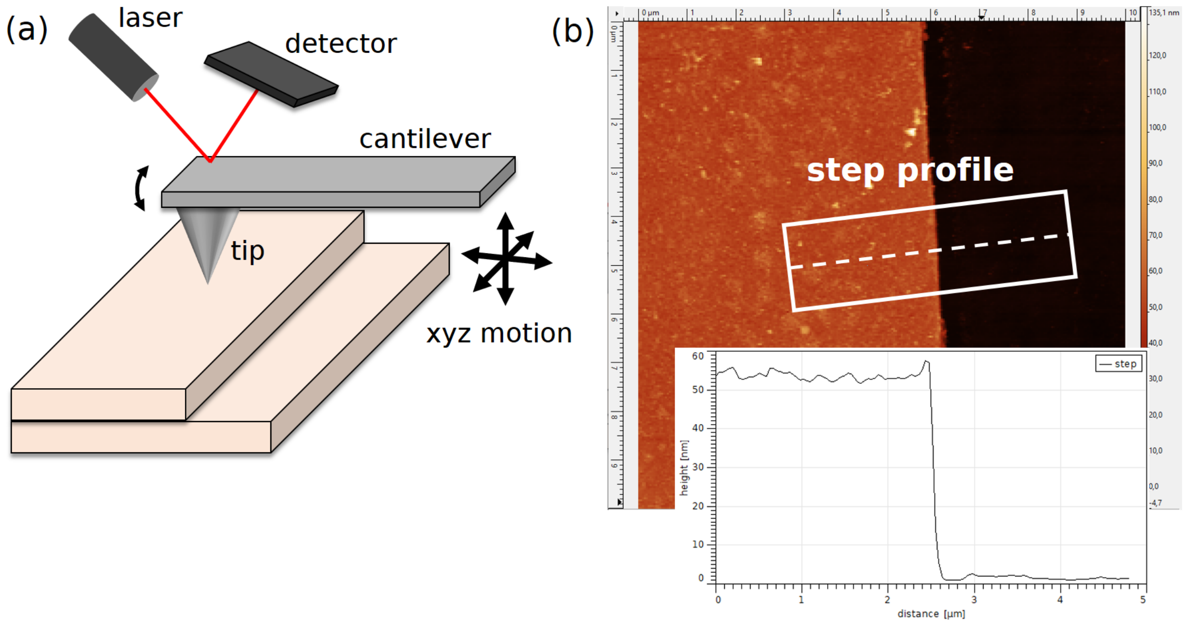

Figure 2.7: (a) Schematic drawing of an AFM setup. A tip at the end of a silicon cantilever is controlled by a piezo-electric xyz stage and follows the surface of a material. A laser reflection is used to follow the deflection of the tip induced by the surface. (b) Example of a 10 x 10 μm scan with a step. The bright colour indicates higher surface. A line profile is performed to measure the step height. The profile is averaged over the width of the white box.

technique ideal to study steps in a material, its roughness and its morphology. A sketch of the setup is shown in Fig. 2.7.(a). A tip with a radius of few nanometres is placed at the end of a silicon cantilever and approached to the surface to image the topography.

Several modes of detection exist for AFM. The most common is the contact mode, where the tip is pressed on the surface to maintain a constant pressure. The cantilever is then moved along x and y and the variation in z are recorded and plotted in a colour map as shown in Fig. 2.7.(b). For fragile samples like 2D materials, we use the peak force mode: the cantilever is vibrated just above the surface and the and the deflection of the cantilever is measured. By plotting this deflection as a function of the vertical piezo-electric motion, one can obtain a force profile with a peak when contact is made with the surface. A control loop can use these information to keep the height above the surface constant and obtain a similar map of the surface topography.

It has to be noted that this technique only allows to measure heights differences. For fully covered films, it is therefore not possible to obtain the thickness with this technique. Moreover, in our lab, we only have access to ex-situ setups working in air, which prevents measurements on air sensitive samples that are usually capped with a protective layer. Thus, we did not perform systematic AFM investigation, but some samples dedicated to AFM study were prepared and measured just after air exposure to limit the degradation of the surface.

The AFM images shown in this document were acquired in the peak force mode of a Bruker's Dimension Icon microscope.

2.1.4 Raman spectroscopy

Raman spectroscopy is a technique to investigate vibrational modes of a molecule or a crystal (called phonons). It relies upon inelastic scattering of photons, known as Raman scattering. A laser is shined on a surface and the interaction with the vibrations in the material results in a gain or loss of energy of the photons. The reflection is measured and the elastic scattering (without energy loss), called the Rayleigh scattering, is filtered out by a notch filter because it has much more intensity. A spectrometer measures the so-called Raman shift induced by the vibration, that are fingerprints of a given molecule or a crystal. A sketch of this setup can be seen in Fig. 2.8.(a).

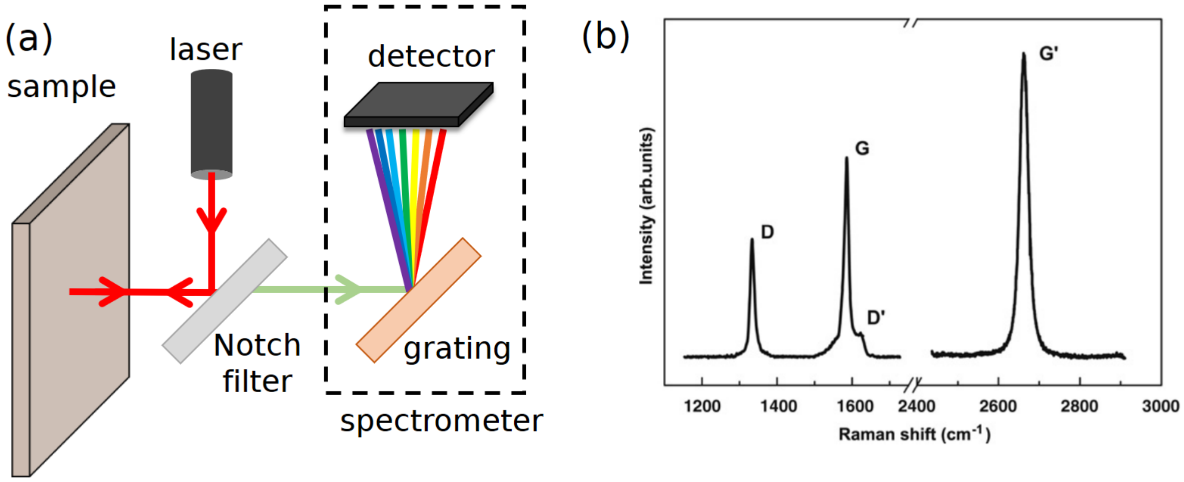

Figure 2.8: (a) Schematic drawing of a Raman spectroscopy setup. (b) Typical graphene Raman spectrum, extracted from [84], showing the D, G and G' bands taken with a laser excitation energy of 2.41 eV.

Figure 2.8.(b) shows how modes are then evidenced as resonances in the spectrum, each being characteristic of a vibration mode. It can be used to identify a material or a molecule. In solid state

physics, we use the width of the peak to correlate it with the crystal quality. We also look for small shifts of the peaks, that can be caused by strain in the lattice, charge transfer from a neighbouring material or different chemical environment (for example the presence of an oxide). The measurements in our lab were performed with a Horiba Raman setup with a 632 nm laser excitation source and a spot size of 0.5 μm. The signal was collected by using a 1800 grooves/mm grating.

2.1.5 Scanning transmission electron microscopy and focused ion beam

STEM is a microscopy technique that uses a beam of electrons, instead of photons as in an optical microscope, to image a sample. Due to the lower wavelength, these microscopes are able to image with a much higher resolution (in the range of 1 Å). To insure that the electrons are able to transmit through the sample, the film must be very thin, of the order of 100 nm. In the case of scanning transmission electron microscopes, the electron beam is focused with electric fields on a specific spot on the sample. A contrast is then obtained, for example the atomic number contrast using the high-angle annular dark field (HAADF) mode. The focused spot is then scanned over the whole surface of the sample to obtain an image of the atomic structure, as can be seen in Fig. 3.14. Energy dispersive x-ray (EDX) spectroscopy can also be used with STEM imaging to obtain an elemental image of a sample.

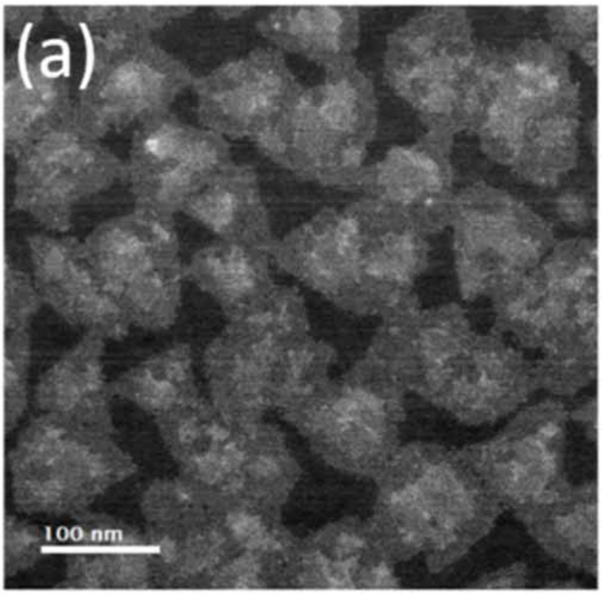

Figure 2.9: HAADF contrast of crystal grains of WSe_2 on a mica substrate imaged by STEM, extracted from [85]. The heavier atoms give the brightest contrast in the image.

In order to study heterostructures, cross section imaging can reveal the atomic stacking, the possible inter-diffusion of some elements and the interfaces between different layers. Focused ion beam (FIB) is a technique to obtain very thin lamella out of large samples that can then be imaged by STEM. Samples have to be protected with a capping layer of Pt and C to avoid the destruction of the crystalline order when cut. Nevertheless, when performed with care, STEM images can reveal the stacking of 2D heterostructures as well as a measurement of the vdW gap between each layer.

In our lab, STEM measurements were performed using a Cs-corrected FEI Themis at 200 kV. HAADF-STEM images were acquired using a convergence angle of 20 mrad and collecting electrons scattered at angles higher than 60 mrad. STEM specimens were prepared by the FIB lift-out technique using Zeiss Crossbeam 550.

2.1.6 Rutherford backscattering spectrometry

RBS is a measurement technique to probe the chemical composition of a material. High-energy (in MeV) $^4He^+$ ions are directed on a sample and the backscattered ones are measured at a given angle. The energy loss after the scattering is measured and the signal plotted is the number of backscattered ions as a function of their energy. Two phenomena explain this energy loss. The first one is the scattering process with the nuclei in the material. The loss is proportional to the mass of the nuclei and therefore characteristic of each material. The signal will therefore exhibit peaks at different energies for the various elements present in the material. By integrating the intensity of these peaks, one can obtain the relative quantity of each element and deduce the stoichiometry of a sample (see for example Fig. 2.10).

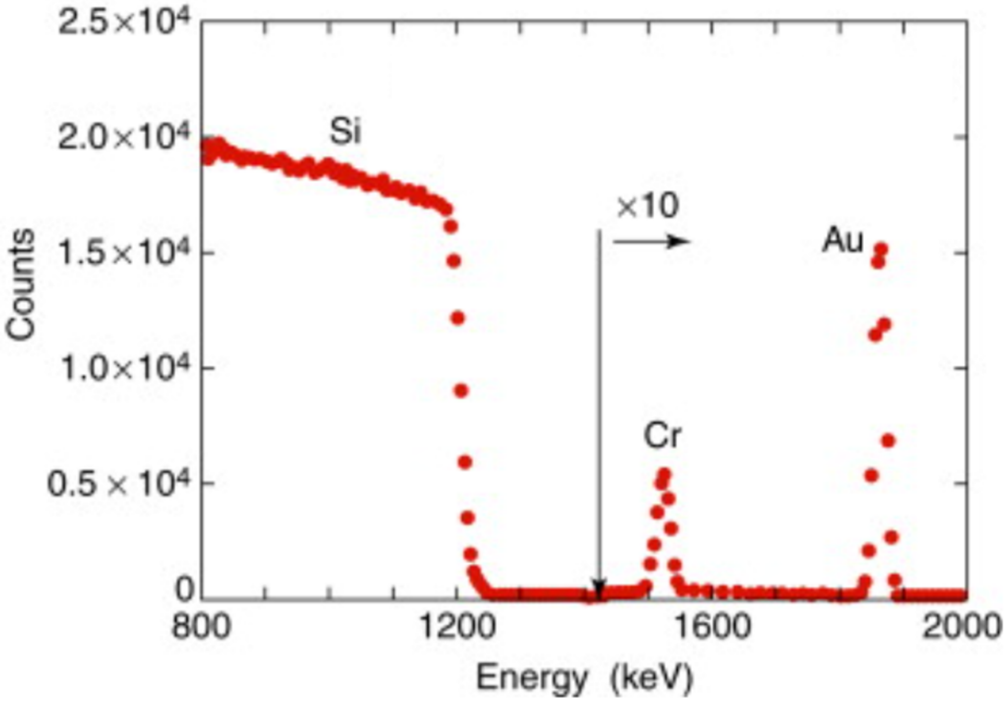

Figure 2.10: Example of an RBS spectrum for thin layers of Cr and Au deposited on a Si substrate, adapted from [86]. The counts are multiplied by 10 for energies larger than 1400 keV.

The second source of energy loss is due to the interaction of high-energy ions with the electrons of the sample. They result in a gradual energy loss as a function of the penetration depth of the ions inside the materia. (easily visible for the Si substrate in the example). This will lead to a shift of the position of the peaks as well as a modification of their width. For thick enough samples, the resolution being of the order of 10 nm, one can deduce a depth profile of the elements.

The measurements presented in this manuscript were performed with a $^4He^+$ beam delivered by the SAFIR Platform at Sorbonne University in Paris at beam energies ranging from 1.5 to 2.0 MeV. For all samples, the scattering angle was set to 160° and the resolution of the detector was 13.5 keV. To avoid channeling effects, the samples were tilted with respect to the normal of the sample in two perpendicular directions.

2.2 Magnetic measurements

Many techniques exist to probe the magnetic order of materials. One can look for example at magnetic domains with the help of magnetic force microscopy (similar to AFM except the the intensity of the signal is proportional to the magnetic stray field instead of the topography), NV magnetometry (the stray field of a material is measured with a nitrogen vacancy at the apex of a tip), photoemission electron microscopy etc. These techniques are best suited for the analyses of magnetic domains, domain walls or spin textures like skyrmions. Ferromagnetic resonance (FMR) measurements can also be used with the absorption of an electromagnetic microwave in a cavity. This technique is typically used to study magnetization dynamics and spin waves in magnetic materials.

However, other techniques were used during the PhD and will now be presented in this section. Their aim is the measurement of a layer magnetization in an external magnetic field.

2.2.1 Magneto-optical Kerr effect

The MOKE is a well-known phenomenon that can be used to measure the magnetization of a sample. When light illuminates a sample, the electric field interacts with it and the reflected wave will depend on the dielectric function of the material. If it is magnetic, the dielectric constant is such that a polarization change will occur. This change is usually expressed as the Kerr rotation and ellipticity, that are both proportional to the magnetization of the layer. A sketch of the effect is shown in Fig. 2.11.

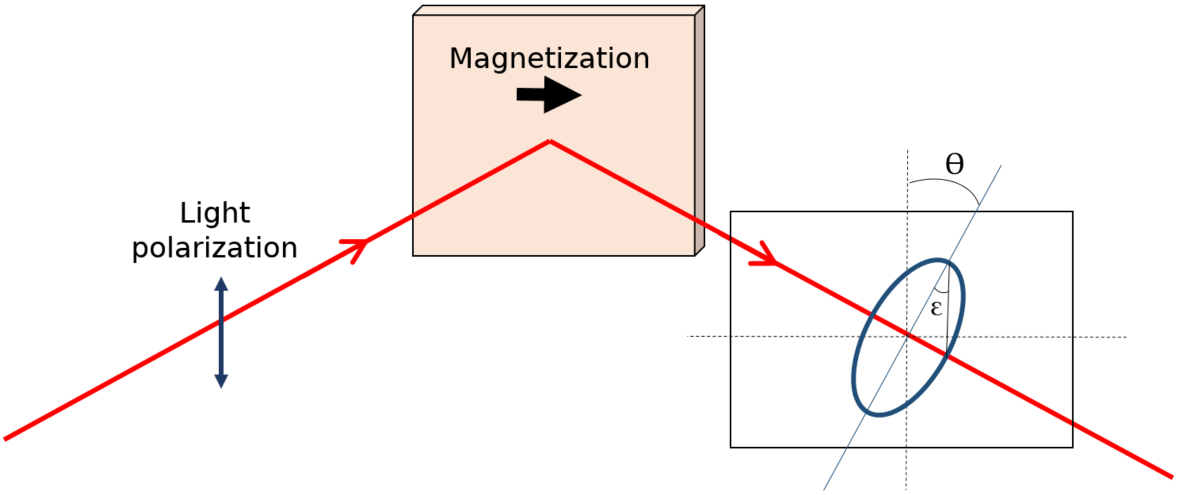

Figure 2.11: Schematic drawing of the polarization change of a linearly polarized light when reflected on a magnetic material. θ and ε respectively stand for the Kerr rotation and ellipticity.

Experimentally, we use two different geometries to measure the magnetic anisotropy of the sample: we use an external magnetic field perpendicular or parallel to the layers plane. In the first case, the experimental setup is called polar MOKE and is illustrated in Fig. 2.12.(a). A laser light is passing though a polarizer to obtain linearly polarized light (the output of the laser is already polarized, so we align it with the polarizer to optimize the signal strength). We use a beam splitter to direct the beam on the sample, standing inside a cryostat and an electromagnet. We then modulate the polarization of the incoming light using a photo-elastic modulator (PEM) at a given frequency. The signal finally passes through an analyser to probe the polarization changes and is measured by a photodiode. The signal is processed by a lock-in amplifier to select only the frequency at which the laser polarization was modulated. For in-plane measurements, the setup is very similar and a schematic drawing is shown in Fig. 2.12.(b).

Due to the windows of the cryostat, a Faraday effect adds a linear contribution with the magnetic field to the signal. However, if an hysteresis is measured, it is a proof of ferromagnetic order in the system. It is not possible to directly deduce the magnetization from the signal amplitude but the temperature

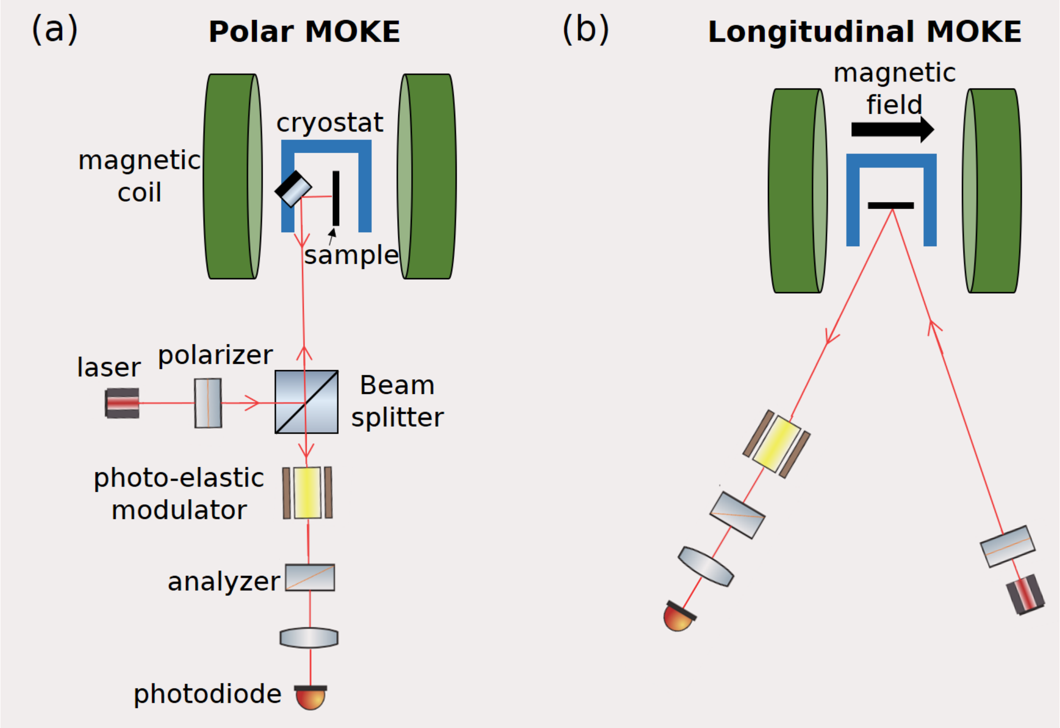

Figure 2.12: Sketch of the experimental setup to perform MOKE measurements. (a) Polar MOKE with the magnetic field perpendicular to the sample plane. (b) Longitudinal MOKE, with the field in plane.

dependence allows to obtain an ordering temperature such as the T_C of the material. By comparing the coercivity in the two geometries, one can deduce the easy axis of magnetization. In the lab, we only have access to magnetic field up to 400 mT, which sometimes prevented to measure any signal in the hard axis configuration. To cool down the samples, a dewar with liquid nitrogen (77K) or liquid helium (4K) is connected to the cryostat.

2.2.2 Superconducting quantum interference device magnetometry

Another instrument we have in the lab to probe the magnetization of magnetic layers is the SQUID magnetometer. The sample is attached with a thin cotton thread and placed into a cryostat in proximity with a superconducting material forming a loop with two Josephson junctions (see Fig. 2.13.(a)). The sample oscillates into the instrument so that its distance to the loop is oscillating. The intensity of the stray field induced by the sample magnetization at the position of the loop is thus varying periodically, which creates an electrical signal by magnetic induction whish is a function of the magnetization.

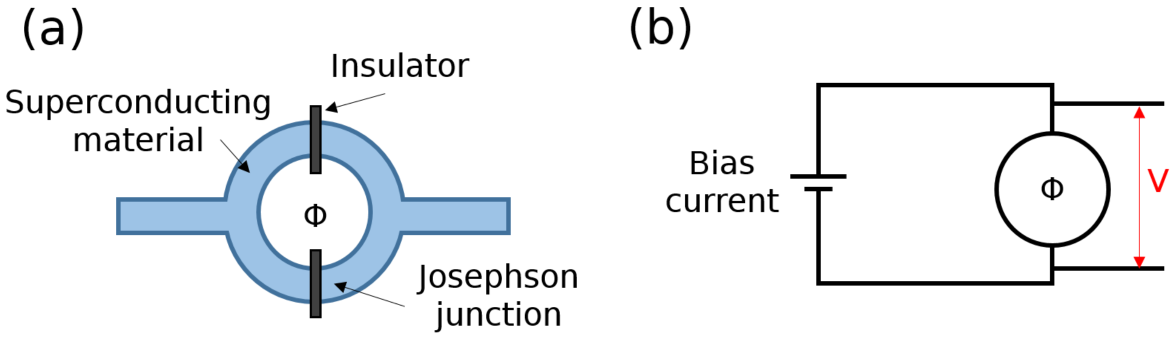

Figure 2.13: (a) Two Josephson junctions forming a superconducting loop. Φ is the magnetic flux crossing the SQUID loop. (b) Simplified equivalent electrical circuit, with the generated voltage V.

The magnetic flux inside a superconducting loop is an integer number of the magnetic flux quantum

Φ_0 = h/(2e). When the sample is moving, the variation of quantized flux is compensated by a current inside the loop. By recording the oscillations of the generated voltage V, defined in Fig. 2.13.(b), one can deduce the magnetic flux created by the sample and therefore its magnetization.

By knowing the geometry of the instrument, this experiment allows to obtain a quantitative measure of the magnetization, unlike MOKE. This setup is extremely sensitive and can detect magnetic moments of the order of few 10^{-9} emu. The measure only gives information about the total magnetization, which can be affected by the presence of impurities (specially if the SQUID chamber was contaminated during previous experiments).

In the case of ferromagnetic parasitic signal (see Fig. 2.14), the usual procedure was to obtain measurements well above the Curie temperature of our material (usually around 350 K) and to subtract this signal from the low temperature measurements. We indeed made the assumptions that the ferromagnetic impurities were mostly iron based, with little variation of their magnetization over this temperature range. The contribution from the substrate had also to be removed, but our substrates only exhibit diamagnetic contribution giving a linear signal with negative slope, which are easily distinguished from a ferromagnetic signal. Finally, some geometric corrections were introduced when comparing measured signals with an applied field perpendicular and parallel to the layers plane. A small difference of saturation magnetization was usually found, which is not intrinsic but caused by a different average distance between the sample and the Josephson junction in the two configurations. The intensity of the signals were therefore corrected to remove this difference by a rigid multiplication of the whole signals to set both saturation magnetization (in-plane and out-of-plane) to the average value of the two.

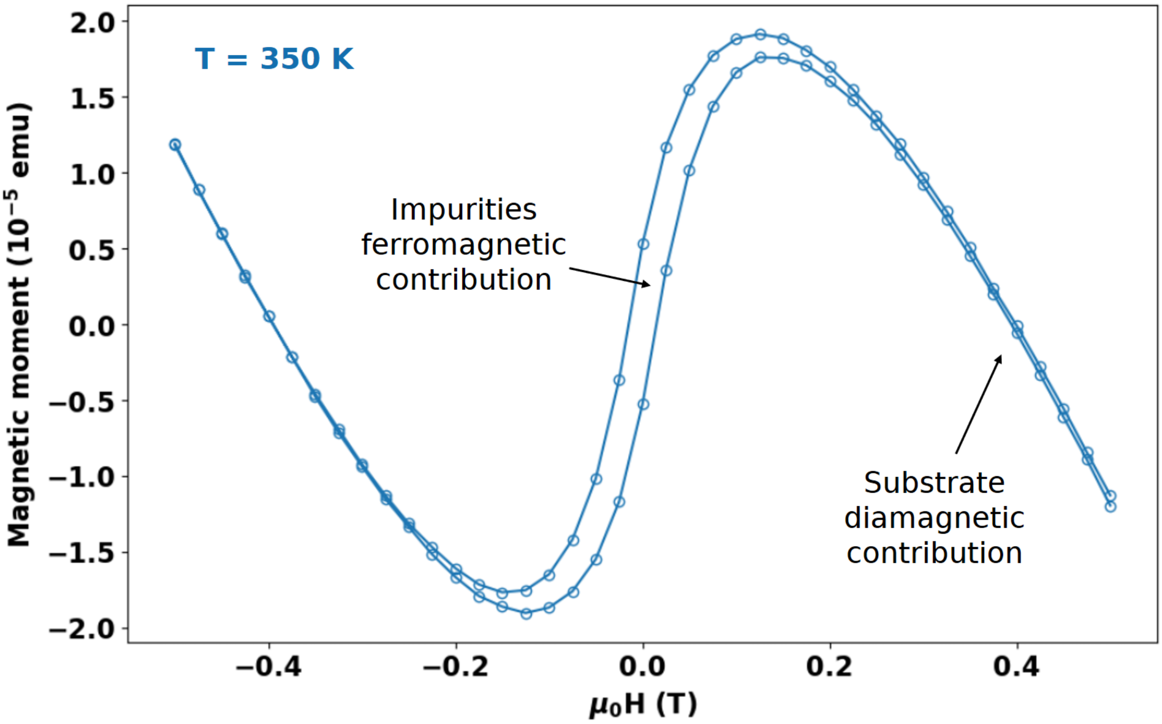

Figure 2.14: Example of high temperature (350 K) measurement with an hysteresis loop caused by ferromagnetic impurities picked up by the supporting cotton thread inside the SQUID chamber.

The measurements were performed using a Quantum Design magnetic property measurement system.

2.2.3 X-ray magnetic circular dichroism

To verify the origin of the measured ferromagnetic signals, we also applied for some beamtime at the French synchrotron radiation facility (SOLEIL, Paris) to perform XMCD measurements. We were able to obtain three different weeks of beamtime to study the signal of various layers over the course of the PhD on the DEIMOS beamline [87].

As mentionned in the introduction, ferromagnetism in a metal leads to an imbalance at the Fermi level of the density of states for spin up and down electrons. Some electrons are excited during an XMCD measurement with x-rays to an higher energy states. Because of the conservation of angular momentum, the absoprtion of a circularly polarized photon (of angular momentum ± 1) triggers electronic transition between energy levels with a difference of orbital angular momentum ± 1. For transition metals such as Fe, Co, Ni or Cr, the probed transition is between 2p and 3d electrons as sketched in Fig. 3.20.(a). The transition rate is proportional to the number of occupied initial states times the number of empty final states. Due to the spin imbalance, the number of empty states is lower for spin up in the 3d band, meaning that the transition rate from the L_3 band will be lower than for spin down, and vice versa for the L_2 band.

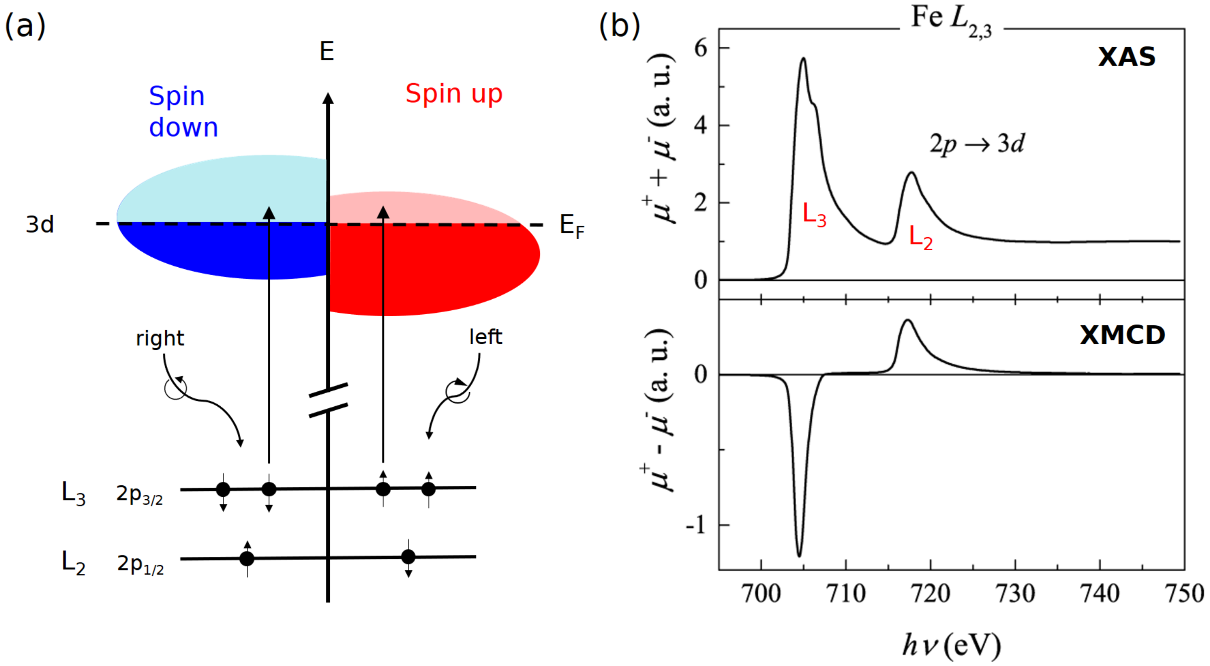

Figure 2.15: (a) Transition between 2p and 3d orbitals. Circularly polarized light only interact with one spin channel. (b) Experimental spectra of XAS and XMCD of 12 nm Fe_5GeTe_2 adapted from [43]. The top pannel is the average of the TEY signal of σ^+ and σ^-. The bottom one is the difference.

In order to experimentally measure this imbalance of the two spin populations, directly proportional to the layer magnetization, circularly polarized light is used to excite only one spin channel. After the excitation, photoelectrons relax to lower energy states in a cascade. This is measured experimentally as a weak electrical current and called the total electron yield (TEY) mode to obtain the absorption for each light helicity. The difference between the two is the XMCD, which allows to deduce the magnetic properties of the measured material. As the energy levels of the transition depend on the nature of the atoms, XMCD is thus an element selective magnetic probe that can measure independently the magnetic moments carried by each element in a multilayer system or an alloy. Finally, the technique is local in the sense that the focus spot of the x-ray beam on the sample has a diameter size in the range of 200 μm. It is therefore important to have samples with homogeneous quality to obtain relatable and reproducible data.

Experimentally, each XMCD spectrum was obtained from four measurements, where both the circular helicity and the direction of the applied magnetic field were flipped. The x-ray absorption spectroscopy (XAS) data were then averaged (the signals of opposite helicity and field) and normalized to the absorption at the pre-edge of chromium (565 eV). This is synthesized and graphically explained in appendix. To exploit the results of this technique, the XMCD sum rules have been derived in the 90s [88] to calculate the spin and orbital angular momentum (μ_s and μ_L) from the experimental spectra. The area of the XMCD peaks at the L_3 and L_2 edges as well as the one of the XAS (after subtraction of the background) are used to get the equations below (only true for 2p → 3d transitions):

$$\mu_s = -\frac{XMCD_{L3} - 2\,XMCD_{L2}}{XAS}\,\mu_B, \qquad \mu_L = -\frac{2}{3}\frac{XMCD_{L3} + XMCD_{L2}}{XAS}\,\mu_B \tag{2.2}$$

2.3 Device fabrication and magnetotransport measurements

Another way to study the magnetic properties of the samples is through electrical measurements. As explained in the previous chapter, the magnetization of a material will affect its magnetotransport properties, notably through the AHE. These measurements allow also to study proximity effects in vdW heterostructures as well as possible magnetic torques to achieve magnetic switching with current pulses.

2.3.1 Clean room preparation

In order to perform these measurements, one has to pattern devices in the shape of Hall bars to be able to control where the current is flowing and to be able to use different geometries when measuring. Symmetries are indeed crucial to disentangle the different contributions to the electrical transport like for instance thermal effects. To avoid contamination of the sample during this device fabrication process, the work is done in a clean room environment. All the users have to wear protective suits to prevent to

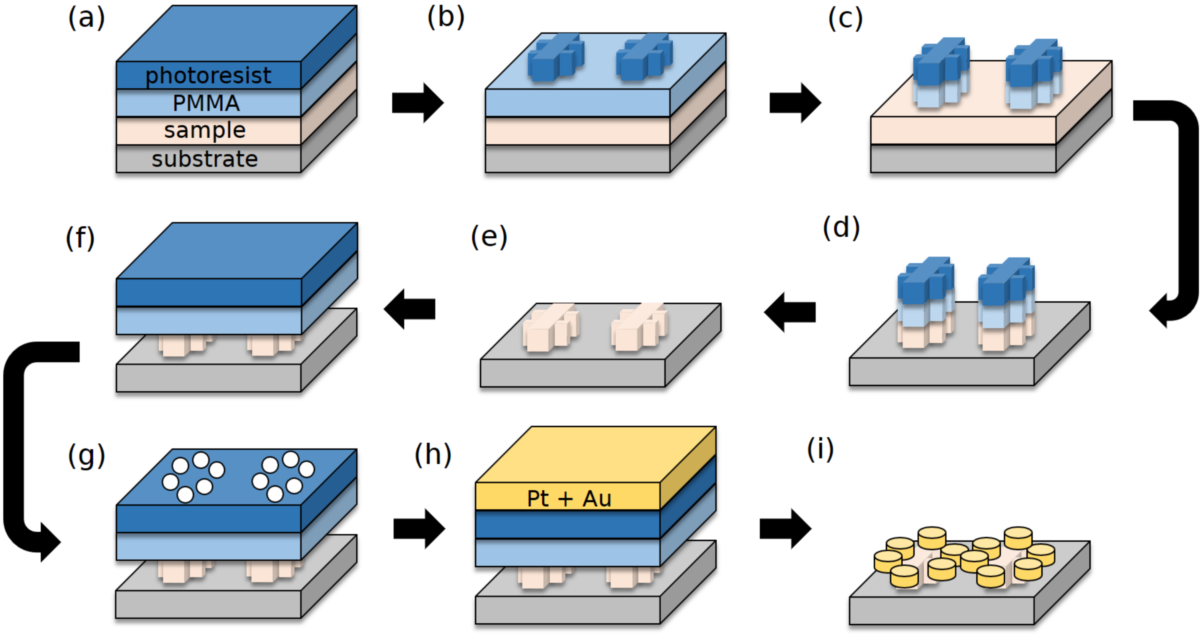

Figure 2.16: Sketch of the process for the preparation of Hall bars connected to gold pads. (a) Spin coating of protective and photosensitive resists. (b) After laser exposure and development. (c) After oxygen plasma. (d) After Ar etching. (e) After lift-off in acetone. (f) New spin coating of resists. (g) After lithography of the contact pads and development. (h) After contact deposition. (i) The end result after lift-off in acetone.

introduce dust or contaminants into the lab room. The whole process is synthesized in Fig. 2.16 and the different steps detailed below.

The first step of the process is to prepare the pattern on the samples using laser lithography. First of all, we spin coat a photosensitive resist over the whole surface of the sample. For 2D materials, the bonding with the substrate is very weak and a double resist process has to be done to protect the layers from delaminating during development. It has to be noted that the samples need to have a large enough surface for this step due to some inhomogeneities of the spin coating on the edges of the order of 1 to 2 mm. The resist is baked and then exposed to a laser light following a predefined pattern (see Fig. 2.17.(a-b)) to change its chemical properties. The part that was exposed is dissolved when put in a basic solution called the developer, so that the whole sample is still under resist except for the patterned regions.

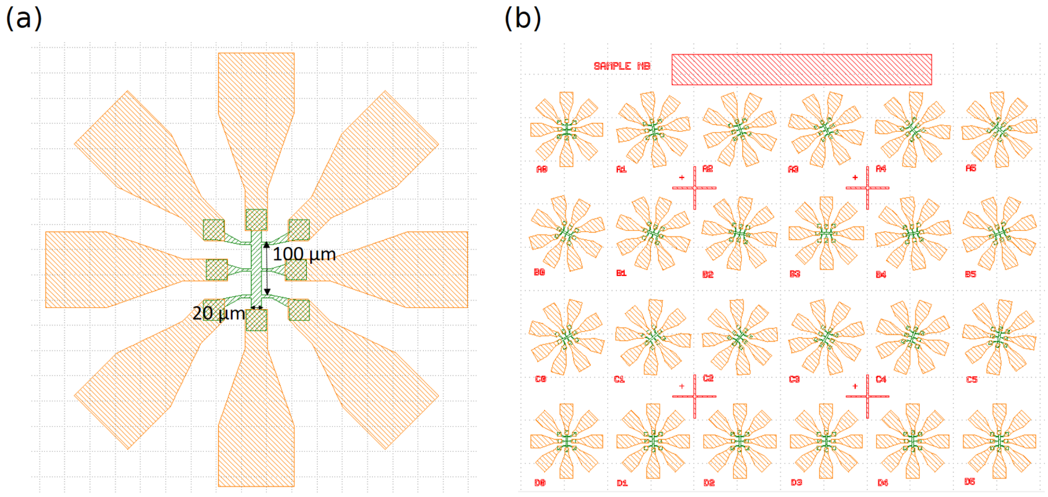

Figure 2.17: Pattern for devices made with the help of KLayout [89]. (a) Zoom on one Hall bar (in green) with the contact pads (in orange). (b) The whole pattern, with rotation of 10° (counter clockwise) every Hall bar. The bottom row is a repetition of the first device.

During the second part of the process in Fig. 2.16, the exposure is called inverted. This means that the whole sample (we define a square around the patterned area) is exposed except the pattern, which means that the only part with resist after development corresponds to the Hall bars. The protective PMMA resist is then removed with an oxygen plasma (very efficient to etch any organic compound such as a resist). The photosensitive resist layer is much thicker than the PMMA one (1.2 μm vs 270 nm). By using an interferometry control of the etching (a laser is reflected on the sample and it interferes with the reflection on the resist so that the intensity oscillates as the thickness is reduced), we can therefore etch the PMMA while preserving a thick enough layer of the other resist.

To remove the sample except at the location of the Hall bars, we expose it to an Ar ions plasma that mechanically etches the layers until we only have the substrate remaining. The resist is then removed from the top of the pattern when dipped in an acetone bath overnight. We then repeat the laser lithography step to pattern regions for electrical contacts. The size of the Hall bar is micrometric. In order to be able to make the bonding, we need contact pads with a side of 150 μm that are connected to the device (see Fig. 2.17.(a)). We have to align the setup with the previously patterned Hall bars, and we repeat the exposure, development and oxygen plasma parts. Finally, by using an e-beam evaporator, we deposit electrical contacts composed of 10 nm Ti for the bonding to the substrate and 100 nm gold to obtain a good conductivity. After lift-off in acetone of the gold excess where the resist was standing, the devices are ready for microbonding.

2.3.2 Microbonding

Once the devices processed, the sample can be glued to a Polychlorinated biphenyls (PCB) connector before it is introduced in the into the Spectromag OXFORD cryostat as can be seen in Fig. 2.18. We use a General Electrics varnish that withstands the strain when cooled down to cryogenic temperatures and that insures good thermal contact.

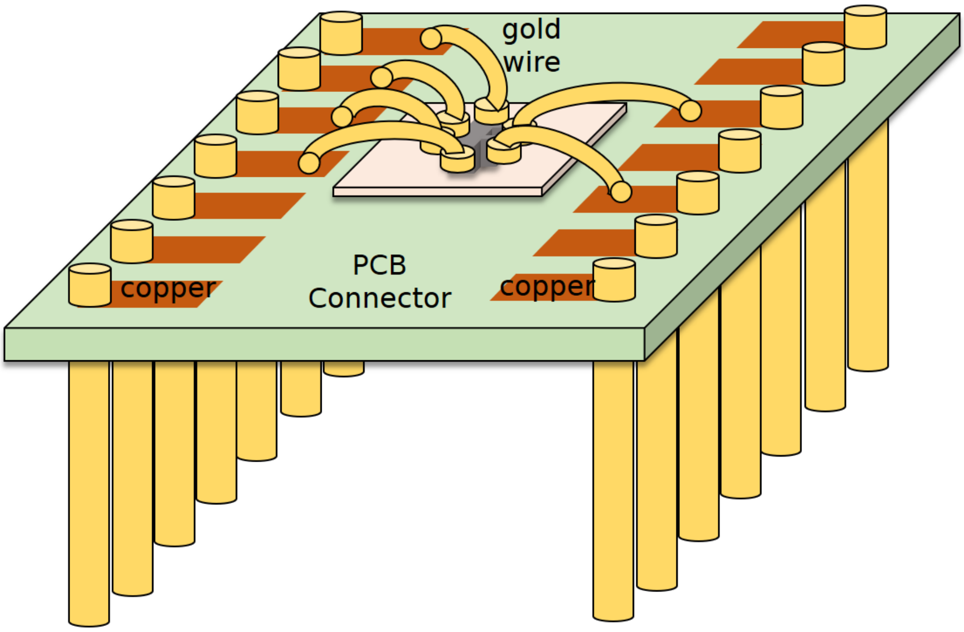

Figure 2.18: Schematic drawing of a device bonded with gold wires to a connector for magnetotransport measurements.

To bond the devices to the copper pads on the connector, we used a technique called ball bonding. A ball of gold is made with an electric arc at the end of a thin gold wire (25 to 50 μm) and is then bonded onto the copper using pressure coupled with ultrasonic vibrations. The second end of the wire is then bonded onto the gold pads contacting the Hall bars of the sample. The copper pads have to be cleaned prior to the bonding (using acid to remove surface oxidation) to obtain a better contact with the gold ball.

2.3.3 Physical property measurement system

To perform the magnetotransport measurements in our lab, we used the SpectromagPT from Oxford Instruments that can operate down to 2 K and with a magnetic field up to 7 T. A sketch of the equipment is shown in Fig. 2.19. The sample is placed into a space in contact with a variable temperature insert (VTI) that is cooled down using successive helium gas compression and expansion in a closed loop. This allows to perform low temperature measurements without the need of using liquid He from an external source like a dewar. The sample space needs to be pumped before cooled down to avoid the formation of ice due to the presence of water vapour in air. To insure the thermal conductivity, we nevertheless could not let the sample space in vacuum. We connected therefore the pumping system with a pressurized bottle of helium gas to inject He in the sample space after pumping. Typical working pressure was around 800 mBar.

To be able to perform intense magnetic field measurements, the system was equipped with a superconducting magnet, that needed to stay under 5 K to avoid the transition from a superconducting to a normal state. Magnetic field ramp rates as well as cooling down rates under field had to be compromised to insure that the magnet temperature was not going to increase above this transition.

The direction of the magnetic field was fixed but the sample holder could rotate with the control of a step motor along the axes of the equipment (see Fig. 2.19). Two connectors were available to have the sample plane perpendicular to the field direction (as in the sketch) or in its plane. The sample is then connected to Keithley nanovoltmeters for DC measurements as well as lock-in amplifiers for second harmonic experiments. Samples had to be manipulated with great care once bonded due to electrical discharge from static electricity. To prevent the destruction of the Hall bars due to these effects, the operator is always connected to the electrical ground with a wrist bracelet attached to a metallic wire when in contact with the sample holder.

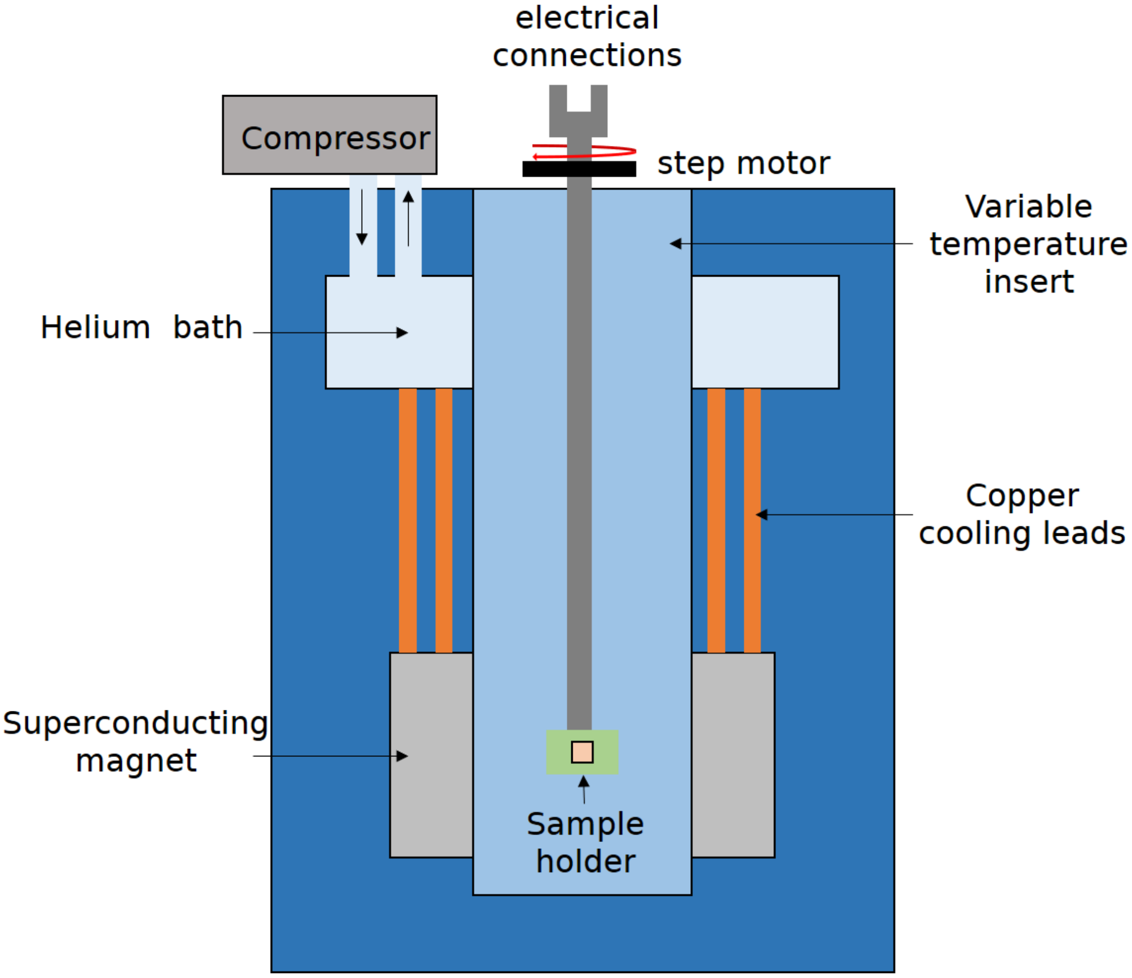

Figure 2.19: Simplified sketch of thethe OXFORD SpectromagPT. A closed-cycle He circuit cools down both the superconducting magnet as well as the VTI. A full 360° rotation of the sample holder can be controlled with a step motor to vary the orientation of the magnetic field with respect to the sample.

Electrical measurements were carried out in the 4-probe configuration, meaning that the current is injected between the top and the bottom of the Hall bar whereas the voltage is measured on the side contacts. This eliminates the contact contribution to the resistance and allows an accurate measurement of the layers resistivity.

CHAPTER

3

2D materials/Cr_2Te_3 vdW heterostructures

As mentioned in the introduction, $Cr_{1+x}Te_2$ compounds have generated a lot of interest due to the large spectrum of reported magnetic properties. Nevertheless, large scale growth of these materials in a controlled manner remains a technological challenge. For similar growth condition in MBE setups, layers of $CrTe_2$ have been obtained on graphene[20], Cr_2Te_3 films were grown on sapphire [50], Si (111) [48], Bi_2Te_3 [73, 90] etc., and Cr_3Te_4 was reported by Lasek et al. grown on MoS_2 [51]. It is therefore interesting to investigate whether the substrate is at the origin of the different reported phases..

In the lab, we performed many epitaxial growths with similar conditions on several substrates as well as 2D materials and always obtained the Cr_2Te_3 phase. We observed vdW bonding of this material when grown on 2D materials as well as strain dependent PMA. The main findings of this part are published in reference [91].

3.1 Epitaxial growth of Cr_2Te_3 on 2D materials

First, the growth of the different layers and heterostructures as well as their full characterization will be presented. Most samples have been grown either on graphene/4H-SiC (0001), WSe_2/GaAs (111) or Bi_2Te_3/Al_2O_3. The latter two will be now thoroughly introduced because the whole process was performed in the lab, unlike the graphitization of SiC.

3.1.1 MBE growth of 2D materials for vdW heterostructures

3.1.1.1 WSe_2 on GaAs (111)

The growth of one ML WSe_2 on GaAs (111) was developed by Hervé Boukari et al [92] and a similar process was adapted for our MBE chamber. The choice of the substrate is not random, as this III-V semiconductor has been very well studied for its integration in optoelectronic devices. It is possible to obtain doped and conducting substrates, insulating ones, or even buffer layers at the surface to act as a dielectric material for electrostatic doping with a backgate voltage.

In order to grow 2D materials on GaAs, the surface must be prepared to be able to form a vdW interface with the desired 2D layer. GaAs has a cubic structure and is cut along the [111] direction to obtain an in-plane hexagonal symmetry at the interface, desired for the growth of TMDs. Dangling bonds are however still present which prevent the growth of materials with large lattice mismatch (17% between GaAs(111) and WSe_2). Substrates can be bought with a Ga rich termination (GaAs (111)A) or As rich termination (GaAs (111)B, as in Fig. 3.1.(a)). When conserved in atmospheric conditions, the substrates oxidize at the surface, which can be seen by RHEED with a diffuse pattern (see Fig. 3.1.(b)). Upon thermal heating, the oxygen is re-evaporated as well as As atoms at the surface. Ga atoms then tend to form droplets at the surface that can be observed as dots in the diffraction image. When this process is performed in a Se rich environment (due to a flux directed on the sample from an effusion cell), the surface can be selenized as shown in Fig. 3.1.(a). If the operation was successful, a flat and well ordered surface can be seen with diffraction (Fig. 3.1.(c)).

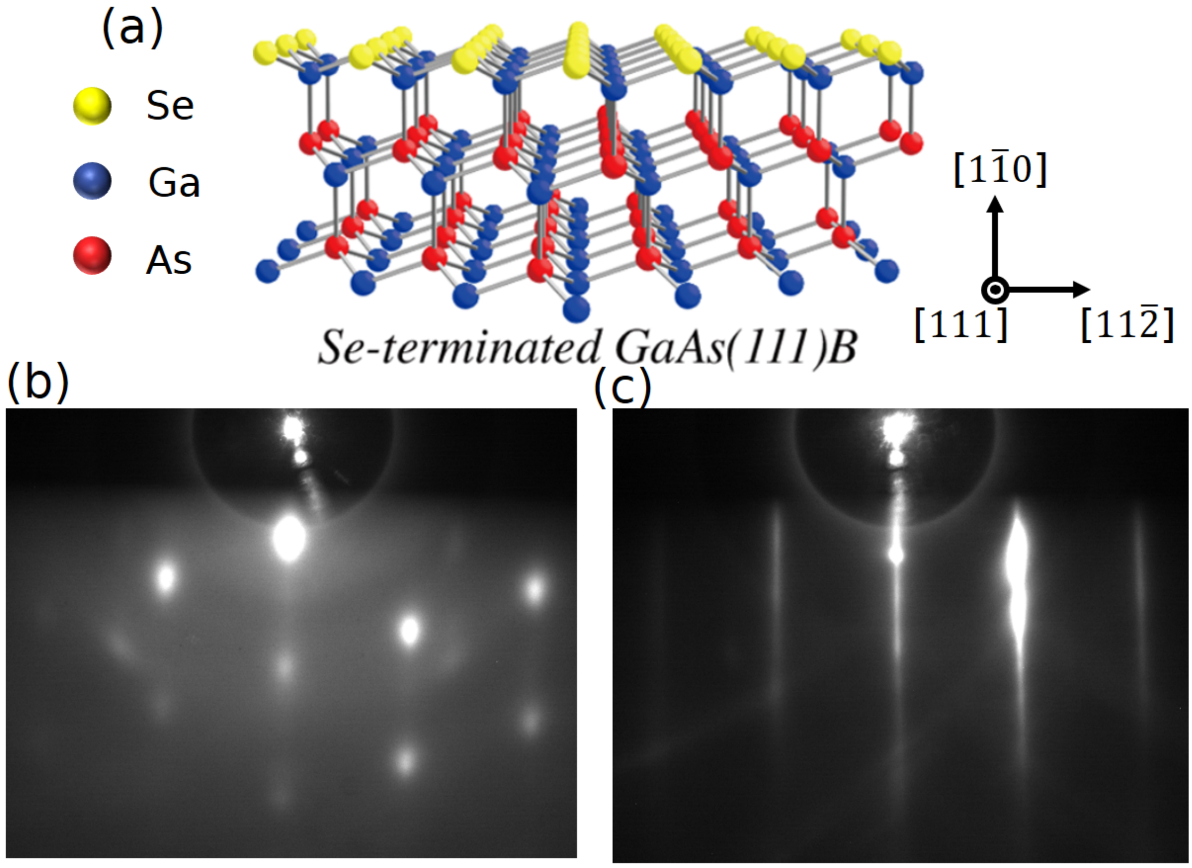

Figure 3.1: Selenization of GaAs (111)B. (a) Crystal structure of selenized GaAs (111)B, adapted from [93]. Se atoms have replaced As sites at the interface. (b) RHEED image of a substrate of GaAs (111)B at the beginning of the desoxidation at 650°C. (c) RHEED image of the same substrate at the end of the selenization at 700°C.

At high temperature (above 350°C), a constant flux of Se was directed towards the substrate to prevent its degradation (evaporation of As). For the growth of WSe_2, the substrate temperature was fixed at 650°C. This allowed a reproducible and high-quality growth, with an optional annealing step of 10 to 20°C for few minutes in order to recover a RHEED pattern similar to the one shown in (Fig. 3.2. A large excess of Se was evaporated due to the high re-evaporation rate of the element from the surface at this temperature. The flux was set to 1.0×10^{-6} mBar with a growth rate of 0.25 ML/min. This is equivalent to an evaporated W:Se ratio around 1:100. This is quite usual for the growth of TMDs by MBE as the deficiency of chalcogens (highly volatile with high vapor pressure) is one of the most common source of defects in these materials.

The crystal axis of WSe_2 are perfectly following the ones of the GaAs substrate as can be seen with the anisotropic RHEED diffraction between the [100] and $[1\bar{1}0]$ azimuths (Fig. 3.2). After the growth of one layer, the rods of the substrate are no more visible, indicating a good coverage of the surface. The width of the diffraction rods is used to assess the quality of the grown film. These optimized layers are of high quality and can be exposed to air without any degradation, which is not the case for the tellurides. To avoid intermixing of Se in Cr_2Te_3 films, the chamber was left to pump 24h after the evaporation of Se.

Some traces could nevertheless still be found, as will be shown with the RBS data.

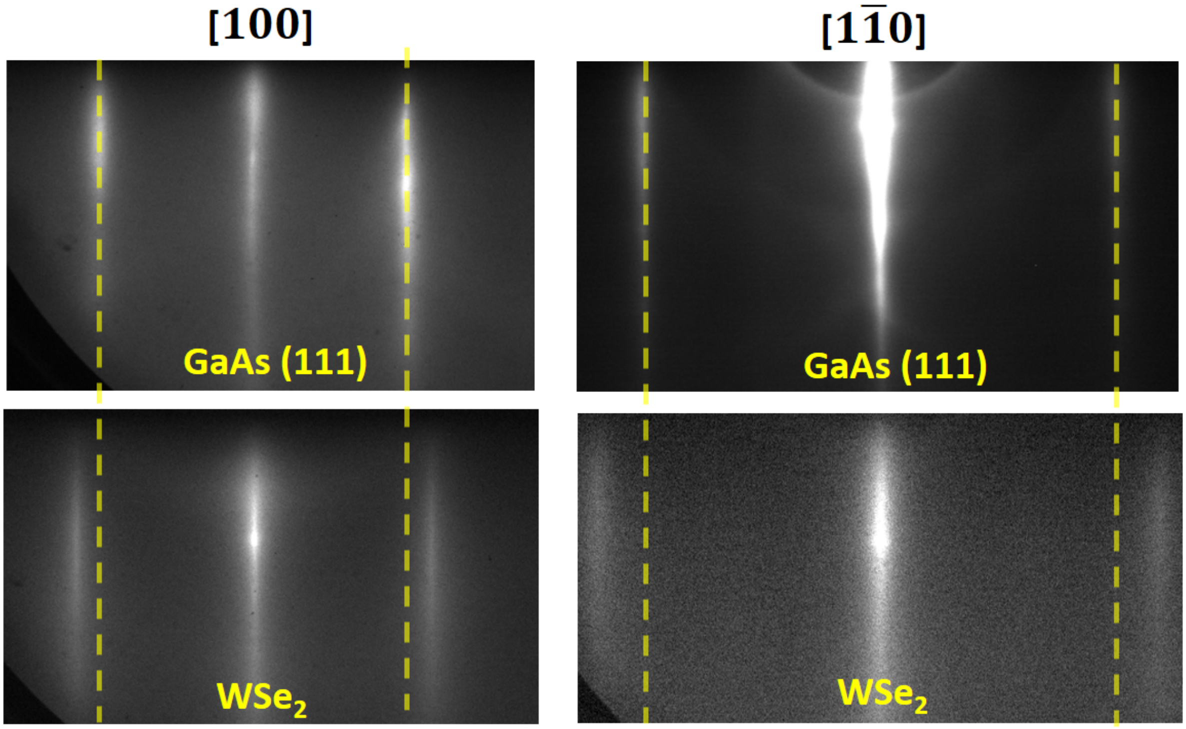

Figure 3.2: RHEED patterns of selenized GaAs (111) before (on top) and after (on the bottom) the deposition of 1 ML WSe_2. Azimuth along the [100] crystal axis of WSe_2 on the left and [1$\bar{1}$0] on the right (in-plane rotation of 30°). Vertical dashed guidelines show the evolution of the lattice parameter.

3.1.1.2 Bi_2Te_3 on Al_2O_3

The growth of Bi_2Te_3 had been studied by other members of the lab before my arrival [94], notably Frédéric Bonell and Mario Ribeiro. 10 nm-thick films (10 quintuple layers (QL)) were grown to obtain a TI phase with edge states. Samples with too low thickness (typically below 6 QL) do not exhibit any Dirac cone when investigated with angle resolved photoemission spectroscopy (ARPES) because the top and bottom surface states overlap [95]. The growth had been developed on sapphire, which is a common substrate in epitaxy with insulating electronic properties. Commercially available wafers are cheap compared to most other used substrates and quite robust. We do not perform any chemical treatment of the surface but the substrates are annealed in air for one hour at 1000°C with a heating ramp of 40 minutes starting from room temperature. They are additionally annealed in the MBE chamber for 30 minutes at 800°C to remove any trace of contaminants.

Bi_2Te_3 films are then grown at a substrate temperature close to 300°C. This value is slightly dependent of the molyblock, so that the operating power (OP) of the manipulator is set to a constant value for every growth in order to optimize the conditions. When the temperature is slightly lower than the optimal one, some Te atomic chains can be deposited on top of the Bi_2Te_3 layers as can be seen with the dots on the RHEED pattern in Fig. 3.3.(a). A step of annealing after the growth can usually remove this excess of Te. On the other hand, if the substrate temperature is set too high, the diffractions rods of Bi_2Te_3 are modulated (see Fig. 3.3.(b)), indicating a rough surface which can affect drastically the growth of other 2D materials on top. However, if the temperature is well optimized, Bi_2Te_3 films produce thin anisotropic diffraction rods after 2 layers (the interface with sapphire is usually a bit defective, leading to diffuse pattern at early stages of the growth). One example is shown in Fig. 3.3.(c). When post-growth annealing is performed, a counter flux of Te is used to limit the creation of Te vacancies or even the evaporation of the Bi_2Te_3 film.

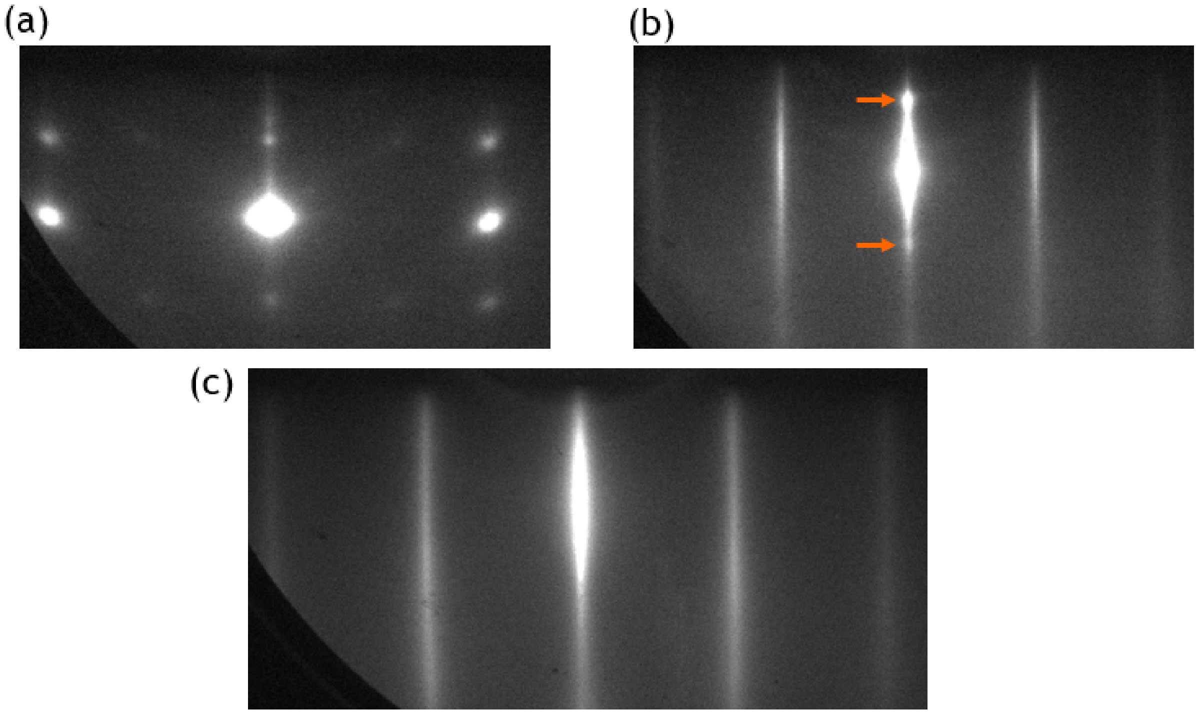

Figure 3.3: RHEED patterns of Bi_2Te_3 films. (a) When the substrate temperature is set too low, epitaxial chains of Te form 3D structures visible as dots. (b) If it is too high, some modulations (evidenced by dots on the specular rod highlighted by the orange arrows) indicate a rougher surface. (c) Flat surface of 10 QL Bi_2Te_3 in good epitaxy with the sapphire substrate.

3.1.2 Structural properties of the grown Cr_2Te_3 films

3.1.2.1 Substrates and growth conditions

As presented in the introduction, several phases of $Cr_{1+x}Te_2$ compounds are stable and we tried in the lab to vary as much as possible the parameters to observe whether we could obtain different phases depending on the substrate chosen for the epitaxy as well as the growth conditions. We have varied the Cr:Te flux ratio, the growth rate, the growth temperature as well as the post-growth annealing temperature of the film. As will be developped just after, the energy given to the system (determined by the growth and annealing temperatures) was found to be the key factor that determines the properites of the grown films. The diagram in Fig. 3.4 recaps the explored parameters as a function of the substrate with a qualitative colour code to reflect the amount of defects in the layers. This latter quantity was assessed using RHEED patterns as well as XRD data. In almost all cases, a large excess of Te was evaporated with a flux ratio of Cr:Te of the order of 1:10. By convention, in this manuscript, a layer of Cr_2Te_3 will refer to one unit cell thickness *i.e.* roughly 1.2 nm. This corresponds to two $CrTe_2$ planes, as can be seen in chapter 2.

On graphene/SiC substrates

Graphene was the first template we used for the epitaxy because of the reported growth of $CrTe_2$ on this material [20]. It is also the heterostructure we studied the most due to its high quality and the simplicity of preparation for us. The atoms mobility on the graphene surface during epitaxial growth is extremely high, which makes it an ideal platform for the growth of other materials. However, for too high growth temperatures, this mobility can hinder the epitaxy due to a very low sticking coefficient of the atoms with the resulting difficulty to nucleate crystal grains on the surface. This leads to the difficulty to fully cover the graphene surface (see rods marked with the orange arrows in Fig. 3.5) and a preferential growth on the already nucleated grains. 3D structures are then obtained as can be seen with the rod modulation highlighted by the green arrows on the RHEED pattern in Fig. 3.5.(a). For very low growth temperature,

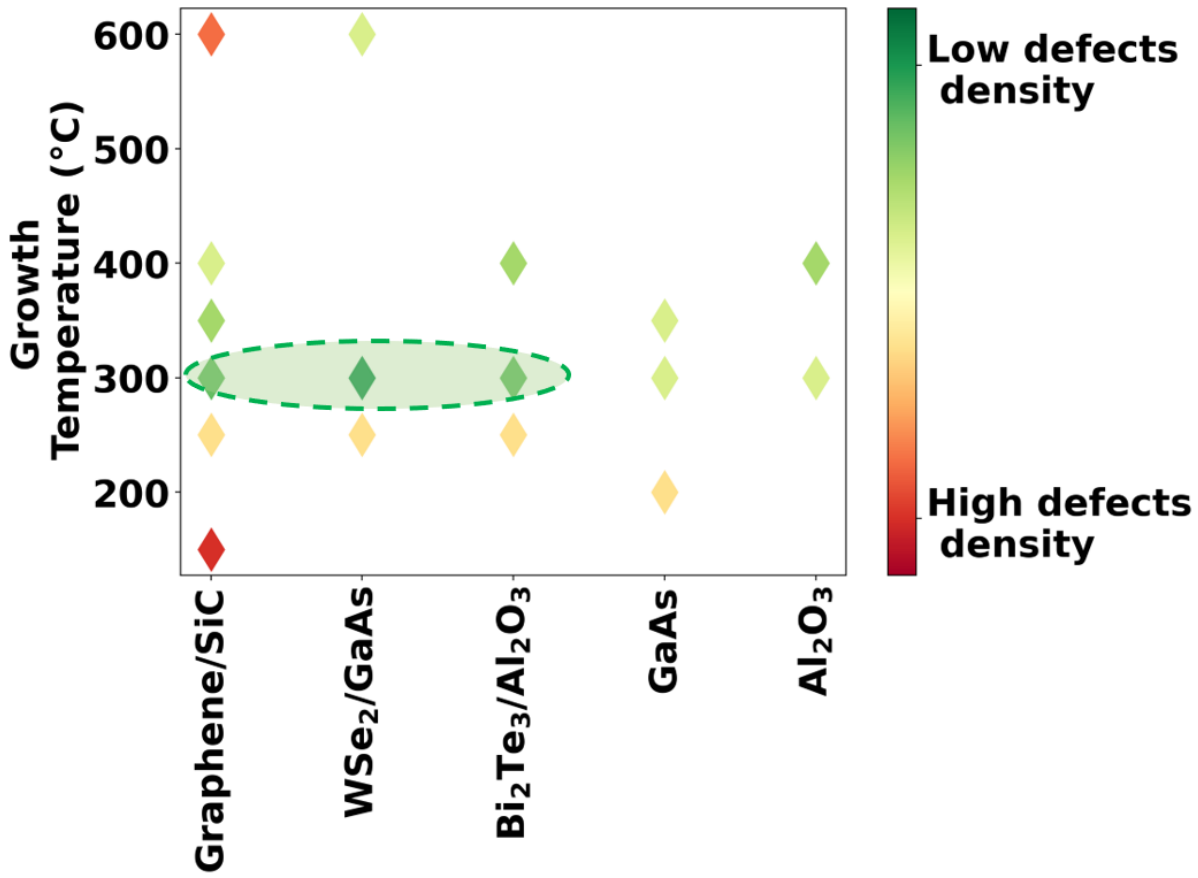

Figure 3.4: Qualitative quality of grown Cr_2Te_3 films depending on the substrate and growth temperature. The green dashed area indicates the experimental optimal conditions.

the evaporated Te atoms stick to the surface and form rapidly 3D chains on the surface that prevent any epitaxy of Cr_2Te_3 on the surface as shown in Fig. 3.5.(b).

Cr_2Te_3films grown on graphene/SiC exhibit very low roughness and large crystal grains demonstrated by the very thin diffraction rods on the RHEED patterns. However, due to the very low interaction with the underlying 2D material, crystal grains nucleate at the early stages of the growth with random orientation leading to a partially isotropic diffraction image, evidenced by the rods indicated by blue arrows in the two azimuthal directions (Fig. 3.5.(d-e)). This is causing some defects at grain boundaries limiting the quality of the samples grown on graphene. For comparison, XRD azimuthal scans (Fig. 3.7) reveal a much better crystal orientation for growth on WSe_2 and Bi_2Te_3.

Other growth parameters were also varied to attempt some improvements like the Cr:Te flux ratio ranging from 1:2 to 1:100. Lee et al. reported an evolution of the structure and magnetic properties with a change of this ratio from 1:3.3 to 1:23 [96]. They observed an increase of the T_C from 180 to 300 K. We did not reproduce this result and only observed very little variation when the Te flux was varied by changing the ratio between 1:5 and 1:100. However, when the Cr:Te flux ratio was greater than 1:5, the grown material was defective with the presence of many rings in the diffraction pattern, indicating polycrystalline growth. The ratio was therefore fixed to 1:10 and kept constant. We also varied the growth rate from 0.1 to 1 ML/min. The changes were rather negligible but the mosaic spread was slightly smaller for samples grown slower. The chosen growth rate was therefore 0.25 ML/min. Finally, we tried to observe some variation of the crystal structure with the thickness but once again we measured no significant structural change for the growth on graphene/SiC. This is consistent with the fact that the layers only interact very little with the 2D material. On the other hand, post-growth annealing was able to significantly improve the crystal quality as evidenced with the width reduction of the diffraction rod in

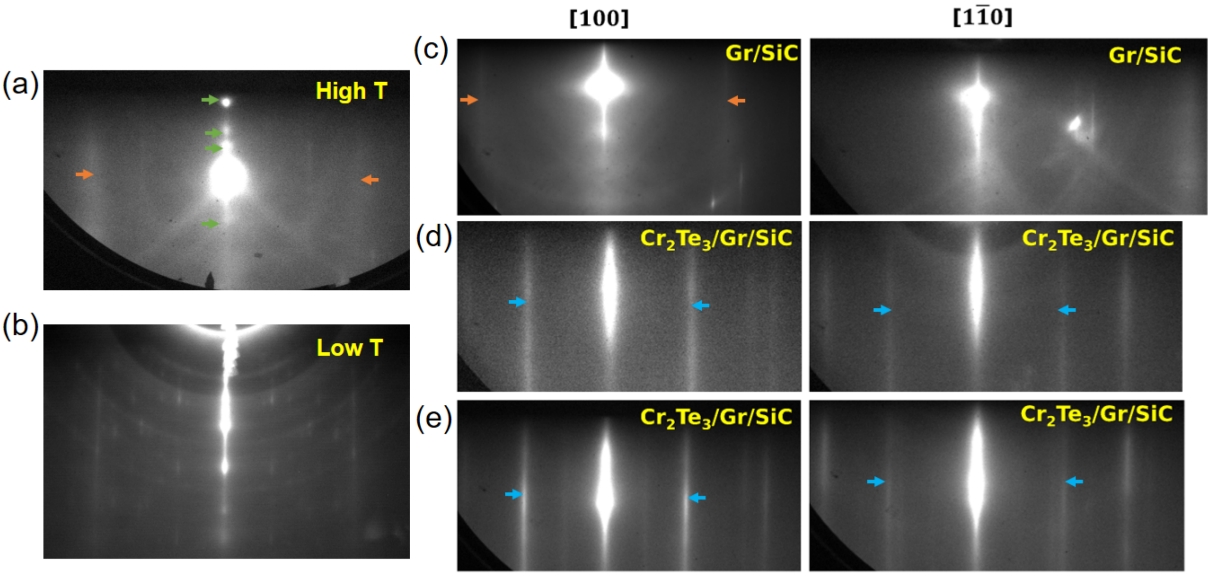

Figure 3.5: RHEED patterns of various Cr_2Te_3 films grown on Gr/SiC substrates. (a) Growth of nominally 10 layers at 600°C. Orange arrows indicate the diffraction rods of the underlying graphene, which is still not covered. Layers roughness is revealed with the dots on the specular highlighted by the green arrows. (b) Rings and spotty RHEED pattern after 30s of deposition at 150°C indicating the presence of Te 3D chains. (c) Gr/SiC substrates after desoxidation in-situ along two main crystal axes. (d) After the growth of 5 layers of Cr_2Te_3 at 300°C. Blue arrows reveal an isotropic crystal grain orientation. (e) After 10 min annealing at 400°C. The width of the peaks is reduced indicating lower defects density and larger grains.

Fig. 3.5.(e).

Based on these experimental findings, we developed the growth procedure sketched in Fig. 3.6 for optimal deposition of Cr_2Te_3 layers on 2D materials. If not specifically mentioned differently, future samples described in this manuscript have been obtained using this recipe.

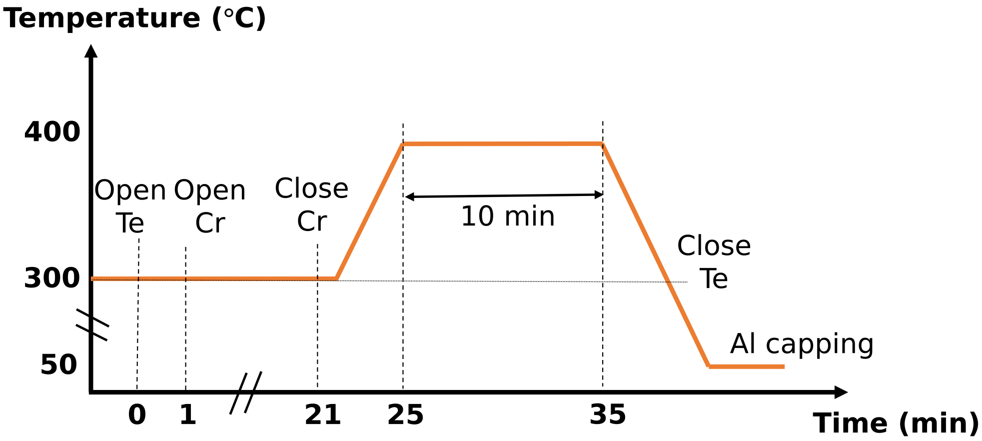

Figure 3.6: Sketch of the deposition procedure for 5 layers of Cr_2Te_3. The growth temperature was 300°C and in situ annealing was performed at 400°C. An Al capping film of 3 nm was then deposited at 50°C.

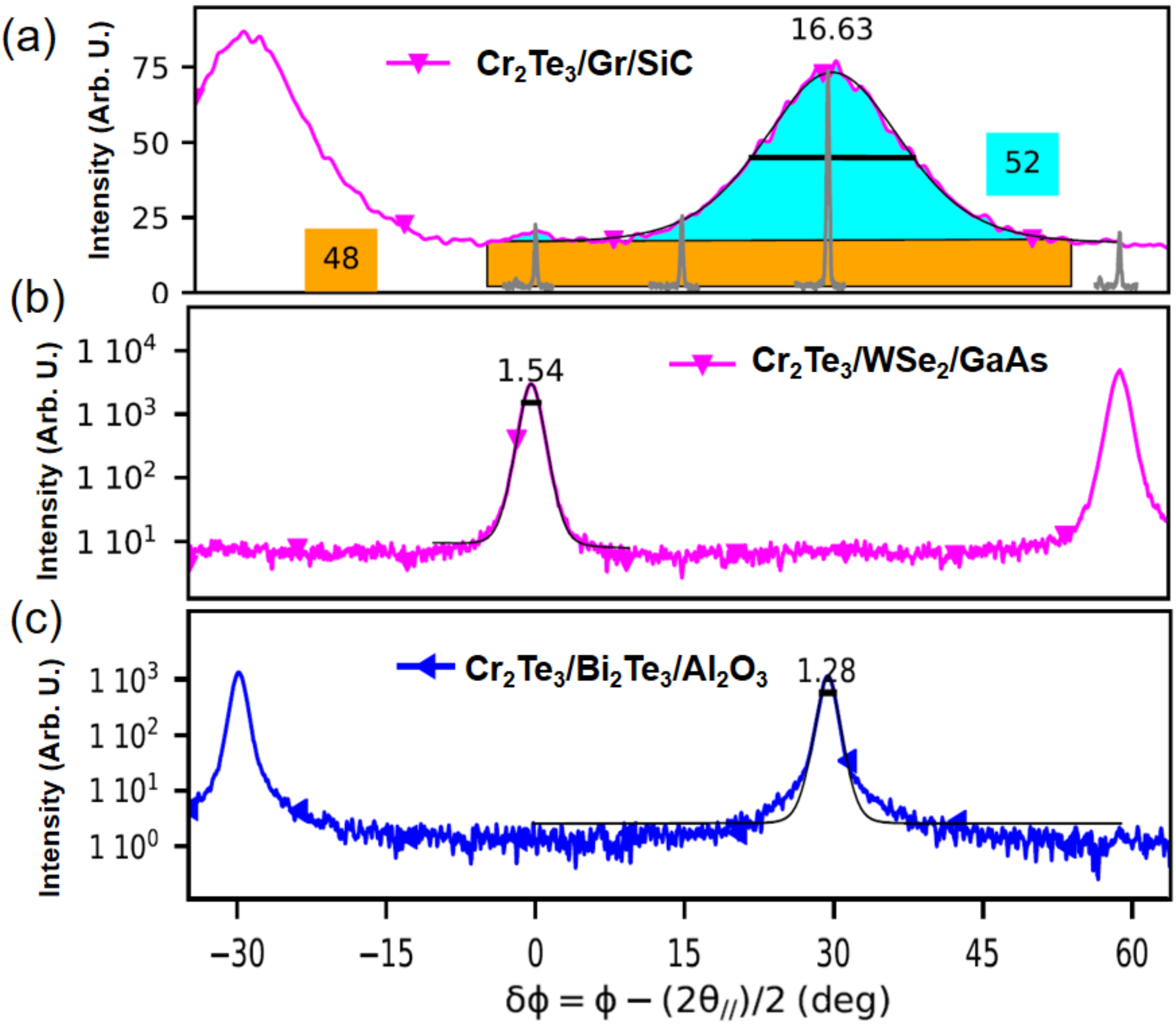

Figure 3.7: Azimuthal XRD scans of the (300) Bragg peak of Cr_2Te_3. (a) Scan of 5 layers of Cr_2Te_3/Gr/SiC. The width of the peak is indicated in degrees above it. The blue area matches the anisotropic contribution (the base level is deduced from the grey curves, which are radial scans around the (300) Bragg peak at the given azimuth). The yellow area crresponds to the isotropic contribution and the numbers indicate the relative weight in % of each on the total area over 60°. (b-c) Scan of 5 layers of Cr_2Te_3 on WSe_2/GaAs (Bi_2Te_3/Al_2O_3).

On other substrates

Cr_2Te_3 films grown on WSe_2/GaAs and Bi_2Te_3/Al_2O_3 substrates showed very similar behaviour and for simplicity, only one growth on WSe_2/GaAs will be presented, with the diffraction patterns in Fig. 3.8. The very thin streaks observed after annealing as well as the low mosaic spread (see Fig. 3.7) indicate the single crystalline character of the films.

Some films were also grown on non vdW materials as presented in Fig. 3.4, namely on GaAs and Al_2O_3. These two substrates have a large lattice mismatch with Cr_2Te_3. At early stages of the epitaxial growth, RHEED diffraction is very diffuse and it is difficult to observe any crystal order but the quality is quickly restored after the growth of a few more layers. We assumed that some defects were present at the interface, but the layers on top were mostly relaxed. We could use these samples as references, notably when analysing magnetotransport measurements.

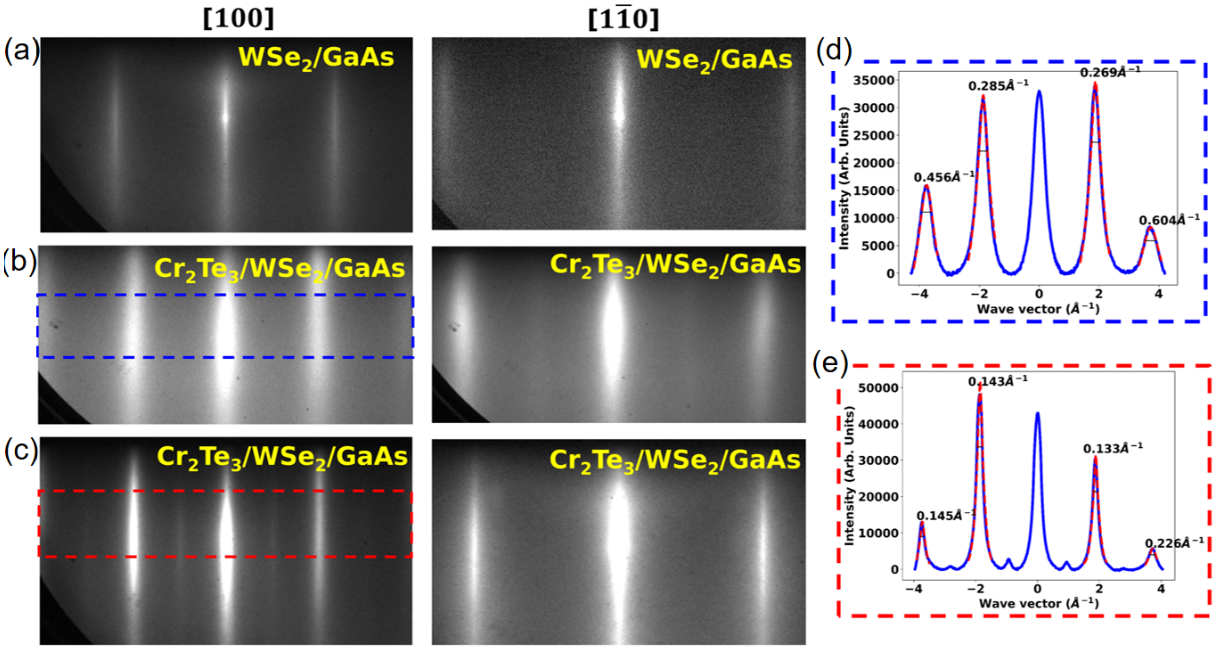

Figure 3.8: (a) RHEED patterns of 1 ML WSe_2 along its two main crystal directions. (b-c) After the growth (annealing) of 5 layers of Cr_2Te_3 at 300 (400) °C. (d-e) Intensity profiles of the RHEED diffraction pattern for images b (blue dashed box) and c (red dashed box) respectively. The wave vector axis was calibrated using the lattice parameter of free standing WSe_2, in agreement with XRD data.

3.1.2.2 Stoichiometry and chemical structure

As claimed before, the phase determination of $Cr_{1+x}Te_2$ compounds is a crucial step to understand grown systems due to the many stable possibilities. In the lab, we have access in another MBE chamber to an XPS setup.

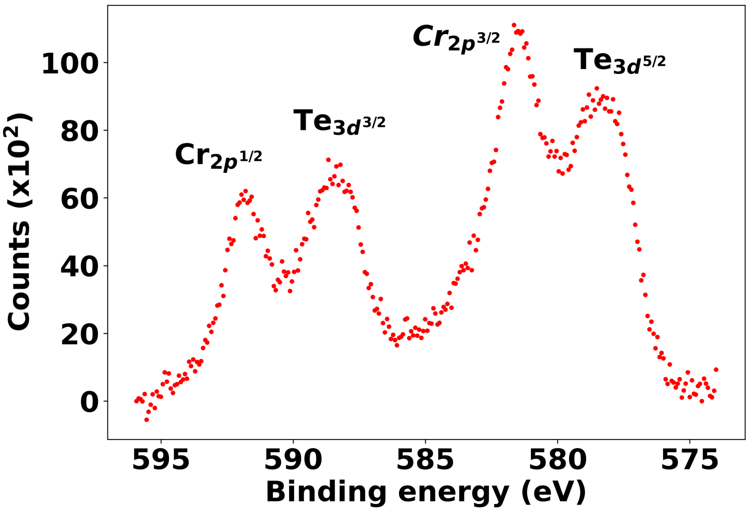

Figure 3.9: XPS spectra of 2 layers of Cr_2Te_3 deposited on Gr/SiC.

XPS probes core level energy transitions by measuring the kinetic energy of emitted photoelectrons induced by x-ray absorption. This energy is characteristic of elements and can also reveal chemical environment due to the shift of peaks (caused by orbital hybridization). Figure 3.9 shows the XPS spectra of 2 layers of Cr_2Te_3 deposited on Gr/SiC. A Mg anode was used to emit photons with an energy of 1253.6 eV. The spectrum displays the binding energy of Cr_{2p} and Te_{3d} core levels. The observed peaks show the presence of these elements in the sample and the absence of doublet for each peak demonstrates that the sample is not oxidized (when Cr or Te are bonded with O atoms, it shifts the photoelectron binding energy to higher values).

It is possible to quantify the stoichiometry of the sample using the area of the peaks. They have to be normalized by a relative sensitivity factor unique for each element core level. The position of the elements in the stack can also affect this measure due to scattering events of the emitted photoelectrons or absorption of x-rays. These two factors also depend on the binding energy. It is however possible to properly disentangle all these factors by measuring reference samples, either pure Cr and Te layers or samples with well-defined stoichiometry. In the lab, we only used this technique to verify the chemical environment of the grown elements and to compare samples on a relative basis.

To obtain the stoichiometry of our layers, we used another technique, namely RBS. The sensitivity of this experiment is much higher and allowed us to obtain the composition of our films with an error of less than 1%. Several samples were measured using this technique grown on graphene/SiC as well as on Bi_2Te_3/Al_2O_3. It was not possible to measure samples on GaAs substrates because of the secondary source of energy loss in RBS measurements: the Bremsstrahlung. Due to the thickness of the substrate (usually between 200 and 300 μm), He ions loose a lot of energy due to the electrons of the substrate. As can be seen in Fig. 3.10, the peaks of the substrate have a continuous spectra below the characteristic energy of each element. Ga and As are both heavier atoms than Cr, meaning that the Cr peak would be hidden in the substrate background signal.

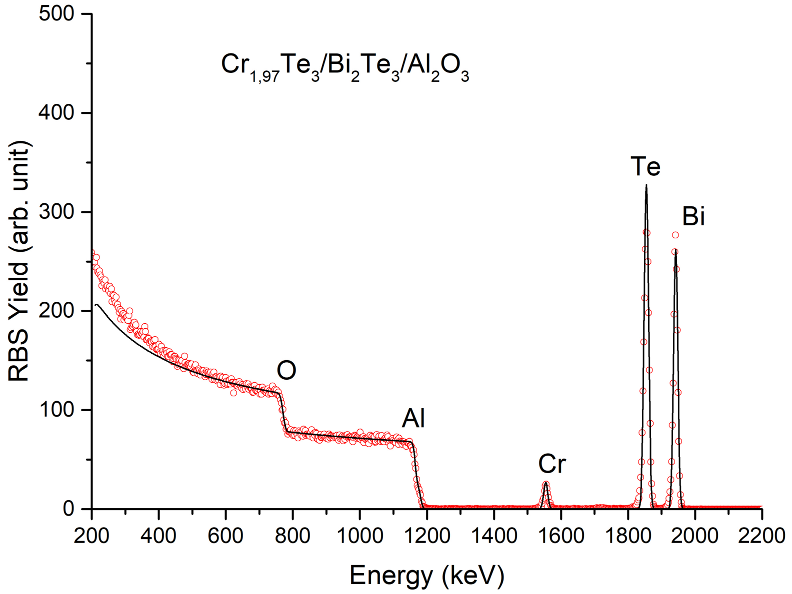

Figure 3.10: RBS of 5 layers of $Cr_{1+x}Te_2$ deposited on Bi_2Te_3/Al_2O_3. To determine the stoichiometry of the ferromagnetic layer, the one of Bi_2Te_3 was assumed to be 2:3.

All the measured samples were found with a stoichiometry of 2 Cr for 3 Te atoms within the uncertainty of the measurement leading to the conclusion that the only phase we could grow by MBE was Cr_2Te_3. It has to be noted that the measured samples were all grown at temperatures lower than 400°C, since we were able to modify the stoichiometry of our samples by high temperature annealing as will be discussed in the next chapter.

The final tool at our disposal in the lab to investigate the chemical structure of our samples was Raman spectroscopy. The Cr_2Te_3 layers have a metallic character and therefore yield low intensity Raman spectra. Other phases of $Cr_{1+x}Te_2$ were reported to have characteristic Raman peaks, like $CrTe_2$

around 100 cm^{-1} [36]. We did not observe any peak associated with our metallic layers but we used Raman spectroscopy to control the integrity of the 2D materials after the growth of Cr_2Te_3 in our vdW heterostructures. Figure 3.11 shows characteristic peaks of WSe_2 and graphene before and after the growth of the ferromagnet. The FWHM and position of the peaks are well preserved, indicating that the deposition of Cr_2Te_3 did not alter the 2D materials. The reference signal of WSe_2/GaAs (green curve) was measured with a 532 nm laser instead of 633 nm as the other samples, explaining the intensity difference.

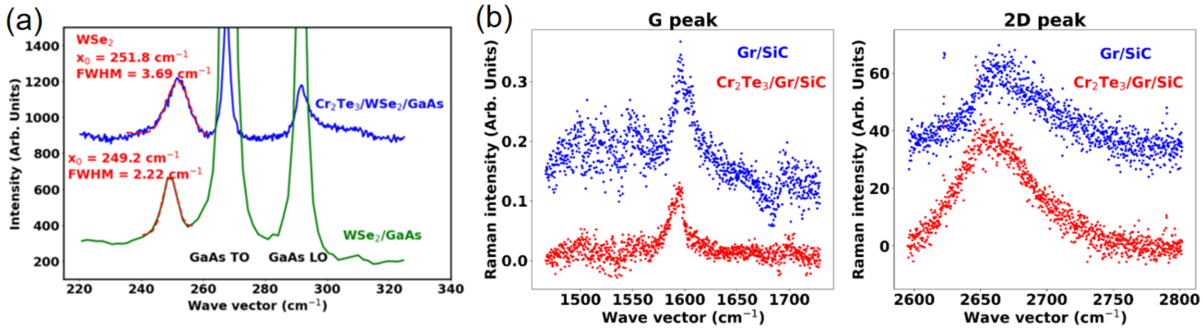

Figure 3.11: (a) Raman spectra of 1 ML WSe_2 on GaAs before and after deposition of 5 layers of Cr_2Te_3. The position and FWHM of the characteristic WSe_2 peak are indicated. (b) Raman spectra of the two main peaks of ML graphene before and after deposition of 5 layers of Cr_2Te_3.

We could also use Raman spectroscopy to study the possible air stability of the grown materials. We let one sample exposed to air without any capping layer and measured the signal shown in Fig. 3.12. Additional peaks compared to the substrate and capped layer are visible and characteristic of TeO_x chains. We concluded that these samples are unfortunately not stable in air and that they degrade very shortly after exposure to ambient conditions.

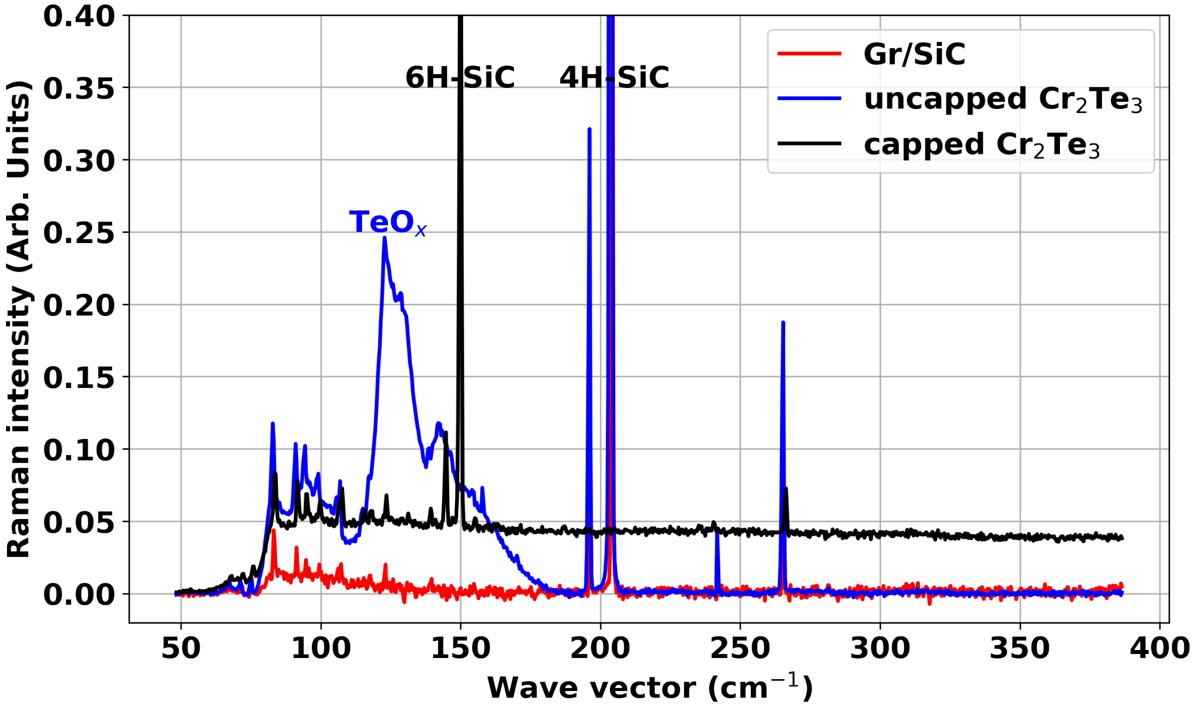

Figure 3.12: Raman spectra of the Gr/SiC substrate as well as 5 layers of Cr_2Te_3 with and without Al capping layer. Graphene was obtained from the graphitization of 4H-SiC or 6H-SiC explaining the different substrates peaks. TeO_x peaks are highlighted on the experimental curve.

3.1.2.3 Interface and surface morphology

Because of the air sensitivity, it was not possible to study the surface morphology of our layers by AFM on a systematic basis. Nevertheless, we performed the growth of a few samples without capping to investigate the early stages of growth. Measurements on a 2 ML-thick film of Cr_2Te_3/graphene/SiC are shown in Fig. 3.13 and give some insight on the epitaxy of this system. This sample was grown with a substrate temperature of 250°C. The long step in the middle of the left picture is from the SiC substrate. The distance between two steps is rather large (greater than 10 μm) and the graphene surface (still visible as small dark areas) is very smooth, confirming the high quality of the 2D material. Because of the high mobility on graphene, it is not fully covered even after the deposition of 2 full layers of Cr_2Te_3. Some small 3D structures are also visible on the surface as bright areas, that we assume are Te chains due to the low growth temperature (optimal was found at 300°C, as mentioned earlier). Except for these, the surface roughness is rather low (average of 216 pm), confirming the good surface quality revealed by RHEED.

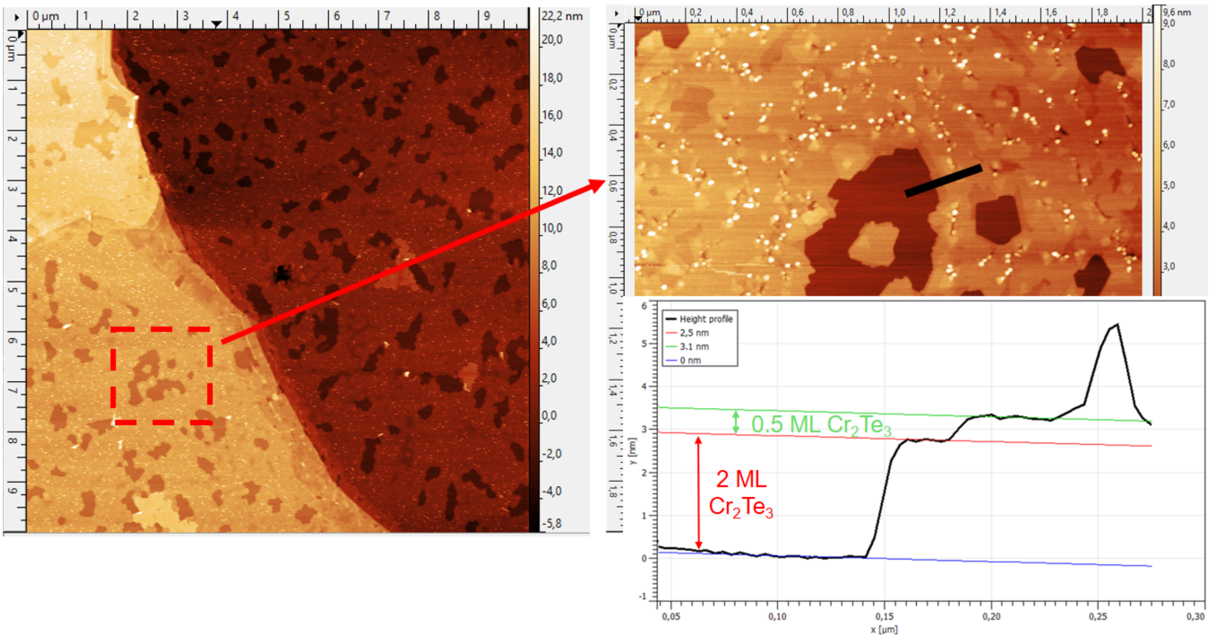

Figure 3.13: AFM images of 2 layers of Cr_2Te_3 deposited on graphene/SiC. On the left, 10×10 μm scan centred around a step of the SiC substrate. The color scale height is defined on the right. The right image is a 2×2 μm zoom of the area in the red dashed square. A line profile is taken along the black line and shown in the graph below, with indication of heights relative to the graphene surface.

A zoom is shown in the right image and a line profile is performed to measure the different steps heights. Using the gwyddion software [97], the heights of the steps are deduced from a fit and shown on the graph. The 2 layers step height of 2,4-2,5 nm is visible and the growth of another layer can also be observed. It is worth noting that at this early stage of a layer growth, a step of 6 Å is measured, that is equivalent to the height of one ML $CrTe_2$.

To assess the quality of interfaces, we performed STEM cross-section imaging as shown in Fig. 3.14.(a). A well ordered crystalline structure of the Cr_2Te_3 layers can be observed as well as a high quality interface, evidenced by the W-Te distance of 5.3 Å. We choose this specific distance to obtain a better experimental determination of the gap (due to the large atomic number of W with respect to Se). It is indeed difficult to determine the position of the Se atoms in the line profile of Fig. 3.14.(b). This corresponds to a vdW gap Δc_{vdW} of 3.5 Å if we assume a relaxed WSe_2 layer, which is in agreement with our XRD data. We also resolve in this line profile an intensity difference for every second Cr planes, that is explained by the intercalated planes where only one third of the lattice sites are occupied.

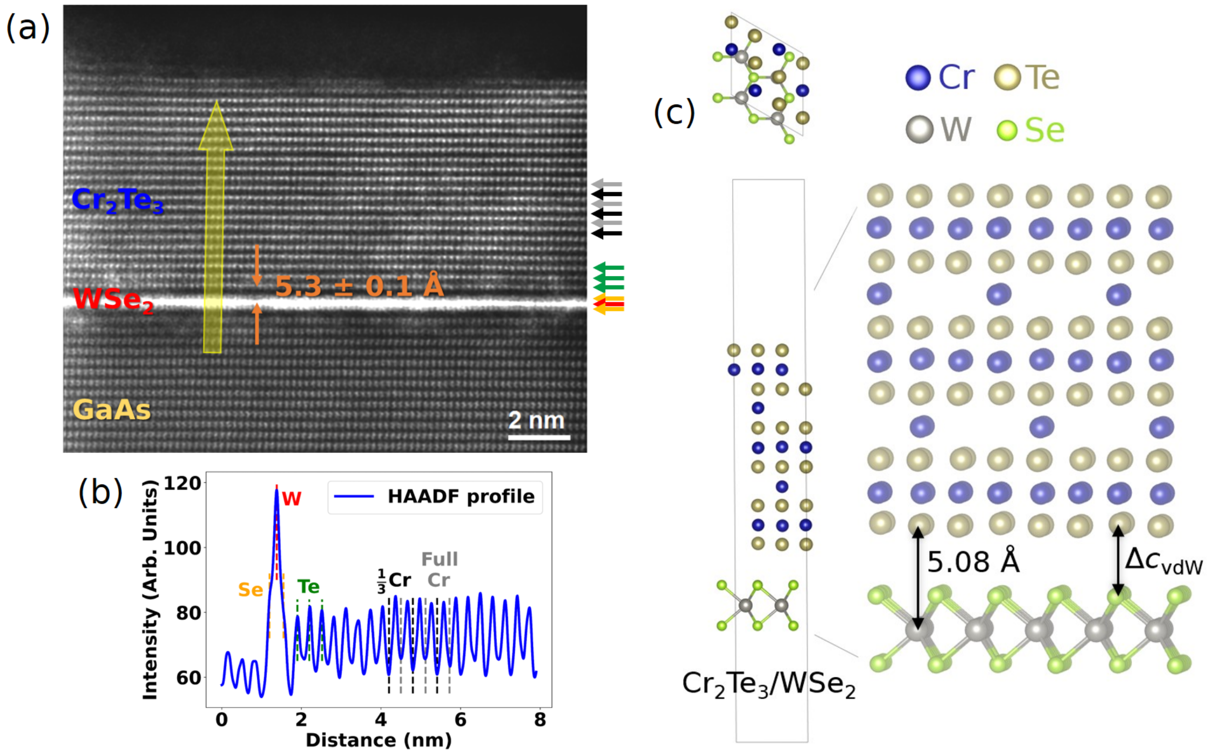

Figure 3.14: (a) Low-pass filtered HAADF-STEM image of 5 layers of Cr_2Te_3/WSe_2/GaAs. The vdW gap between the layers is shown to highlight the high quality of the interface. Arrows on the right side indicate the position of each atomic plane noted (by color) in the line profile. (b) Line profile along the c-direction of Cr_2Te_3 layers (thick yellow arrow) with an intensity difference between partially and fully occupied Cr planes [see crystal structure in (c)]. (c) A unit cell of the calculated Cr_2Te_3/WSe_2 heterostructure. In the interstitial planes, only 1/3 of the lattice sites are occupied by the intercalated Cr atoms. The ab initio-calculated W-Te distance is 5.08 Å.

To further investigate the interface between Cr_2Te_3 and WSe_2, *ab initio* calculations were performed by L. Vojacek, F. Ibrahim and M. Chshiev (also from Spintec, CEA Grenoble) using the density-functional theory (DFT) as implemented in the Vienna *ab initio* simulation package (`VASP`) [98, 99] with the generalized gradient approximation (GGA) pseudopotentials in the Perdew-Burke-Ernzerhof (PBE) parametrization [100]. To compute the relaxed heterostructures of Cr_2Te_3 with 2D materials, the relative orientation of the two materials in the calculation was not taken from an experiment, but chosen in a systematic way [101] to minimize the lattice mismatch. This captures more realistically the weak interactions in the heterostructure.

The obtained structure for a system of 1.5 unit cell thick Cr_2Te_3 on top of a single layer of WSe_2 is shown in Fig. 3.14.(c). The calculated W-Te distance of 5.08 Å is very close to the experimental value, confirming the good quality of the sample. Other calculations were carried out to compute the energy cost of the termination of Cr_2Te_3 layers, as shown in Fig. 3.15. The most stable structure was found for an interface with Te atoms followed by a full Cr plane, which is in good agreement with the HAADF line profile in Fig. 3.14.(b). This proves that this material makes vdW bonding with 2D materials and can be grown on substrates with large lattice mismatch.

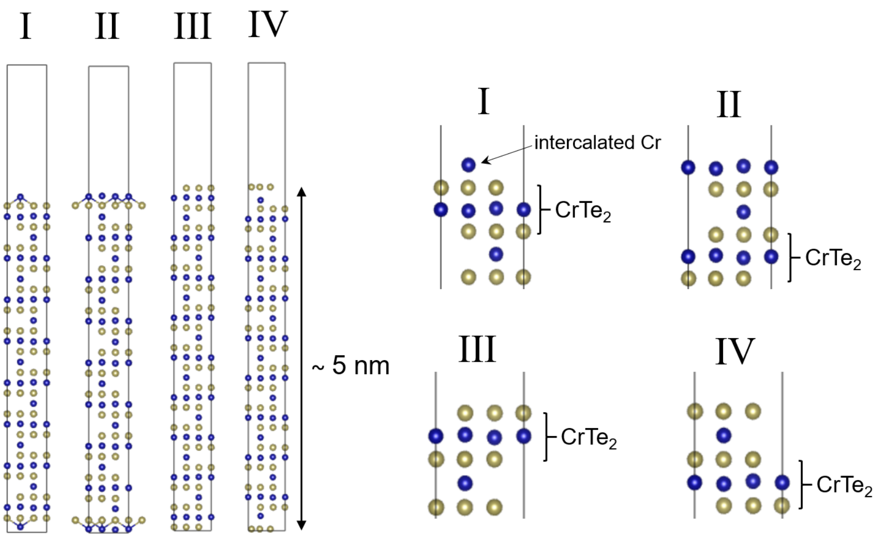

Figure 3.15: Cr_2Te_3 thin films in vacuum used for the calculation of the surface-termination stability. Structure III (terminated by a complete $CrTe_2$ layer) is the most stable, followed by the intercalated Cr-terminated structure I. This corresponds to Ref. [49].

3.1.3 Free standing character of Cr_2Te_3on 2D materials

After the growth of the vdW heterostructures, XRD was performed to measure and control the crystal structure of the obtained materials. Many information were obtained thanks to these scans but the most important ones are the lattice parameters of the grown Cr_2Te_3 layers. Figure 3.16.(a) shows an out-of-plane XRD measurement of 5 layers of Cr_2Te_3 deposited at 300°C and annealed at 400°C on one ML of WSe_2 on a GaAs substrate. Using the Bragg's law and taking the average value from all diffraction peaks of Cr_2Te_3 the out-of-plane lattice parameter c can be experimentally derived and compared to the bulk values of the material. Some other peaks are visible on the graph, attributed to the GaAs substrate. Because the WSe_2 is only 1 ML thick, incident x-rays cannot interfere with reflection on this material, explaining the absence of peaks of this compound.

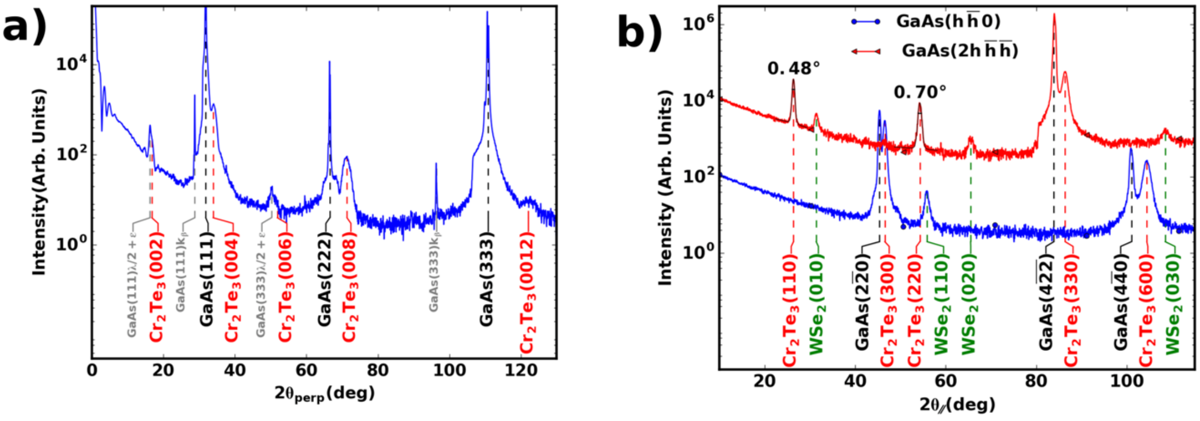

Figure 3.16: Post-growth characterization of the crystal structure of $Cr_2Te_3/WSe_2/GaAs$. (a) Out-of-plane $\Theta/2\Theta$ XRD scan shows, in addition to Cr_2Te_3 (00l) peaks (red), GaAs substrate peaks (black) with weak additional peaks due to spurious radiations not completely eliminated by the mirror and the K_β filter (grey). (b) In-plane radial XRD scans performed along the GaAs substrate R=$(h\bar{h}0)$ direction, and R+30°=$(2h\bar{h}\bar{h})$ direction. These scans show the substrate peaks (black), WSe_2 (green), and Cr_2Te_3 peaks (red) labeled with their FWHM.

The in-plane XRD diffraction of the same sample is displayed in Fig. 3.16.(b) along two directions rotated by 30° from each other. This time, the WSe_2 ML can be observed with a lattice parameter equal to the bulk one, up to the instrument resolution. The FWHM of the Cr_2Te_3 peaks are in the same order of magnitude as high-quality MBE grown Fe_5GeTe_2 [43], confirming the good crystallinity of the samples.

Another information that can be extracted from XRD scans is the thickness of a layer if the surface is flat, and the film thick enough. Figure 3.17 shows the specular (out-of-plane) scan of 20 nm Cr_2Te_3 grown on a graphene/SiC film. Interferences between the reflection on the two interfaces (on top and below) give rise to fringes around the main diffraction peaks, as can be seen in the insets. By fitting these fringes, one can deduce the layer thickness. This information is important to calibrate the growth of thin samples, because some evaporated materials do not exhibit sticking coefficient of 1, especially on graphene.

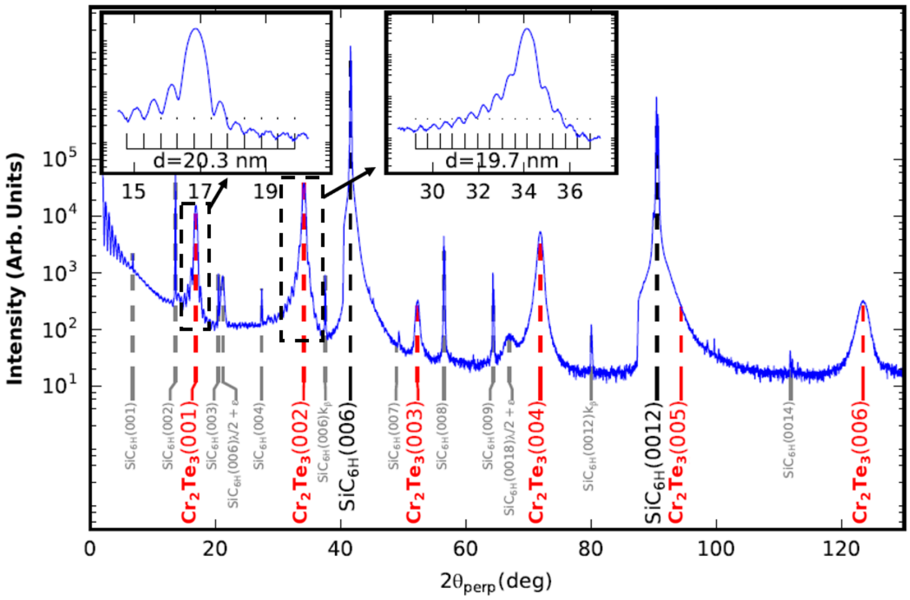

Figure 3.17: Out-of-plane Θ/2Θ XRD scan of 20 nm (17 layers) of Cr_2Te_3/graphene/SiC. Zooms around the main diffraction peaks of Cr_2Te_3 are shown in the insets to evidence the fringes. The fitted thickness of the layer is displayed for each peak.

To better understand the epitaxial relationship between the 2D materials and Cr_2Te_3, L. Vojacek, F. Ibrahim and M. Chshiev performed some *ab initio* calculations to compute the relaxation of Cr_2Te_3 layers on graphene as a function of its thickness (see Fig. 3.18.(a)). A linear trend is observed with a fully relaxed Cr_2Te_3 after only 7 layers. Moreover, one has to consider that in the calculations the two materials are bounded to occupy the same unit cell. This makes their lattice parameters coupled more strongly than in the real system.

Systematic XRD measurements were done to verify this hypothesis on six samples of 5 ML of Cr_2Te_3 grown at 300°C on three different substrates, as detailed in Table 3.1. Half of these samples were annealed in-situ after growth for 10 min at 400°C, as we have shown with RHEED that the crystal quality was improved. Compared to bulk values of Cr_2Te_3 with $a = 6.812$ Å and $c = 12.07$ Å [31], we systematically found an in-plane compressive strain and a resulting out-of-plane expansion (following the Poisson ratio). Despite large lattice mismatches with opposite signs (WSe_2:+19.1%/Gr:+56.3%/Bi_2Te_3:-10.8%), similar Cr_2Te_3 lattice parameters are measured after growth. We assumed that the slight difference between lattice parameters might be due to the surface topography (presence of steps, terraces, etc.) and the microscopic structure of Cr_2Te_3 (grain size, grain boundaries, etc.).

The experimental values are in good agreement with calculations on free standing 5 nm of Cr_2Te_3, as shown in Fig. 3.18.(b). To calculate this effect, slabs of 5 nm of Cr_2Te_3 interfaced with 2 nm of vacuum (see Fig. 3.18.(c)) were relaxed. The DFT+U approach using Dudarev's formulation [102] was applied

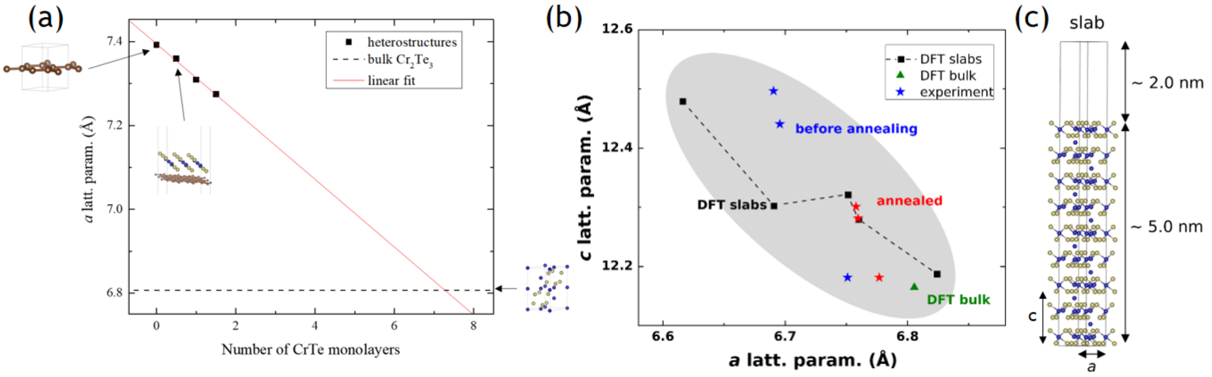

Figure 3.18: (a) Calculated in-plane lattice parameter of Cr_2Te_3/graphene heterostructures with increasing Cr_2Te_3 thickness. (b) The calculated and experimental lattice parameters for free-standing slabs and for bulk structures. The measured values follow well the trend calculated for free-standing Cr_2Te_3 films. (c) Sketch of a slab (5 nm of Cr_2Te_3 interfaced with 2 nm of vacuum) used for the calculations in (b).

2D layer	**Temperature**	***a* (Å)**	$\frac{a-a_{\text{bulk}}}{a_{\text{bulk}}}$	***c* (Å)**	$\frac{c-c_{\text{bulk}}}{c_{\text{bulk}}}$	$\frac{c}{a}$	$\Delta\theta_{//}$	$\Delta\phi$
WSe_2	300°C	6.731	-1.2%	12.44	+3.1%	1.848	1.00°	2.36°
WSe_2	400°C	6.760	-0.76%	12.28	+1.7%	1.817	0.62°	1.54°
graphene	300°C	6.754	-0.88%	12.18	+0.91%	1.804	0.72°	24.8°
graphene	400°C	6.758	-0.79%	12.30	+1.9%	1.820	0.60°	16.6°
Bi_2Te_3	300°C	6.691	-1.8%	12.50	+3.6%	1.868	0.87°	2.77°
Bi_2Te_3	400°C	6.778	-0.50%	12.18	+0.91%	1.797	0.56°	1.28°

Table 3.1: Annealing temperature (all samples were grown at 300°C) and structural parameters measured by x-ray diffraction, with a (c) the in-plane (out-of-plane) lattice parameter, the radial width ($\Delta\theta_{//}$) of the (300) diffraction peak and the mosaic spread ($\Delta\phi$) measured on the same Bragg peak.

with an effective Hubbard correction $U_{\text{eff}} = 2.1$ eV to localize the Cr d-orbitals. A Cr pseudopotential with semicore p electrons was chosen and an energy cutoff of 330 eV was used for the plane-wave basis. The van der Waals interaction was approximated by the DFT-D3 method [103] with the Becke-Johnson damping [104]. The in-plane lattice parameter a was fixed for each slab and the out-of-plane c was relaxed to minimize the system energy.

Samples annealed at 400°C grown on graphene/SiC and WSe_2/GaAs perfectly fall on the calculated curve, justifying the assumption that with enough thermal energy given to the system, Cr_2Te_3 layers can relax to their free standing structure, even for 5 layers thick films. The sample grown on Bi_2Te_3/Al_2O_3 and annealed at 400°C was shaded in Table 3.1 and does not fall on this curve because of the degradation of the Bi_2Te_3 layer at this temperature, as will be shown in the next paragraph.

3.1.4 Thermal annealing of Cr_2Te_3/Bi_2Te_3 heterostructures

Figure 3.19.(a) shows the Raman spectra of Cr_2Te_3/Bi_2Te_3/Al_2O_3 at different stages of growth. Two characteristic peaks of Bi_2Te_3 were observed at 101.8 cm^{-1} and 133.5 cm^{-1}, which correspond to the E_g^2 and A_{1g}^2 vibrational modes. They have also been reported in [105]. After the deposition of 5 layers of Cr_2Te_3 at 300°C, those peaks remained unchanged (the amplitude drop is explained by the partial absorption of the laser fluence in the metallic Cr_2Te_3 layer). However, when the sample was annealed at 400°C, the two characteristic peaks of Bi_2Te_3 disappeared. Indeed, x-ray diffraction measurements performed before and after annealing in Fig. 3.19.(b) clearly show the disappearance of Bi_2Te_3 after thermal annealing. Finally, in Fig. 3.19.(c), RBS measurements on the annealed sample show the absence of any Bi in the heterostructure. We thus assume that Bi_2Te_3 was evaporated during annealing leaving the Cr_2Te_3 film on the pristine sapphire substrate.

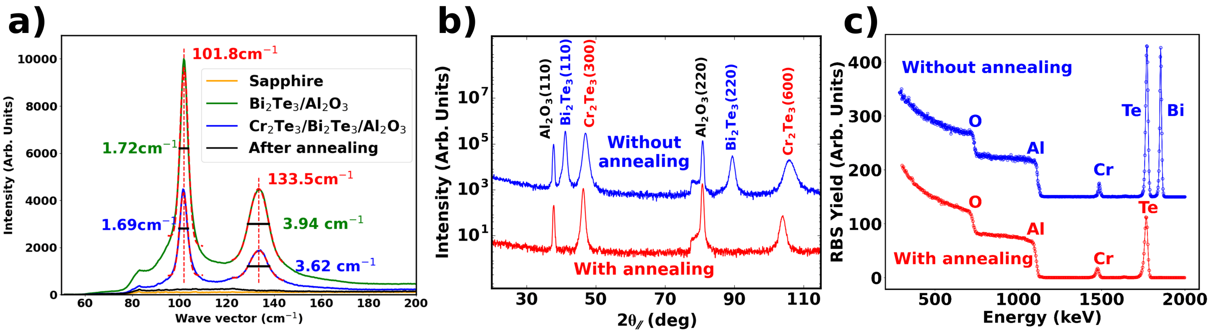

Figure 3.19: Structural properties of Cr_2Te_3 on Bi_2Te_3/Al_2O_3. (a) Raman spectra of the sapphire substrate, Bi_2Te_3/sapphire, and Cr_2Te_3/Bi_2Te_3/sapphire with and without annealing. Positions and full widths at half maximum of Bi_2Te_3 peaks are indicated. (b) Radial x-ray diffraction spectra for $Cr_2Te_3/Bi_2Te_3/Al_2O_3$ without (top in blue) and after (bottom in red) annealing. (c) RBS of Cr_2Te_3 grown on Bi_2Te_3/ Al_2O_3 without (top in blue) and with (bottom in red) annealing. No elemental Bi can be found after annealing.

In this case, the substrate is no more vdW and defects might have been created in Cr_2Te_3 by evaporation of the Bi_2Te_3 layer underneath. This probably explains why this sample did not exhibit similar relaxations as the ones of films grown on graphene and WSe_2 in Fig. 3.18.(b).

3.2 Magnetic properties of 2D/Cr_2Te_3 heterostructures

3.2.1 Magnetic anisotropy energy dependence on the crystal structure

After the structural and chemical characterizations of the MBE grown vdW heterostructures, we correlate them to their magnetic properties. Measurements were carried out by MOKE, SQUID and XMCD techniques as presented in the experimental techniques chapter. Long range ferromagnetic order was systematically observed with PMA and T_C ranging from 110 to 180 K.

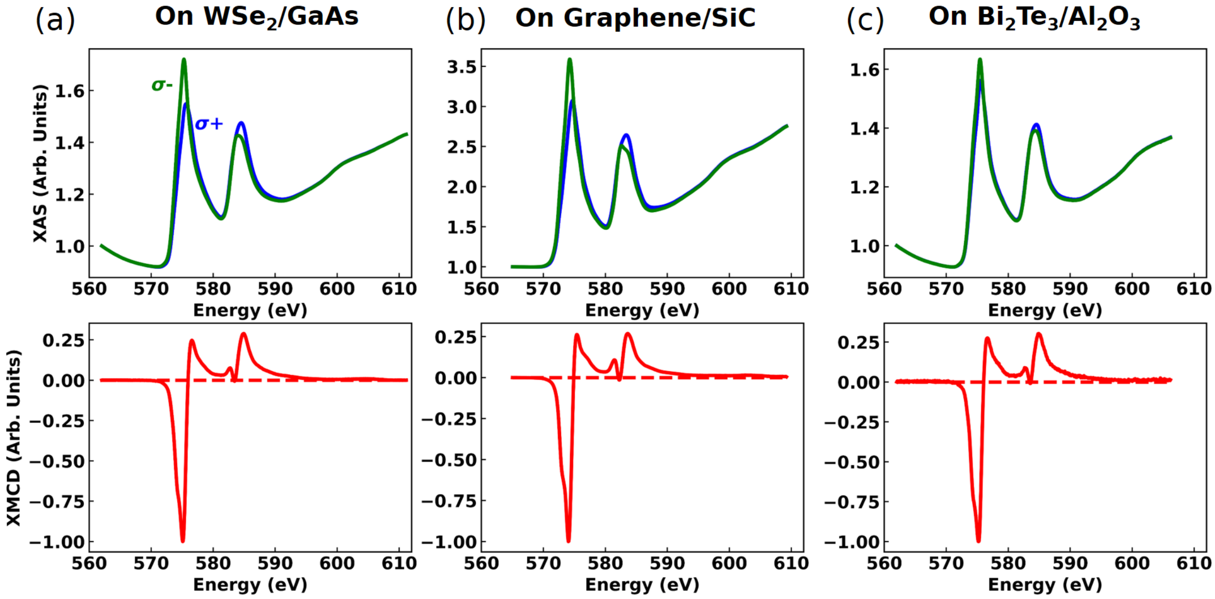

Figure 3.20: Top: x-ray absorption spectroscopy (XAS) and bottom: x-ray magnetic circular dichroism (XMCD) measurements performed on 5 layers thick Cr_2Te_3 grown and annealed at 400°C on (a) WSe_2, (b) graphene and (c) Bi_2Te_3. The signals were obtained at a sample temperature of 5 K.

The origin of ferromagnetism in the heterostructures was confirmed by XMCD performed at the SOLEIL synchrotron radiation source and is shown in Fig. 3.20. Local beamline scientists F. Choueikani and P. Ohresser participated actively to the measurements and their analysis. The x-ray beam was illuminating perpendicularly the samples that were cooled down to 5 K. A clear magnetic dichroism signal with a similar spectral shape was obtained at the Cr L_2 and L_3 edges for the three different substrates. This proves that the chemical environment of Cr atoms in Cr_2Te_3 films is essentially independent of the substrate. The lower magnetic moment for the sample on Bi_2Te_3/Al_2O_3 (Fig. 3.20.(c)) is explained by a lower sample thickness (three monolayers instead of five).

In order to quantitatively compare the six samples introduced in Table 3.1, SQUID magnetometry was carried out by applying external magnetic field both in-plane and perpendicularly to the heterostructures. The obtained data are plotted in Fig. 3.21. The coercive field is systematically reduced for the samples annealed at 400°C, consistent with an improved crystallinity. The measured saturation magnetization M_s of the layers is between 300 and 400 kA/m *i.e.* 2.0 and 2.6 μ_B/Cr atom. It is significantly lower than the expected one from theory of more than 3.0 μ_B/Cr [46]. The explanation lies in the canted spin textures of Cr_2Te_3, as explained in the introduction chapter. Cr_I atoms, in the intercalated planes, have their spins tilted with respect to the ones in the fully occupied planes leading to a lower total magnetization. This also might explain the observed differences between the samples. If some disorder is present in the intercalated planes, it could lead to a different tilt angle and therefore different magnetization.

The magnetic anisotropy energy (MAE) was also determined for each sample by integrating the difference of area between the out-of-plane and the in-plane magnetization curves. We could correlate the observed variation with the slight strain measured by XRD as can be seen in Fig. 3.22. A linear trend can

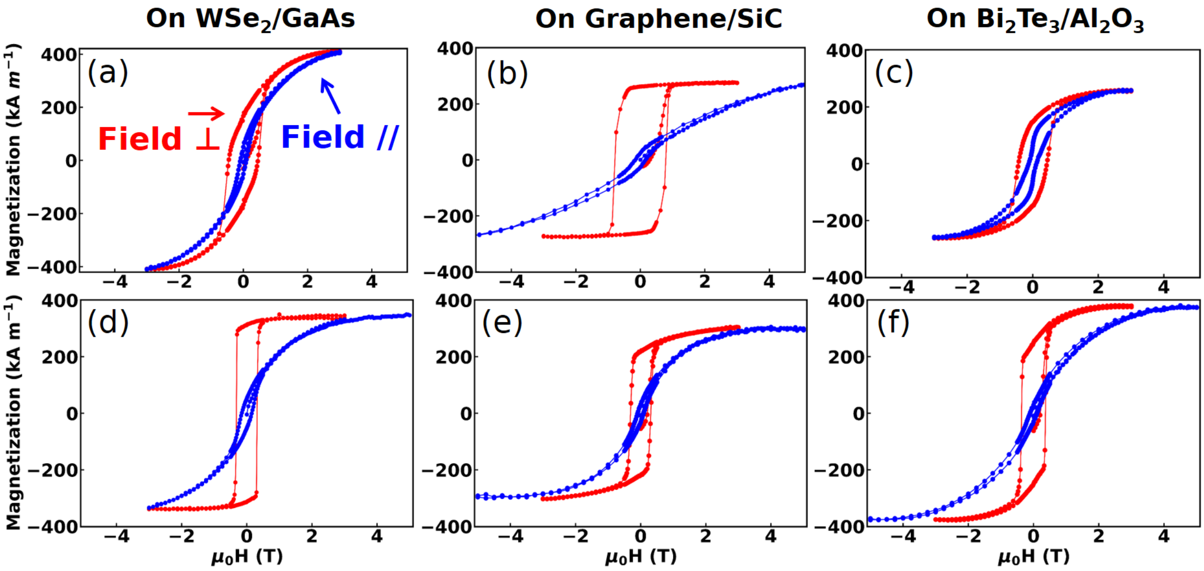

Figure 3.21: SQUID hysteresis loops with out-of-plane (⊥) and in-plane (//) applied magnetic field measured at 5 K are plotted after the removal of the substrate diamagnetic contribution. (a) (b) (c) Measurements on samples grown at 300°C on WSe_2/GaAs, graphene/SiC, and Bi_2Te_3/Al_2O_3. (d) (e) (f) Same measurements on samples annealed at 400°C after growth.

be observed between the PMA and the ratio of the out-of-plane to in-plane lattice parameters. This result was reproduced with the DFT calculations of the MAE as a function of the crystal structure. The slight variation between theory and experience could be explained by the fact that surface anisotropy was not taken into account in the calculations.

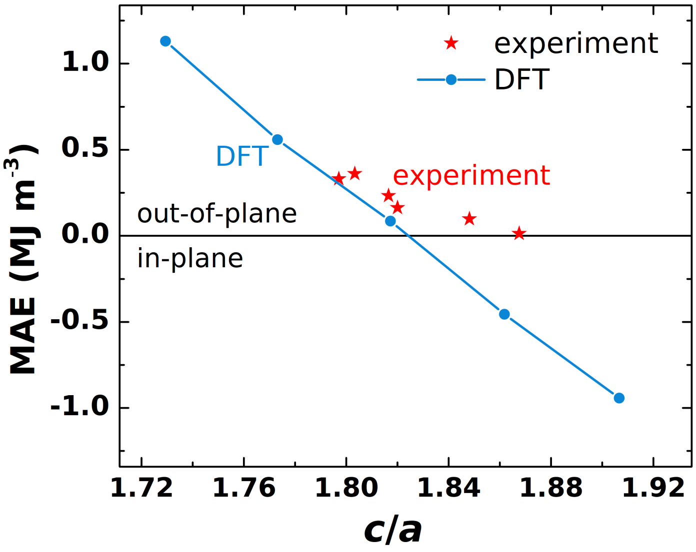

Figure 3.22: Magnetic anisotropy energy of bulk Cr_2Te_3 as a function of strain from theory and experiments. It is the sum of the DFT-calculated magnetocrystalline energy and a demagnetizing energy contribution of -0.06 MJ/m^3 corresponding to the experimentally measured magnetization of $\approx$ 300 kA/m.

The magnetic anisotropy energy is calculated as the difference between the ground state free energies when the magnetization points in-plane and out-of-plane [106]. A 9x9x5 k-point mesh was found to be sufficient. The volume was fixed at its calculated equilibrium bulk value, while the in-plane and out-of-plane lattice parameters (a and c) were varied. A demagnetizing energy contribution $E_{\mathrm{demag}} = -\mu_0 M_s^2/2$ was added to the calculated magnetocrystalline energy, using the experimental M_s value ≈ 300 kA/m.

The substrate was not found to have a direct impact on the magnetic properties but the lattice strain during growth was shown to proportionally affect the MAE of the heterostructures. If the strain is controlled during the growth, notably by adapting the annealing temperature, one can control the magnetic anisotropy of the layers. This is an advantage for the potential integration of this material in spintronic applications.

3.2.2 T_C dependence on structural properties

3.2.2.1 Growth temperature dependence

All the MBE grown layers exhibited the Cr_2Te_3 phase that, in the bulk form, has a T_C of 180 K [46]. We measured the temperature dependent magnetic properties of our high quality heterostructures (grown at 300°C and annealed at 400°C) and obtained similar values for 5 layers thick films. To record the remanent magnetization, we first used a saturation field of 5 T perpendicular to the samples and measured then the magnetization with 5 K steps and no external field as a function of temperature (Fig. 3.23). These results are very close to the values obtained in other similar studies on thin films [90, 107]. It has to be noted that a lower remanent magnetization is observed for the sample grown on graphene. Indeed, the Cr_2Te_3 layers on graphene have a larger in-plane mosaicity and therefore we expect the grain boundaries to host more defects like point dislocations. These can act as nucleation centers (where the magnetic anisotropy is lowered) for magnetic domains and lead to a decrease of the magnetization at the remanence.

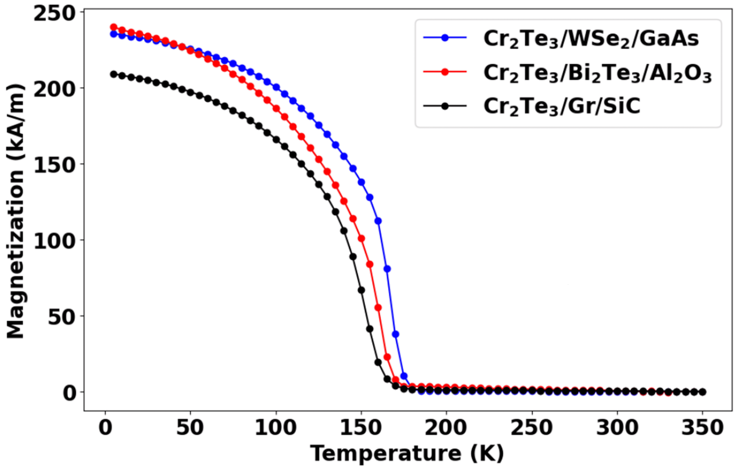

Figure 3.23: Remanent magnetization of 5 layers thick Cr_2Te_3 samples deposited on WSe_2/GaAs, Bi_2Te_3/Al_2O_3 and graphene/SiC. Samples were first cooled down to 5 K, magnetically saturated with a perpendicular field of 3 T and then heated to above RT. A T_C close to 180 K is found for the three heterostructures.

We have shown in Fig. 3.4 that layers of Cr_2Te_3 could be obtained with higher density of residual defects for different growth temperatures. It is interesting to see if these samples, despite having the same chemical composition, would behave magnetically differently and if the T_C could be raised with strain, as reported in Ref [96]. Figure. 3.24 displays remanent curves of samples with similar thickness but different growth temperature. XRD and RHEED confirmed that the samples grown at low temperature exhibit more structural defects as well as larger strain with respect to bulk Cr_2Te_3 structure. The experimental trend is that these defects act as a perturbation on the magnetic order of Cr_2Te_3, leading to a decrease of the T_C with disorder. We could not reproduce any increase of T_C with strain.

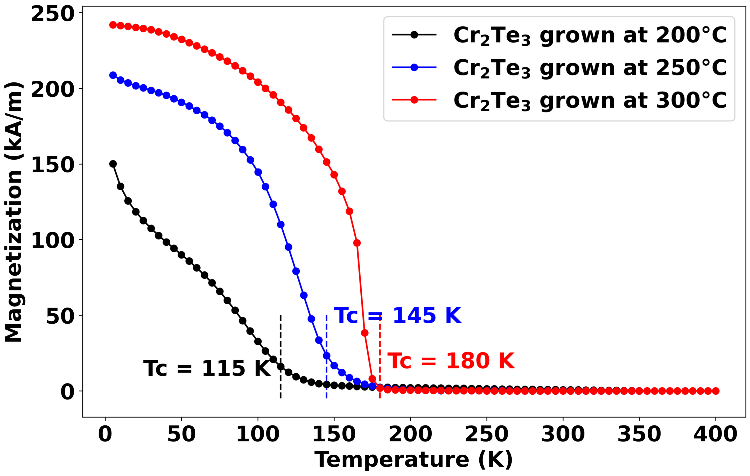

Figure 3.24: Remanent magnetization (after out-of-plane saturation) of 5 layers thick Cr_2Te_3 samples grown at different substrate temperatures. The measured T_C is indicated for each curve. The value is chosen at the inflection point of the remanent curve.

3.2.2.2 Thickness dependence

Another study by Wen *et al.* [49] reported an increase of T_C in the thin limit up to RT. We grew a set of samples using optimal growth and annealing conditions with thicknesses ranging from 1 to 20 ML. For the thinnest samples (1 and 2 ML), we used XMCD to measure the magnetic properties due to the sensitivity limit of the SQUID. Magnetic hysteresis loops recorded at 5 K are shown in Fig. 3.25. The samples do not exhibit ferromagnetic order, but have a paramagnetic behavior with no opening in the hysteresis loop.

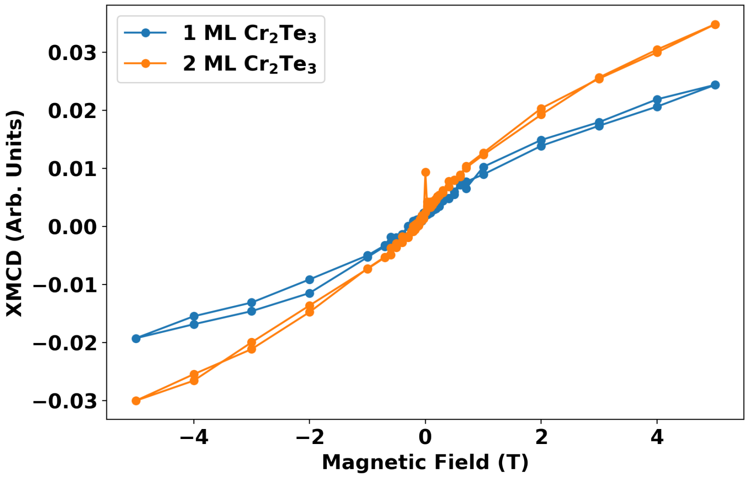

Figure 3.25: Hysteresis loop of thin Cr_2Te_3 samples deposited on graphene/SiC. The magnetic field is applied perpendicularly to the samples. The XMCD signal was obtained by subtracting the XAS at the energy of the maximum of the dichroism at the L_3 edge with the signal at the Cr pre-edge (565 eV) for both light helicities (see Appendix A).

We concluded that long range order only appears, for MBE samples thicker than 3 layers. One explanation could be the reduction of the nearest Cr neighbors in the 2D limit but also some defects at the interface that alter the quality of very thin films. A Te/Se capping layer was used to prevent the degradation of the surface due to the otherwise used Al cap layer. This chalcogenide capping was thermally removed inside the DEIMOS beamline chamber. We used Te cap at the interface to prevent the substitution of Te by Se in Cr_2Te_3 during the annealing step for the evaporation of the protective layer. We added Se on top because amorphous Se is more stable in air than Te that is always leaving residues on the final surface.

We used SQUID magnetometry to record the remanent curves of the other samples that are displayed in Fig. 3.26. No variation of the T_C is observed between 20 and 5 ML, which is expected as this is already the bulk value. However, the thinnest sample exhibits a slightly lower value of 160 K. This is in agreement with a weaker ferromagnetic order when thinning down the sample, confirmed by the absence of it in the thinnest ones.

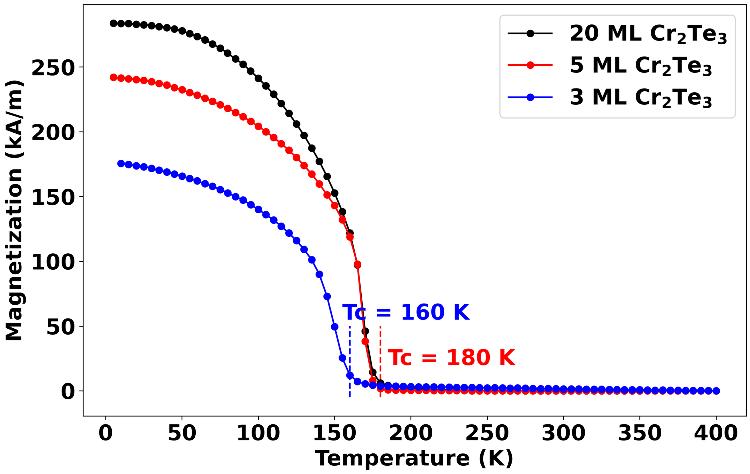

Figure 3.26: Remanent magnetization (after out-of-plane saturation) of Cr_2Te_3 samples grown on graphene/SiC with different thicknesses. The measured T_C is indicated for each curve. The value is chosen at the inflexion point of the remanent curve.

In conclusion, we could not reproduce the results of Wen *et al.* [49]. However, our results are more consistent with the physical picture that a reduction of thickness leads to more disorder and an average reduction of the atomic coordination leading to weaker ferromagnetic order. This is also the case for most other materials, even the ones with ferromagnetism in the monolayer limit such as CrI_3 and $CrGeTe_3$.

CHAPTER

4

Annealing of thin Cr_2Te_3 films to change the stoichiometry

During the exploration of the growth conditions of Cr_2Te_3, one sample stood out from the rest in terms of temperature dependent properties. The sample was grown at 500°C on graphene/SiC and a T_C above 200 K was measured, which is significantly higher than the one of bulk Cr_2Te_3 of 180 K. Unfortunately, growth at high temperature on graphene leads to poor substrate coverage and rough surface as demonstrated in the previous chapter. After analysis of the literature, we came upon the study by Fujisawa et al. [50], where 80 nm thick Cr_2Te_3 films were grown by MBE on sapphire at 300°C and then annealed with varying temperature from 450°C to 700°C. As presented in the introduction, they reported a gradual increase of the T_C from 180 K to 350 K as well as the change of the magnetic anisotropy from out-of-plane easy axis to in-plane (see Fig. 4.1).

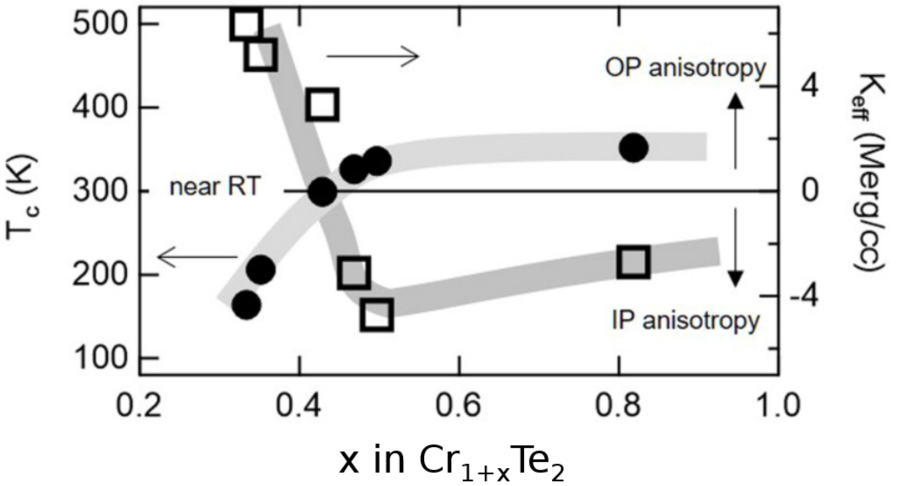

Figure 4.1: Evolution of the magnetic properties of Cr_2Te_3 after post-growth annealing to varying temperatures, extracted from [50]. The properties are indicated as function of the measured stoichiometry with black dots indicating the T_C (left axis) and empty squares the uniaxial effective anisotropy constant (right axis).

Their interpretation to these varying magnetic properties was an evolution of the films composition due to the evaporation of Te. They indeed observed an evolution of the stoichiometry using energy dispersive x-ray spectroscopy (EDX) from x = 0.33 to x = 0.82 in $Cr_{1+x}Te_2$ films.

We decided to reproduce their study but using instead thin films of 5 ML Cr_2Te_3 grown on a 2D material, namely graphene on SiC. We kept the low temperature (300°C) deposition and performed, on different samples, annealing for 10 min of the layers with steps of 50°C starting from 450°C (we already showed in the previous chapter that the properties for samples annealed at 400°C were close to free standing Cr_2Te_3). We kept increasing the annealing temperature until the layers degradation at 700°C, as will be presented in this chapter.

We also observed an increase of the Cr content in our layers associated with a change of T_C and magnetic anisotropy but obtained different behaviour than for thicker films deposited on sapphire.

4.1 Structural properties of annealed Cr_2Te_3 samples

4.1.1 Crystal structure analysis

Following the recipe developed in the previous chapter, the growth of Cr_2Te_3 was performed on graphene/SiC. We carried out structural characterization on the samples after the annealing step to investigate any possible changes in the structure of the grown layers. First of all, in-situ RHEED images are compared (see Fig. 4.2.(a-d)). These pictures were taken along graphene [100] azimuthal direction (equivalent to $\Phi = 0°$ in Fig. 4.2.(e)). The first sample (Fig. 4.2.(a)) corrsponds to Cr_2Te_3, as shown in the previous chapter. For samples annealed at 500°C and 600°C, the diffraction rods are thinner but very similar to each other. Finally, graphene rods are visible on the sample annealed at 700°C, as evidenced by the blue arrows. This indicates that the layers start to reevaporate or dewet the surface and explains why

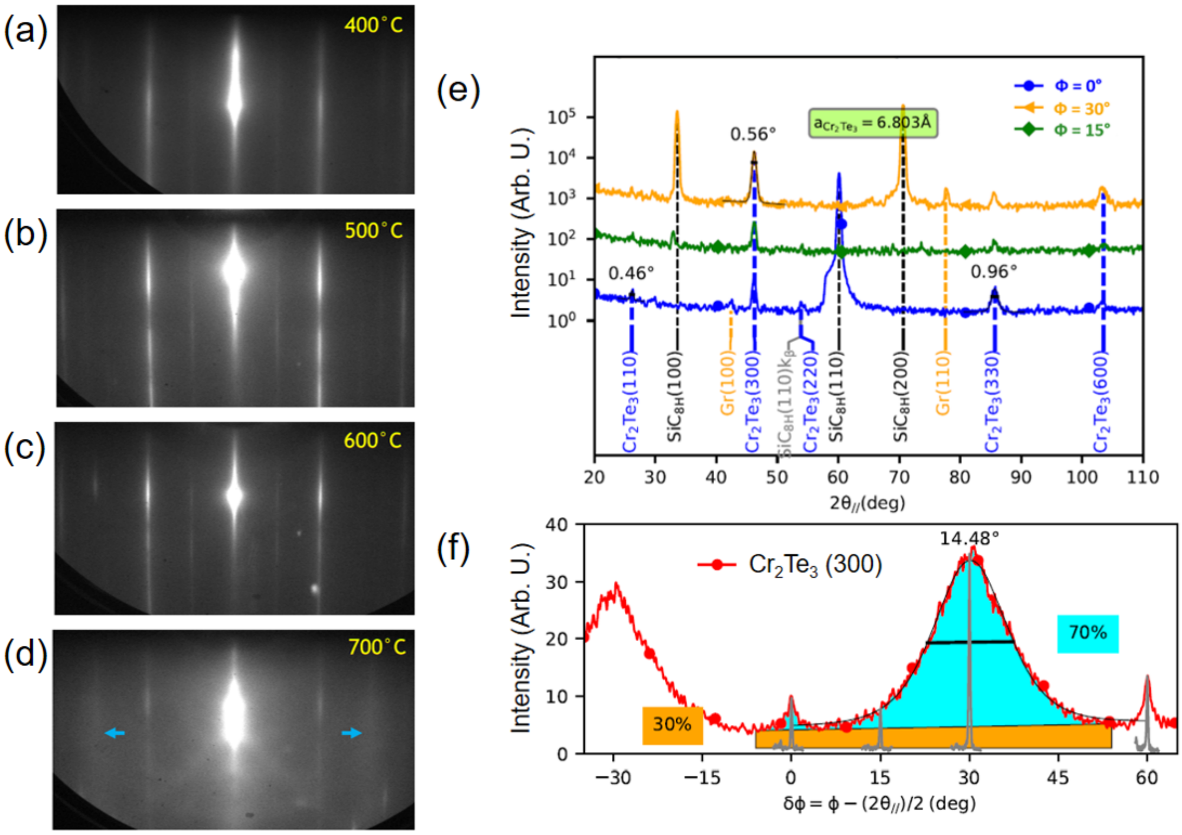

Figure 4.2: (a-d) RHEED images after annealing of 5 ML Cr_2Te_3 deposited on graphene/SiC at the temperature indicated in the top right corner. Blue arrows indicate the position of graphene (100) diffraction rod. (e) Radial XRD experiment of 5 layers Cr_2Te_3 annealed at 450°C. The scans are performed with three values of Φ, i.e. the angle between the diffusion vector (K_out - K_in) and the sample. The value is set to 0° when the scan direction is aligned with graphene [100] crystal axis. The FWHM of the main Cr_2Te_3 peaks are indicated. (f) Azimuthal scan of the same sample performed on the Cr_2Te_3 (300) Bragg position. The isotropic and anisotropic areas are shown on the experimental curve.

this temperature was chosen as the maximum of this study.

Some faint rods (Fig. 4.2.(a-d)) reveal on all the samples that the crystal orientation of the $Cr_{1+x}Te_2$ layers is not completely matching the one of graphene. Some XRD experiments were performed to analyse quantitatively the evolution of the crystal structure with the annealing. Figure 4.2.(e) shows radial XRD scans of the sample annealed at 450°C and the deduced in-plane lattice parameter. Three directions of radial scans were performed: 0 and 30° that correspond to the main crystal axis of the substrate as well as 15° for reference. Graphene and SiC peaks are only visible in the first two cases, but Cr_2Te_3 peaks also exhibit small intensity (the scan intensity is shown on a logarithmic scale) for every directions. To quantify the mosaic spread, the FWHM of Cr_2Te_3 (300) peak is displayed in Fig. 4.2.(f). As shown in the graph, this spread only characterizes the crystallites with anisotropic orientation with respect to the substrate. Close to one third of the crystal grains have random orientation.

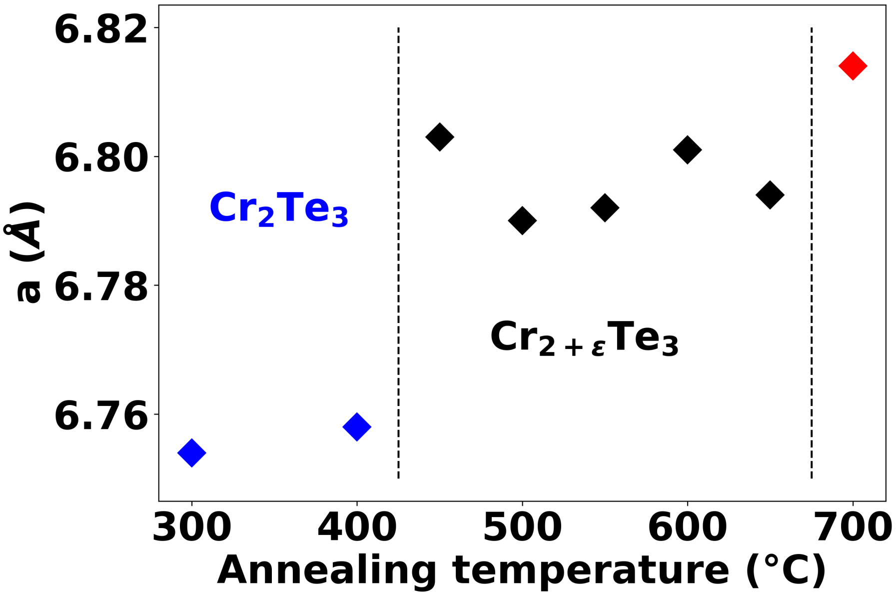

Figure 4.3: Evolution of the in-plane lattice parameter of 5 ML Cr_2Te_3 deposited on graphene/SiC after different annealing temperatures. Samples with the Cr_2Te_3 phase are indicated in blue, and the ones with higher Cr content in black. The sample annealed at 700°C is displayed in red due to the degradation at high temperature.

Similar measurements were performed on all the samples. The evolution of the in-plane lattice parameter is pictured in Fig. 4.3 as a function of the annealing temperature (T_A). For value lower than 400°C, the ferromagnet phase was found to be Cr_2Te_3 (see chapter 3). For $T_A > 400$°C, comparatively richer Cr content were found as will be demonstrated with RBS measurements and parametrized with a positive ε in $Cr_{2+\varepsilon}Te_3$. A clear increase of the lattice parameter close to 0.6 % is observed with the phase change at $T_A = 450$°C. Then, very little variation is measured while T_A is varied between 450 and 650°C. For the sample annealed at 700°C, the signal intensity is very weak, due to the probable reevaporation of the layer. An increased lattice parameter is also found and indicated with a red symbol.

The measure of the evolution of the out-of-plane lattice parameter was also carried out and the results are shown in Fig. 4.4. It was described in the previous chapter that the Cr_2Te_3 layers relaxed after the annealing at 400°C, explaining the increase of c from $T_A = 300$°C to 400°C. Identical values are found for all the other samples with the exception of the one at 700°C, not shown due to a value of c = 13.6 Å. This indicates a sharp discontinuity and most probably a different phase for the last sample (mostly metallic Cr, as will be shown with RBS). However, the gradual annealing steps did not lead to a gradual evolution of the lattice parameters, neither in-plane nor out-of-plane. Very similar lattice parameters are indeed found after the phase change at 450°C.

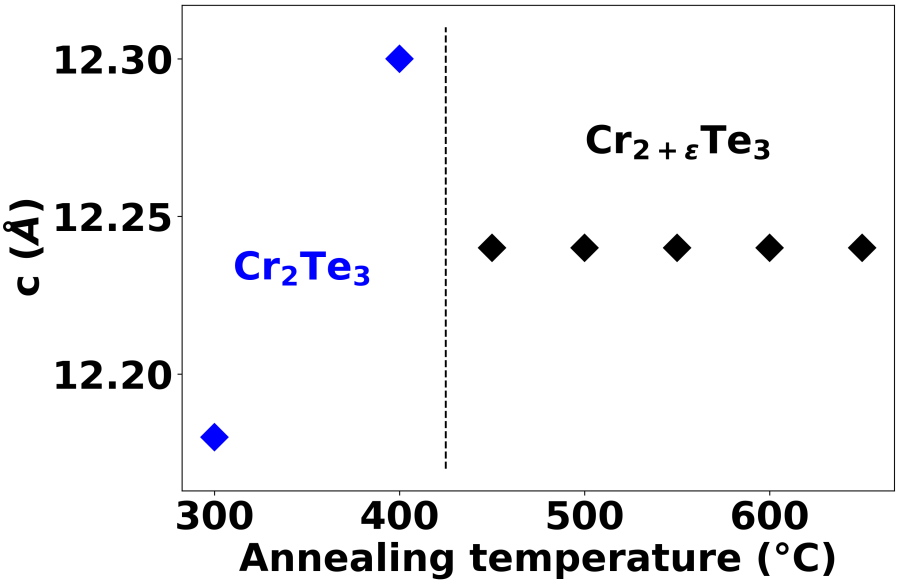

Figure 4.4: Evolution of the out-of-plane lattice parameter of 5 ML Cr_2Te_3 deposited on graphene/SiC after different annealing temperatures. Samples with the Cr_2Te_3 phase are indicated in blue, and the ones with higher Cr content in black.

The evolution of the quality of the layers was also assessed with the help of the FWHM of the Cr_2Te_3 (300) XRD peak in the radial scan (noted $\Delta_{//}$ in Fig. 4.5). A monotonic decrease of the peak's width is first observed for $T_A \leq 550$°C, followed by a steady increase for higher temperature. It appears that the annealing improves at first the layers quality with larger crystal grains due to the energy given to the system. This observation supports the thinning of rods in RHEED patterns. For high values of the annealing temperature, the evaporation of Te from the layers could lead to crystal defects explaining the experimental trend.

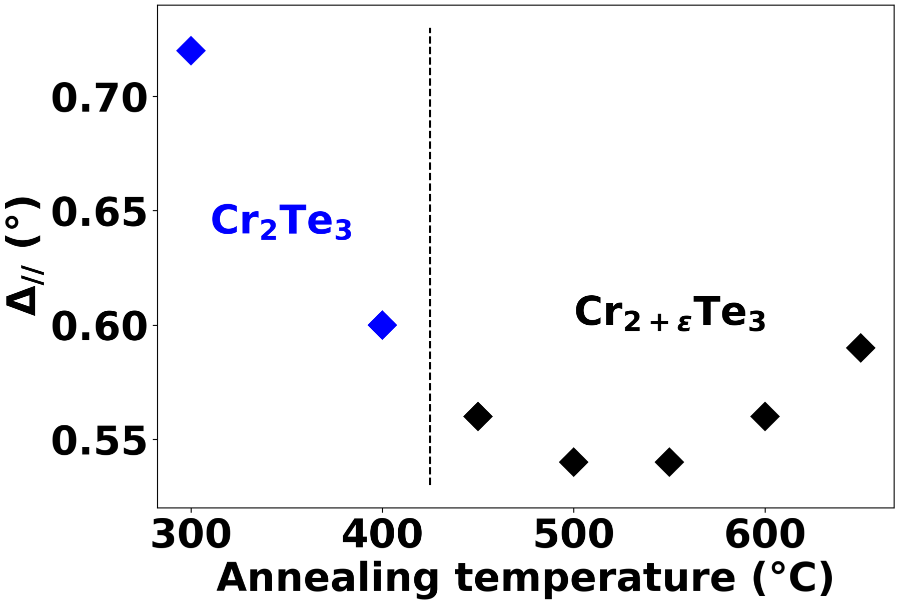

Figure 4.5: Evolution of the FWHM of the Cr_2Te_3 (300) XRD peak in the radial scan (noted $\Delta_{//}$) after different annealing temperatures. Samples with the Cr_2Te_3 phase are indicated in blue, and the ones with higher Cr content in black.

The evolution of the orientation of the crystal grains is also shown in Fig. 4.6, with an almost continuous decrease of the mosaic spread with T_A. The anisotropic proportion (see Fig. 4.2.(f)) is also increasing with T_A, demonstrating an improvement of the crystal orientation with the annealing temperature. The evolution is however small above 500°C.

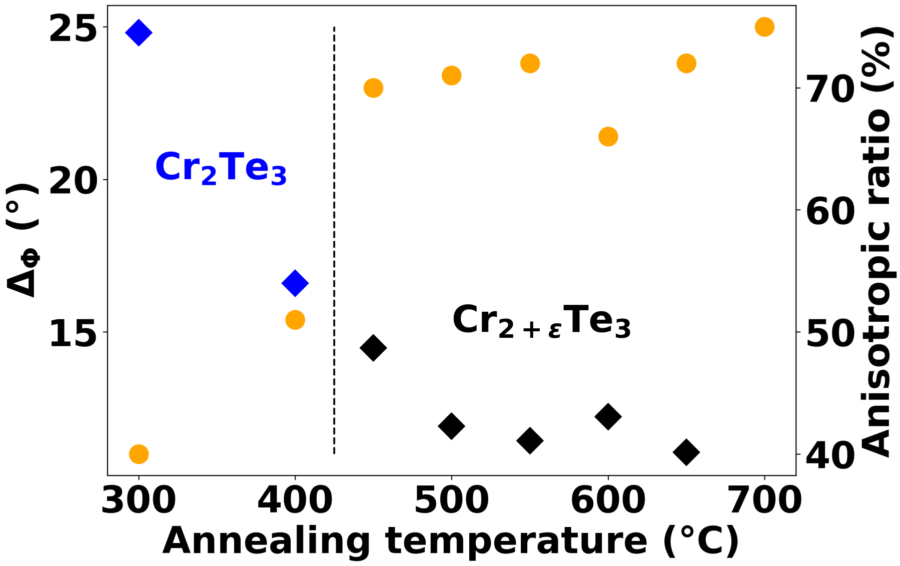

Figure 4.6: Indicated on the left axis, evolution of the FWHM of the Cr_2Te_3 (300) XRD peak (squares) in the azimuthal scan (noted Δ_Φ) after different annealing temperatures. Samples with the Cr_2Te_3 phase are indicated in blue, and the ones with higher Cr content in black. The anisotropic ratio, as defined in Fig. 4.2.(f), is displayed with orange circles and the values are shown on the right axis.

To conclude, the crystal structure of the layers was affected by the annealing temperature with a decrease of the mosaic spread and an evolution of the radial width of the main $Cr_{1+x}Te_2$ XRD peak. The lattice parameters varied however very little within the experimental resolution.

4.1.2 Stoichiometry evolution after annealing

In order to quantify the possible evolution of the stoichiometry of the layers as a function of T_A, we performed RBS measurements on all the grown samples. Figure 4.7 presents one example graph for T_A = 500°C. The substrate elements (Si and C) are easily distinguishable as well as two other peaks at energies corresponding to Cr and Te atoms. By carefully fitting the area of each peak, one can deduce the stoichiometry of this sample: $Cr_{1.375}Te_2$. This means that $x > 0.33$, *i.e.* a higher Cr content than for Cr_2Te_3. The increase of Cr content with respect to Cr_2Te_3 is close to 3%, and the deduced Cr:Te ratio is 40.7 %. The uncertainty of the measurement is close to 1% on this ratio, which means that the Cr increase is at the detection limit.

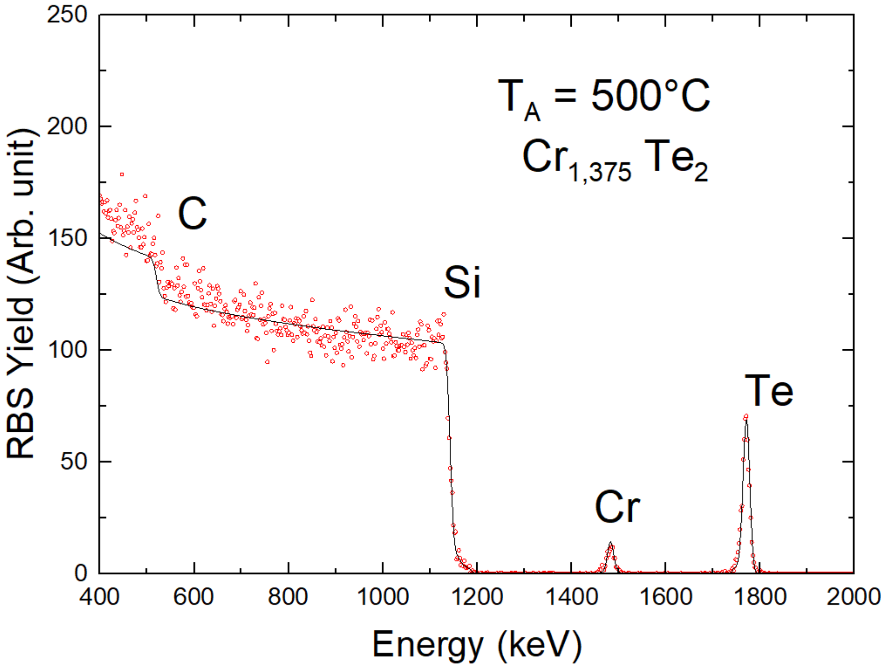

Figure 4.7: RBS spectrum of 5 ML Cr_2Te_3 deposited on graphene/SiC and annealed at 500°C. The different detected elements are indicated on the graph as well as the deduced stoichiometry of the sample.

All the data collected by RBS are indicated in the Table 4.1, as well as the calculated thickness and stoichiometry of the layers. Assuming a unit cell close to the one of Cr_2Te_3 (as verified by XRD), the Cr content was used to estimate the thickness of the samples. It was found systematically lower than the targeted one of 6.1 nm. The origin of this difference can be probably attributed to channelling effects during the measurements (when the ion source is aligned with crystal directions of the sample), that affect the estimation of the atoms quantity. On the other hand, the stoichiometry is not supposed to be affected by this aberration as both elements quantity would be changed proportionally. It is worth noting, that despite the good sample quality after growth of the sample annealed at 450°C, an absurd value of the stoichiometry was found ($x = 0.16$ in $Cr_{1+x}Te_2$), much lower than $x = 0.33$ in the case of Cr_2Te_3. Many samples were measured over the course of this PhD and this is the lowest value ever measured. Moreover, the measured magnetic properties reported just after indicate an increase of the stoichiometry and not the opposite. The cause could either be experimental or linked with the Te counter flux used during the annealing phase. If some Te was deposited on top of the surface, it would also be measured by RBS and would alter the stoichiometry. Finally, a last hypothesis could be a degradation of the sample caused by mishandling during the transport from the synchrotron for XMCD measurements to the lab in Bordeaux for RBS. In any case, this value will be disregarded for the analysis since preliminary results as well as the other samples indicate an increase of the stoichiometry after annealing and not a decrease.

T_A	**Cr content**	**Deduced thickness**	**Te content**	**x in $Cr_{1+x}Te_2$**
450°C	5.43 ($\times 10^{15}/cm^2$)	5.0 nm	9.36 ($\times 10^{15}/cm^2$)	0.16
500°C	6.26 ($\times 10^{15}/cm^2$)	5.7 nm	9.11 ($\times 10^{15}/cm^2$)	0.375
550°C	3.68 ($\times 10^{15}/cm^2$)	3.4 nm	5.26 ($\times 10^{15}/cm^2$)	0.40
600°C	4.12 ($\times 10^{15}/cm^2$)	3.8 nm	5.97 ($\times 10^{15}/cm^2$)	0.380
650°C	5.49 ($\times 10^{15}/cm^2$)	5.0 nm	5.66 ($\times 10^{15}/cm^2$)	0.940
700°C	5.90 ($\times 10^{15}/cm^2$)	5.4 nm	0.60 ($\times 10^{15}/cm^2$)	18.7

Table 4.1: RBS results as a function of the annealing temperature. The deduced thickness is estimated from the unit cell of Cr_2Te_3. The obtained value for the stoichiometry of the sample with T_A = 450°C is abnormal and not in agreement with all other measurements. It is therefore indicated in red.

The stoichiometry of the other samples is always richer in Cr than Cr_2Te_3, with a value close to x = 0.4 until T_A = 600°C. Above this temperature, the stoichiometry is changing drastically until the almost complete evaporation of Te at 700°C (pure metallic Cr is remaining). Another interesting result is the deduced thickness based on the experimentally obtained Cr content. For bulk Cr_2Te_3, the atom density of one ML is 1.36×10^{15} Cr/cm^2. At first order, (valid for $T_A \leq 600$°C), the ratio of the Cr content with this value can give a number of layers for the grown films and therefore an estimated thickness. This calculation is probably not correct for high values of T_A, as the structure is different from Cr_2Te_3 because of the discrepancy of stoichiometries. We find (despite the uncertainty linked with the channelling effects) a reduction of the total thickness for T_A = 550°C, 600°C. This could indicate that some fraction of the Cr_2Te_3 layers fully evaporates upon annealing at intermediate temperatures, and not just Te. On the other hand, the quantity of Cr is unchanged at T_A = 700°C, indicating there the evaporation of Te only.

Finally, it is worth questioning the structure of the sample annealed at 650°C. XRD measurements indicate a crystal structure very similar to the other samples with lower T_A, and a slightly degraded crystallinity (radial FWHM of the diffraction peak). Considering the lower thicknesses of the two previous samples, it could be assumed that it behaves in between the samples with below and above annealing temperatures. This means that both the Te and Cr_2Te_3 evaporated, leading to layers of $Cr_{1+x}Te_2$ with x close to the previous samples plus some traces of metallic Cr due to the Te evaporation. However, we do not have any experimental support for this assumption, which is therefore only suggested here.

4.2 Magnetic properties

4.2.1 SQUID magnetometry

After we demonstrated the evolution of the $Cr_{1+x}Te_2$ phase with post-growth annealing, the magnetic properties of the layers were investigated to measure whether an associated magnetic evolution took place. Two samples of 5 ML $Cr_{1+x}Te_2$ were first compared using SQUID magnetometry. Both were grown on graphene/SiC substrates and annealed respectively at 400°C and 500°C. The first one exhibited a phase of Cr_2Te_3, whereas the second one was found to be $Cr_{2.13}Te_3$ (this sample was grown and measured for preliminary results). First of all, the evolution of the T_C was assessed by performing remanent magnetization measurements (see Fig. 4.8) after saturation of the magnetization with a magnetic field value of 3 T perpendicular to the films.

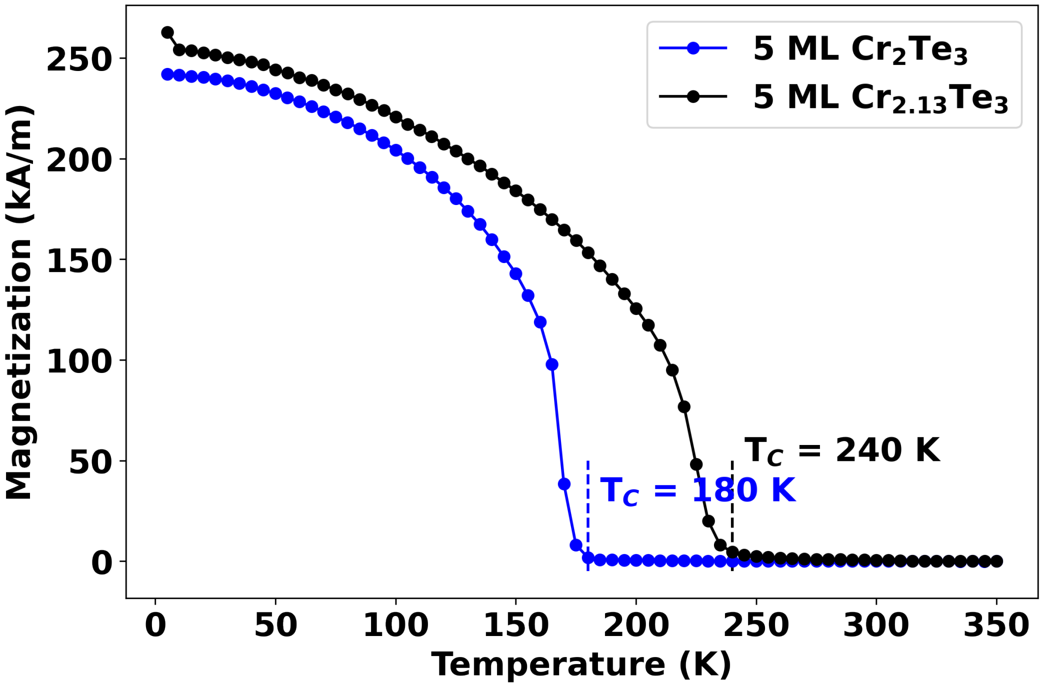

Figure 4.8: Remanent magnetization curves (after out-of-plane saturation) of 5 ML Cr_2Te_3 deposited on graphene/SiC measured with SQUID magnetometry without external field. The first sample was annealed post-growth at 400°C, leading to a Cr_2Te_3 phase. The second one was annealed at 500°C with a final phase of $Cr_{2.13}Te_3$. The measured T_C are highlighted on the figure.

The T_C is largely increased (+33%) from 180 K to 240 K. This confirms that the control of the stoichiometry of $Cr_{1+x}Te_2$ compounds indeed allows a control of the ordering temperature of the system, as reported by Fujisawa et al. [50].

In their paper, the authors also reported an evolution of the magnetic anisotropy energy of their layers. Some hysteresis loops were recorded at low temperature (5 K) for both samples to investigate the consequences of the phase change. The signals are displayed in Fig. 4.9 for the two films with both direction of the external applied field. The layers annealed at 500°C (open symbols) exhibit a larger saturation magnetization than the one annealed at 400°C (full symbols). This is probably a consequence of the larger number of Cr atoms in the structure leading to different coupling. As explained in the introduction, some non collinear spin textures in Cr_2Te_3 lead to a lower magnetization than what the calculation predicts. When the amount of Cr in the intercalated layers changes, spins reorient in the same direction increasing the magnetization.

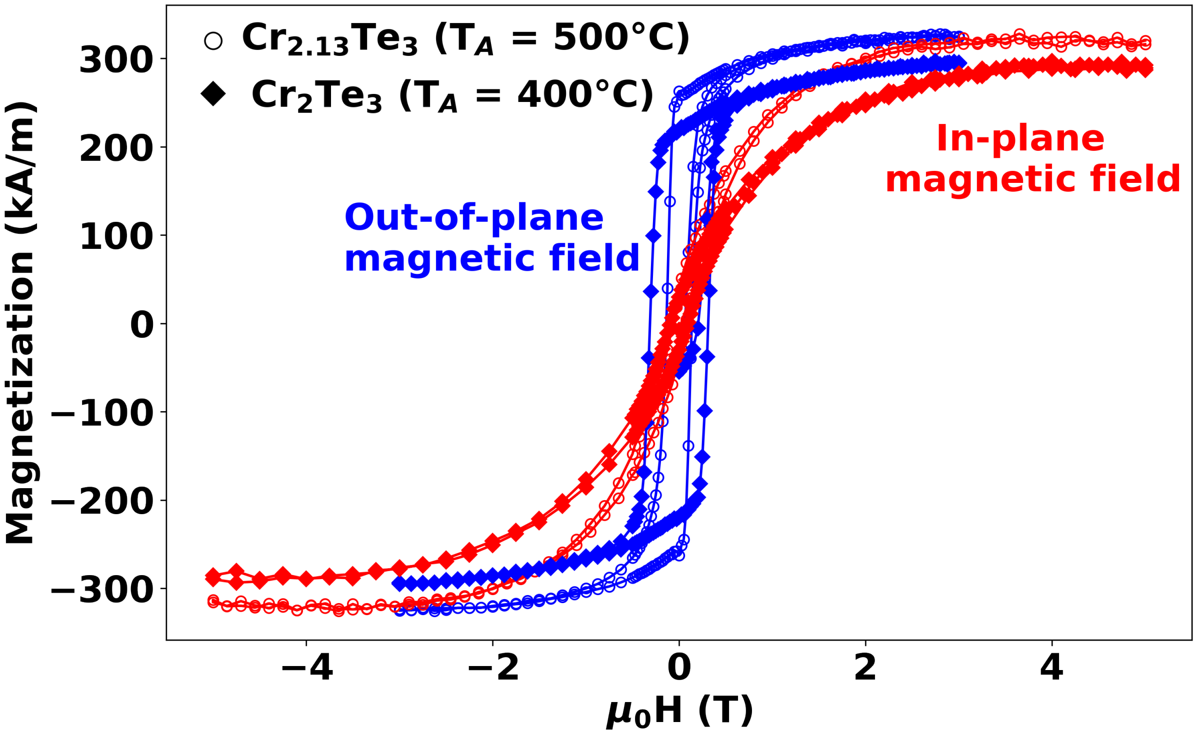

Figure 4.9: Hysteresis loops obtained by SQUID of two phases of $Cr_{1+x}Te_2$(open and full symbols). The signals were measured at 5 K with a magnetic field applied either perpendicularly (in blue) or parallel (red) to the layers. The diamagnetic contribution of the substrate is subtracted and a geometric correction is applied as explained in the techniques chapter.

Besides, a reduction of the coercivity can be observed for the sample with T_A = 500°C in the out-of-plane configuration. This indicates that the magnetization reversal demands less energy in this case, caused probably by a reduction of the out-of-plane magnetic anisotropy. Samples with more crystalline defects usually have larger distribution of coercive fields, as can be seen with the sharper reversal for the sample annealed at 500°C. This is a consequence of a larger number of nucleation sites for the magnetic domains. The decrease of the magnetic anisotropy energy is measured for the $Cr_{2.13}Te_3$ phase compared to $Cr_2Te_3$from 0.171 MJ/m^3 to 0.139 MJ/m^3. This is in agreement with the reported results of Fujisawa et al. [50], even though the PMA is still preserved for this sample. In order to study the evolution of the properties with T_A, we performed measurements at the Soleil synchrotron source for all the samples presented in the structural analysis.

4.2.2 XMCD

Several techniques can efficiently measure the magnetic properties of the grown layers but among all of them, XMCD also allows to obtain element specific magnetic information thanks to the energy dependent signal. In this annealing study, it was therefore ideal to investigate the samples with this technique in order to measure whether the evolution of the stoichiometry could be correlated with some spectroscopic changes in XAS and XMCD signals. Indeed, due to the different valence numbers of the Cr atoms in the intercalated planes, it could be expected to see some energy shifts in the absorption peaks or at least differences in the shouldering. Finally, as this study is focused on very thin films (5 ML), this technique is optimal due to the surface sensitivity character of the method.

4.2.2.1 Low temperature measurements

In order to get information about the magnetic anisotropy of the samples, measurements were performed in two different geometries: with the magnetic field (and the x-ray beam) perpendicular and grazing (30° off the in-plane direction) to the sample plane. In each configuration, the beam was centred on the sample. Due to the good homogeneity over the whole surface of the sample obtained thanks to MBE growth, the two signals could be compared to obtain information about the magnetic anisotropy as will be shown.

First of all, the XAS and XMCD measurements of the sample annealed at T_A = 450°C are displayed in Fig. 4.10. Both light helicity signals in the XAS were normalized (as explained in appendix) and a clear dichroic signal is observed. In order to insure that this difference is of magnetic origin, the measurements were performed with opposite magnetic fields (of ± 3 T) and averaged (σ^+ signal at +3T is averaged with σ^- signal at -3T and vice versa). Similar results were recorded for all the samples in the two geometric configurations.

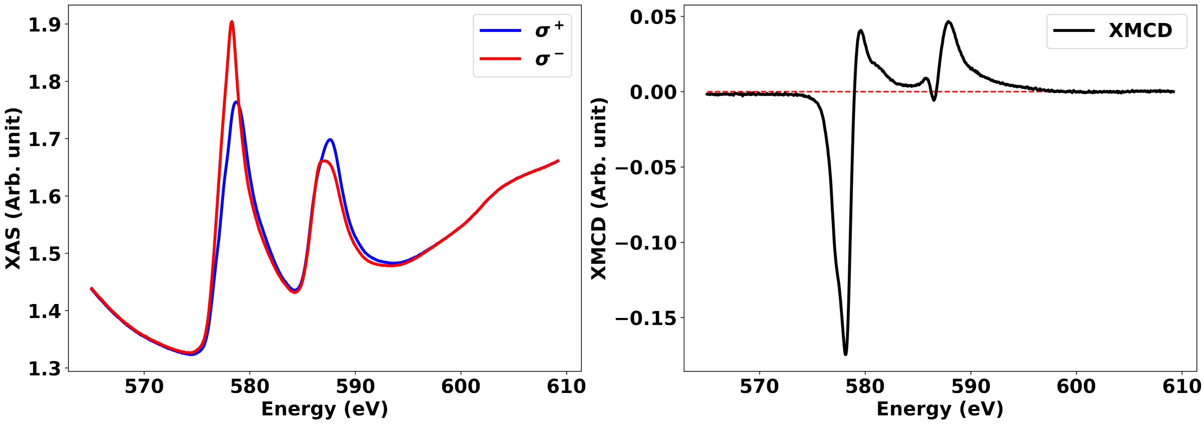

Figure 4.10: XAS (on the left) and XMCD (on the right) of 5 ML Cr_2Te_3 annealed at 450°C. The measurements are performed at 5 K with a magnetic field of ± 3 T perpendicular to the sample. The normalization and drift corrections applied are described in appendix.

Figure 4.11 shows the XMCD measurements performed with the magnetic field perpendicular to the samples for a series of annealing temperature. On the left, the data are shown after an intensity normalized with respect to the XAS edge (see the method in appendix). Some small variations are observed for T_A ranging from 450°C to 650°C. These intensity differences can have different interpretations. As observed with SQUID magnetometry, a different Cr content can lead to a different magnetization. A maximum of intensity is found for T_A = 500°C and 550°C with a decrease for higher temperatures. The signal decrease can be due to the gradual evaporation of the layers at high temperatures and lower thicknesses for the samples annealed at highest temperatures. This is particularly true for the sample annealed at 700°C. The intensity is much lower, probably due to a very low thickness. RBS data revealed a similar content of Cr atoms but RHEED indicated a poor substrate coverage as graphene rods were well visible. The atoms are therefore probably organized in metallic Cr clusters, that are not or poorly magnetic hence the low dichroic signal.

In order to compare the spectroscopic traces of the different samples, a zoom on the L_3 edge is plotted on the right of Fig. 4.11. All the intensities have been normalized such that the minimum is -1 in order to investigate possible energy shifts or different shouldering. As can be observed, all the curves are superposed except for the sample with T_A = 500°C. Drift of the beam line could though lead to rigid energy shifts due to an offset between the undulator and monochromator. To conclude, we could not report any significant spectroscopic change in the XMCD signal after annealing.

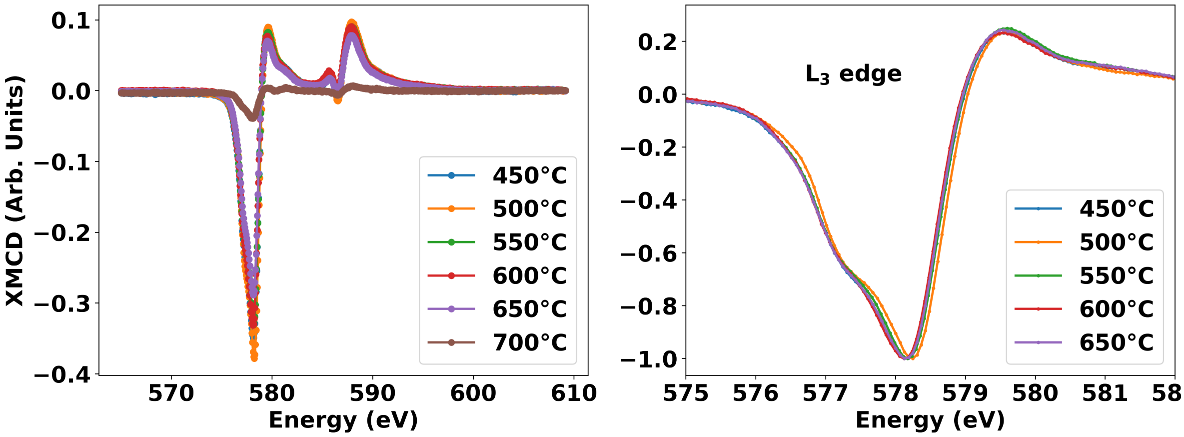

Figure 4.11: On the left, superposition of the XMCD signals of the samples as a function of T_A. Measurements are performed at 5 K with perpendicularly applied magnetic field of ± 3 T. On the right, zoom on the L_3 edge after intensity normalization to -1 for spectroscopic comparison.

To be able to obtain information about the magnetic anisotropy from the XAS and XMCD measurements, one has to use the XMCD sum rules presented in the techniques chapter. Bruno's model [108] relates magneto-crystalline anisotropy energy (E^{MCA}) and orbital momentum with the equation:

$$E^{MCA} \approx \frac{\xi}{4} \Delta m_{orb} \tag{4.1}$$

ξ is a SOC constant and the orbital momentum anisotropy is defined by $\Delta m_{orb} = m_{orb}^{\perp} - m_{orb}^{//}$. Experimentally, as explained before, we can only measure with a 30° off the in-plane direction but we still get a good estimation of the magneto-crystalline anisotropy. Figure 4.12 presents the method used in this manuscript to be able to apply the sum rules to the experimental measurements. To obtain the area of the XAS spectrum, it is necessary to remove the background in the signal measured by TEY. Two "jumps" are visible at the two edges caused by inelastic processes. Indeed, photons with energy higher than the 2p $\rightarrow$ 3d transition can still contribute to the absorption with some scattering in the material leading to energy losses. To remove these contributions, two step functions (mathematically, the arctan function is chosen) are used centred around each edge with an intensity ratio of 2:1. Indeed, the number of states for J = 3/2 (L_3 edge) is twice bigger than that of J = 1/2 (L_2). Moreover some extended x-ray absorption fine structure (EXAFS) leads to contributions at higher energies (in the fit, above 595 eV). To remove this part, the background fit just reproduces the experimental data. The resulting signal after background subtraction is shown in orange and used to compute the orbital momentum of Cr atoms with the sum rules. It has to be noted that the L_3 and L_2 edges overlap experimentally for Cr due to low SOC, which prevents the application of the sum rules for the spin momentum, proportional to the difference of areas for each edge in the XMCD signal.

Using the method described above, the orbital momentum anisotropy was calculated for all the samples at 5 K and the results are shown in Fig. 4.13. Overall, the orbital momentum values are quite low (0.065

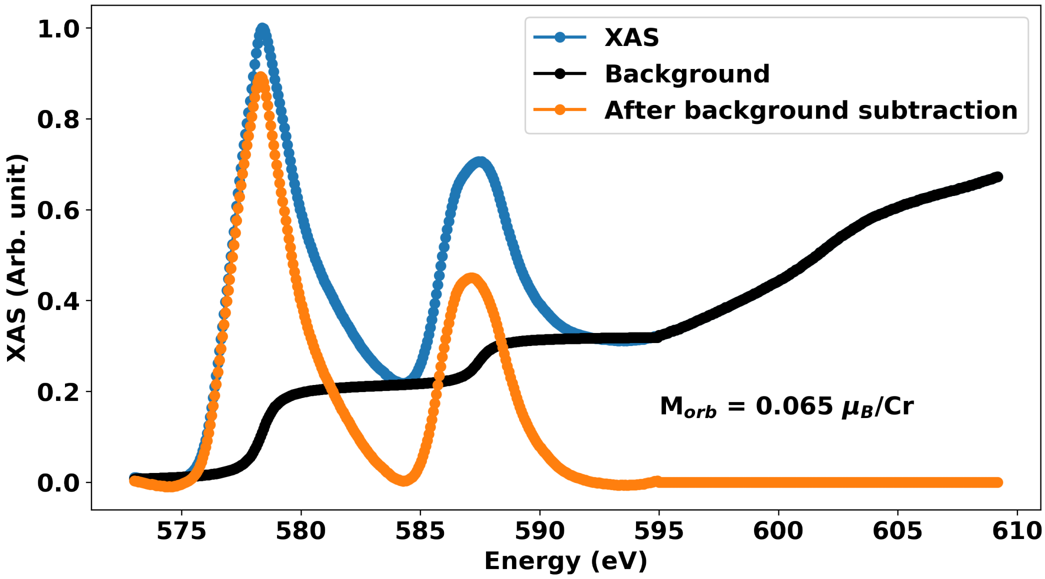

Figure 4.12: Example of background correction on the XAS signal to apply the XMCD sum rules, with the calculated orbital momentum. The spin momentum cannot be determined experimentally due to the overlap of the L_3 and L_2 edges of Cr atoms.

μ_B/Cr for T_A = 450°C with perpendicular applied field). The energy value chosen as the end of the L_2 edge in the background correction can affect a little the deduced value of orbital momentum and the uncertainties on these results are probably quite significant compared to the values themselves. Despite this, it can be observed that positive values of E^{MCA} are measured for lower T_A (until 500°C) and negative ones above. This correlates with the reported results of a decrease and suppression of the PMA of Cr_2Te_3 after the stoichiometry change. The overall shape of the signal reproduces quite well the results of Fujisawa *et al.* (see Fig. 4.1). The lower value of Δm_{orb} for T_A = 450°C compared to the one for T_A = 500°C could be related to the very different stoichiometry measured for this sample.

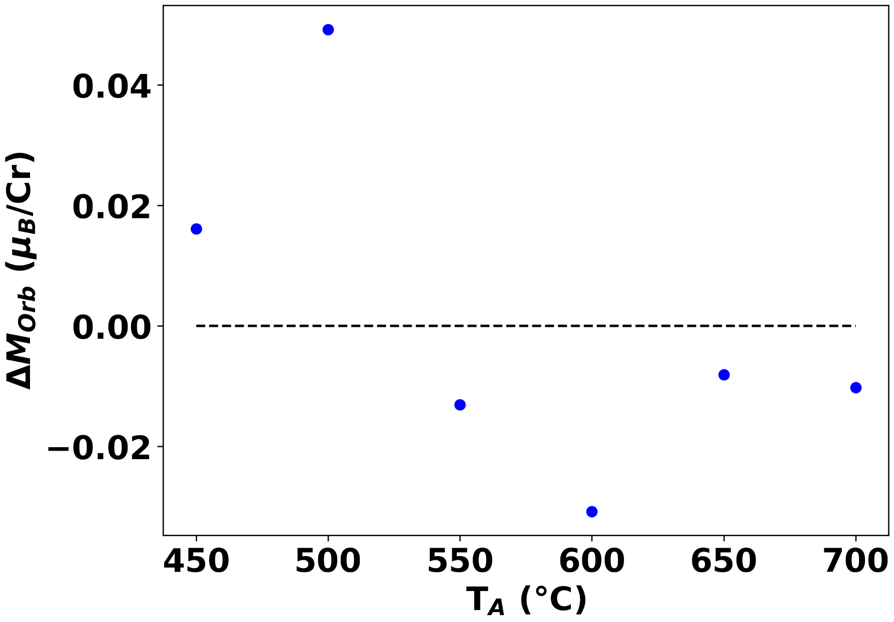

Figure 4.13: Anisotropic orbital moment as a function of T_A. Δm_{orb} is defined as $m_{orb}^{\perp}$ - $m_{orb}^{//}$.

4.2.2.2 Temperature dependent properties

The main objective of this annealing study was to determine if the T_C of the system could be increased after the stoichiometry change. Some temperature dependent measurements were therefore performed to assess the validity of this method. First of all, results on a sample annealed at 500°C but grown at a different time than the other samples will be presented. All the samples were though analysed with the same method.

Figure 4.14 shows the temperature dependent magnetic properties of the sample under two different values of the magnetic field (applied perpendicularly to the sample): at a low field with respect to the coercive field of the sample (a) and one well above the saturating field (b). The samples were not measured by averaging opposite magnetic fields, as it would require to saturate the magnetization in the other direction before the measurement of the remanence. The whole XMCD spectrum was recorded for different temperatures to prevent uncertainty due to energy shifts over time caused by the optics of the beamline. The absolute value of the maximum of the XMCD signal, which is proportional to the magnetization of the sample, is then plotted as a function of temperature. When a large magnetic field is applied, correlation between spins remain well above the ordering temperature, which makes it difficult to obtain the Curie temperature. On the other hand, from the remanent curve (a), a T_C of 250 K can be deduced for this sample.

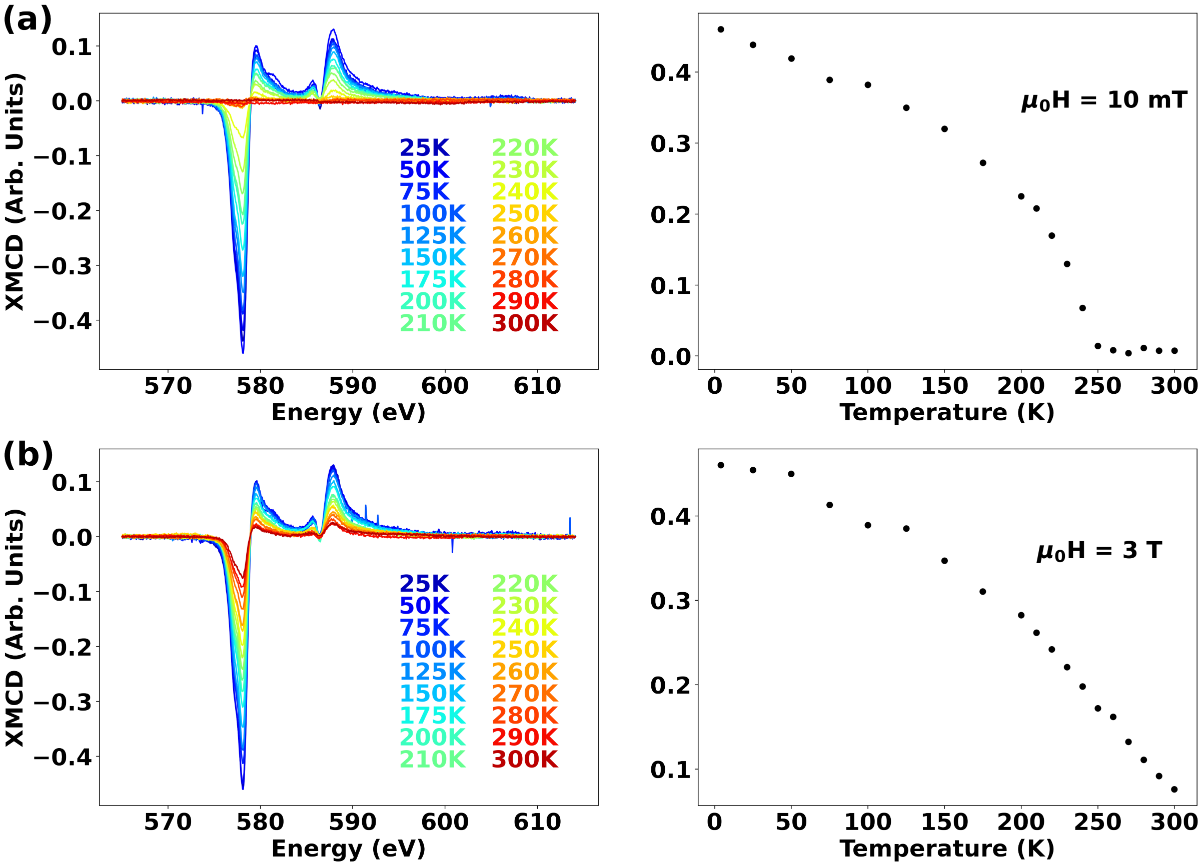

Figure 4.14: Temperature dependent properties of 5 ML Cr_2Te_3 annealed at 500°C measured by XMCD. (a-b) On the top (bottom), a magnetic field of 10 mT (3 T) is applied perpendicular to the sample. On the left pannels, the XMCD spectra are displayed as a function of the sample temperature. On the right, the absolute value of the maximum of the dichroism is plotted as a function of temperature.

Following the same procedure, the maximum of dichroism was obtained for the samples annealed at various temperatures under a magnetic field of 10 mT. The results can be observed in Fig. 4.15.

Unfortunately, one of the heater of the experimental chamber was out of order during the beamtime, which caused some temperature instability (the sample temperature was typically oscillating between ± 5 K of the set temperature). This explains that the curves are more noisy than the one presented earlier. However, it can be observed that all the samples with $T_A \leq 600$°C exhibit a T_C very close to 250 K, whereas the one annealed at 650°C is of the order of 230 K. The first observation correlates well with the almost constant stoichiometry found for these samples. The second one could be explained by the large change of stoichiometry and a larger evaporation of the film (as explained with the hypothesis of a reduction of the thickness plus some metallic Cr clusters). The sample annealed at 700°C has a very low ordering temperature as its structure was strongly degraded.

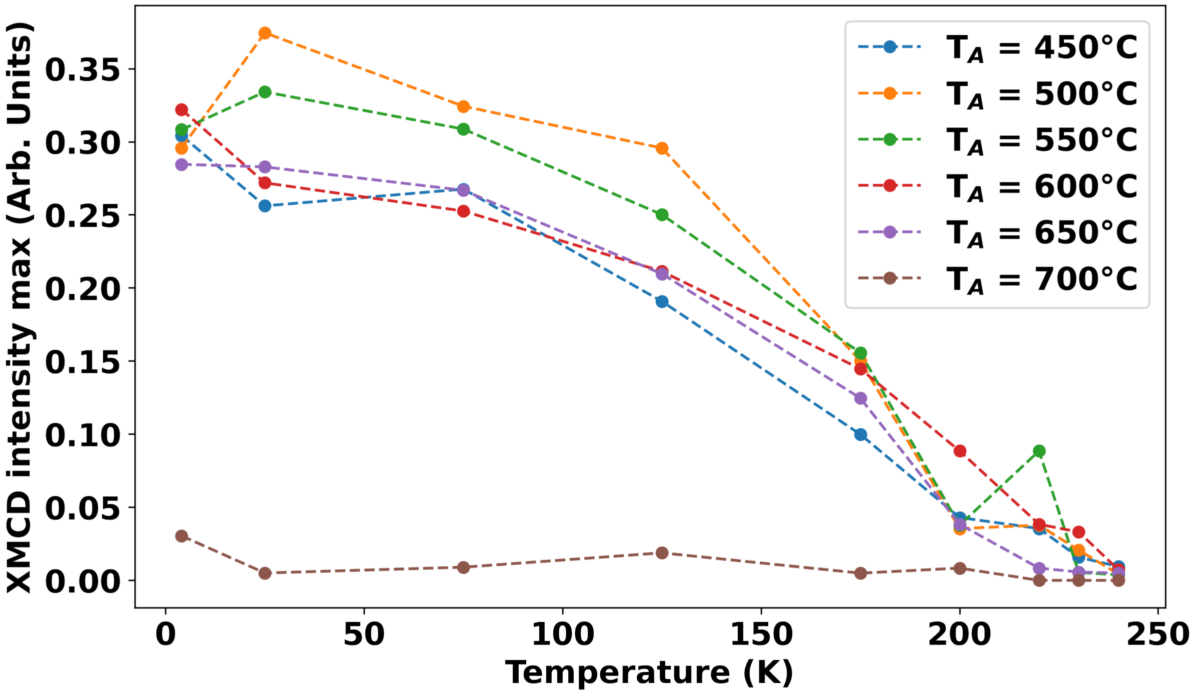

Figure 4.15: Remanent magnetization curves of annealed Cr_2Te_3 films as a function of T_A measured with a perpendicular magnetic field of 10 mT.

To conclude on this chapter, it was shown that post-growth annealing at temperatures ranging from 450°C to 700°C can change the stoichiometry of Cr_2Te_3 layers. Partial evaporation of the Te explains this change. A fraction of the Cr_2Te_3 layers was also reevaporated at intermediate annealing temperatures, until the formation of metallic Cr clusters for T_A = 700°C. The crystal structure was also affected by the annealing with an improved crystallinity but little variation of the lattice parameters. Finally, it was demonstrated that the magnetocrystalline anisotropy of the samples was changed from out-of-plane to in-plane upon annealing associated with an increase of the T_C by 33 % compared to the value of bulk Cr_2Te_3.

CHAPTER

5

Magnetotransport in Cr_2Te_3/ 2D materials heterostructures

The development of new vdW ferromagnetic materials for the integration in 2D and vdW heterostructures holds great opportunities for the field of spintronics. As explained in the introduction, new systems are required with atomically sharp interfaces, PMA and strong SOC for efficient spin manipulation. We have demonstrated in the two previous chapters that Cr_2Te_3 based heterostructures could be grown with high quality and exhibit interesting magnetic properties that can be tuned with the energy brought to the system in the form of post-growth annealing.

The focus of this chapter will be the study of these heterostructures with electrical means to assess the potential for the integration to current technologies. In a first section, magnetotransport measurements will be presented with a continuous applied current in processed Hall bars. Experiments were performed on several 2D materials, namely graphene on SiC, WSe_2 on GaAs and Bi_2Te_3 deposited on Al_2O_3. Complementary results for layers directly grown on insulating sapphire will be shown for comparison. *Ab initio* calculations are also presented to bring some light on a non trivial sign change of the anomalous Hall resistivity measured as a function of sample temperature. The results will be discussed with the Berry phase calculations depending on strain in the layers, charge transfer with 2D materials as well as the non-colinear spin structures of Cr_2Te_3. These findings are published in the reference [91].

In a second section, preliminary results on second harmonic measurements of Cr_2Te_3/Bi_2Te_3 heterostructures are discussed to characterize SOTs and electrical magnetization reversal. The setup used for the measurements will be presented as well as the corrections of spurious effects (mostly of thermal origin such as the anomalous Nernst effect). Some comparison with recent results reported in the literature will be carried out.

5.1 DC measurements

5.1.1 Electrical characterization of Cr_2Te_3 properties

As presented in the experimental techniques chapter, samples were processed in a clean room environment prior to electrical measurements. Figure 5.1 shows a photography of a device at the end of the process. The dark background is the sapphire substrate after etching the layers. The brightest areas correspond to the metallic pads made of 10 nm Ti and 100 nm Au. The area with Cr_2Te_3 in dark grey is visible at the centre as well as at the edges of the contact pads in the shape of squares, where the current can flow from the pads to the Hall bar. The contact area is large in order to limit the risk of electrical breakdown. This happens when the current density is too high, leading to large Joule heating and possibly the deterioration of the Hall bar. As can be seen, pads on the sides are connected to the Hall bar with very thin channels (5 μm wide), which limits the transverse current density. The current is therefore injected between the top and bottom contacts as evidenced by the blue arrow on the image. Magnetic field can be applied whether perpendicular or parallel to the sample plane (a full 360° rotation is possible with a step motor inside the SpectromagPT). Hall resistance is usually measured at the centre of the Hall bar for symmetry reason (no heat gradient along the x direction in the middle), whereas magnetoresistance can be indifferently acquired between two lateral contacts (from the same side). All the devices are checked after wire bonding before performing the measurements.

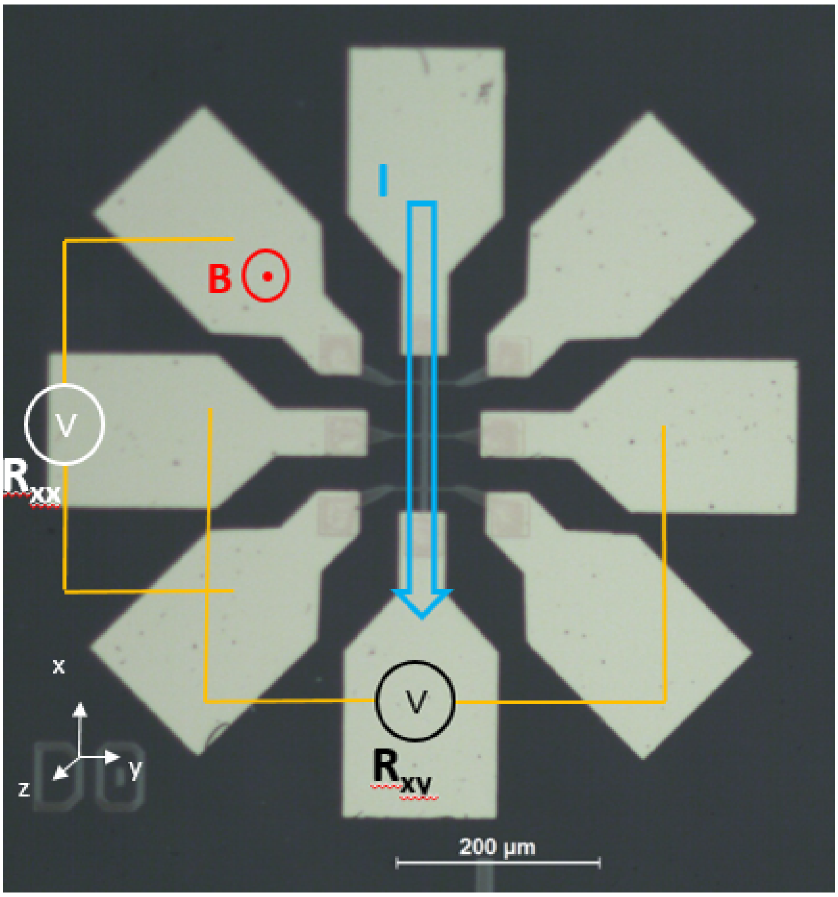

Figure 5.1: Photography of a Hall bar processed in a clean room of 5 ML Cr_2Te_3 deposited on sapphire. Contact pads are made of 100 nm Au deposited on 10 nm Ti for better adhesion to the surface. The direction of the injected electrical current I and the external magnetic field B are indicated as well as the position of the probes for magnetoresistance R_{xx} and Hall resistance R_{xy} measurements. The scale of the image is shown at the bottom.

5.1.1.1 Temperature dependent resistivity

After the introduction of a sample in the Spectromag setup, the resistivity of the sample was first measured to verify the Hall bar continuity as well as the bonding contacts. A typical temperature dependent resistivity of Cr_2Te_3 layers is plotted in Fig. 5.2. The sample was deposited on sapphire, which is insulating, so that all the injected current is flowing through the deposited material. The measured resistivity is increasing with temperature, which is typical of metals. Indeed, the electron-phonon scattering rate increases with temperature, which leads to a higher resistivity.

Another observable feature of this experimental curve is a clear slope change between 150 K and 200 K. This a consequence of the phase transition from ferromagnetic to paramagnetic above the T_C. When the material is ferromagnetic, spin waves or magnons are present in the material that can act as a complementary source of electron scattering, leading therefore to steeper resistivity increase below T_C. Finally, at very low temperature (usually below 20 K), the resistivity starts to slightly increase when the sample is cooled. This could be caused by the freezing out of some defects conduction which are still present in the material despite the metallic nature.

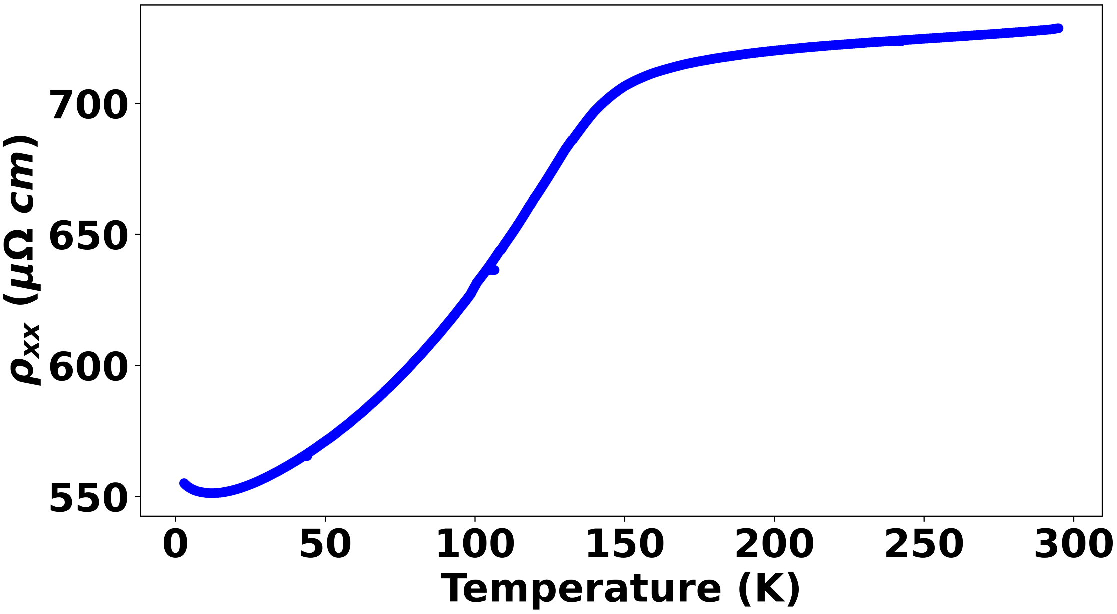

Figure 5.2: Longitudinal electrical resistivity of 5 ML Cr_2Te_3 deposited on sapphire as a function of temperature.

The resistivity is of the order of few hundreds of $\mu\Omega$.cm, which is quite high for a metal. For comparison, Al has a resistivity of 2.65 $\mu\Omega$.cm and pure Cr of 12.5 $\mu\Omega$.cm at RT [109]. This high resistivity can nevertheless be an asset for spintronics, notably for SOTs. Indeed, in an heterostructure combining Cr_2Te_3 with a metal with large SOC like Pt or Ta, most of the electrical current will flow in the non magnetic material, generating therefore efficient spin current for magnetization manipulation.

5.1.1.2 I-V curve of Cr_2Te_3

In order to verify that the measurements were operated in an Ohmic regime (with linear I-V curve), we obtained the current voltage characteristics of the samples by measuring the voltage on the same contacts where the current was injected (two-probes measurements). The results are plotted in Fig. 5.3, with an applied current between -500 μA and + 500 μA. The measured voltage is linear with the current, showing an Ohmic behaviour and no saturation in this current range. We deduced that we could perform our magnetotransport measurements for any chosen value of applied current lower or equal to 500 μA.

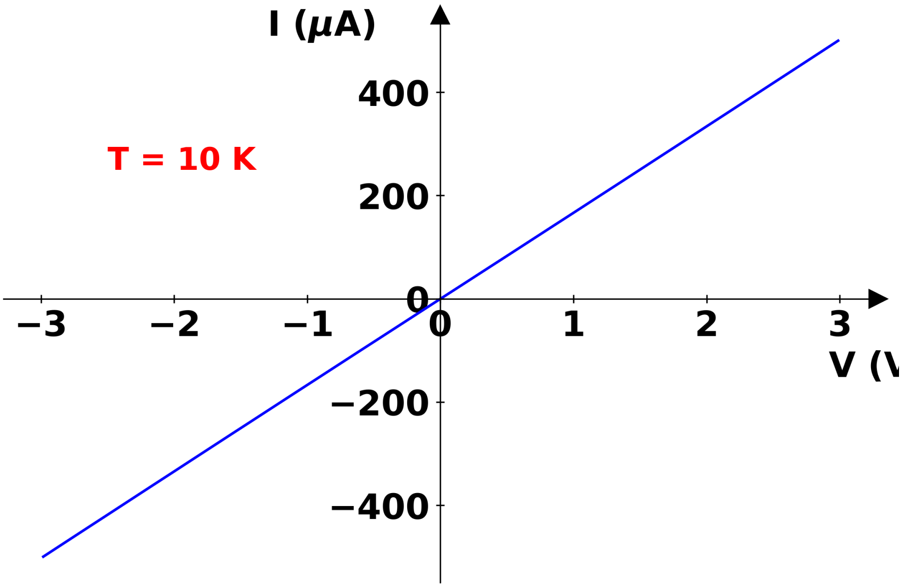

Figure 5.3: Current voltage characteristics of 5 ML Cr_2Te_3 measured at 10 K.

5.1.2 Field dependence of the longitudinal resistivity

5.1.2.1 Anisotropic magnetoresistance effect and magnon magnetoresistance

In any metallic ferromagnet, the resistivity of the material will be affected by the magnetic field. The anisotropic magnetoresistance (AMR) effect was first discovered by Kelvin [86] and states that the resistivity depends on the relative direction of the applied magnetic field and injected current. Because of SOC, electron orbitals orientation can be determined by the direction of an external magnetic field. This causes more (less) scattering events of the conduction electrons when the direction of the current is parallel (perpendicular) to the magnetic field. The resistance can therefore increase or decrease as a function of the applied magnetic field (see Fig. 5.4). If θ is the angle between the current direction and the magnetization, the resistivity can be expressed with the equation:

$$\rho = \rho_{\perp} + (\rho_{//} - \rho_{\perp}) cos^2\theta \tag{5.1}$$

$\rho_{\perp}$ and $\rho_{//}$ are respectively the resistivities of the material when the field is applied perpendicular or parallel to the current direction. θ depends on the magnetic field, as can be seen with the sketches. However, as evidenced by the equation, no AMR effect will affect the longitudinal resistivity of the material if the magnetization remains perpendicular to the current direction (cos(π/2) = 0).

As presented with the temperature dependent resistivity of Cr_2Te_3, scattering events with magnons can also affect the longitudinal resistivity of ferromagnetic materials. These quasiparticles have a quadratic energy dispersion with an energy gap proportional to the effective magnetic field felt by the magnons:

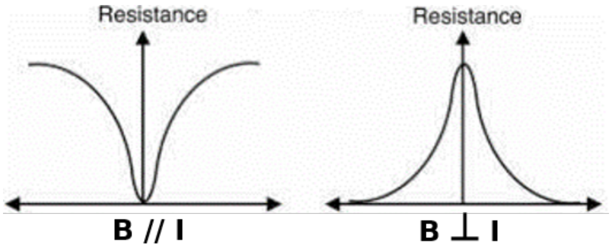

Figure 5.4: Sketch of the resistance of a ferromagnetic material as a function of the external magnetic field (B) direction with respect to the one of the current (I), adapted from [86].

$$E(k) = Dk^2 + g\mu_B B_{eff} \tag{5.2}$$

D and g are respectively the exchange stiffness constant of the material and the Landé factor. As a consequence, when the effective field (sum of the external field and the contribution of anisotropy, demagnetizing and exchange fields) increases, the dispersion curve is shifted to higher energy and thus the magnon population decreases. During an hysteresis loop in a ferromagnet starting from saturation, the external field and magnetization are initially parallel. When the field decreases, the magnon population increases leading to more scattering events and a higher resistivity. After the external field crosses zero, the effective field does not directly change sign due to the remanent magnetization in the ferromagnet. The resistivity will therefore continue to increase until the coercivity of the material is reached. After the magnetization reversal, the direction between external field and magnetization abruptly changes from antiparallel to parallel, causing a discontinuity in the magnon population and a resistivity drop. This effect can be nicely observed experimentally with the results in Fig. 5.5.

5.1.2.2 Magnetoresistance measurements of Cr_2Te_3 layers on different 2D materials

a) WSe_2

Using the same geometry as the one presented in Fig. 5.1, the longitudinal resistivity of a device of 5 ML Cr_2Te_3 deposited on WSe_2/GaAs was measured with the magnetic field applied perpendicularly to

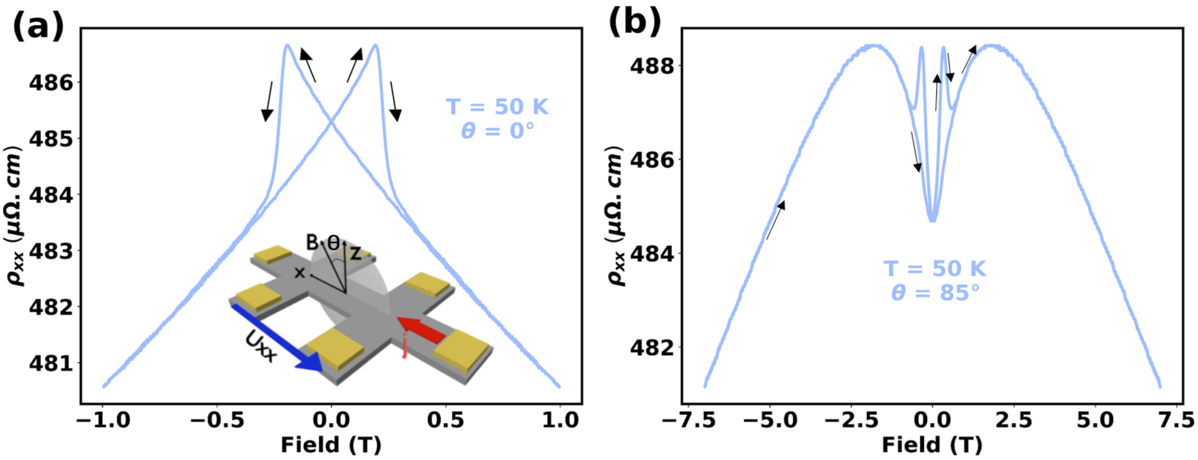

Figure 5.5: Magnetoresistance of 5 ML Cr_2Te_3 deposited on WSe_2/GaAs as a function of magnetic field. Measurements are performed at 50 K. (a) The magnetic field is applied perpendicularly to the sample plane (and therefore also to the current direction). Black arrows indicate the field ramping direction in the hysteresis loop. A sketch of the setup and its geometry are shown below the curve. (b) Similar measurement with the field tilted by 85°. Arrows indicate the signal for ramping up magnetic field.

the sample (see Fig. 5.5.(a)). The current value chosen for the measurements was 50 μA. A sketch of the geometry is shown below the experimental curve with the angle θ between the field and the current direction, with the convention of $\theta = 0°$ for the applied field perpendicular to the sample. The GaAs substrate was chosen intrinsic (without doping) in order to have an insulating material. All of the injected current is therefore flowing in the Cr_2Te_3 layers (WSe_2 is a semiconductor).

Because of the PMA, the magnetization remains perpendicular to the current and no AMR is visible on the experimental curve (on the left). However, a clear magnon negative magnetoresistance effect is visible. To evidence it, black arrows show the ramping direction of the magnetic field. When the field is ramped up from negative saturation, the resistivity increases until the coercivity with a drop close to 1% at the coercive field. Above it, the resistivity decreases as the magnon density is reduced. In Fig. 5.5.(b), the sample is rotated by 85° in the ZX plane, as shown in the sketch. This time, both AMR and magnon magnetoresistance can be observed. Black arrows indicate the signal with ramping up magnetic field. At high field, magnon magnetoresistance dominates and a linear trend can be seen because the magnetization is pinned along the field direction. Above -2T, magnetization starts to rotate to its easy axis (perpendicular) and thus the resistivity decreases due to AMR (this is the case where field and current direction are parallel in Fig. 5.4). Above the field sign change, both AMR and magnon magnetoresistance contribute positively to the resistivity hence the higher slope. Then, at the coercivity, the resistivity drops due to the abrupt change of the magnon population as in the perpendicular case. Finally, above 2T the contribution of AMR saturates and the resistivity starts to decrease linearly again due to the reduction of magnon density.

b) Bi_2Te_3

For a thickness of 10 ML, Bi2Te3 is a 3D topological insulator with a very low bulk bandgap (0.12 eV [95]). As a consequence, part of the current might flow in bulk Bi_2Te_3 (especially in MBE-grown layers where Te vacancies induce n-type doping) for magnetotransport in Cr_2Te_3/Bi_2Te_3 heterostructures. Moreover, the conducting topologically protected surface states of the material also contribute to the transport in the material. Nevertheless, similar observations were made for samples of Cr_2Te_3 deposited on 10 ML Bi_2Te_3 on Al_2O_3. The resistivity of the stack at 50 K is 385 $\mu\Omega$.cm. If we make the assumption that the one of Cr_2Te_3 is unchanged (valid hypothesis on a first order due to the weak vdW interaction between the layers) and we model the transport with two resistive parallel paths, we obtain the following equations:

$$\frac{1}{R_{BT}} + \frac{1}{R_{CT}} = \frac{1}{R_{tot}} \tag{5.3}$$

$$\delta I_{BT} = \frac{I_{BT}}{I_{tot}} = \frac{R_{CT}}{R_{CT} + R_{BT}} \tag{5.4}$$

BT and CT stand respectively for Bi_2Te_3 and Cr_2Te_3. Using the resistivity of 485 $\mu\Omega$.cm for Cr_2Te_3 measured in Fig. 5.5, we obtain that only 20% of the current is flowing through Bi_2Te_3.

c) Graphene

Finally, similar measurements were performed on 5 ML Cr_2Te_3 deposited on monolayer graphene that are displayed in Fig. 5.6. Graphene is semimetallic with a very high mobility as presented in the introduction, so that the injected current is going to flow in both materials. Experimental curves are recorded at very low temperatures (2 and 10 K) because of the quantum effects that can be observed in graphene in this temperature range. It has to be noted that this sample of Cr_2Te_3 was grown at 300°C but not annealed, contrary to the other samples presented in this chapter (annealed at 400°C). This probably explains the larger longitudinal resistivity due to a higher density of structural defects in Cr_2Te_3.

Several effects need to be accounted for in order to explain the measurements at 2 K (black curve). In the low field range, typical magnon magnetoresistance behaviour is recognizable due to the conduction in Cr_2Te_3. More surprisingly, two peaks are observed close to the coercivity as if there was two magnetization reversals (like two ferromagnetic systems uncoupled). This peculiarity will be further discussed with the Hall resistivity results. At higher field, the resistivity increases again, which is typical of the magnetoresistance of graphene that scales as B^2 [110]. Besides, some oscillations can be observed that are called Schubnikov de Haas (SdH) oscillations. This effect occurs in 2D electron gas at low temperature and intense magnetic field. The density of states drops to zero except for some energies called Landau level as in a periodic oscillator. Each Landau level are split by the cyclotron energy. The energy splitting between Landau levels thus increases with the applied magnetic field. Experimentally, we can access up to ± 7 T and a temperature down to 2 K, which only allows for the observation of twoSdH oscillations. Finally, a last effect observed is an hysteresis of the resistivity as a function of the magnetic field *i.e.* a difference of the resistivity for field ramping up and down. This is not observed at 10 K as can be seen with the blue curve. We do not have any satisfying explanation for this observation, that seems like a drift but that is reproducible from one experiment to another.

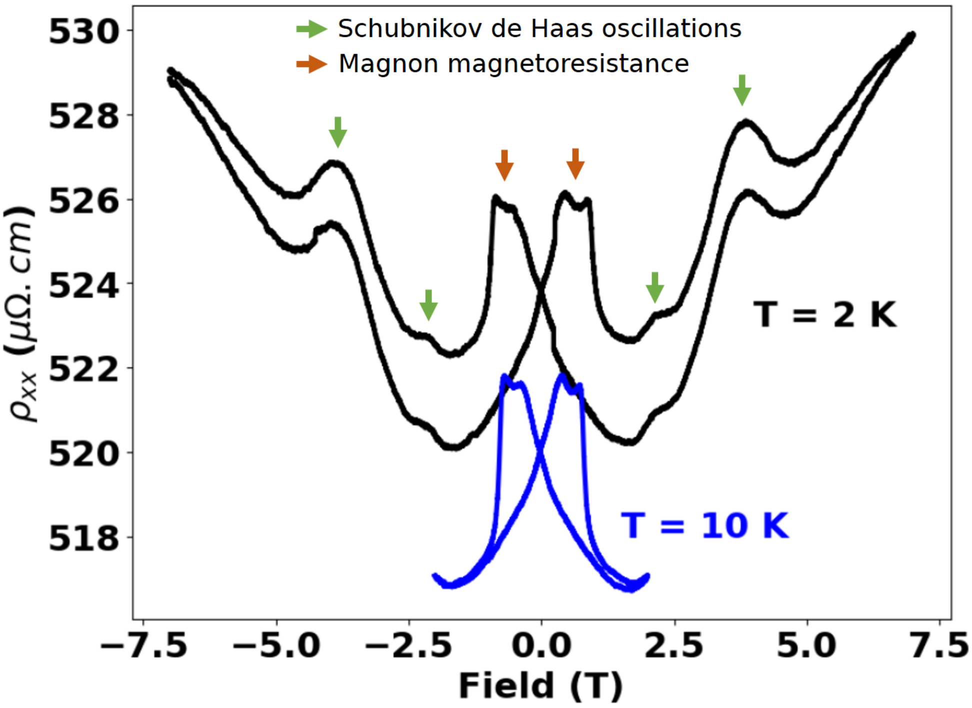

Figure 5.6: Magnetoresistance of 5 ML Cr_2Te_3 deposited on 1ML graphene on SiC. Measurements are performed at 2 and 10 K. Some coloured arrows highlight physical effects on the experimental curves.

To conclude this part, it was demonstrated that the field dependence of the magnetoresistance of Cr_2Te_3 layers is typical of a metallic ferromagnet. When interfaced with conducting 2D materials, electrical transport occurs in both layers and characteristic transport features of graphene were evidenced at low temperature, proving once again the good interface between Cr_2Te_3 and 2D materials as well as the preservation of their properties.

5.1.3 Anomalous Hall effect characterization as a function of strain, Berry phase and charge transfer

As presented in the introduction, the measurement of a transverse voltage allows the detection of many magnetotransport effects. The focus of this part will be directed towards one of them, the anomalous Hall effect (AHE), that is dependent on the magnetization of the material. Experimental observations will be compared with the direct measurements of the magnetic properties. Some *ab initio* calculations of the band structure of the material will also be presented to bring some light on the reported results.

5.1.3.1 Experimental observation of a sign change in the anomalous Hall effect resistivity

Exactly as for the magnetoresistance, the Hall resistivity was measured with an injected current of 50 μA. Temperature was varied between 50 K and 170 K and the out-of-plane magnetic field between ± 1 T. Using the linear slope at high field, ordinary Hall effect (OHE) was fitted and subtracted from the experimental curves shown in Fig. 5.7. When electrical transport is dominated by a single charge carrier, the slope or Hall coefficient R_H can be linked to the carrier concentration n with the simple formula $R_H = \frac{1}{ne}$, with e the electron charge. Experimentally, we extracted a carrier density of 1.6×10^{15} holes/cm^2 at 50 K for the 5 ML Cr_2Te_3 deposited on WSe_2 (Fig. 5.7.(a)) and 4.5×10^{15} holes/cm^2 for the ones deposited (prior to its evaporation) on Bi_2Te_3 (Fig. 5.7.(b)). We also measured the electrical properties of layers directly grown on sapphire (see Fig. 5.8) and measured a carrier density of 7.0×10^{15} holes/cm^2. This indicates some charge transfer between WSe_2 and Cr_2Te_3. Since the ferromagnet is directly standing on sapphire after the evaporation of Bi_2Te_3, we attributed the difference in doping levels to the formation of defects acting as dopants at the interface after the layers degradation.

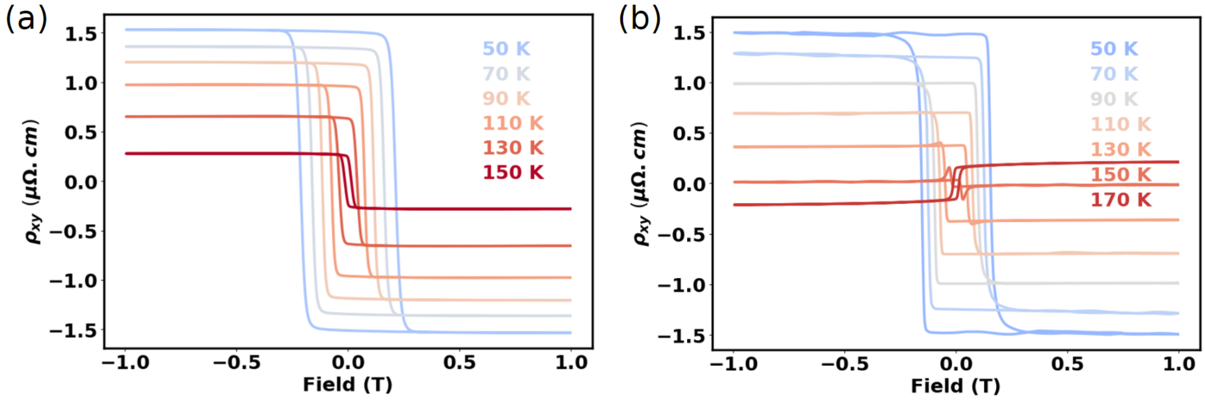

Figure 5.7: (a) Hall resistivity as a function of temperature of 5 ML Cr_2Te_3 deposited on WSe_2/GaAs after subtraction of the ordinary Hall slope. Magnetic field was applied perpendicularly to the sample plane. (b) Same measurements on a sample of 5 ML Cr_2Te_3 deposited on Bi_2Te_3 after annealing at 400°C (and evaporation of the Bi_2Te_3 layers). The ordinary Hall slope was also removed.

The AHE hysteresis loops of the 5 ML Cr_2Te_3 deposited on WSe_2/GaAs are in good agreement with the measurements by SQUID magnetometry in terms of coercivity and temperature dependence. For the signals in Fig. 5.7.(b), an additional effect is observed with a change of sign of the AHE between 150 K and 170 K. In order to verify whether the evaporation of Bi_2Te_3 was at the origin of this result, a similar sample was grown directly on Al_2O_3. The temperature dependent Hall resistivity is displayed in Fig. 5.8.(a), and a similar change of sign of the AHE is observed, but at a different temperature, close to 120 K.

In order to highlight this change of sign of the AHE, experimental curves were fitted as shown in Fig. 5.9. OHE was modelled with a linear slope and AHE with an hyperbolic tangent function. The AHE coefficient is plotted in Fig. 5.8.(b) for different samples as a function of temperature. As observed on the Hall resistivity measurements, a clear change of sign of the AHE is seen below the T_C for the two samples standing on sapphire but not for Cr_2Te_3 deposited on WSe_2. Comparable results have also been reported

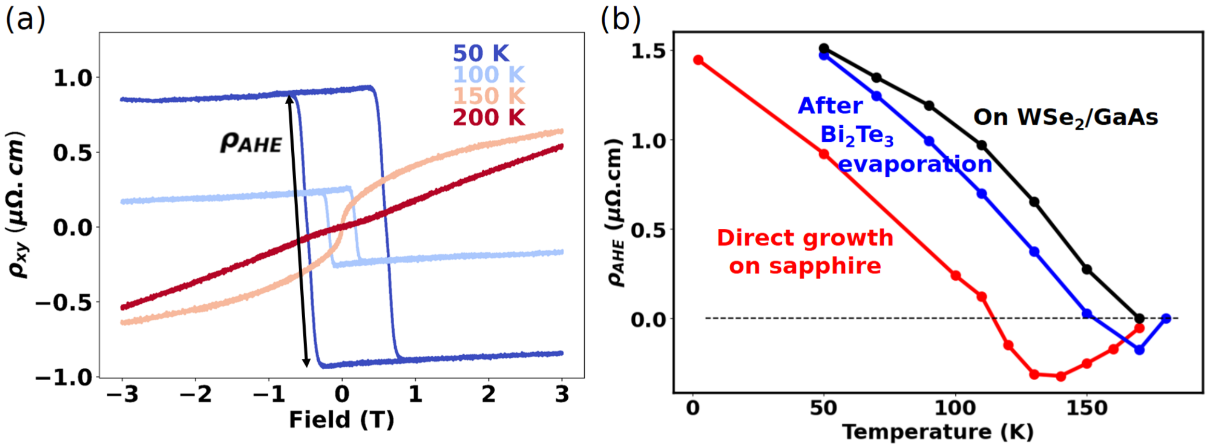

Figure 5.8: (a) Hall resistivity as a function of temperature of 5 ML Cr_2Te_3 deposited on sapphire substrate with the indication of the anomalous Hall coefficient ρ_{AHE}. The ordinary Hall slope is not subtracted. (b) Anomalous Hall resistivity coefficient temperature dependence for samples of Cr_2Te_3 grown on various substrates.

in the literature [90, 111, 112], but the physical origin of this effect is still under debate. Our assumptions will be developed in light of our *ab initio* results. First of all, we discuss the humps in the AHE signal observed at the coercive field in Fig. 5.7.(b), for temperatures below the change of sign.

5.1.3.2 Investigation of possible topological Hall effect in Cr_2Te_3/Bi_2Te_3 heterostructures

As stated in the introduction, several groups have reported THE in Cr_2Te_3/Bi_2Te_3 heterostructures [73, 75, 76]. This effect is the consequence of the presence of topological spin structures called skyrmions that occur in presence of strong DMI. It can be evidenced (among other ways) in the form of peaks of the transverse resistivity centred around the nucleation field of these skyrmions. These structures are usually only stable for a given range of temperature and magnetic field, close to the coercive field of the material where the spin direction is not imposed by the external magnetic field. Experimentally, similar features can be observed for temperatures between 100 K and 150 K for Cr_2Te_3 deposited on Bi_2Te_3.

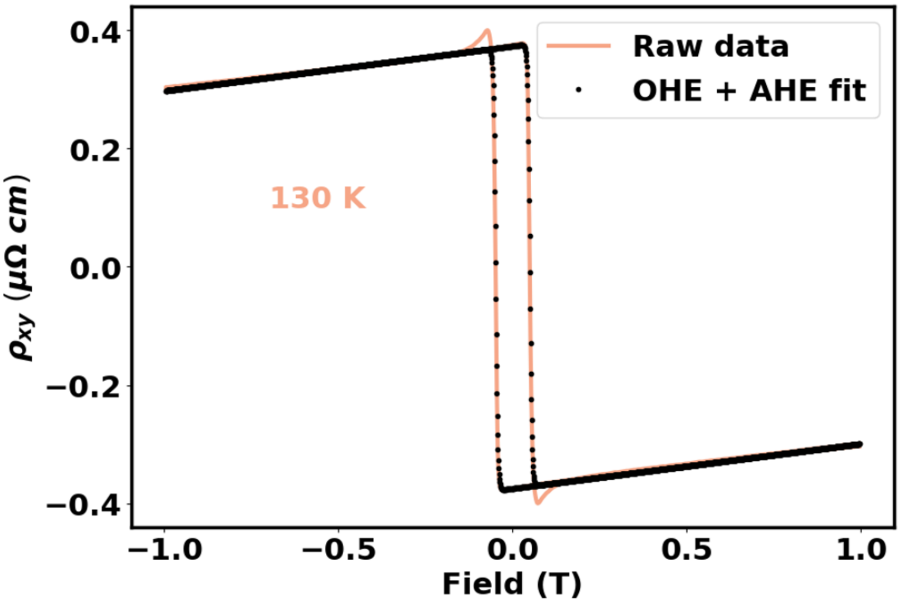

Figure 5.9: Fit of the OHE and AHE for the Hall resistivity at 130 K for 5 ML Cr_2Te_3 deposited on Bi_2Te_3.

To evidence this phenomenon, these experimental curves were fitted using a simple model of the OHE and AHE as can be seen in Fig. 5.9. These fits were then subtracted to the results to observe the difference, as plotted in Fig. 5.10. Bumps are clearly visible below the change of sign temperature of the AHE as well as a reduction of the width with increasing temperature. This latter observation is probably a consequence of the decrease of the coercive field with temperature of Cr_2Te_3 layers. No peak is observed at 170 K but only noise due to the error of the fitting model compared to the experimental curve.

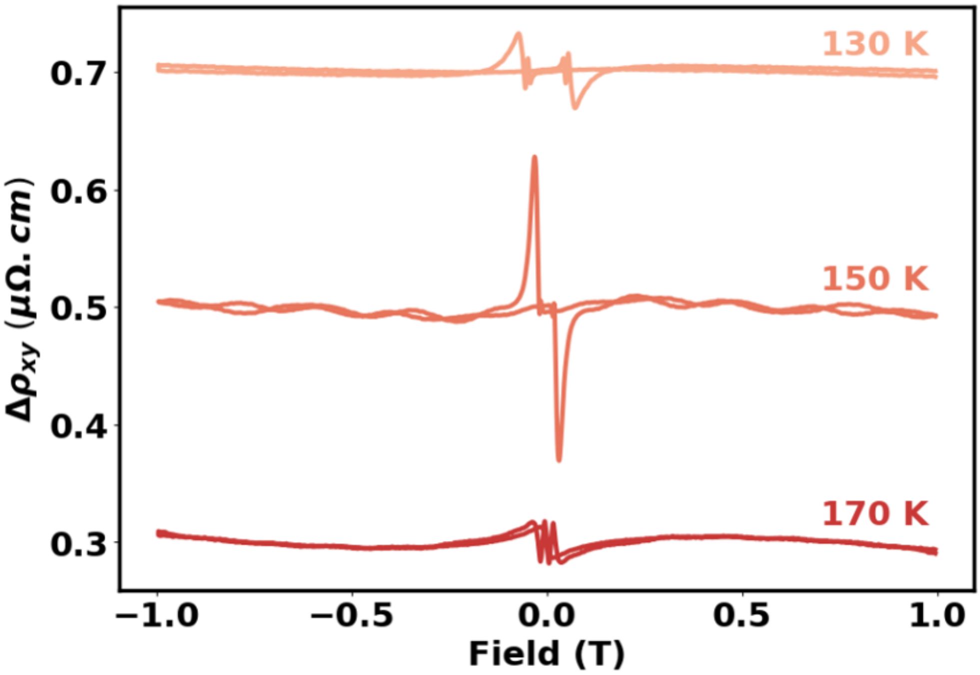

Figure 5.10: Hall resistivity of Cr_2Te_3 deposited on Bi_2Te_3 after subtraction of the OHE and AHE fits measured at different temperatures below and above the change of sign of the AHE. The curves are vertically shifted for better visual.

Several explanations to these humps have been proposed in the literature: THE as explained before, but also two contributions to the AHE with opposite signs [80]. It was shown in the introduction how the sum of two hysteresis loops can mimic THE like behaviour, but it remains the question of the origin of these contributions with opposite sign. Magnetic measurements performed on this sample (and similar studies) show unambiguously a single magnetic reversal behaviour, which makes the hypothesis of two decoupled phases unlikely. However, it is worth noting, that these bumps are always correlated with the change of sign of the AHE [73, 90] and usually decay very fast above the sign change temperature. This seems to be an argument for the two opposite contributions, as it is clear in these samples that Cr_2Te_3 can lead to both positive and negative values of AHE coefficients. Moreover, as it was shown with the AHE temperature dependence in Fig. 5.8.(b), the temperature of the sign change depends on the sample. Empirically, this temperature increases as the holes density decreases (with a value greater than T_C for the sample on WSe_2). This behaviour will be further discussed with *ab initio* calculations and the observed charge transfer possibly giving the origin of these peaks. Indeed, for a real sample with structural defects (notably the one where Bi_2Te_3 was evaporated), some local disorder in the crystalline structure can lead to slightly different local carrier densities and therefore different sign change temperatures. For measurements at a temperature within the sign change temperature distribution, opposite AHE contributions will thus be added.

Another explanation was proposed during the Intermag conference 2023 in Sendai (Japan) by Hao Zeng [113]. The results are not yet published but the authors attributed the two opposite contributions of the AHE to the different Cr planes. Fully occupied Cr planes with valence numbers of 2 and 3 contribute with an opposite sign to the Cr in the intercalated planes with a valence number of 1. The relative intensity of the two signals depends, in their model, on the canting angle of the magnetic moment of these intercalated Cr. This angle can change with temperature, and therefore lead to a sign change whether the one or the other contribution is dominant. These results were unfortunately not yet supported by calculations to verify the relevance of these hypotheses but the two models (our explanation of the sign change will be presented just after) are not incompatible and could both contribute to explain these humps in the AHE resistivity signals.

5.1.3.3 Band structure calculations and Berry phase of Cr_2Te_3 layers

Three effects are at the origin of the AHE, as explained in the introduction: two extrinsic effects (skew scattering and side jump) and one intrinsic to the ferromagnetic material (the Berry phase). The amplitude of the first two can change with temperature as they usually scale with the longitudinal conductivity (in a linear or quadratic way) but their sign is not expected to change. On the other hand, the Berry phase of Cr_2Te_3 depends on the band structure of the material and can change without restriction in temperature. Moreover, the intrinsic contribution to the AHE is dominant and cannot be neglected in the experimental longitudinal resistivity range as shown in the reference [112].

The intrinsic AHE was therefore computed for bulk Cr_2Te_3 by constructing a tight-binding Hamiltonian [114] based on maximally localized Wannier functions using the `Wannier90` package [115]. We verified carefully that the model reproduces well the band structure of Cr_2Te_3 from the original DFT calculation. Using the `WannierBerri` package [116, 117], the Berry curvature was then calculated for a dense k-point mesh and integrated over the Brillouin zone to obtain the Berry phase, proportional to the intrinsic anomalous Hall conductivity (AHC), at various Fermi level positions. These calculations were performed as a function of the strain in the lattice (expressed with the ratio of the lattice parameters c/a) and the deduced AHC is displayed in Fig. 5.11. The transverse conductivity can be expressed as a function of the magnetoresistance and the Hall resistance with the equation:

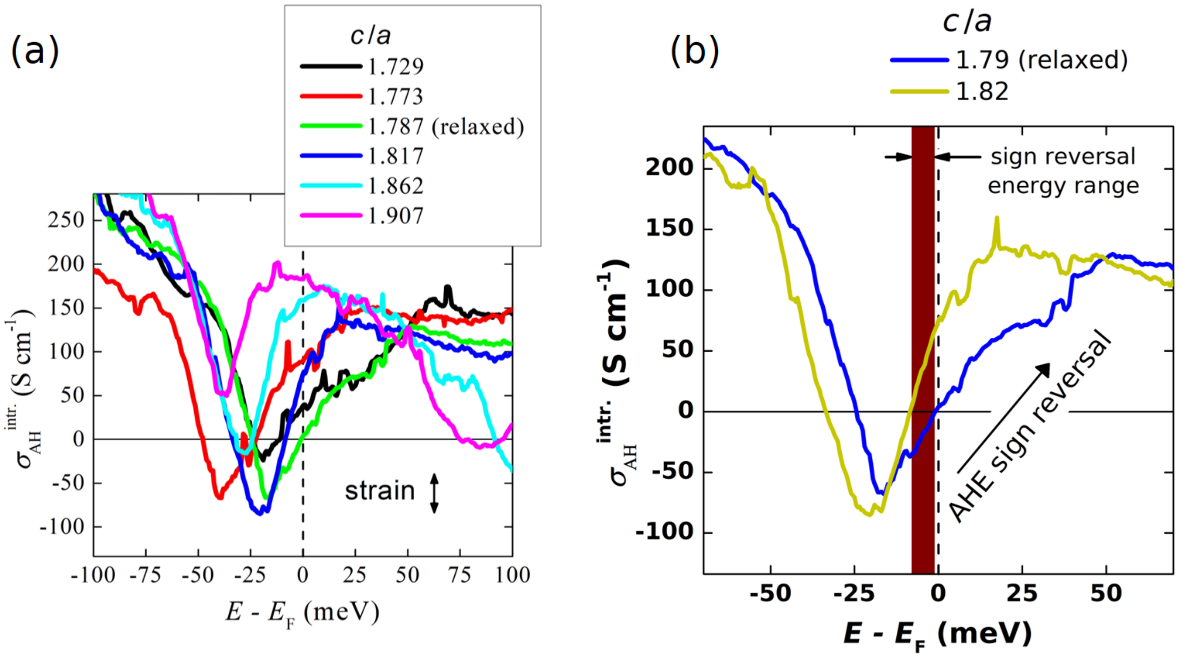

Figure 5.11: Intrinsic anomalous Hall conductivity of Cr_2Te_3 as a function of energy close to the Fermi level. (a) Strain dependent calculation for various c/a ratios. (b) Same curves for ratios close to the experimental values with an highlighted energy area. It indicates the energies where a sign change of the conductivity would be observed after relaxation of the structure from c/a = 1.82 to c/a = 1.79.

$$\sigma_{xy} = \frac{\rho_{xy}}{\rho_{xx}^2 + \rho_{xy}^2} \approx \frac{\rho_{xy}}{\rho_{xx}^2} \tag{5.5}$$

Because the longitudinal resistivity is much larger than the transverse one, transverse conductivity and resistivity are close to be proportional to each other so that any analysis on the AHC can directly be compared to the experimental findings on the resistivity. Figure 5.11.(a) depicts the intrinsic AHC of Cr_2Te_3 layers close to the Fermi level energy (E_F) as a function of strain. A change of sign can be observed for most structures within a few tens of meV around E_F, unlike in previous reported results, where it was calculated at more than 330 meV of E_F [77]. This difference is due to the inclusion of the vdW corrections in the DFT calculations. Our results are in a better agreement with experimental findings, as no change of sign of the AHE would be seen in the measurements if the energy cost was as large as 300 meV. Another interesting result evidenced by the calculation is the fact that the change of sign energy of the AHC depends on the crystalline structure as can be seen with the different curves.

We identified two phenomena from these calculations explaining the origin of the sign change of the AHE with temperature. First of all, as the sample is heated, the energy of the electrons at the Fermi level is broadened due to the thermal energy of the order of k_BT (around 15 meV for ΔT = 180 K). As the AHC is energy dependent, this broadening could lead to a change of its value and potentially a sign change depending on the strain. However, we obtained a mostly linear dependence of $\sigma_{\mathrm{AH}}^{\mathrm{int.}}$ on energy close to the Fermi level (see Fig.5.11.(b)). The contributions above and below E_F would therefore cancel out as the thermal broadening is symmetric.

The second effect is associated with the temperature dependent contraction of the layers: anisotropic lattice expansion with temperature was reported for $Cr_{1+x}Te_2$ [118], which directly affects the c/a ratio and the AHC. To illustrate this argument, two strain values close to our experimental results were chosen for the curves shown in Fig.5.11.(b). During the cooling down of the sample, the structural ratio could change from one value to the other due to contraction (this is a qualitative argument with arbitrary values). In that case, any sample with E_F in the red shaded area (with a width of 8 meV) would experience a sign change of AHC with temperature. The initial value of the Fermi level is therefore key to determine whether sign change will be observed or not. This could also explain why some samples did exhibit it and some not.

5.1.3.4 Charge transfer with 2D materials

We evidenced thanks to the Berry phase calculations that the sign of the intrinsic AHC depends both on the Fermi level position of the material as well as on the structural strain. In order to see whether charge transfer can occur in the grown heterostructures, direct calculations were carried out and the results are displayed in Fig.5.12. A positive electron transfer to Cr_2Te_3 is observed in all three cases, which is in agreement with the reduction of the holes density experimentally observed compared to the sample directly grown on sapphire (where no charge transfer is occurring). The resulting shift of the Cr_2Te_3 Fermi level compared to its bulk value is estimated by dividing the number of transferred electrons/unit cell by the density of states of bulk Cr_2Te_3 at E_{F} (in this case, 8.05 electrons/eV).

The shift of E_F is calculated to be the most significant for the growth on graphene, that, similarly to the sample on WSe_2, did not exhibit any sign change with temperature and the lowest carrier density with 1.4×10^{14} holes/cm^2 (one order of magnitude lower than other samples). Magnetotransport in this heterostructure was nevertheless harder to analyse, as already seen with the magnetoresistance.

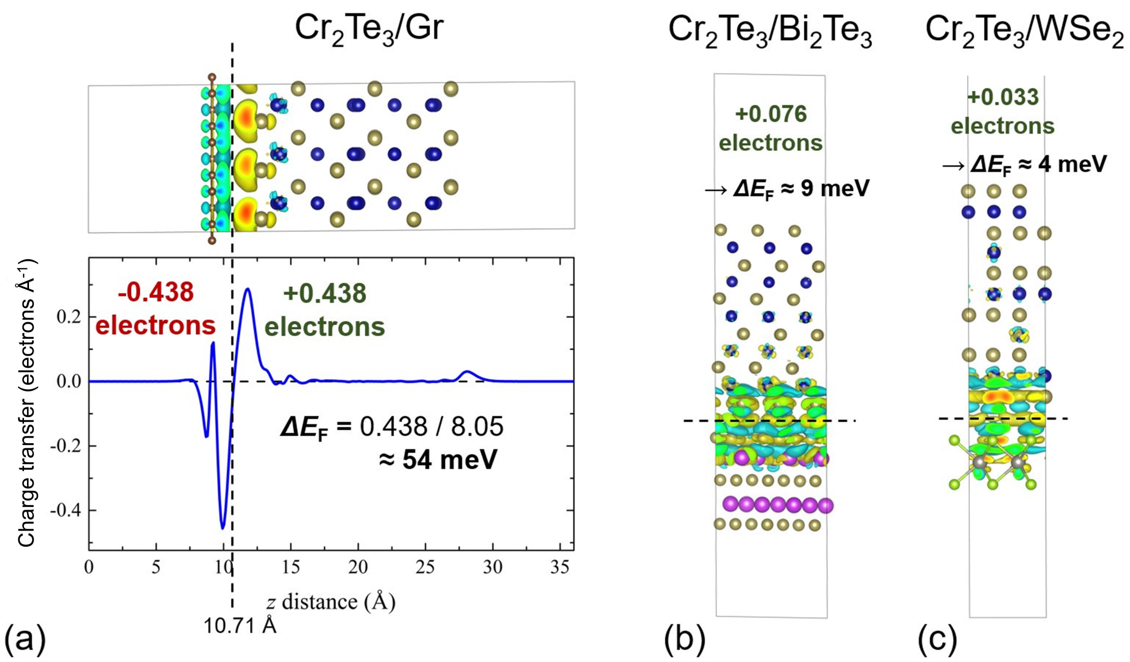

Figure 5.12: *Ab initio* calculations of charge transfer between 1.5 ML Cr_2Te_3 and (a) graphene monolayer, (b) one quintuple layer of Bi_2Te_3 and (c) one monolayer of WSe_2. Electron orbitals are pictured in the figure with the convention that yellow (blue) cloud means positive (negative) electron transfer. The associated shift of the Fermi level is indicated for each heterostructure.

5.1.4 Hall resistivity of Cr_2Te_3/graphene heterostructures

Finally, the results of the heterostructure grown on graphene/SiC are presented in Fig. 5.13, with firstly the raw data measured at 2 K in (a). The first observation is that the signal is not linear at high field as it would be for OHE with a single carrier type. In the case of several carriers with different mobilities, OHE can exhibit a non linear behaviour as shown in the reference [119]. As graphene is semimetallic, conduction occurs in both materials. This could be one origin for the several carrier types experimentally observed. By fitting the slope close to zero field, a carrier density was extracted in holes/cm^2, as presented before but this calculation might be flawed due to the presence of several carriers with different mobilities.

As presented with the magnon magnetoresistance in Fig. 5.6, two steps can be observed mimicking two AHE contributions at respectively 0.4 T and 0.9 T. The second one matches with the reversal measured by magnetic measurements, but the first one is absent from these experiments. Hysteresis loops after subtraction of the estimated OHE are shown in Fig. 5.13.(b) as a function of temperature. The two-step signal behaviour vanishes progressively when increasing the temperature and disappears around 100 K, well below the Curie temperature.

The interpretation of this effect is beyond our current understanding as we did not have time to model this system with calculations reproducing these results. It could be the signature of a hump before the coercivity caused by skyrmions, as reported in Cr_2Te_3/Bi_2Te_3 or Cr_2Te_3/Cr_2Se_3. Low temperature imaging of the magnetic structure would be required to verify this assumption as well as a measurement of the DMI at the interface between Cr_2Te_3 and graphene. Another possibility could be some induced magnetic moments in graphene by proximity with Cr_2Te_3, but our preliminary calculations seem to show that the induced magnetic moments are very weak.

To conclude on this heterostructure, further experiments and modelling are required in order to explain these original magnetotransport results. It was nevertheless shown that interfacing Cr_2Te_3 with 2D materials can affect magnetotransport, opening the way to new architectures for the future of spintronics.

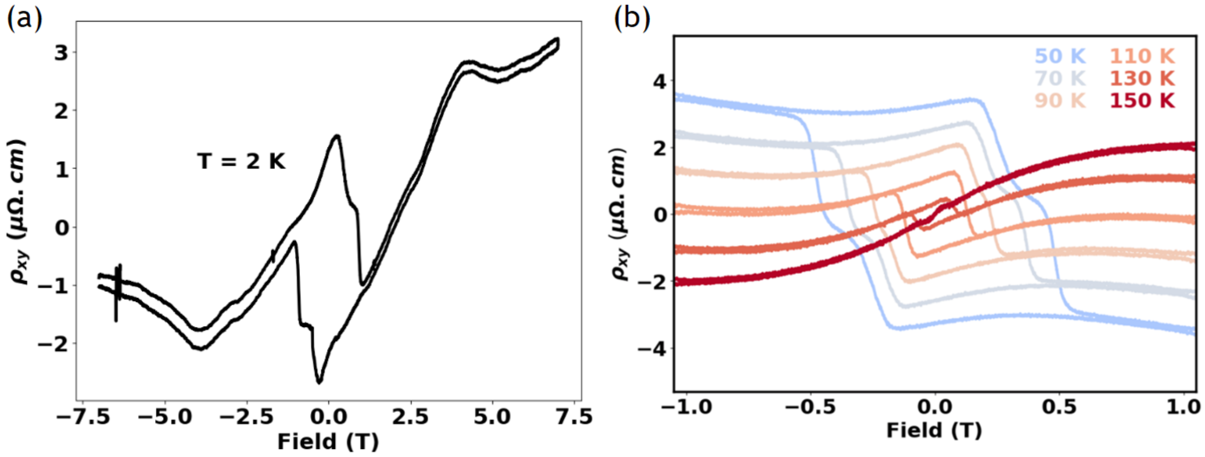

Figure 5.13: (a) Hall resistivity of 5 ML Cr_2Te_3 on graphene/SiC measured at 2 K, without any treatment of the data. (b) Temperature dependent signal after subtraction of an arbitrary slope of 4 $\mu\Omega$.cm/T for comparison with Fig. 5.7.

5.2 AC measurements

5.2.1 Geometric configuration and mathematical expression of non linear transport effects

In this section, the focus will be on non linear effects. In order to evidence and measure these effects, a sinusoidal current I = $I_0\sin(\omega$ t) was injected in the Hall bar along the x direction, with a value ranging from 500 μA to 1 mA. If we consider small variations of the resistance, we can estimate that at first order:

$$V(I) = R(I) \times I = R_0 I + R_1 I^2 + O(I^2) \tag{5.6}$$

R_0 and R_1 are Taylor expansion coefficients. If we express the result with harmonic contributions, we obtain:

$$V(I) = \frac{1}{2}R_1 I_0^2 + R_0 I_0 sin(\omega t) + \frac{1}{2}R_1 I_0^2 sin(2\omega t - \pi/2) \tag{5.7}$$

In order to evidence possible non linear effects, a lock-in amplifier is used to measure the first harmonic of the signal with a phase offset of 0° (in phase) as well as another one to record the second harmonic with a phase delay of 90°. For the rest of the section, we will use the notation for the two harmonic signals $R^{1\omega}$ = R_0 and $R^{2\omega}$ = $\frac{1}{2}R_1 I_0$.

Field-like and damping-like torques

The main effects that we are looking for with this study of non linear transport effects are the SOTs exerted on the magnetization. Indeed, when a charge current is injected in a material with large SOC such as Bi_2Te_3, a spin accumulation perpendicular to the current is induced $\delta m^{\perp} \propto z \times I$. In the presence of a magnetized layer, another accumulation occurs in the plane $\delta m^{//} \propto (z \times I) \times M$. When put into contact with a ferromagnet and because of exchange interaction, these two spin accumulations lead respectively to the field-like torque $T^{\perp} \propto M \times \delta m^{\perp}$ and the damping-like torque $T^{//} \propto M \times \delta m^{//}$. These torques as well as first harmonic measurements are shown in Fig. 5.14.

Spherical coordinates (see Fig. 5.14.(d)) are used to express the field direction. Experimentally, θ_B (direction of the external magnetic field) is varied with the rotation of the sample holder with respect to the field direction, whereas ϕ (in-plane rotation of the sample) is varied either by measuring two different devices with perpendicular orientation or by removing the sample from the cryostat and reattaching it to the PCB holder after rotation. Figures 5.14.(e-f) present the transverse resistance for two experimental

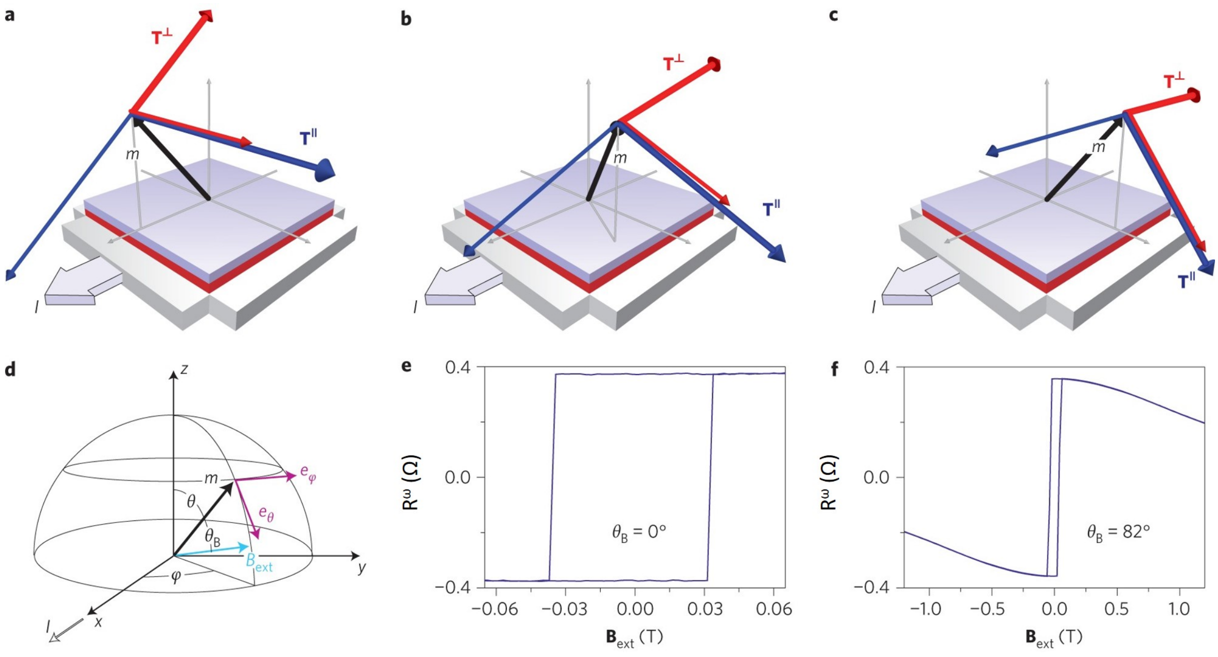

Figure 5.14: SOTs and magnetization measurements in ferromagnets/heavy metal bilayers, adapted from [120]. (a-c) Hall bar with current and magnetization direction tilted by ϕ = 0° (a), 60° (b) and 90° (c). Thick arrows indicate the SOTs ($T^{\perp}$ in red and $T^{//}$ in blue) and the thin arrows indicate the equivalent fields. (d) Coordinate system with the notations. (e-f) First harmonic measurement (proportional to M) of Co/Pt stacks as a function of magnetic field applied perpendicular to the sample θ_B = 0° (e) and almost in-plane θ_B = 82° (f).

configurations as a function of the magnetic field. When the field is along the easy-axis of magnetization, the amplitude of the AHE can be deduced from the first harmonic measurement. When the field is applied along a hard axis-direction, the ratio of the resistance with the AHE coefficient allows the deduction of the equilibrium position of the magnetization θ. SOTs are easier to measure in this configuration as the magnetization is away from the easy axis given by the magnetic anisotropy, so that spin current can lead to the precession of magnetization around its equilibrium position.

In order to deduce SOTs from the transport measurements, the transverse voltage is used as will be shown with the derived equations. The following part was adapted from the results presented in the reference [120]. In general, one has:

$$V_{xy} = R_{AHE} I cos(\theta) + R_{PHE} I sin^2(\theta) sin(2\phi) \tag{5.8}$$

Here, the OHE is neglected (it has to be removed from experimental curves). The planar Hall effect (PHE) is another Hall effect (causes a transverse voltage with respect to the injected current) that occurs for in-plane magnetized samples. Its origin is AMR but in our case, as will be shown experimentally, its amplitude will be neglected compared to the one of the AHE. We will use this fact to simplify the equations. Experimentally, SOTs cause small oscillations of the magnetization around the equilibrium position (θ_0,ϕ_0), which is determined from the Zeeman and anisotropy energy. The transverse voltage can therefore be expanded to first order with $V_{xy}(I) \approx V_{xy}(\theta_0,\phi_0) + I \frac{dV_{xy}}{dI}|_{\theta_0,\phi_0}$. After differentiation of equation 5.8 and identification with the definition of the two harmonic contributions, one obtains $\frac{dV_{xy}}{dI} = R^{\omega}_{xy} + R^{2\omega}_{xy}(I)$ where the first and second harmonic Hall resistances are given by:

$$R^{\omega}_{xy} = R_{AHE} cos(\theta_0) \tag{5.9}$$

and

$$R^{2\omega}_{xy} = I R_{AHE} \frac{dcos(\theta)}{dI}|_{\theta_0} = I R_{AHE} \frac{dcos(\theta)}{dB_{ext}} \frac{1}{sin(\theta_B - \theta_0)} b_\theta \tag{5.10}$$

We have expressed the derivative in terms of current induced effective field (associated with the SOTs) and b_θ stands for the derivative with respect to the current. Finally, after expressing these effective fields in spherical coordinates using the above equations (A, B, C and D are amplitudes):

$$B^{\perp}(\theta,\phi) = -cos\phi A e_{\phi} + cos\theta sin\phi B e_{\theta} \tag{5.11}$$

and

$$B^{//}(\theta,\phi) = cos\phi C e_{\theta} - cos\theta sin\phi D e_{\phi} \tag{5.12}$$

It appears that I $b_\theta(\phi=0°)$ = $B^{//}$ and I $b_\theta(\phi=90°)$ = $B^{\perp}$ /cos(θ). The torques can therefore be expressed from the measured signals with this equation (measured with the appropriate ϕ):

$$B^{\perp}/cos(\theta)\ or\ B^{//} = \frac{R_{xy}^{2\omega} sin(\theta_B - \theta_0)}{\frac{dRxy^{\omega}}{dB_{ext}}|_{\theta_0}} \tag{5.13}$$

Experimentally, one first derives the equilibrium angle $\theta_0(B_{ext})$ = arccos$\left|\frac{R_{xy}^{\omega}(B_{ext})}{R_{AHE}}\right|$. Then using the high field signal of the second harmonic as well as the derivative of the first harmonic (see equation 5.13), one can deduce the SOTs. Domain wall motion gives an extra contribution to the signal at low field, which is therefore disregarded for the fit of the signal.

Thermal effects

All these equations were derived by neglecting other contributions to the second harmonic voltage. However, thermal effects such as the anomalous Nernst effect (ANE) also contribute to the signal and need to be decorrelated for an appropriate determination of the SOTs. The origin of these effects is the Seebeck effect: when a temperature gradient is present in a material, charge carriers diffuse from the hot side to the cold one creating an electric field. In the presence of magnetic field, this current leads to a transverse voltage, similarly to the Hall effect. This is the Nernst effect, and in the case of a magnetized sample, the ANE is the equivalent of the AHE. The heat gradient caused by a sinusoidal current has the same temporal dependence as the current itself. However, the created transverse voltage is proportional to the product of the heat gradient and the current, and therefore contributes to the second harmonic signal, similarly to the SOTs . The expression of the created electric field by the ANE is:

$$\vec{E}_{ANE} \propto \vec{\nabla} T \times \vec{M} \tag{5.14}$$

We obtain therefore the following contributions to the magnetotransport:

$$R_{xx}^{2\omega}(ANE) \propto \nabla T_z M_y - \nabla T_y M_z \tag{5.15}$$

$$R_{xy}^{2\omega}(ANE) \propto \nabla T_x M_z - \nabla T_z M_x \tag{5.16}$$

Figure 5.15 presents the origin of heat gradients in patterned Hall bars, when a current is injected. Due to the difference of heat dissipation between vacuum (or He atmosphere) and the underlying sapphire substrate, heat accumulates at the top interface of the sample leading to a vertical heat gradient (see Fig. 5.15.(a)). Moreover, the contact with gold pads, which has a greater thermal conductivity than the layers, lead to an accumulation of heat at the centre of the Hall bar and a longitudinal thermal gradient (see Fig. 5.15.(b)). Nevertheless, the device has been designed with a symmetry such that the gradient vanishes at the centre of the Hall bar, where the transverse voltage is measured.

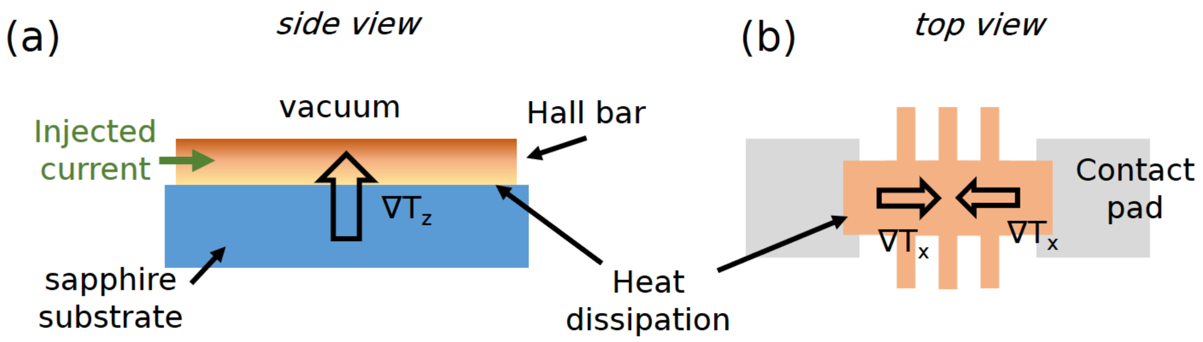

Figure 5.15: Schematic drawings of the patterned Hall bar to illustrate the origin of heat gradients. (a) Side view of the Hall bar and the substrate. The big arrow shows the vertical heat gradient. Heat dissipation is stronger at the interface with the substrate than with vacuum (or He in the sample space of the cryostat). (b) Top view, where the longitudinal heat gradients can be seen due to the heat dissipation in gold contact pads.

As presented earlier, the 2^{nd} harmonic of the transverse resistance is used to extract the SOTs. Unfortunately, both an in-plane and out-of-plane thermal gradient can be present during measurements. However, the signal induced by the longitudinal gradient is vanishing at high field for θ_B close to 90° ($M_z \rightarrow 0$). Besides, it can easily be fitted when the field is applied perpendicularly to the sample ($\theta_B = 0°$). The vertical heat gradient only contributes in the transverse resistance if M // x, *i.e.* for $\phi = 0°$. In order to subtract this contribution, the longitudinal second harmonic signal is measured for M // y ($\phi = 90°$). According to equation 5.15, the signal is proportional to the vertical heat gradient. To be able to subtract this signal to the transverse resistance, one has to use a scaling factor corresponding to the geometrical ratio of the Hall bar (length divided by width).

5.2.2 Second harmonic results of Cr_2Te_3/Bi_2Te_3 heterostructures

First of all, we investigated PHE in Cr_2Te_3 layers to verify whether the assumption to neglect it was valid. Therefore, we studied the angular dependence of the first harmonic of the transverse resistance for a sample of 5 ML Cr_2Te_3 deposited on sapphire. The measurements were carried out at T = 2 K by varying the angle of the external magnetic field in the ZY plane (*i.e.* for $\phi = 90°$), as can be seen in Fig. 5.16. In order to decorrelate AHE and PHE, one can use symmetry as the first one is odd under magnetic field inversion whereas the latter one is even. Using equation 5.8, we know that PHE depends on the angle of the magnetization with a $\sin^2(\theta)$ function.

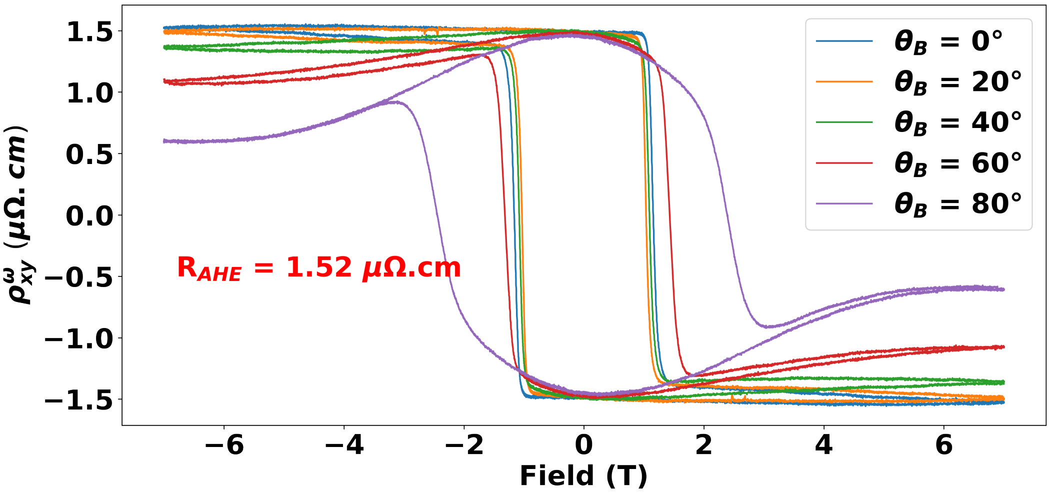

Figure 5.16: First harmonic transverse resistivity of 5 ML Cr_2Te_3 deposited on sapphire after subtraction of the OHE. The angle θ_B of the direction of the external magnetic field with respect to the normal of the sample plane is varied in the ZY plane ($\phi = 90°$). The AHE resistivity is deduced from the measurement at 0°.

In order to determine θ, we compute the arccosine of the ratio of the resistivity with R_{AHE} to obtain the equilibrium position, as shown in Fig. 5.17.(a). This formula only applies to the high field range. We observe nevertheless a stabilization of the magnetization aligned with the external field at 7 T, as expected.

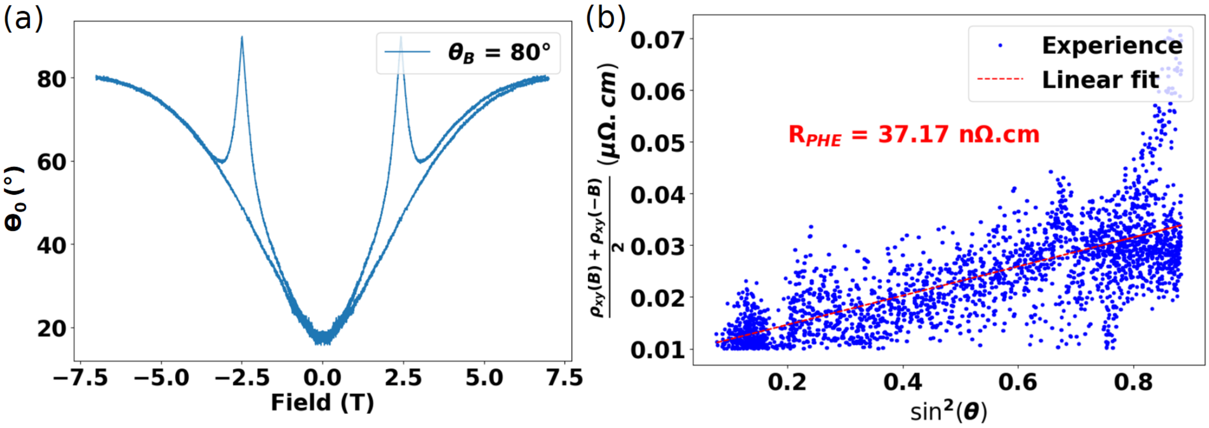

Figure 5.17: (a) Extracted equilibrium direction of the magnetization as a function of the external magnetic field. The sample is the same as in the previous figure for an external field applied with an angle of 80° from the normal of the sample. (b) Even part of the resistivity as a function of the magnetic field (PHE) for different directions of the magnetization. The extracted PHE coefficient is indicated in the figure.

This angle could be used to determine the PHE as displayed in Fig. 5.17.(b). The even part with respect to the magnetic field of the transverse resistivity is plotted as a function of $\sin^2(\theta)$. A linear trend is observed despite the contribution of the non-physical high values of θ that causes the dispersion close to $\sin^2(\theta) = 1$. A PHE resistivity of 37.17 nΩ.cm is extracted, which gives a ratio with the AHE resistivity lower than 2.5%. We assumed this ratio low enough to be able to neglect the PHE.

Figueiredo-Prestes et al. reported large values of field-like torques [90] for samples of Cr_2Te_3 grown on Bi_2Te_3. At 15 K, they extracted a value of $B^{\perp} = 115$ mT with a current density of 10^{11} A/m^2. For comparison, this is more than one order of magnitude larger than in conventional Co/Pt stacks. We carried out therefore second harmonic measurements at 10 K on samples grown on Bi_2Te_3 to try to reproduce these results. Figure 5.18 shows the measurements of the first and second harmonics of the longitudinal and transverse resistances with a rotation of the external magnetic field in the ZX plane (see the inset at the middle of the figure). This corresponds to an angle $\phi = 0°$. As explained before, the measurements were performed with the field direction perpendicular to the sample plane ($\theta_B = 0°$) to extract the AHE coefficient from $\rho_{xy}^{1\omega}$ and with a direction close to in-plane ($\theta_B = 85°$) in order to measure the SOTs. The amplitude of the second harmonic signal is indeed much stronger in the second configuration.

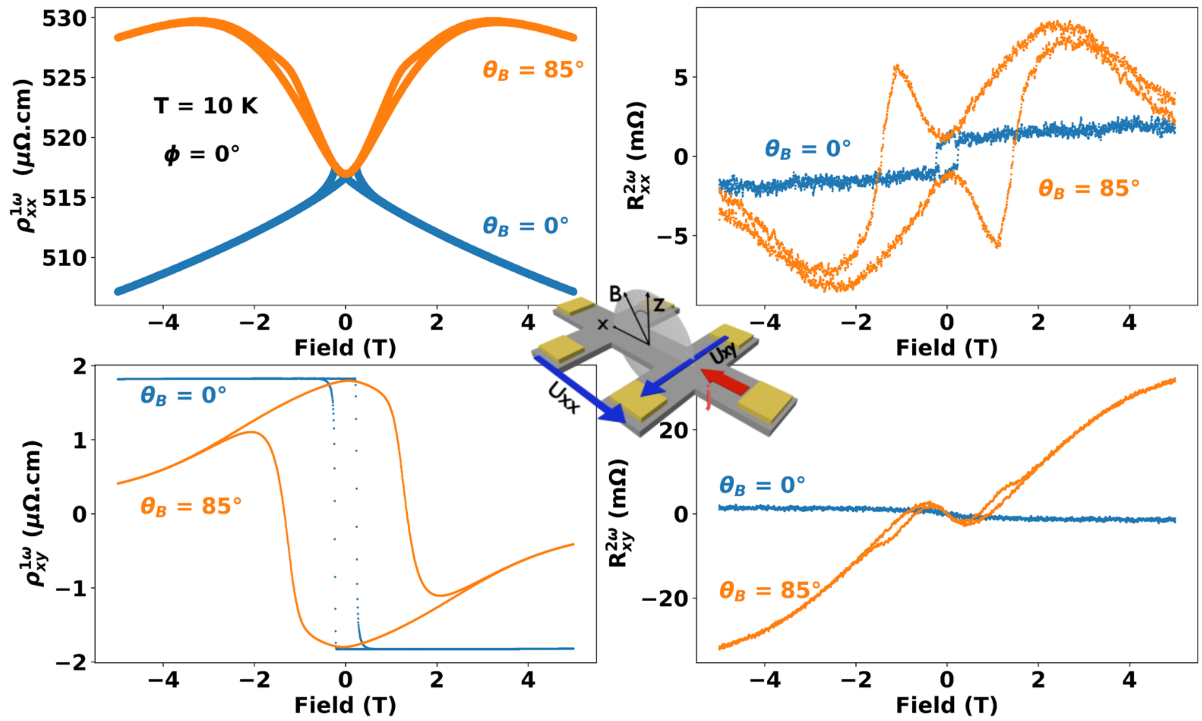

Figure 5.18: First and second harmonic measurements of 5 ML Cr_2Te_3 deposited on Bi_2Te_3/Al_2O_3. Those curves were obtained at 10 K for two different directions of the magnetic field in the ZX plane (see the inset in the middle of the figure). OHE was subtracted from $\rho_{xy}^{1\omega}$. Second harmonic results are displayed without normalization by the surface and length of the Hall bar, in mΩ.

Second harmonic measurements of the SOTs are expected to be odd with respect to the external field. The experimental signals are therefore anti-symmetrized in order to remove some spurious contributions (for example due to some small misalignment of the Hall bar during patterning). It is worth noting that in this configuration, we expected $R_{xx}^{2\omega}$ to be close to zero. Indeed, the ANE contribution to the longitudinal 2^{nd} harmonic signal is the sum (see equation 5.15) of signals proportional to M_y and ∇T_y. Both of them are supposed to be zero when $\phi = 0°$. Nevertheless, the in-plane alignment of the Hall bar with the field direction (*i.e.* ϕ) is performed by hand when the sample is attached to the PCB. This necessarily includes some error, hence the origin of a non zero M_y component. Moreover, misalignment of the Hall bar can also lead to a heat gradient // y and ANE (as can be seen from the signal at $\theta_B = 0°$). As explained, the signal of $R_{xy}^{2\omega}$ in this configuration is the sum of the damping-like torque contribution as well the signals induced by the vertical and longitudinal heat gradients.

Similar measurements were carried out on another device of the same sample rotated by 90° during the patterning process (see Fig. 5.19). Similar (but not the same due to AMR) results are obtained for 1^{st} harmonic signals, that are used again to determine the equilibrium position of the magnetization as well as the derivative of $\rho_{xy}^{1\omega}$ with respect to the magnetic field.

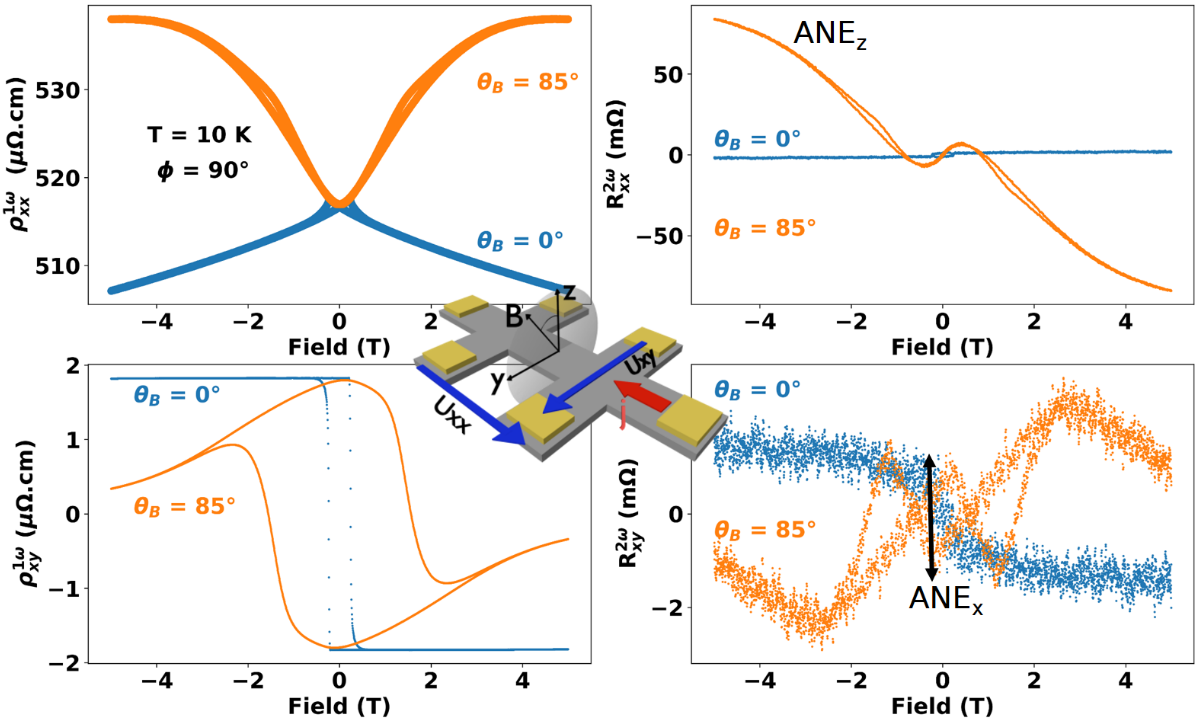

Figure 5.19: First and second harmonic measurements of 5 ML Cr_2Te_3 deposited on Bi_2Te_3/Al_2O_3. The curves were obtained at 10 K for two different directions of the magnetic field in the ZY plane (see the inset in the middle of the figure). OHE was subtracted from $\rho_{xy}^{1\omega}$. Contribution of the ANE are evidenced on the 2^{nd} harmonic measurements (the ANEx is extracted for $\theta_B = 0°$ *i.e.* the blue curve).

Upon analysis of $R_{xx}^{2\omega}$, a similar shape to the signal of $R_{xy}^{2\omega}$ at $\phi = 0°$ can be identified, with an opposite sign. The explanation lies again in the equations of the ANE. The ANE contribution due to the vertical heat gradient is present with a positive sign in $R_{xx}^{2\omega}$ when M // y ($\phi = 90°$) and a negative one in $R_{xy}^{2\omega}$ when M // x ($\phi = 0°$). The shape of this contribution as well as its amplitude can therefore be fitted from these measurements and subtracted to $R_{xy}^{2\omega}$ for $\phi = 0°$ with the appropriate geometric coefficient (ratio of the width to length of the Hall bar). From $R_{xy}^{2\omega}$ with the magnetic field perpendicular to the sample, one can extract the shape of the contribution of the longitudinal heat gradient. This signal is proportional to M_z, so that it has to be multiplied by the ratio of $\rho_{xy}^{1\omega}$ over the AHE coefficient to correct accurately the transverse resistance signals for $\theta_B = 85°$. Other effects such as unidirectional spin Hall magnetoresistance (USMR) were neglected in the analysis of these data.

5.2.3 SOTs and Nernst effects fitting

After careful fitting of the ANE as described in the previous paragraph, these contributions were subtracted to $R_{xy}^{2\omega}$ measured at $\theta_B = 85°$ for the two in-plane configurations of the sample. The results are shown in Fig. 5.20, where two areas can be identified for each curve. At low magnetic field, the signal exhibits an hysteresis, which means that the spins are not only precessing due to the SOTs (odd in magnetic field, as explained). The origin of this effect is still under debate but is usually attributed to AC domain-wall motion close to the coercivity of the material. On the other hand, at large fields, the loops are closed and the origin of the signal can be explained by the SOTs. The contribution of the domain-wall motion decays at large field because there are no more magnetic domains. Since we removed the ANE contribution, we can assume that only the torques contribute to the signal.

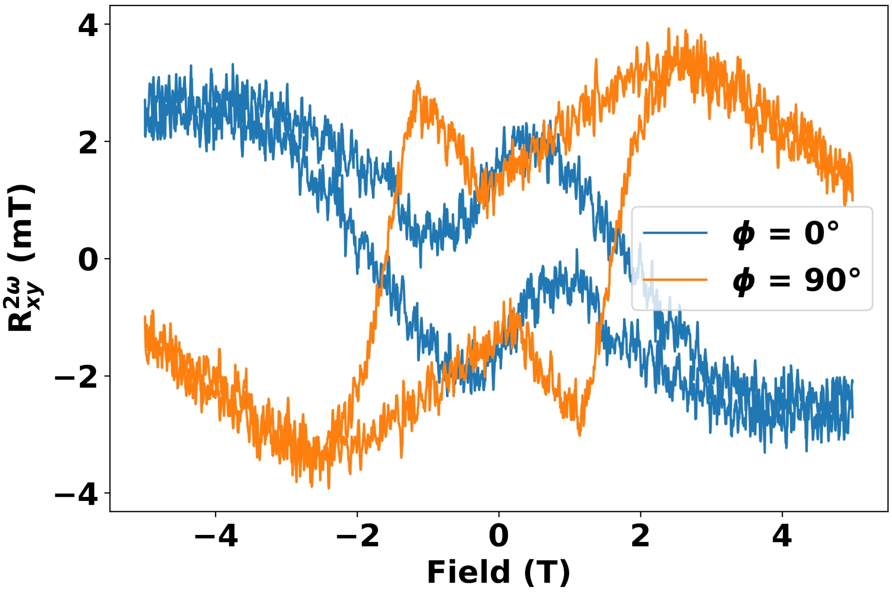

Figure 5.20: Second harmonic transverse resistance of 5 ML Cr_2Te_3 deposited on Bi_2Te_3 after subtraction of the fitted ANE contributions. The results are shown for an applied magnetic field at 85° off the normal along the x direction ($\phi = 0°$) and y direction ($\phi = 90°$).

First of all, it has to be noted that the amplitude of the signals are weak compared to the ones originally measured, which means that the contribution of the ANE is very significant in the harmonic measurements of the SOTs for this system, and their careful removal is fully necessary for extraction of the torques. Besides, for $\phi = 0°$ (M // x), a very low slope of the signal can be observed at high values of the magnetic field. This means that the damping-like torque in this system is relatively weak. On the opposite, for $\phi = 90°$ (M // y), a strong negative slope can be seen revealing much stronger field-like torque, as reported by Figueiredo-Prestes et al. [90].

The quantitative analysis of these torques is performed by plotting the signal as a function of the derivative of the 1^{st} harmonic signal and the angle of equilibrium of the magnetization (see equation 5.13). This is carried out in Fig. 5.21, where a linear fit of the data is performed to extract the SOTs. As stated above, the value of the damping-like torque is much smaller compared to the field-like. Moreover, it can be seen that the linear fit is very approximative as the data are really scattered (probably caused by the electronic noise of such weak signals). It is therefore safer to claim the value of the damping like torque is smaller than the error bars. Nevertheless, despite some dispersion of the data as well, a clear slope can be evidenced from the data at $\phi = 90°$.

The extracted amplitude of the torque (26.5 mT for a current density of 10^{11} A/m^2) is however 4 to 5 times weaker than the results reported by Figueiredo-Prestes et al. (115 mT at 15 K). The most probable

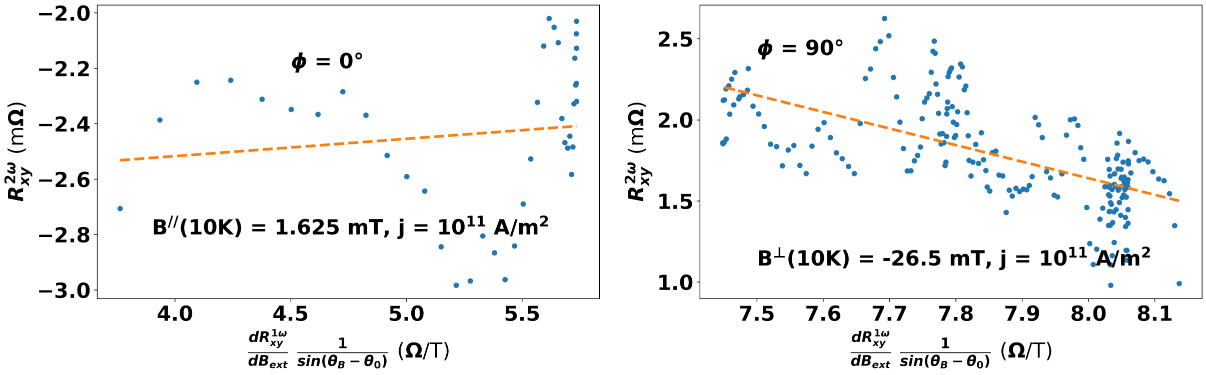

Figure 5.21: Using equation 5.13, the 2^{nd} harmonic transverse resistance (after removal of the ANE) is plotted as a function of $R_{xy}^{1\omega}$ and the equilibrium angle of the magnetization θ_0. A linear fit is performed to extract the damping-like torque ($B^{//}$) and the field-like torque ($B^{\perp}$).

cause of the difference is the degradation of the Bi_2Te_3, as presented in chapter 3, due to the annealing of the heterostructure at 400°C. This also explains the absence of damping-like torques, as ISHE is very weak in sapphire. Other samples were therefore prepared: 5 and 10 ML Cr_2Te_3 on Bi_2Te_3 without annealing as well as 5 and 10 ML Cr_2Te_3 on sapphire, annealed at 400°C followed by the deposition of Bi_2Te_3 on top. The goal was to study the thickness dependence of the SOTs as well as the role of the interfaces with Bi_2Te_3. However, for technical reasons, it was not possible to perform the SOT measurements.

To conclude this section, it was demonstrated that Cr_2Te_3/Bi_2Te_3 heterostructures hold great promises for the realisation of efficient spintronics devices. Further characterizations are however required in order to study the thickness dependent properties (torques are usually inversely proportional to the ferromagnet thickness, as this is an interface effect) as well as a more thorough analysis of the ANE in these systems, that strongly hinders the accurate determination of SOTs.

CHAPTER

6

Perspectives

In this last chapter, some preliminary results will be presented on other projects that also aim at the development of new vdW blocks for the integration in spintronics devices. First of all, some results on the epitaxy of WTe_2 that was developed in the first year of the PhD will be presented. The goal of this project was to develop Cr_2Te_3/WTe_2 heterostructures for electrical control of the magnetization. This material is a type II Weyl semimetal with topologically protected spin textures that make it an ideal candidate for the realisation of efficient 2D spin-charge interconversion devices. When brought in proximity with a 2D ferromagnet, strong DMI is predicted by the theory due to the broken inversion symmetry of the crystal structure and large SOC, which could pave the way for the nucleation of skyrmions. The large SOC in the material should also lead to efficient electrical control of the magnetization thanks to SOTs. A very brief review of the literature on this material will be presented as well as the MBE growth on graphene/SiC.

Another project that was started this year with the arrival in the group of the master student Cyriack Jego (he will also continue in the group for a PhD on the project) is the growth of $CrSnTe_3$. Similarly to $CrGeTe_3$, that was presented in the introduction, this material is predicted to be a 2D semiconducting ferromagnet with a T_C value between 100 K and 120 K. Due to its electronic nature, the application of a vertical electric field with the help of a gate voltage should allow, as was demonstrated for $CrGeTe_3$, to increase the T_C of the material, potentially up to RT. Besides, the realisation of semiconducting ferromagnets is ideal for spintronics. Indeed, as explained in this manuscript, it is preferable that the current flows in the material sourcing the spin current in heterostructures made of a magnetic material and high SOC one. If the resistivity of the magnetic material is high, a lower current density is necessary to obtain the same SOTs in the heterostructure. There are no report in the literature of MBE growth of this material, so that we did not know what to expect from the growth. Our preliminary results will be presented, both in terms of structural characterization and magnetic properties of the grown layers.

6.1 Towards heterostructures of Cr_2Te_3/WTe_2

6.1.1 Topological Weyl semimetal and spin-charge interconversion in WTe_2

As stated above, WTe_2 is a type II Weyl semimetal. Some sketches are shown in Fig. 6.1 to explain this class of material. Similarly to TIs, Weyl semimetals are topologically protected materials with large SOC. In the case of inverted bands in the electronic structure (see Fig. 6.1.(a-b)), *i.e.* when the top of the Valence band is at a higher energy than the bottom of the conduction bands, SOC can lead to an hybridization of the electronic orbitals. For TIs, this leads to the opening of a band gap with topological surface states that connect the two bands, as explained in the introduction. For Weyl semimetals, the two bands are gapless, which means that they connect at specific points called Weyl nodes. The energy dispersion around these points is linear, exactly as in the graphene band structure. What distinguISHEs a Weyl semimetal from a Dirac semimetal is the breaking of time reversal or inversion symmetry in the crystal structure. This leads to a splitting of each Dirac point in two Weyl nodes. Topological surface states called Fermi arcs connect these Weyl nodes that act as source or sink of Berry curvature.

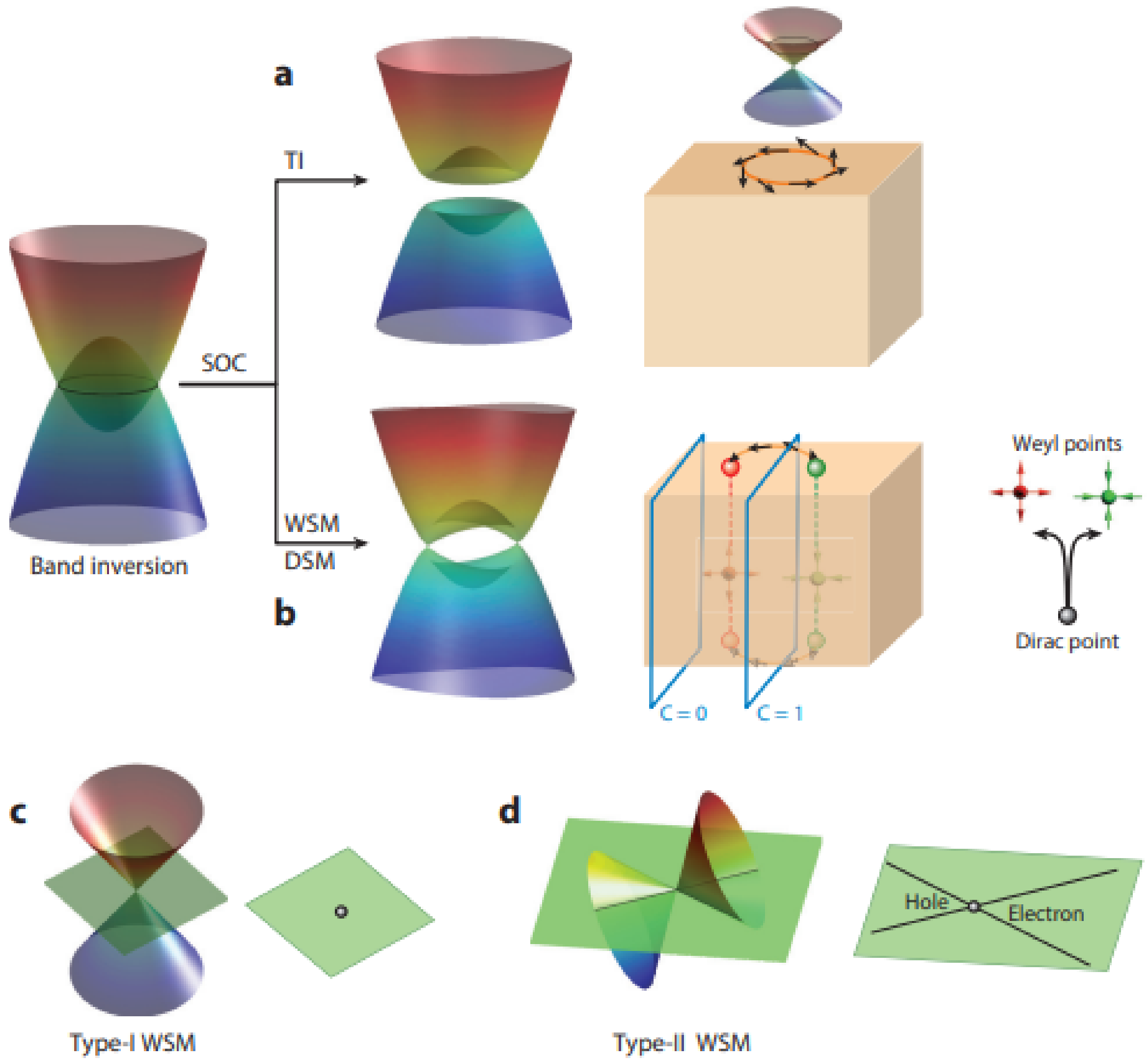

Figure 6.1: Schematic drawings of the band structures of Weyl semimetals, extracted from [121]. (a) In a TI, SOC leads to the opening of a bandgap of inverted electronic bands as well as surface states (see the introduction chapter). (b) In a Dirac or Weyl semimetal, bands cross at specific points called Dirac or Weyl nodes. Topological surface states called Fermi arcs connect these nodes. In the case of broken time-reversal or inversion symmetry, the degeneracy of Dirac points is lifted to form two Weyl nodes. (c) For a type I Weyl semimetal, all Weyl nodes are at the Fermi level with dispersion cones symmetric in energy with respect to E_F. (d) In a type II Weyl semimetal, the dispersion cones are tilted. The Weyl nodes connect electron and holes pockets in the Fermi surface.

In a type I Weyl semimetal (Fig. 6.1.(c)) such as TaAs or TaP [122], the Dirac cones axis of revolution is vertical in the band structure. The Fermi surface only consists of the Weyl nodes. On the opposite, the dispersion cones are tilted for type II Weyl semimetals (Fig. 6.1.(d)), which means that the energy of the Weyl nodes can be different than E_F. The Fermi surface crosses both the valence and conduction band, leading to holes and electrons pockets at the Fermi level as shown in the figure. This leads to interesting properties for the excitonic physics (excitons are quasiparticles composed of an electron and a hole bonded by Coulomb interaction) or for example charge compensation in WTe_2. Valentin Labracherie showed in his PhD thesis how this causes non-saturating magnetoresistance of more than 10^5 % [123] at high magnetic fields.

WTe_2 is a TMD with the particularity of having a distorted crystal structure at in his ground state, as described in Fig. 6.2. As for TMDs with a 1T structure, the top and bottom chalcogen layers are rotated by 30° with respect to each other. On top of this rotation, some W atoms are displaced with respect to their position in the honeycomb lattice resulting in an asymmetry between the x and y directions of the crystal structure. The unit cell is orthorhombic with a = 3.48 Å, b = 6.27 Å and c = 14.05 Å. One consequence of this distortion is the band inversion and the fact that WTe_2 is a type II Weyl semimetal. In the TMD family, $MoTe_2$ and WSe_2 can also be grown in the 1T' phase on appropriate substrates, even though this is not their most energetically favourable phase.

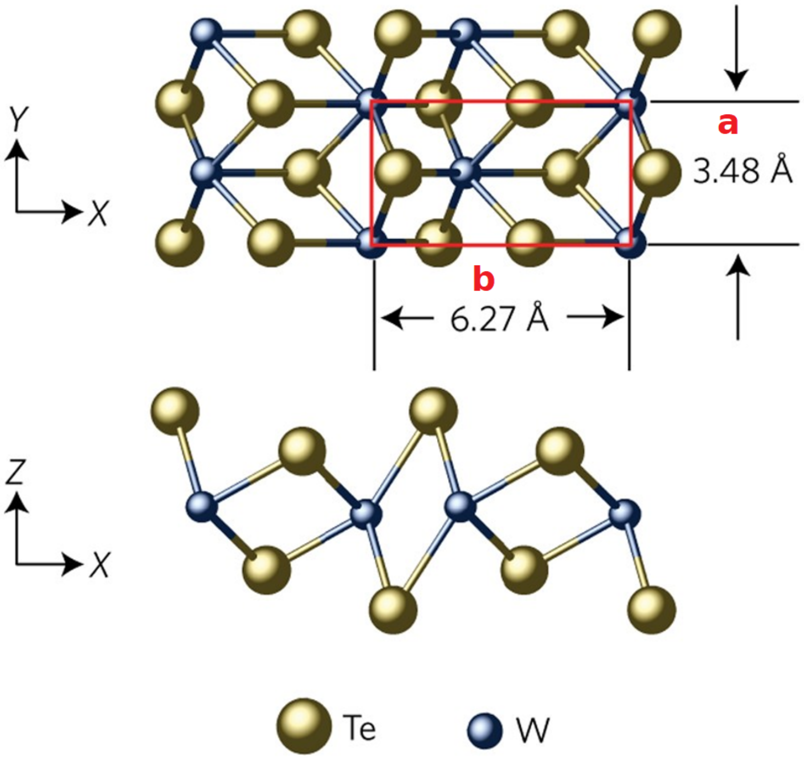

Figure 6.2: Crystal structure of 1T'-WTe_2, adapted from [124]. The two in-plane lattice periodicities are indicated on the figure.

Moreover, the thickness of the layers has an impact on the properties of the material. For one monolayer of WTe_2, Fatemi et al. showed [125] that the material behaves as a quantum spin Hall insulator (QSHI) at low temperature and that a transition to a superconducting phase could be achieved with electrical control, as presented in Fig. 6.3. A QSHI is a 2D TI, that features quantized spin Hall conductance in the absence of a magnetic field. Using a backgate voltage, the authors could tune the carrier concentration in the monolayer and measured a drop of the resistance to zero.

These phenomena are of great interest for quantum applications, but not necessarily for spintronics as these are very low temperature effects. As explained above, for bulk WTe_2, holes and electrons pockets coexist at the Fermi level, with a strong spin-momentum locking. One consequence is the very large spin Hall angle reported in this material that allows efficient spin-charge interconversion [126]. As can be seen in Fig. 6.4.(a), an electrode of WTe_2 is connected to another ferromagnetic electrode through a graphene conducting channel (this configuration is usually called a lateral spin valve). In the SHE measurement, a charge current is injected in WTe_2, that creates a transverse spin current due to the SHE that is injected

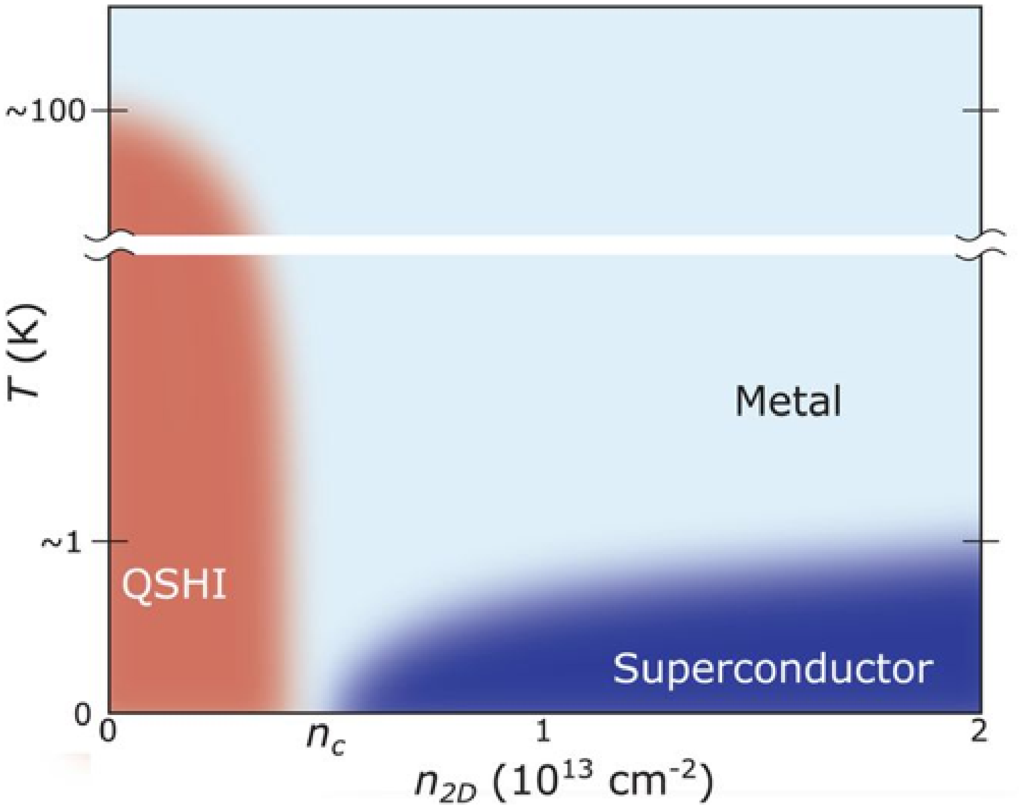

Figure 6.3: Phase diagram of monolayer WTe_2 as a function of temperature and carrier density, extracted from the reference [125]. At low temperature and carrier density, the material was found to be a quantum spin Hall insulator (2D TI). For T < 1 K and high carrier density, the resistance of the material drops to zero, which means that it becomes superconducting.

in graphene and detected with the help of the Co electrode. In the ISHE experiment, a charge current flows through the ferromagnet and is therefore spin polarized as a function of the magnetization of Co, controlled with an external magnetic field. The inverse SHE creates a charge current in WTe_2 detected as a change of the resistance (defined as the measured voltage across WTe_2 divided by the injected current). The deduced spin Hall angle is larger than 1% at RT. This demonstrates the great opportunity to use this material in spintronics especially since high quality vdW interfaces can be obtained with 2D ferromagnets.

SOTs study on Py/WTe_2 heterostructures were also performed [127] and revealed an anisotropic spin conductivity (and SOTs) in the layer plane. This effect is associated with the Fermi arcs, that are oriented along the elongated direction of the crystal structure. The topological nature of the material can thus be used to realise spin sensors, for instance.

To conclude on this short review of the opportunities offered by the type II Weyl semimetal WTe_2, the large SOC of the material as well as the topologically protected surface states allow the realisation of ultra efficient and compact spintronics devices. The realisation of large scale (all these studies were done on exfoliated flakes) and high quality WTe_2 holds therefore great opportunities.

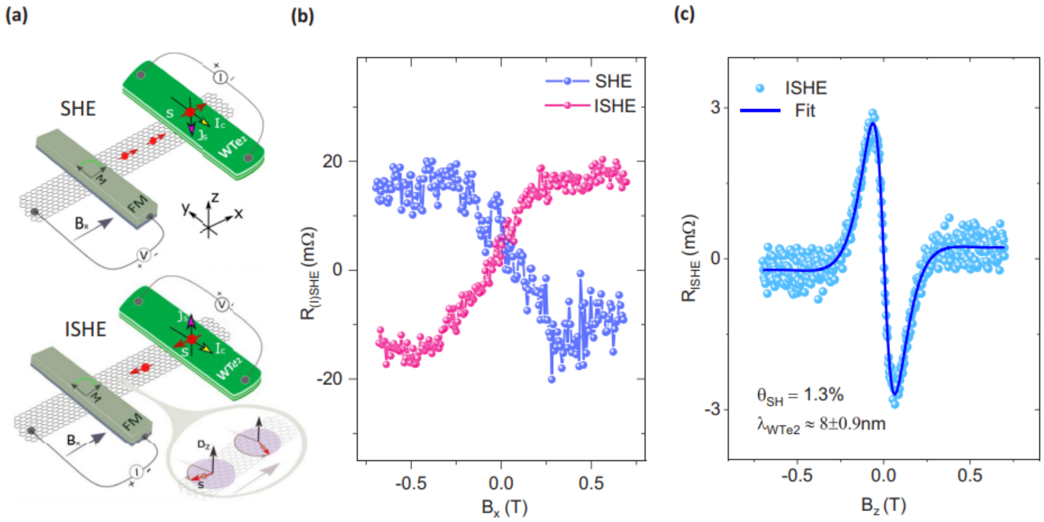

Figure 6.4: Spin-charge interconversion in few layers WTe_2, taken from the reference [126]. (a) Experimental setup for the measurement of the SHE and inverse SHE. An electrode of WTe_2 is connected to another of Co through a graphene channel. (b) The resistance induced by the SHE (ISHE) as a function of the in-plane magnetic field. (c) Precession of the spin current with a vertical magnetic field allows to measure the spin diffusion length and spin Hall angle in WTe_2.

6.1.2 MBE growth of WTe_2

The epitaxial growth of WTe_2 is a real technological challenge, because most growth techniques of this material result in Te deficient materials. During crystallization, the formation of W-W bonds can lead to the destruction of the 2D order and must be prevented. Walsh et al. [128] carried out the growth of few layers WTe_2 by MBE using vdW materials as templates for the growth (notably HOPG, Bi_2Te_3 and MoS_2). A flux ratio of several hundreds of Te for one W atom was used as well as a beam interrupted technique. The W shutter was periodically opened and closed to artificially increase the flux ratio during the growth.

We first tried to perform the epitaxial growth on the semiconducting substrates GaAs(111) and Ge(111), as can be seen in Fig. 6.5.(a-b). However, polycrystalline films were obtained as well as 3D structures (attributed to GeTe) revealed by the rings and dots in the RHEED patterns. We moved on to the growth on graphene/SiC substrates providing a large atomic mobility at its surface (atoms diffuse easily during the growth, which might favour the formation of W-Te bonds). In order to optimize the effective Te:W ratio on the surface, the substrate temperature was set as low as possible to limit the reevaporation of Te but high enough to avoid the deposition of Te chains on the surface. Due to the difficulty of stabilizing low W evaporation rates (this element radiates a lot when heated, which causes instabilities in the flux reading with the quartz microbalance), we also used the beam interrupted technique.

Figure 6.5.(c) presents RHEED patterns of close to 1 ML of WTe_2 on graphene/SiC. The first remark is that the background is not very dark, which means that the overall diffraction pattern is quite diffuse. Some amorphous layer is present on the surface and causes this degradation of the whole contrast of the image. Secondly, the buffer layer of graphene on SiC is visible (the elongated short rods forming half of a circle at the bottom of the image). This is common for the deposition of very thin films. The diffraction rods of the graphene layer are not visible any more, indicating a rather good surface coverage. Then, two families of diffraction rods can be seen, as identified by the green and yellow arrows in the figure. We attributed them to the two different periodicities of 1T'-WTe_2, as the deduced value after calibration on the graphene lattice parameter are close to the expected ones. The fact that both are visible along the same azimuth can be explained by the 6-fold symmetry of the underlying layer and therefore the coexistence of three variants rotated by 120° from each others. It could also be indicating a poor orientation of the layers

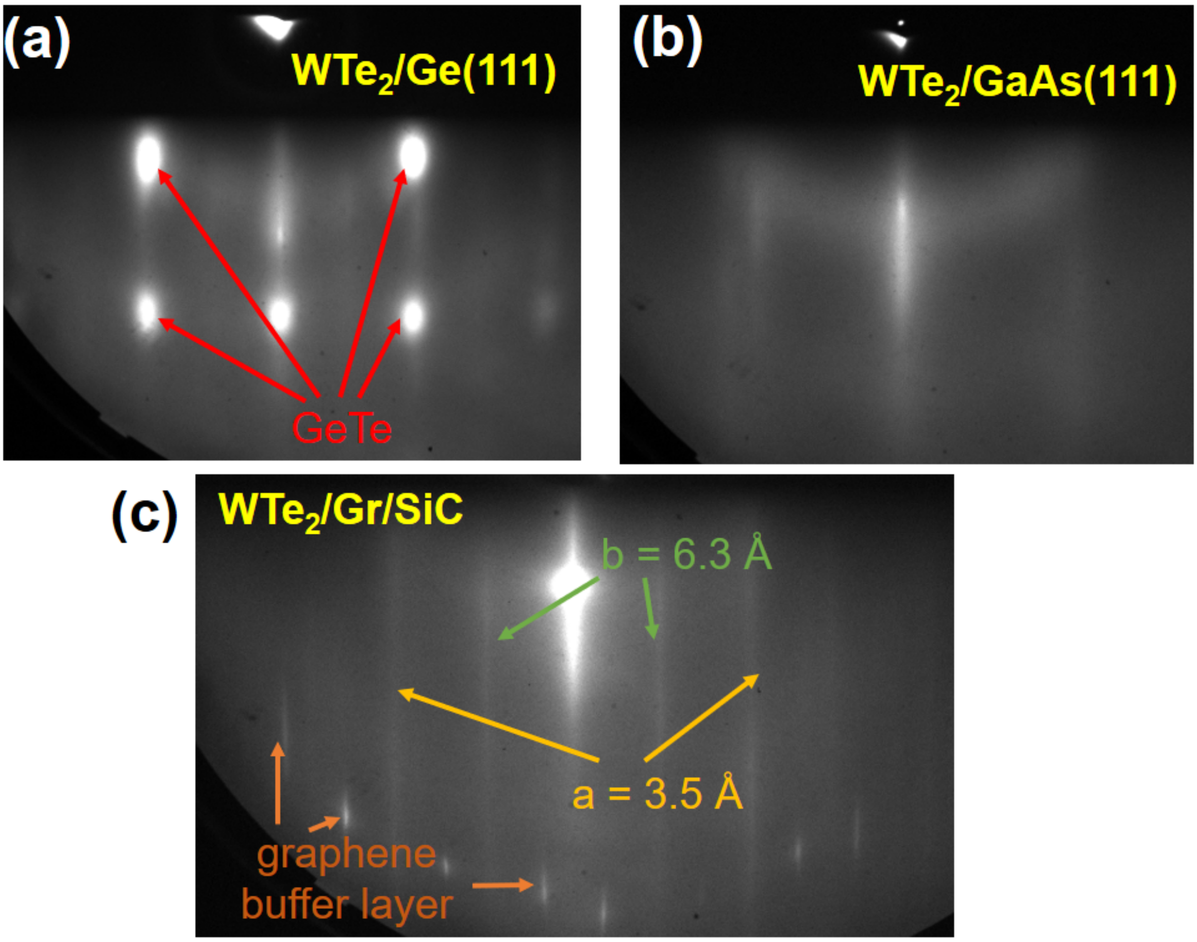

Figure 6.5: RHEED profiles of MBE grown WTe_2 layers. (a) Growth on a Ge(111) substrate, with the formation of 3D structures of GeTe. (b) Growth on a GaAs(111) substrate, with polycrystalline growth of WTe_2 grains, shown by the presence of a diffuse ring. The material is probably Te deficient, explaining the poor crystallinity. (c) Growth of 1 to 2 ML WTe_2 on graphene/SiC, with evidence of the 1T' phase.

with respect to graphene. As presented with Cr_2Te_3, this is common for the growth on graphene/SiC due to the weak vdW interaction. Finally, some faint traces of rings seem to appear on the diffraction image.

When the growth is continued to obtain several layers-thick films, these rings (similar to what can be seen in Fig. 6.5.(b)) show a stronger intensity, whereas the diffraction rods disappear. This means that the growth conditions of the homoepitaxy (growth of the material on itself) are different to the ones on graphene. The consequence was that we could not grow well crystallized samples thicker than one or two monolayers. We assumed that even higher Te:W ratio was necessary to obtain better growth conditions for the homoepitaxy, which was not experimentally accessible in our MBE setup.

In order to understand this degradation of the RHEED pattern after the growth of the first two layers, AFM measurements were performed to study the films morphology. Figure 6.6 shows the topography of the surface of a film with a nominal thickness of two layers. A good coverage of the graphene (between 80 and 90 %) can be seen, with circular shaped crystal grains. A height profile reveals the steps height of two layers. Moreover, some high crystallites are located randomly close to the centre of the WTe_2 crystal grains. These could be 3D structures of defective WTe_2, as a consequence of the bad homoepitaxy. We assumed that when the growth is continued, these grains would grow until they recover the surface.

Finally, XRD experiments were carried out on a sample capped with Te, that crystallized in chains despite its deposition at RT. As can be seen in Fig. 6.7.(a), some diffraction peaks of WTe_2 are evidenced,

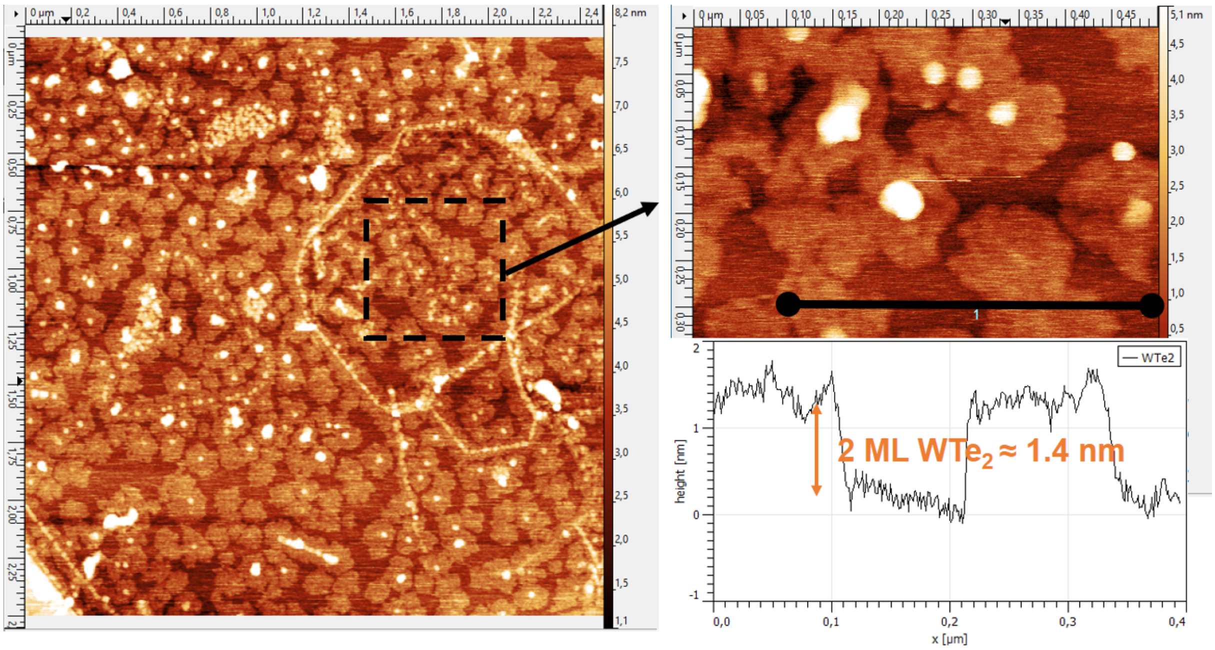

Figure 6.6: AFM images of WTe$_2$ layers deposited on graphene/SiC. The nominal thickness is 2 ML, as revealed by the line profile along the black line shown on the 500×500 nm scan.

but some match exactly with Te peaks, which hinders the interpretation of the results. The (310) and (020) peaks seem to evidence some anisotropy. Besides, Raman spectroscopy was realised (Fig. 6.7.(b)) on the same sample to look for characteristic vibrational modes of WTe$_2$. The two main peaks as identified in the reference [129], A_g^2 at 216 cm^{-1} and A_g^3 at 164 cm^{-1} , are clearly visible in the experiment.

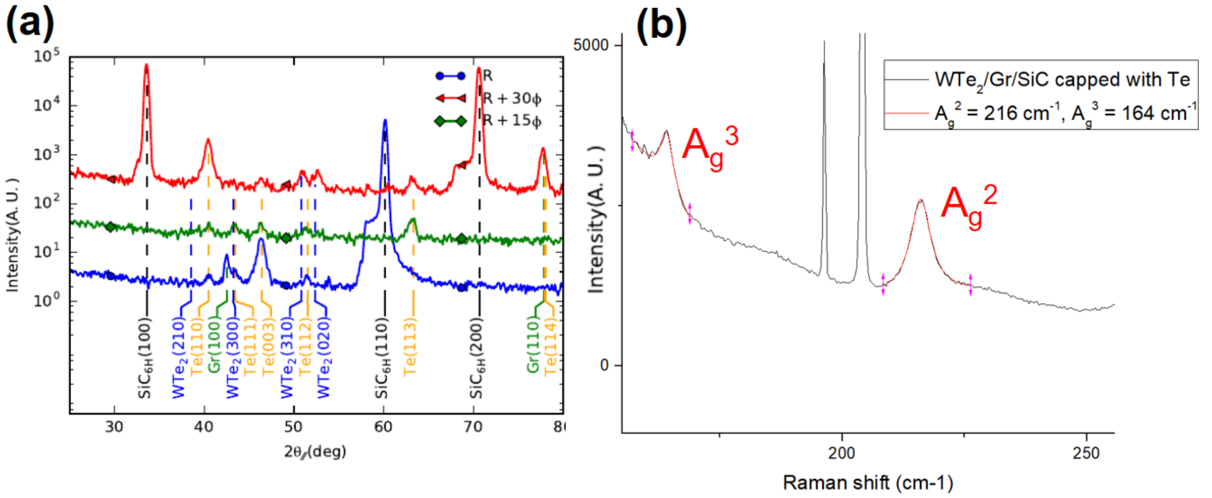

Figure 6.7: (a) XRD radial scan of 1 ML WTe$_2$ deposited on graphene/SiC. Measurements are performed along three azimuthal directions. Two of them are the graphene main crystal direction (R and R+30°) and one is 15° off for reference. (b) Raman spectroscopy of the same sample, revealing two characteristic vibrational modes of WTe$_2$.

To conclude on this study, large scale epitaxial growth of monolayer 1T'-WTe$_2$ was successfully achieved. However, experimental growth conditions for the realisation of multilayers films were not met in our lab. The growth of this material is still an experimental challenge. Another material could be investigated like 1T'-MoTe$_2$, whose growth was reported on bilayer graphene [130].

6.2 Towards Sn incorporation in Cr_2Te_3 layers

No literature review of $CrSnTe_3$ will be presented as this material has never been grown. The crystal structure as well as the electronic properties are predicted to be similar to $CrGeTe_3$, that was presented in introduction. However, another crystalline phase was obtained during the epitaxial growth, as will be revealed with XPS data. This will explain the unexpected magnetic properties that were measured.

6.2.1 MBE growth of $CrSnTe_3$

The approach we tried to follow for the determination of the optimal growth conditions of $CrSnTe_3$ was to start from the growth of Cr_2Te_3, and to gradually increase the amount of Sn in the material. A similar study was achieved for the growth of $CrGeTe_3$ [131], where they succeeded to form the targeted phase using a flux ratio of Ge:Cr = 4.2. However, in our case, it soon appeared that the SnTe compound forms during the growth, even for low Sn fluxes, for a growth at T = 300°C (usual growth temperature of Cr_2Te_3). The RHEED pattern after a growth is shown in Fig. 6.8.(a). The visible rods match well with the lattice parameter of Cr_2Te_3, and upon study with specular XRD, the dots were attributed to SnTe 3D islands.

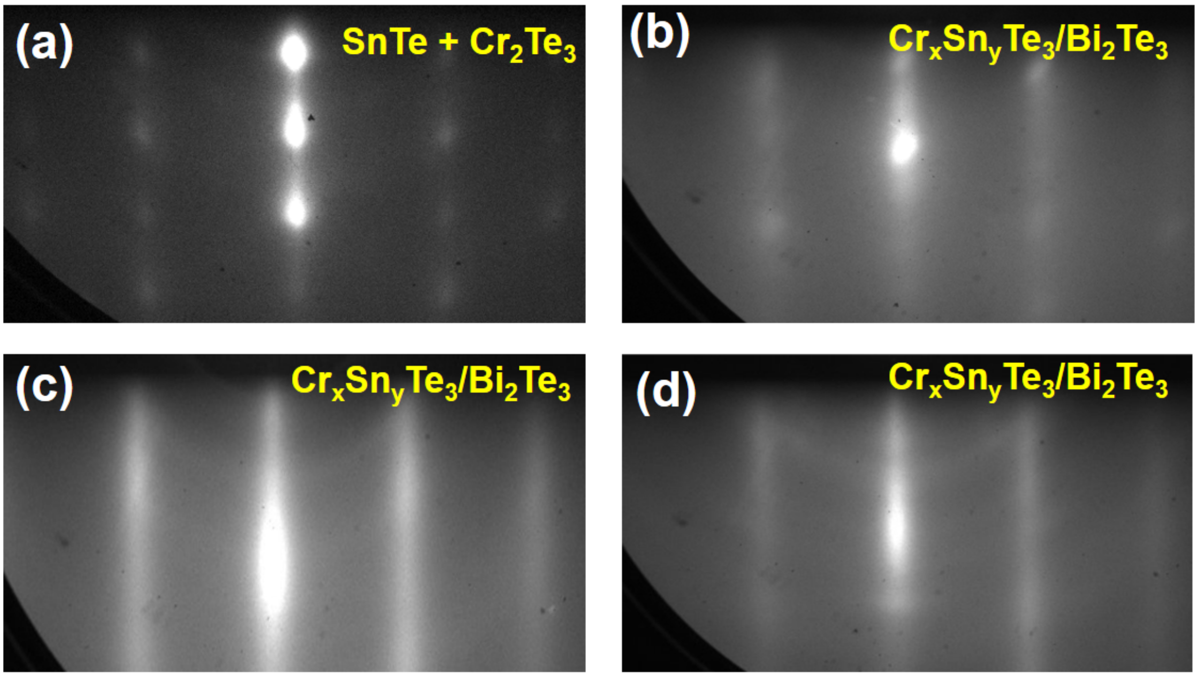

Figure 6.8: RHEED patterns of epitaxial growth with coevaporation of Cr, Sn and Te. (a) After a growth performed at 300°C, a diffraction pattern with dots is visible, revealing the presence of SnTe crystallites. (b) For a growth carried out at 180°C on 2 QL Bi_2Te_3. The pattern is slightly diffuse but diffraction rods are visible and no dots can be observed. (c) After the annealing of the film at 350°C, the diffraction pattern is improved with a reduction of the rods width as well as a better contrast. (d) After the repetition of the steps in (b-c) 3 times in order to obtain a film thickness close to 7.5 nm. The image is more diffuse but the diffraction rods can still be identified.

In order to avoid the formation of this compound, another growth was performed on a buffer layer of 2 quintuple layers (QL) of Bi_2Te_3. The growth temperature was set at 180°C with a flux ratio close to Sn:Cr = 0.5. When a higher Sn flux was used, the systematic formation of SnTe was observed. Figure 6.8.(b) presents the RHEED patterns obtained after the deposition of 2.5 nm of $Cr_xSn_yTe_3$. The phase grown by MBE is not $CrSnTe_3$, as will be shown just after, and is therefore indicated with unknown stoichiometry. For the growth of thicker films, the RHEED pattern was more and more diffuse until the point, where we could not recover a good surface after annealing. For this reason, we alternated growth steps of 2.5 nm of the material at 180°C and annealing steps at 350°C (see Fig. 6.8.(c)). A sample of 7.5 nm thickness (after

3 cycles) can be observed in Fig. 6.8.(d). Faint traces of rings start to appear but the diffractions rods of the material are still clearly visible. A capping layer of 3 nm Al was then deposited on the sample below 50°C in order to prevent any oxidation when transferred in air.

6.2.2 Structural characterization of $Cr_xSn_yTe_3$

After the growth presented above, we performed simple electrical measurements on the sample to study the nature of the film. We measured a resistivity in the same order of magnitude as Cr_2Te_3, with an increasing value with temperature. This means that the grown sample was metallic and not semiconducting as targeted, and that the obtained phase is not $CrSnTe_3$. In order to identify the crystalline phase, XRD measurements were carried out. An in-plane lattice parameter a = 6.859 Å was found, as well as an out-of-plane lattice parameter c = 12.36 Å. For comparison, bulk Cr_2Te_3 has a structure with a = 6.812 Å and c = 12.07 Å. The values are relatively close, with approximately 1% strain, suggesting a crystal structure close to the one of Cr_2Te_3.

To obtain the composition of the film, XPS measurements were performed by by Nicolas Gauthier at the Nanocharacterization Platform (PFNC) of the CEA , as displayed in Fig. 6.9.(a). Thanks to well calibrated cross sections of the different elements, the stoichiometry was deduced (Fig. 6.9.(b)), with the assumption of a stoichiometric deposition of Bi_2Te_3. The amount of Te is separated in two values, as can be in seen in the figure. The first part is attributed to the Bi_2Te_3 layer and the second one to $Cr_xSn_yTe_3$. The first observation one can make, is that the ratio between Cr and Te remains very close to 2:3, despite the incorporation of Sn, as evidenced by the blue dashed ellipse. Finally, a Sn:Cr ratio of 0.2 is measured.

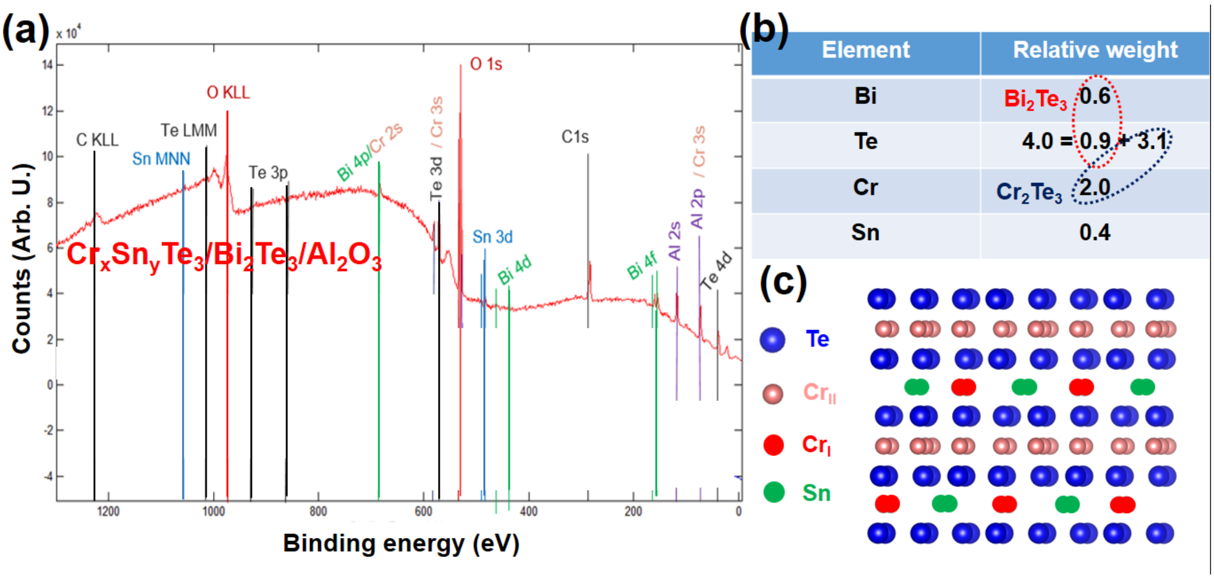

Figure 6.9: (a) XPS broadband spectrum of an heterostructure of $Cr_xSn_yTe_3/Bi_2Te_3$ deposited on sapphire. C, Sn, Te, O, Bi, Cr and Al are evidenced in this sample. (b) Using the cross section of each element, a relative weight (in %) was attributed to each element. Te is split into two layers: one part in Bi_2Te_3, as evidenced by the red dashed ellipse and one in $Cr_xSn_yTe_3$, as shown with the blue one. (c) Proposed crystal structure for $Cr_2Sn_{0.4}Te_3$, based on Cr_2Te_3. Sn atoms lie in the unoccupied sites of the Cr intercalated planes.

Based on this experiment, we assumed the sample to be $Cr_2Sn_{0.4}Te_3$ with a crystal structure shown in Fig. 6.9.(c). Blue and red atoms (respectively Te and Cr) occupy the same position (if strain is ignored) as in Cr_2Te_3, and green (Sn) atoms fill the unoccupied sites of the Cr intercalated planes. Cross-section TEM will be performed to verify this hypothesis, but the results are not yet available to confirm this assumption.

6.2.3 Magnetic properties of $Cr_2Sn_{0.4}Te_3$

Finally, the magnetic properties of the layers were investigated. As can be seen with the remanent magnetization curve in Fig. 6.10, a T_C very close to RT is extracted from this sample. It appears that the extra Sn atoms change the exchange interaction in the material and allow an increase of the ordering temperature of close to 100 K.

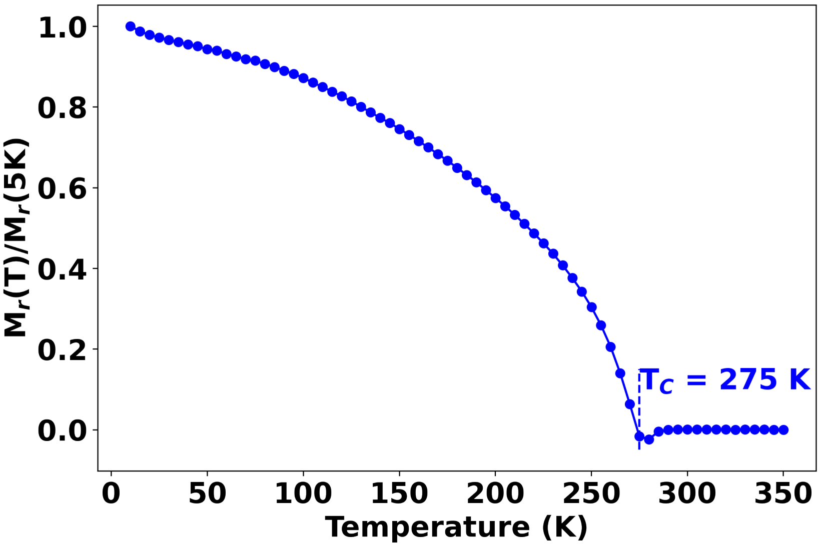

Figure 6.10: Remanent magnetization curve of $Cr_2Sn_{0.4}Te_3$ deposited on 2 QL Bi_2Te_3. The sample was measured without external field after magnetic saturation in-plane at 3 T.

We confirmed this measurement by recording magnetic hysteresis loops with an applied field parallel to the sample planes (Fig. 6.11). Clear hysteresis loops are visible until 280 K. Unfortunately, no XMCD measurement on the Sn edge could be performed to investigate the magnetic moment of Sn atoms.

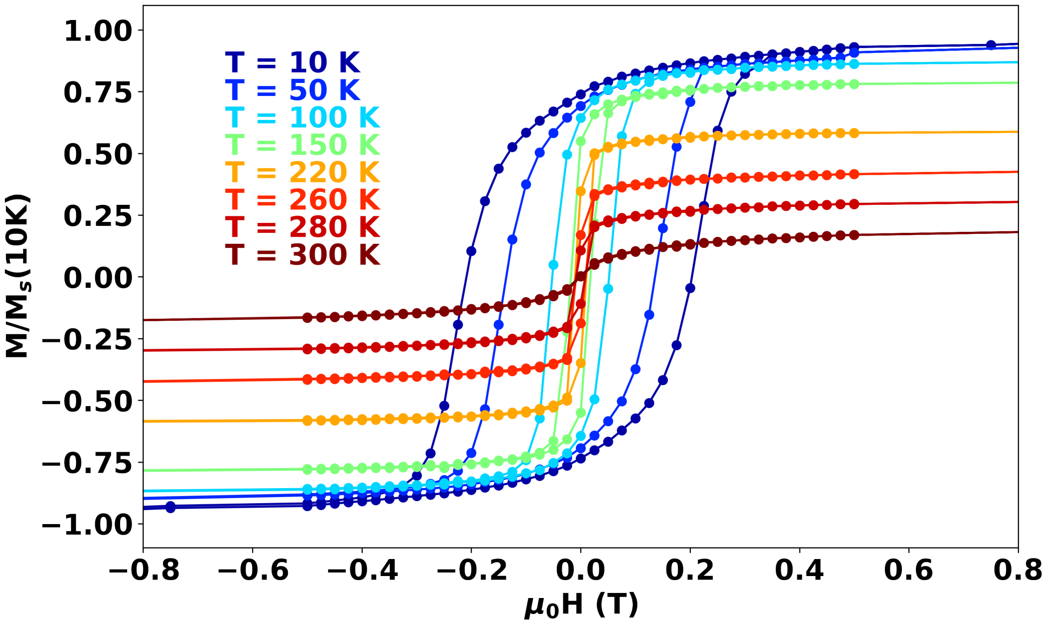

Figure 6.11: Hysteresis loops of $Cr_2Sn_{0.4}Te_3$ as a function of temperature. The magnetic field is applied in-plane. M_s(10K) was measured to be 443 kA/m.

The saturation magnetization at 10 K (M_s(10K)) is 443 kA/m, which is 10 to 20% larger than the values reported for Cr_2Te_3 (see chapter 4). As for annealed Cr_2Te_3 at temperatures higher than 450°C (chapter 5), the presence of Sn in the intercalated Cr planes could lead to a change of the non-collinear spin textures of the material and hence its magnetization. Besides, a change of the magnetic anisotropy was evidenced, as can be seen in Fig. 6.12. The sample shows an in-plane easy axis of magnetization with an effective MAE of 0.073 MJ/m^3. It has to be noted that this value is smaller than the contribution of the shape anisotropy $\frac{1}{2}\mu_0 M_s^2 = 0.123$ MJ/m^3. This indicates that the magnetocrystalline anisotropy of the material is perpendicular to the sample plane, as for Cr_2Te_3.

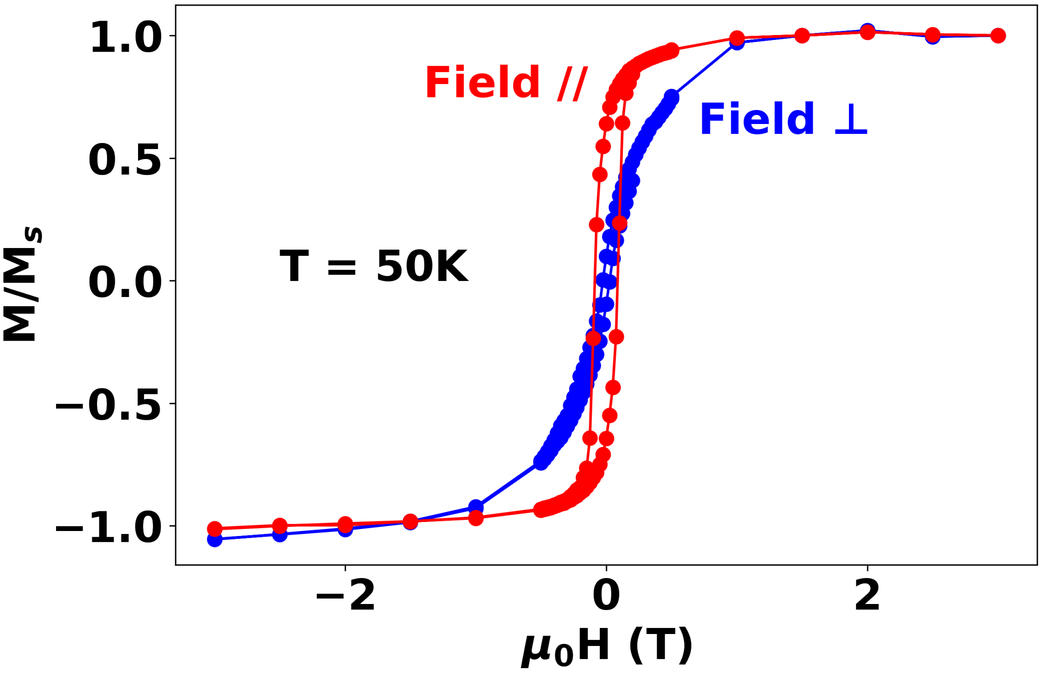

Figure 6.12: Hysteresis loops of $Cr_2Sn_{0.4}Te_3$ measured at 50 K with in-plane (red curve) and out-of-plane (blue curve) applied magnetic field.

To conclude on this study, we could not perform the growth by MBE of the $CrSnTe_3$ phase. Nevertheless, Sn was successfully incorporated in Cr_2Te_3 with an increase of the T_C of 100 K. This is very promising as this opens the way to RT measurements, which are crucial for potential applications. A change of the effective anisotropy from out-of-plane to in-plane was evidenced, but the sample conserved an out-of-plane magnetocrystalline contribution. Growing thicker samples could allow to obtain films with PMA. Sn intercalation is therefore an alternative way to post-growth annealing in order to tune the magnetic properties of Cr_2Te_3.

Conclusion

This manuscript presented our work focused on the development of new vdW heterostructures for spintronics. I could rely on the long experience in the group of the molecular beam epitaxy technique as well as the experience on 2D materials growth that is carried out for close to 10 years in our lab. Since the discovery of ferromagnetism in the 2D limit in the year 2017, intense research has been carried out to obtain new fully vdW heterostructures with the goal of using this magnetic ordering for spin detection (sensors) or spin storage (memories). However, most reported works on 2D ferromagnets are still performed with exfoliated flakes, that cannot be used for potential applications, or performed at cryogenic temperatures. This PhD was therefore aiming at the realisation of new large scale vdW heterostructures based on Cr_2Te_3 as well as tuning their properties in order to address spintronics current technological issues.

In the third chapter, the epitaxial growth of Cr_2Te_3 was detailed on three different 2D materials. Graphene (obtained by the graphitization of SiC) is a semimetal with extraordinary mobility and a unique electronic band structure. WSe_2 is a TMD semiconductor with intense photoluminescence in the monolayer form. Bi_2Te_3 is a 3D TI with topologically protected surface states and very large spin-charge interconversion thanks to strong SOC. Cr_2Te_3 was shown to form sharp interfaces separated by a vdW gap with these layered materials and the crystal structure of the material was fully relaxed for 5 unit cell thick films despite the huge lattice mismatch. The energy given to the system during growth, in the form of the sample temperature, was determined as the driving factor to control the structure of the ferromagnet. T_C close to the bulk value of 180 K was extracted from SQUID magnetometry measurements and a correlation between the MAE and the crystal structure was found experimentally and confirmed with *ab initio* calculations.

The fourth chapter was focused on an annealing study of thin Cr_2Te_3 films grown on graphene/SiC. Samples were heated for 10 min under Te flux at temperatures ranging from 450°C to 700°C. Little lattice parameter variation was observed until 650°C until the degradation and evaporation of most of the Te at 700°C. The width of diffraction peaks was found lowest for T_A close to 550°C and the mosaic spread decreasing with T_A. RBS measurements revealed an increase of the relative Cr amount starting at T_A = 500°C with respect to Cr_2Te_3. An associated increase of the T_C up to 250 K as well as changes of the magnetic anisotropy were evidenced with XMCD experiments at the Soleil synchrotron. Unlike a previous study on thicker films grown on sapphire, no gradual evolution of the T_C was though observed.

Electrical measurements on Cr_2Te_3 based heterostructures were presented in the fifth chapter. Hall bars were processed in a clean room environment in order to measure longitudinal and transverse resistivities. The metallic nature of Cr_2Te_3 was revealed as well as magnons related effects below T_C. Typical AMR for a metallic ferromagnet was observed in the longitudinal resistivity measurements and the electrical conduction in the two materials was shown for samples grown on graphene/SiC. The preservation of the intrinsic properties of the 2D material proved again the high quality interface of the heterostructures. Transverse resistivity measurements revealed a sign change of the AHE with temperature for Cr_2Te_3

on sapphire but not graphene and WSe_2. Using band structure calculations, the Berry phase change induced by thermal contraction was evidenced as a mechanism leading to the sign change of the instrinsic AHC. Charge transfer with 2D materials was also shown to affect this picture as the initial position of the Fermi level determines whether a sign change will be measured below T_C. Finally, harmonic measurements of Cr_2Te_3/Bi_2Te_3 heterostructures (after the thermal evaporation of Bi_2Te_3) investigated potential SOTs and the possibility to control electrically the magnetization of the ferromagnet. Strong ANE was evidenced, leading to a complex interpretation of the experimental data. After appropriate corrections, strong field-like torque was revealed but very weak damping-like that would allow to reverse the magnetization with current pulses.

Finally, preliminary results of MBE growth of a new class of material were presented. The type II Weyl semimetals have exotic spin textures that can be used for very efficient spin-charge interconversion. This could open the way to the realisation of ultra-thin heterostructures (potentially 1 ML ferromagnet on 1 ML Weyl semimetal) with low current consumption for magnetic sensors or memories. Unfortunately, MBE growth of 1T'-WTe_2 remains a technological challenge that was only partially addressed, as the growth was limited to one or two layers on a single substrate. Besides, another way to tune the properties of Cr_2Te_3 was presented with the incorporation of Sn. An increase of the T_C of 100 K was reported, bringing T_C close to room temperature with a conservation of the perpendicular magnetocrystalline anisotropy.

Glossary

T_C The Curie temperature of a ferromagnetic material is the ordering temperature under which magnetic moments in the material start to spontaneously align with each others. iv, 1, 2, 10, 18–24, 37, 51, 62, 74, 76–80, 86, 91, 92, 95, 100, 102, 115, 124–127

2D Two-dimensional crystal only exhibit in-plane covalent bonds. They can be elemental layers of layered systems. 1, 3

AFM Atomic force microscopy is a technique to measure the topography of a surface. It can be used to measure atomic steps or to estimate the roughness of a surface. 46

AMR Anisotropic magnetoresistance effect states that the resistivity of a magnetic material depends on the relative direction of applied magnetic field and injected current. 96

ANE The anomalous Nernst effect is a thermal effect in magnetotransport originating from the Seebeck effect in ferromagnets. A heat gradient causes an electric field that can lead to a transverse voltage in case of a perpendicular applied field (regular Nernst effect) or in a magnetized sample (ANE), similarly to AHE. 109

bcc Body centred cubic is a Bravais lattice where the base is reproduced along the corners of a cube as well as at its centre. 3, 4

BZ The first Brillouin Zone is the primitive cell of a Bravais lattice in the reciprocal space. High-symmetry points are usually highlighted. 7

CVD Chemical vapour deposition is a crystal growth technique using gases in a reaction chamber and a heating adsorption surface. A precursor gas is used to catalyse the reaction. Thin films can be grown with large crystal grain size. 12

DFT Density-functional theory is a computational modelling method to compute in a quantitative manner electronic structures with the laws of quantum physics. 69

DMI Dzyaloshinskii-Moriya interaction is an antisymmetric contribution to classical magnetic exchange interaction. It favours canting of the spin and is proportional to the cross product of two neighbouring spins. 38

E_F The Fermi level of a crystal is the energy limit, at 0 K, of the occupied states in the band structure. 104

eV The electronvolt is an energy unit. 1 eV $\approx 1.6*10^{-19}$ J. 8

fcc Face centred cubic is a Bravais lattice where the base is reproduced along the corners of a cube as well as at its faces' centre. 3, 4

FIB Focused ion beam is a technique to prepare very thin (in the order of a few μm) lamella for cross sectional imaging with STEM. 48

FWHM The full width at half maximum of peak is the width of the peak at half intensity of its maximum.. 44, 67

HAADF High-angle annular dark field is a STEM technique to obtain an atomic number contrast when imaging atomic structures. 48

LEED Low-energy electron diffraction is a diffraction technique to image the structure of the grown crystals. When varying the kinetic energy of the diffracting electron, some interference will create diffraction spots on a screen as function of the crystal structure. 12

MAE The magnetic anisotropy energy of magnetic material is the sum of the contribution of the shape anisotropy and magnetocrystalline anisotropy. 74

MBE Molecular beam epitaxy stands for a crystal growth technique or setup. 1, 24, 39

ML A monolayer is a single layer of atoms or molecules. For 2D materials, due to the vdW gap between layers, samples of few layers are usually described as samples of few monolayers. 1, 86

MOKE Magneto-optical Kerr effect is the modification of a light polarization after reflection on a magnetic material. For linearly polarized light, the change in the angle of the light polarization as well as the ellipticity is proportional to the magnetic moment of the reflection layer. However, this effect does not give direct quantitative information on the amplitude of the magnetic moment. 20, 50

MRAM A magnetic random-access memory is storing information based on the difference of two resistive states due to the giant magnetoresistance effect.. 33

MTJ A magnetic tunnel junction is a stack of two ferromagnets separated by a tunnel barrier used in MRAMs.. 33

PHE The planar Hall effect causes a transverse voltage to the applied current, as other Hall effects. It occurs in ferromagnets with in-plane magnetization and is related to a change of the AMR. 107

PMA A magnetic layer that exhibits perpendicular magnetic anisotropy has an easy axis of magnetization perpendicular to the layer plane. 1, 15, 17, 21, 58

RBS Rutherford backscattering spectrometry is a measurement technique to probe the chemical composition of a material.High-energy (in MeV) He^{2+} ions are directed on a sample and the backscattered ones are measured at a given angle. 12, 39, 49, 84

RHEED Reflective high-energy electron diffraction is a technique used in MBE chambers to control in-situ the morphology and structure of the surface of grown crystals. It images the in plane reciprocal space of a crystal by recording the truncation rods of the diffraction peaks of the first atomic planes (the electron beam is very grazing). 43

RT Room temperature usually stands for 293K i.e. 20°C. 1, 8

SOC Spin-orbit coupling in quantum mechanics refers to the interaction for a particle between its spin and its momentum. 9, 15

SOT A spin-orbit torque is a torque exerted on a magnetic layer by injecting electric current in a material with spin-orbit coupling. This material will generate thanks to spin-to-charge conversion a spin-current that will exert a torque on the magnetization. 31

SQUID A superconducting quantum interference device is a magnetometer using the dipolar field of magnetic materials to measure their magnetization. 42

STEM Scanning transmission electron microscopy allows imaging with a resolution to the atomic level. Distinction between different elements is possible using high-angle annular dark field (HAADF) technique. 39, 48

STT A spin transfer torque is a torque exerted on a magnetic layer by injecting spin-polarized current (or pure spin current) along a different axis than the magnetization of the magnetic layer. 31

TEY Total electron yield is a technique based on the voltage created by cascading electrons and used to probe XAS. 53, 89

TI A topological insulator is a material that has bulk insulating electric properties but also topologically protected edge or surface states inside its band gap. 1, 29

TMD A transition metal dichalcogenides material is a 2D crystal formed from a stack of trilayers: one layer of a transition metal (Cr, W, Mo, etc.) between two layers of a chalcogen (S, Se, Te). 1, 5, 8

UHV Ultra-high vacuum stands for pressure levels below 10^{-8} mbar. Typical pressure of operation of an MBE chamber is around 10^{-10} mbar. 39, 40

vdW Van der Waals interaction is a weak electrostatic attractive force, which decays very fast with the distance between the two atoms or molecules. 1, 5

XAS X-ray absorption spectroscopy is a technique to investigate th absorption of photons by elements in a material, revealing transitions between occupied and unoccupied electronic states. It yields information about the chemical environment of the element and can be used to perform XMCD measurements. 54

XMCD X-ray magnetic circular dichroism spectroscopy refers to a magnetic measurement technique. XAS is measured for incident light with circular left and right polarization. The difference of absorption is indicating an imbalance at the Fermi level of spin up and down population, which can be traced back to the magnetic moment of a material. This technique is element sensitive. 22

XPS X-ray photoelectron spectroscopy is a chemical analysis technique. X-rays are shined on a sample and cause the emission of photoelectrons, whose energy spectrum reveals elements that are present as well as some information on the bonds they form with others. 12, 13, 65

XRD X-ray diffraction is a technique to map the reciprocal space of a stack of crystals. The obtained information allow to deduce the crystal structure as well as information on the grain size of a grown material and its orientation with respect to its substrate. 39

Bibliography

1. Mahan, G. D. *Crystal | Definition, Types, Structure, & Facts | Britannica* `https://www.britannica.com/science/crystal` (2023).
2. Girvin, S. M. & Yang, K. *Modern Condensed Matter Physics* (Cambridge University Press, 2019).
3. Geim, A. K. & Grigorieva, I. V. Van der Waals heterostructures. *Nature* **499,** 419–425 (2013).
4. Prasad, S. V. S., Mishra, R. K., Gupta, S., Prasad, S. B. & Singh, S. *Introduction, History, and Origin of Two Dimensional (2D) Materials* (eds Singh, S., Verma, K. & Prakash, C.) 1–9 (Springer, 2021).
5. Novoselov, K. S., Geim, A. K., Morozov, S. V., Jiang, D., Zhang, Y., Dubonos, S. V., Grigorieva, I. V. & Firsov, A. A. Electric Field Effect in Atomically Thin Carbon Films. *Science* **306,** 666–669 (2004).
6. Bundy, F. P. Pressure-temperature phase diagram of elemental carbon. *Physica A: Statistical Mechanics and its Applications* **156,** 169–178 (1989).
7. Partoens, B. & Peeters, F. M. From graphene to graphite: Electronic structure around the K point. *Physical Review B* **74,** 075404 (2006).
8. De Fazio, D., Purdie, D. G., Ott, A. K., Braeuninger-Weimer, P., Khodkov, T., Goossens, S., Taniguchi, T., Watanabe, K., Livreri, P., Koppens, F. H. L., Hofmann, S., Goykhman, I., Ferrari, A. C. & Lombardo, A. High-Mobility, Wet-Transferred Graphene Grown by Chemical Vapor Deposition. *ACS Nano* **13,** 8926–8935 (2019).
9. Cassabois, G., Valvin, P. & Gil, B. Hexagonal boron nitride is an indirect bandgap semiconductor. *Nature Photonics* **10,** 262–266 (2016).
10. Momma, K. & Izumi, F. VESTA 3 for three-dimensional visualization of crystal, volumetric and morphology data. *Journal of Applied Crystallography* **44,** 1272–1276 (2011).
11. Splendiani, A., Sun, L., Zhang, Y., Li, T., Kim, J., Chim, C.-Y., Galli, G. & Wang, F. Emerging Photoluminescence in Monolayer MoS2. *Nano Letters* **10,** 1271–1275 (2010).
12. Zhang, Y. J., Yoshida, M., Suzuki, R. & Iwasa, Y. 2D crystals of transition metal dichalcogenide and their iontronic functionalities. *2D Materials* **2,** 044004 (2015).
13. C. Ferrari, A., Bonaccorso, F., Fal'ko, V., S. Novoselov, K., Roche, S., Bøggild, P., Borini, S., L. Koppens, F. H., Palermo, V., Pugno, N., A. Garrido, J., Sordan, R., Bianco, A., Ballerini, L., Prato, M., Lidorikis, E., Kivioja, J., Marinelli, C., Ryhänen, T., Morpurgo, A., N. Coleman, J., Nicolosi, V., Colombo, L., Fert, A., Garcia-Hernandez, M., Bachtold, A., F. Schneider, G., Guinea, F., Dekker, C., Barbone, M., Sun, Z., Galiotis, C., N. Grigorenko, A., Konstantatos, G., Kis, A., Katsnelson, M., Vandersypen, L., Loiseau, A., Morandi, V., Neumaier, D., Treossi, E., Pellegrini, V., Polini, M., Tredicucci, A., M. Williams, G., Hong, B. H., Ahn, J.-H., Kim, J. M., Zirath, H., Wees, B. J. v., Zant, H. v. d., Occhipinti, L., Matteo, A. D., A. Kinloch, I., Seyller, T., Quesnel, E., Feng, X., Teo, K., Rupesinghe, N., Hakonen, P., T. Neil, S. R., Tannock, Q., Löfwander, T. &

Kinaret, J. Science and technology roadmap for graphene, related two-dimensional crystals, and hybrid systems. *Nanoscale* **7,** 4598–4810 (2015).

14. Zhu, Z. Y., Cheng, Y. C. & Schwingenschlögl, U. Giant spin-orbit-induced spin splitting in two-dimensional transition-metal dichalcogenide semiconductors. *Physical Review B* **84,** 153402 (2011).
15. Schaibley, J. R., Yu, H., Clark, G., Rivera, P., Ross, J. S., Seyler, K. L., Yao, W. & Xu, X. Valleytronics in 2D materials. *Nature Reviews Materials* **1,** 1–15 (2016).
16. Geremew, A. K., Rumyantsev, S., Kargar, F., Debnath, B., Nosek, A., Bloodgood, M. A., Bockrath, M., Salguero, T. T., Lake, R. K. & Balandin, A. A. Bias-Voltage Driven Switching of the Charge-Density-Wave and Normal Metallic Phases in 1T-TaS2 Thin-Film Devices. *ACS Nano* **13,** 7231–7240 (2019).
17. Hamill, A., Heischmidt, B., Sohn, E., Shaffer, D., Tsai, K.-T., Zhang, X., Xi, X., Suslov, A., Berger, H., Forró, L., Burnell, F. J., Shan, J., Mak, K. F., Fernandes, R. M., Wang, K. & Pribiag, V. S. Two-fold symmetric superconductivity in few-layer NbSe2. *Nature Physics* **17,** 949–954 (2021).
18. Freitas, D. C., Weht, R., Sulpice, A., Remenyi, G., Strobel, P., Gay, F., Marcus, J. & Núñez-Regueiro, M. Ferromagnetism in layered metastable 1 T -CrTe $_2$. *Journal of Physics: Condensed Matter* **27,** 176002 (2015).
19. Purbawati, A., Coraux, J., Vogel, J., Hadj-Azzem, A., Wu, N., Bendiab, N., Jegouso, D., Renard, J., Marty, L., Bouchiat, V., Sulpice, A., Aballe, L., Foerster, M., Genuzio, F., Locatelli, A., Menteş, T. O., Han, Z. V., Sun, X., Núñez-Regueiro, M. & Rougemaille, N. In-Plane Magnetic Domains and Néel-like Domain Walls in Thin Flakes of the Room Temperature CrTe2 Van der Waals Ferromagnet. *ACS Applied Materials & Interfaces* **12,** 30702–30710 (2020).
20. Zhang, X., Lu, Q., Liu, W., Niu, W., Sun, J., Cook, J., Vaninger, M., Miceli, P. F., Singh, D. J., Lian, S.-W., Chang, T.-R., He, X., Du, J., He, L., Zhang, R., Bian, G. & Xu, Y. Room-temperature intrinsic ferromagnetism in epitaxial CrTe2 ultrathin films. *Nature Communications* **12,** 2492 (2021).
21. Carr, S., Massatt, D., Fang, S., Cazeaux, P., Luskin, M. & Kaxiras, E. Twistronics: Manipulating the electronic properties of two-dimensional layered structures through their twist angle. *Physical Review B* **95,** 075420 (2017).
22. He, F., Zhou, Y., Ye, Z., Cho, S.-H., Jeong, J., Meng, X. & Wang, Y. Moiré Patterns in 2D Materials: A Review. *ACS Nano* **15,** 5944–5958 (2021).
23. Lu, A.-Y., Zhu, H., Xiao, J., Chuu, C.-P., Han, Y., Chiu, M.-H., Cheng, C.-C., Yang, C.-W., Wei, K.-H., Yang, Y., Wang, Y., Sokaras, D., Nordlund, D., Yang, P., Muller, D. A., Chou, M.-Y., Zhang, X. & Li, L.-J. Janus monolayers of transition metal dichalcogenides. *Nature Nanotechnology* **12,** 744–749 (2017).
24. Zhang, J., Jia, S., Kholmanov, I., Dong, L., Er, D., Chen, W., Guo, H., Jin, Z., Shenoy, V. B., Shi, L. & Lou, J. Janus Monolayer Transition-Metal Dichalcogenides. *ACS Nano* **11,** 8192–8198 (2017).
25. Ju, L., Bie, M., Shang, J., Tang, X. & Kou, L. Janus transition metal dichalcogenides: a superior platform for photocatalytic water splitting. en. *Journal of Physics: Materials* **3,** 022004 (2020).
26. Gong, C., Li, L., Li, Z., Ji, H., Stern, A., Xia, Y., Cao, T., Bao, W., Wang, C., Wang, Y., Qiu, Z. Q., Cava, R. J., Louie, S. G., Xia, J. & Zhang, X. Discovery of intrinsic ferromagnetism in two-dimensional van der Waals crystals. *Nature* **546,** 265–269 (2017).
27. Huang, B., Clark, G., Navarro-Moratalla, E., Klein, D. R., Cheng, R., Seyler, K. L., Zhong, D., Schmidgall, E., McGuire, M. A., Cobden, D. H., Yao, W., Xiao, D., Jarillo-Herrero, P. & Xu, X. Layer-dependent ferromagnetism in a van der Waals crystal down to the monolayer limit. *Nature* **546,** 270–273 (2017).
28. Rassekh, M., He, J., Farjami Shayesteh, S. & Palacios, J. J. Remarkably enhanced Curie temperature in monolayer CrI3 by hydrogen and oxygen adsorption: A first-principles calculations. *Computational Materials Science* **183,** 109820 (2020).

29. Liu, N., Gallaro, C. M., Shayan, K., Mukherjee, A., Kim, B., Hone, J., Vamivakas, N. & Strauf, S. Antiferromagnetic proximity coupling between semiconductor quantum emitters in WSe2 and van der Waals ferromagnets. *Nanoscale* **13,** 832–841 (2021).

30. Seo, J., Kim, D. Y., An, E. S., Kim, K., Kim, G.-Y., Hwang, S.-Y., Kim, D. W., Jang, B. G., Kim, H., Eom, G., Seo, S. Y., Stania, R., Muntwiler, M., Lee, J., Watanabe, K., Taniguchi, T., Jo, Y. J., Lee, J., Min, B. I., Jo, M. H., Yeom, H. W., Choi, S.-Y., Shim, J. H. & Kim, J. S. Nearly room temperature ferromagnetism in a magnetic metal-rich van der Waals metal. *Science Advances* **6** (2020).

31. Andresen, A. F., Zeppezauer, E., Boive, T., Nordström, B. & Brändén, C. Magnetic structure of Cr2Te3, Cr3Te4, and Cr5Te6. *Acta Chem. Scand.* **24,** 3495–3509 (1970).

32. Bertaut, E. F., Roult, G., Aleonard, R., Pauthenet, R., Chevreton, M. & Jansen, R. Structures magnétiques de Cr3X4 (X = S, Se, Te). *Journal de Physique* **25,** 582–595 (1964).

33. Chevreton, M., Bertaut, E. F. & Jellinek, F. Quelques remarques sur le système Cr–Te. *Acta Crystallographica* **16,** 431–431 (1963).

34. Lasek, K., Coelho, P. M., Zberecki, K., Xin, Y., Kolekar, S. K., Li, J. & Batzill, M. Molecular Beam Epitaxy of Transition Metal (Ti-, V-, and Cr-) Tellurides: From Monolayer Ditellurides to Multilayer Self-Intercalation Compounds. *ACS Nano* **14,** 8473–8484 (2020).

35. Gao, Z., Tang, M., Huang, J., Chen, J., Ai, W., Wu, L., Dong, X., Ma, Y., Zhang, Z., Zhang, L., Du, Y., Fu, H., Yuan, H., Wu, J. & Luo, F. Near room-temperature ferromagnetism in air-stable two-dimensional Cr1–xTe grown by chemical vapor deposition. *Nano Research* **15,** 3763–3769 (2022).

36. Sun, X., Li, W., Wang, X., Sui, Q., Zhang, T., Wang, Z., Liu, L., Li, D., Feng, S., Zhong, S., Wang, H., Bouchiat, V., Nunez Regueiro, M., Rougemaille, N., Coraux, J., Purbawati, A., Hadj-Azzem, A., Wang, Z., Dong, B., Wu, X., Yang, T., Yu, G., Wang, B., Han, Z., Han, X. & Zhang, Z. Room temperature ferromagnetism in ultra-thin van der Waals crystals of 1T-CrTe2. *Nano Research* **13,** 3358–3363 (2020).

37. Coughlin, A. L., Zhang, J.-J., Bourji, S., Wei, B., Ye, G., Ye, Z., Hong, J., Zhang, T., Andrade, M., Zhan, X., He, R., Wang, J., Yakobson, B., Losovyj, Y., Chu, C.-W., Deng, L. & Zhang, S. Extreme Air Sensitivity and Nonself-Limited Oxidation of Two-Dimensional Magnetic Tellurides. *ACS Materials Letters,* 1945–1953 (2023).

38. Peierls, R. On Ising's model of ferromagnetism. *Mathematical Proceedings of the Cambridge Philosophical Society* **32,** 477–481 (1936).

39. Wang, Q. H., Bedoya-Pinto, A., Blei, M., Dismukes, A. H., Hamo, A., Jenkins, S., Koperski, M., Liu, Y., Sun, Q.-C., Telford, E. J., Kim, H. H., Augustin, M., Vool, U., Yin, J.-X., Li, L. H., Falin, A., Dean, C. R., Casanova, F., Evans, R. F. L., Chshiev, M., Mishchenko, A., Petrovic, C., He, R., Zhao, L., Tsen, A. W., Gerardot, B. D., Brotons-Gisbert, M., Guguchia, Z., Roy, X., Tongay, S., Wang, Z., Hasan, M. Z., Wrachtrup, J., Yacoby, A., Fert, A., Parkin, S., Novoselov, K. S., Dai, P., Balicas, L. & Santos, E. J. G. The Magnetic Genome of Two-Dimensional van der Waals Materials. *ACS Nano* **16,** 6960–7079 (2022).

40. Song, T., Cai, X., Tu, M. W.-Y., Zhang, X., Huang, B., Wilson, N. P., Seyler, K. L., Zhu, L., Taniguchi, T., Watanabe, K., McGuire, M. A., Cobden, D. H., Xiao, D., Yao, W. & Xu, X. Giant tunneling magnetoresistance in spin-filter van der Waals heterostructures. *Science* **360,** 1214–1218 (2018).

41. Verzhbitskiy, I. A., Kurebayashi, H., Cheng, H., Zhou, J., Khan, S., Feng, Y. P. & Eda, G. Controlling the magnetic anisotropy in Cr2Ge2Te6 by electrostatic gating. *Nature Electronics* **3,** 460–465 (2020).

42. Fei, Z., Huang, B., Malinowski, P., Wang, W., Song, T., Sanchez, J., Yao, W., Xiao, D., Zhu, X., May, A. F., Wu, W., Cobden, D. H., Chu, J.-H. & Xu, X. Two-dimensional itinerant ferromagnetism in atomically thin Fe3GeTe2. *Nature Materials* **17,** 778–782 (2018).

43. Ribeiro, M., Gentile, G., Marty, A., Dosenovic, D., Okuno, H., Vergnaud, C., Jacquot, J.-F., Jalabert, D., Longo, D., Ohresser, P., Hallal, A., Chshiev, M., Boulle, O., Bonell, F. & Jamet, M. Large-scale epitaxy of two-dimensional van der Waals room-temperature ferromagnet Fe5GeTe2. *npj 2D Materials and Applications* **6,** 1–9 (2022).

44. Dieny, B. & Chshiev, M. Perpendicular magnetic anisotropy at transition metal/oxide interfaces and applications. *Rev. Mod. Phys.* **89,** 025008 (2 2017).

45. Fu, S., Kang, K., Shayan, K., Yoshimura, A., Dadras, S., Wang, X., Zhang, L., Chen, S., Liu, N., Jindal, A., Li, X., Pasupathy, A. N., Vamivakas, A. N., Meunier, V., Strauf, S. & Yang, E.-H. Enabling room temperature ferromagnetism in monolayer MoS2 via in situ iron-doping. *Nature Communications* **11,** 2034 (2020).

46. Dijkstra, J., Weitering'i, H. H., van Bruggen, C. F., Haast, C. & de Groot. Band-structurecalculations, and magnetic and transport properties of ferromagnetic chromium tellurides (CrTe, Cr3Te4,Cr,Te,) 22 (1989).

47. Coughlin, A. L., Xie, D., Yao, Y., Zhan, X., Chen, Q., Hewa-Walpitage, H., Zhang, X., Guo, H., Zhou, H., Lou, J., Wang, J., Li, Y. S., Fertig, H. A. & Zhang, S. Near Degeneracy of Magnetic Phases in Two-Dimensional Chromium Telluride with Enhanced Perpendicular Magnetic Anisotropy. *ACS Nano* **14,** 15256–15266 (2020).

48. Pramanik, T., Roy, A., Dey, R., Rai, A., Guchhait, S., Movva, H. C., Hsieh, C.-C. & Banerjee, S. K. Angular dependence of magnetization reversal in epitaxial chromium telluride thin films with perpendicular magnetic anisotropy. *Journal of Magnetism and Magnetic Materials* **437,** 72–77 (2017).

49. Wen, Y., Liu, Z., Zhang, Y., Xia, C., Zhai, B., Zhang, X., Zhai, G., Shen, C., He, P., Cheng, R., Yin, L., Yao, Y., Getaye Sendeku, M., Wang, Z., Ye, X., Liu, C., Jiang, C., Shan, C., Long, Y. & He, J. Tunable Room-Temperature Ferromagnetism in Two-Dimensional Cr $_2$ Te $_3$. *Nano Letters* **20,** 3130–3139 (2020).

50. Fujisawa, Y., Pardo-Almanza, M., Garland, J., Yamagami, K., Zhu, X., Chen, X., Araki, K., Takeda, T., Kobayashi, M., Takeda, Y., Hsu, C. H., Chuang, F. C., Laskowski, R., Khoo, K. H., Soumyanarayanan, A. & Okada, Y. Tailoring magnetism in self-intercalated Cr1+xTe 2 epitaxial films. *Physical Review Materials* **4,** 114001 (2020).

51. Lasek, K., Coelho, P. M., Gargiani, P., Valvidares, M., Mohseni, K., Meyerheim, H. L., Kostanovskiy, I., Zberecki, K. & Batzill, M. Van der Waals epitaxy growth of 2D ferromagnetic Cr(1+δ)Te2 nanolayers with concentration-tunable magnetic anisotropy. *Applied Physics Reviews* **9,** 011409 (2022).

52. Luo, F.-S., Ying, J.-S., Zhang, Y., Li, S.-S., Tang, F., Chen, T.-W., Wang, Z.-C., Zhang, S.-J., Fang, Y. & Zheng, R.-K. The effects of substrate temperature on the magnetic and magnetotransport properties of Cr1-xTe epitaxial films. *Journal of Magnetism and Magnetic Materials* **550,** 169084 (2022).

53. Li, H., Wang, L., Chen, J., Yu, T., Zhou, L., Qiu, Y., He, H., Ye, F., Sou, I. K. & Wang, G. Molecular Beam Epitaxy Grown Cr $_2$ Te $_3$ Thin Films with Tunable Curie Temperatures for Spintronic Devices. *ACS Applied Nano Materials* **2,** 6809–6817 (2019).

54. Zhou, J., Song, X., Chai, J., Wong, N. L. M., Xu, X., Jiang, Y., Feng, Y. P., Yang, M. & Wang, S. Structure dependent and strain tunable magnetic ordering in ultrathin chromium telluride. *Journal of Alloys and Compounds* **893,** 162223 (2022).

55. Li, Q.-Q., Li, S., Wu, D., Ding, Z.-K., Cao, X.-H., Huang, L., Pan, H., Li, B., Chen, K.-Q. & Duan, X.-D. Magnetic properties manipulation of CrTe2 bilayer through strain and self-intercalation. *Applied Physics Letters* **119,** 162402 (2021).

56. Baibich, M. N., Broto, J. M., Fert, A., Van Dau, F. N., Petroff, F., Etienne, P., Creuzet, G., Friederich, A. & Chazelas, J. Giant Magnetoresistance of (001)Fe/(001)Cr Magnetic Superlattices. *Physical Review Letters* **61,** 2472–2475 (1988).

57. Binasch, G., Grünberg, P., Saurenbach, F. & Zinn, W. Enhanced magnetoresistance in layered magnetic structures with antiferromagnetic interlayer exchange. *Physical Review B* **39,** 4828–4830 (1989).
58. Herman, F. & Skillman, S. *Atomic structure calculations* (Prentice-Hall, 1963).
59. Dyakonov, M. I. & Perel, V. I. Current-induced spin orientation of electrons in semiconductors. *Physics Letters A* **35,** 459–460 (1971).
60. Kato, Y. K., Myers, R. C., Gossard, A. C. & Awschalom, D. D. Observation of the Spin Hall Effect in Semiconductors. *Science* **306,** 1910–1913 (2004).
61. Wang, Y., Deorani, P., Qiu, X., Kwon, J. H. & Yang, H. Determination of intrinsic spin Hall angle in Pt. *Applied Physics Letters* **105,** 152412 (2014).
62. Mellnik, A. R., Lee, J. S., Richardella, A., Grab, J. L., Mintun, P. J., Fischer, M. H., Vaezi, A., Manchon, A., Kim, E.-A., Samarth, N. & Ralph, D. C. Spin-transfer torque generated by a topological insulator. *Nature* **511,** 449–451 (2014).
63. Bychkov, Y. A. & Rashba, E. I. Oscillatory effects and the magnetic susceptibility of carriers in inversion layers. *Journal of Physics C: Solid State Physics* **17,** 6039 (1984).
64. *Introduction to topology* `https://horizonofreason.com/magic/topological-magic-tricks/` (2023).
65. Slonczewski, J. C. Current-driven excitation of magnetic multilayers. *Journal of Magnetism and Magnetic Materials* **159,** L1–L7 (1996).
66. Miron, I. M., Garello, K., Gaudin, G., Zermatten, P.-J., Costache, M. V., Auffret, S., Bandiera, S., Rodmacq, B., Schuhl, A. & Gambardella, P. Perpendicular switching of a single ferromagnetic layer induced by in-plane current injection. *Nature* **476,** 189–193 (2011).
67. Lin, X. & Zhu, L. Magnetization switching in van der Waals systems by spin-orbit torque. *Materials Today Electronics* **4,** 100037 (2023).
68. Yang, H., Valenzuela, S. O., Chshiev, M., Couet, S., Dieny, B., Dlubak, B., Fert, A., Garello, K., Jamet, M., Jeong, D.-E., Lee, K., Lee, T., Martin, M.-B., Kar, G. S., Sénéor, P., Shin, H.-J. & Roche, S. Two-dimensional materials prospects for non-volatile spintronic memories. *Nature* **606,** 663–673 (2022).
69. Shao, Q., Yu, G., Lan, Y.-W., Shi, Y., Li, M.-Y., Zheng, C., Zhu, X., Li, L.-J., Amiri, P. K. & Wang, K. L. Strong Rashba-Edelstein Effect-Induced Spin–Orbit Torques in Monolayer Transition Metal Dichalcogenide/Ferromagnet Bilayers. *Nano Letters* **16,** 7514–7520 (2016).
70. Yao, Q.-F., Cai, J., Tong, W.-Y., Gong, S.-J., Wang, J.-Q., Wan, X., Duan, C.-G. & Chu, J. H. Manipulation of the large Rashba spin splitting in polar two-dimensional transition-metal dichalcogenides. *Physical Review B* **95,** 165401 (2017).
71. Vélez-Fort, E., Hallal, A., Sant, R., Guillet, T., Abdukayumov, K., Marty, A., Vergnaud, C., Jacquot, J.-F., Jalabert, D., Fujii, J., Vobornik, I., Rault, J., Brookes, N. B., Longo, D., Ohresser, P., Ouerghi, A., Veuillen, J.-Y., Mallet, P., Boukari, H., Okuno, H., Chshiev, M., Bonell, F. & Jamet, M. Ferromagnetism and Rashba Spin–Orbit Coupling in the Two-Dimensional (V,Pt)Se2 Alloy. *ACS Applied Electronic Materials* **4,** 259–268 (2022).
72. Zhang, Y., Tan, Y.-W., Stormer, H. L. & Kim, P. Experimental observation of the quantum Hall effect and Berry's phase in graphene. *Nature* **438,** 201–204 (2005).
73. Chen, J., Wang, L., Zhang, M., Zhou, L., Zhang, R., Jin, L., Wang, X., Qin, H., Qiu, Y., Mei, J., Ye, F., Xi, B., He, H., Li, B. & Wang, G. Evidence for Magnetic Skyrmions at the Interface of Ferromagnet/Topological-Insulator Heterostructures. *Nano Letters* **19,** 6144–6151 (2019).
74. Kang, W., Huang, Y., Zhang, X., Zhou, Y. & Zhao, W. Skyrmion-Electronics: An Overview and Outlook. *Proceedings of the IEEE* **104,** 2040–2061 (2016).

75. Chen, J., Zhou, L., Wang, L., Yan, Z., Deng, X., Zhou, J., Mei, J.-w., Qiu, Y., Xi, B., Wang, X., He, H. & Wang, G. Conformal Growth of Cr $_2$ Te $_3$ on Bi $_2$ Te $_3$ Nanodots with a Topological Hall Effect. *Crystal Growth & Design* **22,** 140–147 (2022).

76. Zhou, L., Chen, J., Chen, X., Xi, B., Qiu, Y., Zhang, J., Wang, L., Zhang, R., Ye, B., Chen, P., Zhang, X., Guo, G., Yu, D., Mei, J.-W., Ye, F., Wang, G. & He, H. Topological Hall Effect in Traditional Ferromagnet Embedded with Black-Phosphorus-Like Bismuth Nanosheets. *ACS Applied Materials & Interfaces* **12,** 25135–25142 (2020).

77. Jeon, J. H., Na, H. R., Kim, H., Lee, S., Song, S., Kim, J., Park, S., Kim, J., Noh, H., Kim, G., Jerng, S.-K. & Chun, S.-H. Emergent Topological Hall Effect from Exchange Coupling in Ferromagnetic Cr2Te3/Noncoplanar Antiferromagnetic Cr2Se3 Bilayers. *ACS Nano,* 9 (2022).

78. Saha, R., Meyerheim, H. L., Göbel, B., Hazra, B. K., Deniz, H., Mohseni, K., Antonov, V., Ernst, A., Knyazev, D., Bedoya-Pinto, A., Mertig, I. & Parkin, S. S. P. Observation of Néel-type skyrmions in acentric self-intercalated Cr1+δTe2. *Nature Communications* **13,** 3965 (2022).

79. Fijalkowski, K., Hartl, M., Winnerlein, M., Mandal, P., Schreyeck, S., Brunner, K., Gould, C. & Molenkamp, L. Coexistence of Surface and Bulk Ferromagnetism Mimics Skyrmion Hall Effect in a Topological Insulator. *Physical Review X* **10,** 011012 (2020).

80. Tai, L., Dai, B., Li, J., Huang, H., Chong, S. K., Wong, K. L., Zhang, H., Zhang, P., Deng, P., Eckberg, C., Qiu, G., He, H., Wu, D., Xu, S., Davydov, A., Wu, R. & Wang, K. L. Distinguishing the Two-Component Anomalous Hall Effect from the Topological Hall Effect. *ACS Nano* **16,** 17336–17346 (2022).

81. Ueno, K., Saiki, K., Shimada, T. & Koma, A. Epitaxial growth of transition metal dichalcogenides on cleaved faces of mica. *Journal of Vacuum Science & Technology A* **8,** 68–72 (1990).

82. Ohuchi, F. S., Parkinson, B. A., Ueno, K. & Koma, A. van der Waals epitaxial growth and characterization of MoSe2 thin films on SnS2. *Journal of Applied Physics* **68,** 2168–2175 (1990).

83. Kumar, B., Baraket, M., Paillet, M., Huntzinger, J.-R., Tiberj, A., Jansen, A., Vila, L., Cubuku, M., Vergnaud, C., Jamet, M., Lapertot, G., Rouchon, D., Zahab, A.-A., Sauvajol, J.-L., Dubois, L., Lefloch, F. & Duclairoir, F. Growth protocols and characterization of epitaxial graphene on SiC elaborated in a graphite enclosure. *Physica E: Low-dimensional Systems and Nanostructures* **75,** 7–14 (2016).

84. Malard, L. M., Pimenta, M. A., Dresselhaus, G. & Dresselhaus, M. S. Raman spectroscopy in graphene. *Physics Reports* **473,** 51–87 (2009).

85. Vergnaud, C., Dau, M.-T., Grévin, B., Licitra, C., Marty, A., Okuno, H. & Jamet, M. New approach for the molecular beam epitaxy growth of scalable WSe2 monolayers. *Nanotechnology* **31,** 255602 (2020).

86. Buschow, K. H. J., Cahn, R. W., Flemings, M. C., Ilschner, B., Kramer, E. J. & Mahajan, S. Encyclopedia of Materials: Science and Technology. *MRS Bulletin* **29,** 512–512 (2004).

87. Ohresser, P., Otero, E., Choueikani, F., Chen, K., Stanescu, S., Deschamps, F., Moreno, T., Polack, F., Lagarde, B., Daguerre, J.-P., Marteau1, F., Scheurer, F., Joly, L., Kappler, J.-P., Muller, B., Bunau, O. & Sainctavit, P. DEIMOS: A beamline dedicated to dichroism measurements in the 350–2500 eV energy range. *Review of Scientific Instruments* **85,** 013106 (2014).

88. Thole, B. T., Carra, P., Sette, F. & van der Laan, G. X-ray circular dichroism as a probe of orbital magnetization. *Physical Review Letters* **68,** 1943–1946 (1992).

89. *Klayout open source software* `https://www.klayout.de/`.

90. Figueiredo-Prestes, N., Tsipas, P., Krishnia, S., Pappas, P., Peiro, J., Fragkos, S., Zatko, V., Lintzeris, A., Dlubak, B., Chaitoglou, S., Heuken, M., Reyren, N., Jaffrès, H., Seneor, P., Dimoulas, A. & George, J.-M. Large Fieldlike Spin-Orbit Torque and Magnetization Manipulation in a Fully Epitaxial van der Waals Two-Dimensional-Ferromagnet/Topological-Insulator Heterostructure Grown by Molecular-Beam Epitaxy. *Physical Review Applied* **19,** 014012 (2023).

91. Guillet, Q., Vojáček, L., Dosenovic, D., Ibrahim, F., Boukari, H., Li, J., Choueikani, F., Ohresser, P., Ouerghi, A., Mesple, F., Renard, V., Jacquot, J.-F., Jalabert, D., Okuno, H., Chshiev, M., Vergnaud, C., Bonell, F., Marty, A. & Jamet, M. Epitaxial van der Waals heterostructures of Cr_2Te_3 on two-dimensional materials. *Physical Review Materials* **7,** 054005 (2023).

92. Pierucci, D., Mahmoudi, A., Silly, M., Bisti, F., Oehler, F., Patriarche, G., Bonell, F., Marty, A., Vergnaud, C., Jamet, M., Boukari, H., Lhuillier, E., Pala, M. & Ouerghi, A. Evidence for highly p-type doping and type II band alignment in large scale monolayer WSe 2 /Se-terminated GaAs heterojunction grown by molecular beam epitaxy. *Nanoscale* **14,** 5859–5868 (2022).

93. Ohtake, A. & Sakuma, Y. Evolution of Surface and Interface Structures in Molecular-Beam Epitaxy of MoSe2 on GaAs(111)A and (111)B. *Crystal Growth & Design* **17,** 363–367 (2017).

94. Bonell, F., Cuxart, M. G., Song, K., Robles, R., Ordejón, P., Roche, S., Mugarza, A. & Valenzuela, S. O. Growth of Twin-Free and Low-Doped Topological Insulators on BaF2(111). *Crystal Growth & Design* **17,** 4655–4660 (2017).

95. Li, Y.-Y., Wang, G., Zhu, X.-G., Liu, M.-H., Ye, C., Chen, X., Wang, Y.-Y., He, K., Wang, L.-L., Ma, X.-C., Zhang, H.-J., Dai, X., Fang, Z., Xie, X.-C., Liu, Y., Qi, X.-L., Jia, J.-F., Zhang, S.-C. & Xue, Q.-K. Intrinsic Topological Insulator Bi2Te3 Thin Films on Si and Their Thickness Limit. *Advanced Materials* **22,** 4002–4007 (2010).

96. Lee, I. H., Choi, B. K., Kim, H. J., Kim, M. J., Jeong, H. Y., Lee, J. H., Park, S.-Y., Jo, Y., Lee, C., Choi, J. W., Cho, S. W., Lee, S., Kim, Y., Kim, B. H., Lee, K. J., Heo, J. E., Chang, S. H., Li, F., Chittari, B. L., Jung, J. & Chang, Y. J. Modulating Curie Temperature and Magnetic Anisotropy in Nanoscale-Layered Cr2Te3 Films: Implications for Room-Temperature Spintronics. *ACS Applied Nano Materials* **4,** 4810–4819 (2021).

97. Nečas, D. & Klapetek, P. Gwyddion: an open-source software for SPM data analysis. *Central European Journal of Physics* **10,** 181–188 (1 2012).

98. Kresse, G. & Hafner, J. *Ab initio* molecular-dynamics simulation of the liquid-metal–amorphous-semiconductor transition in germanium. *Physical Review B* **49,** 14251–14269 (1994).

99. Kresse, G. & Furthmüller, J. Efficiency of ab-initio total energy calculations for metals and semiconductors using a plane-wave basis set. *Computational Materials Science* **6,** 15–50 (1996).

100. Perdew, J. P., Burke, K. & Ernzerhof, M. Generalized Gradient Approximation Made Simple. *Physical Review Letters* **77,** 3865–3868 (1996).

101. Choudhary, K., Garrity, K. F., Hartman, S. T., Pilania, G. & Tavazza, F. Efficient Computational Design of 2D van der Waals Heterostructures: Band-Alignment, Lattice-Mismatch, Web-app Generation and Machine-learning. *arXiv preprint arXiv:2004.03025* (2020).

102. Dudarev, S. L., Botton, G. A., Savrasov, S. Y., Humphreys, C. J. & Sutton, A. P. Electron-energy-loss spectra and the structural stability of nickel oxide: An LSDA+U study. *Physical Review B* **57,** 1505–1509 (1998).

103. Grimme, S., Antony, J., Ehrlich, S. & Krieg, H. A consistent and accurate *ab initio* parametrization of density functional dispersion correction (DFT-D) for the 94 elements H-Pu. *The Journal of Chemical Physics* **132,** 154104 (2010).

104. Grimme, S., Ehrlich, S. & Goerigk, L. Effect of the damping function in dispersion corrected density functional theory. *Journal of Computational Chemistry* **32,** 1456–1465 (2011).

105. Wang, C., Zhu, X., Nilsson, L., Wen, J., Wang, G., Shan, X., Zhang, Q., Zhang, S., Jia, J. & Xue, Q. In situ Raman spectroscopy of topological insulator Bi2Te3 films with varying thickness. *Nano Research* **6,** 688–692 (2013).

106. Hallal, A., Dieny, B. & Chshiev, M. Impurity-induced enhancement of perpendicular magnetic anisotropy in Fe/MgO tunnel junctions. *Physical Review B* **90,** 064422 (2014).

107. Roy, A., Guchhait, S., Dey, R., Pramanik, T., Hsieh, C.-C., Rai, A. & Banerjee, S. K. Perpendicular Magnetic Anisotropy and Spin Glass-like Behavior in Molecular Beam Epitaxy Grown Chromium Telluride Thin Films. *ACS Nano* **9,** 3772–3779 (2015).

108. Bruno, P. Tight-binding approach to the orbital magnetic moment and magnetocrystalline anisotropy of transition-metal monolayers. *Physical Review B* **39,** 865–868 (1989).

109. Giancoli, D. C. Physics for Scientists and Engineers Third Edition. *Physics Education* **35,** 370 (2000).

110. Wei, Y., Zhang, Y., Liu, Z., Wang, Y., Ke, F., Meng, J., Guo, Y., Ma, P., Feng, Q. & Gan, Z. High quality and large-scale manually operated monolayer graphene pasters. *Nanotechnology* **25,** 275704 (2014).

111. Chi, H., Ou, Y., Eldred, T. B., Gao, W., Kwon, S., Murray, J., Dreyer, M., Butera, R. E., Foucher, A. C., Ambaye, H., Keum, J., Greenberg, A. T., Liu, Y., Neupane, M. R., de Coster, G. J., Vail, O. A., Taylor, P. J., Folkes, P. A., Rong, C., Yin, G., Lake, R. K., Ross, F. M., Lauter, V., Heiman, D. & Moodera, J. S. Strain-tunable Berry curvature in quasi-two-dimensional chromium telluride. *Nature Communications* **14,** 3222 (2023).

112. Fujisawa, Y., Pardo-Almanza, M., Hsu, C.-H., Mohamed, A., Yamagami, K., Krishnadas, A., Chang, G., Chuang, F.-C., Khoo, K. H., Zang, J., Soumyanarayanan, A. & Okada, Y. Widely Tunable Berry Curvature in the Magnetic Semimetal Cr1+δTe2. *Advanced Materials* **35,** 2207121 (2023).

113. Bian, M., He, K., Seddon, S. D., Milde, P., Huai, C., Zang, J., Sabirianov, R., Bird, J. P., Cheng, X., Miao, G., *et al. Unconventional Anomalous Hall Effect in Cr2Te3 Thin Films* `https://www.intermag2023digest.com/AH-09_COC-10.pdf`.

114. Wang, X., Yates, J. R., Souza, I. & Vanderbilt, D. Ab initio calculation of the anomalous Hall conductivity by Wannier interpolation. *Physical Review B* **74,** 195118 (2006).

115. Mostofi, A. A., Yates, J. R., Pizzi, G., Lee, Y.-S., Souza, I., Vanderbilt, D. & Marzari, N. An updated version of wannier90: A tool for obtaining maximally-localised Wannier functions. *Computer Physics Communications* **185,** 2309–2310 (2014).

116. Tsirkin, S. S. High performance Wannier interpolation of Berry curvature and related quantities with WannierBerri code. *npj Computational Materials* **7,** 33 (2021).

117. Destraz, D., Das, L., Tsirkin, S. S., Xu, Y., Neupert, T., Chang, J., Schilling, A., Grushin, A. G., Kohlbrecher, J., Keller, L., Puphal, P., Pomjakushina, E. & White, J. S. Magnetism and anomalous transport in the Weyl semimetal PrAlGe: possible route to axial gauge fields. *npj Quantum Materials* **5,** 5 (2020).

118. Li, C., Liu, K., Jiang, D., Jin, C., Pei, T., Wen, T., Yue, B. & Wang, Y. Diverse Thermal Expansion Behaviors in Ferromagnetic Cr1-dTe with NiAs-Type, Defective Structures. *Inorganic Chemistry* **61,** 14641–14647 (2022).

119. Caton, R., Sarachik, M. P. & Bloomfield, P. E. Hall coefficient of dilute Cu-Au(Fe) alloys. I. Experiment. *Physical Review B* **10,** 2987–2994 (1974).

120. Garello, K., Miron, I. M., Avci, C. O., Freimuth, F., Mokrousov, Y., Blügel, S., Auffret, S., Boulle, O., Gaudin, G. & Gambardella, P. Symmetry and magnitude of spin–orbit torques in ferromagnetic heterostructures. *Nature Nanotechnology* **8,** 587–593 (2013).

121. Yan, B. & Felser, C. Topological Materials: Weyl Semimetals. *Annual Review of Condensed Matter Physics* **8,** 337–354 (2017).

122. Liu, Z. K., Yang, L. X., Sun, Y., Zhang, T., Peng, H., Yang, H. F., Chen, C., Zhang, Y., Guo, Y. F., Prabhakaran, D., Schmidt, M., Hussain, Z., Mo, S.-K., Felser, C., Yan, B. & Chen, Y. L. Evolution of the Fermi surface of Weyl semimetals in the transition metal pnictide family. *Nature Materials* **15,** 27–31 (2016).

123. Labracherie, V. *Electrical transport in nanostructures of the Weyl semimetal WTe2* PhD thesis (Université Grenoble Alpes [2020-....] ; Technische Universität (Dresde, Allemagne), 2021).

124. Tang, S., Zhang, C., Wong, D., Pedramrazi, Z., Tsai, H.-Z., Jia, C., Moritz, B., Claassen, M., Ryu, H., Kahn, S., Jiang, J., Yan, H., Hashimoto, M., Lu, D., Moore, R. G., Hwang, C.-C., Hwang, C., Hussain, Z., Chen, Y., Ugeda, M. M., Liu, Z., Xie, X., Devereaux, T. P., Crommie, M. F., Mo, S.-K. & Shen, Z.-X. Quantum spin Hall state in monolayer 1T'-WTe2. *Nature Physics* **13,** 683–687 (2017).

125. Fatemi, V., Wu, S., Cao, Y., Bretheau, L., Gibson, Q. D., Watanabe, K., Taniguchi, T., Cava, R. J. & Jarillo-Herrero, P. Electrically tunable low-density superconductivity in a monolayer topological insulator. *Science* **362,** 926–929 (2018).

126. Zhao, B., Khokhriakov, D., Zhang, Y., Fu, H., Karpiak, B., Hoque, A. M., Xu, X., Jiang, Y., Yan, B. & Dash, S. P. Observation of Spin Hall Effect in Weyl Semimetal WTe2 at Room Temperature. *Physical Review Research* **2,** 013286 (2020).

127. Li, P., Wu, W., Wen, Y., Zhang, C., Zhang, J., Zhang, S., Yu, Z., Yang, S. A., Manchon, A. & Zhang, X.-x. Spin-momentum locking and spin-orbit torques in magnetic nano-heterojunctions composed of Weyl semimetal WTe2. *Nature Communications* **9,** 3990 (2018).

128. Walsh, L. A., Yue, R., Wang, Q., Barton, A. T., Addou, R., Smyth, C. M., Zhu, H., Kim, J., Colombo, L., Kim, M. J., Wallace, R. M. & Hinkle, C. L. W Te $_2$ thin films grown by beam-interrupted molecular beam epitaxy. *2D Materials* **4,** 025044 (2017).

129. Cao, Y., Sheremetyeva, N., Liang, L., Yuan, H., Zhong, T., Meunier, V. & Pan, M. Anomalous vibrational modes in few layer WTe $_2$ revealed by polarized Raman scattering and first-principles calculations. *2D Materials* **4,** 035024 (2017).

130. Tang, S., Zhang, C., Jia, C., Ryu, H., Hwang, C., Hashimoto, M., Lu, D., Liu, Z., Devereaux, T. P., Shen, Z.-X. & Mo, S.-K. Electronic structure of monolayer 1T‘-MoTe2 grown by molecular beam epitaxy. *APL Materials* **6,** 026601 (2017).

131. Mogi, M., Tsukazaki, A., Kaneko, Y., Yoshimi, R., Takahashi, K. S., Kawasaki, M. & Tokura, Y. Ferromagnetic insulator Cr2Ge2Te6 thin films with perpendicular remanence. *APL Materials* **6,** 091104 (2018).

Appendix

A Normalisation of the XAS and XMCD experimental curves

For the acquisition of XAS and XMCD spectra at a given field B, 8 scans are recorded: 2 measurements for each combination of ± B, $\sigma\pm$, with σ the light helicity. The averaged XAS and XMCD signals are then expressed with the formulas:

$$XAS_{avg} = \frac{XAS(+B,\sigma+) + XAS(-B,\sigma-) + XAS(+B,\sigma-) + XAS(-B,\sigma+)}{4} \tag{A.1}$$

$$XMCD_{avg} = \frac{XAS(+B,\sigma+) + XAS(-B,\sigma-) - XAS(+B,\sigma-) - XAS(-B,\sigma+)}{4} \tag{A.2}$$

The base intensity of the XAS profile is normalized with a simple division by the value at the pre edge of Cr (565 eV). The XAS L_3 edge intensity is then defined as shown in Fig. A.1. The XMCD intensity is calculated as the dichroism (highlighted at the L_3 edge energy in the right panel) divided by the XAS L_3 edge intensity. As a result, the XMCD intensity is expressed as a percentage of the XAS L_3 edge intensity.

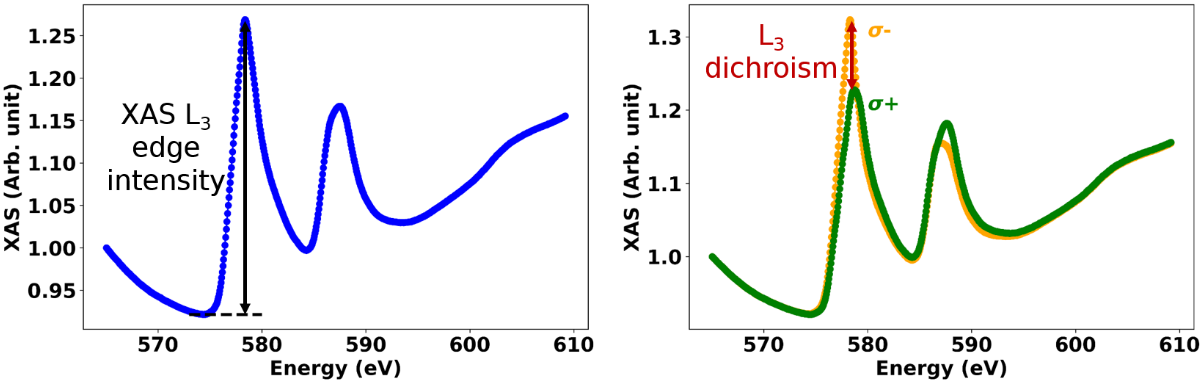

Figure A.1: On the left, average XAS spectrum of 5 ML of Cr_2Te_3 deposited on graphene/SiC. A perpendicular magnetic field of ± 3 T is applied. The XAS L_3 edge intensity is defined as the difference between the value at the L_3 edge energy and the one just before the edge. On the right, the XAS signals for left and right circular polarized light.

During the beamtime, it was also possible to record hysteresis loops as presented in the manuscript. A different undulator was used, which allowed to switch light polarization for each measurement point. The measurement of a full hysteresis cycle requires between 20 min and 1h, depending on the number of measurement points desired. Drift of the alignment cannot be neglected on these time scales. In order to solve this issue, the signals for both light helicities were recorded one after the other, before the change of the magnetic field to the next value. The time difference for each point was thus reduced under one minute, a time length over which the drift is negligible. Moreover, the dichroism was measured at two energy values during the magnetic field sweep: the maximum of the dichroism in the L_3 edge as well as a preedge value (565 eV).

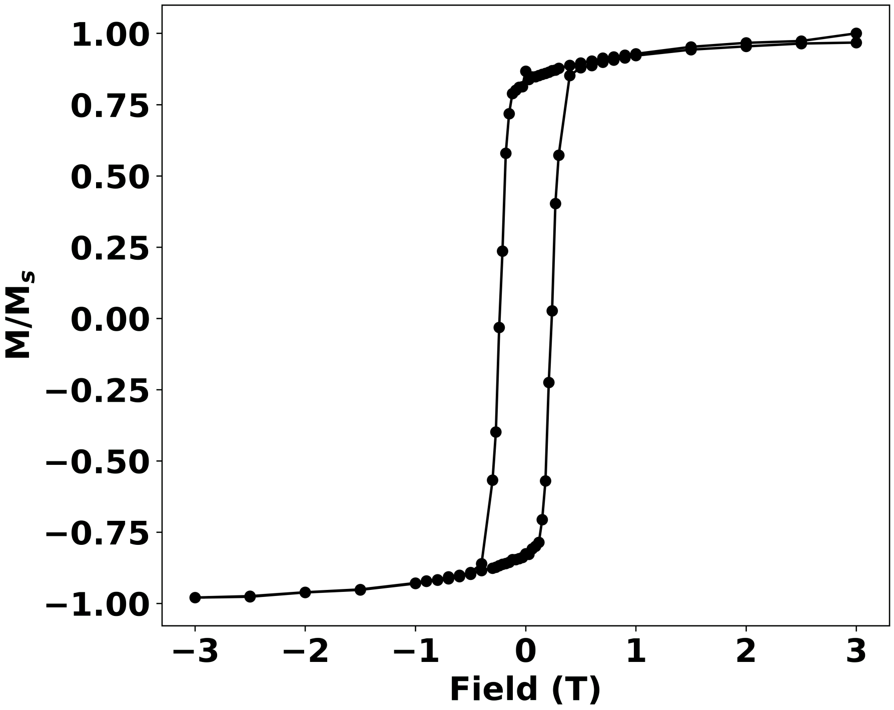

Figure A.2: Hysteresis loop of Cr_2Te_3/Graphene/SiC measured at 5 K with a perpendicular applied magnetic field.

The plotted signal in Fig. A.2 is the difference between the dichroism at the two energies, which allows to correct possible drift.